Additive Manufacturing in Biotechnology

Methods, Inks and Analytics for Biocatalytic Applications of Extrusion-Based 3D Bioprinting

Zur Erlangung des akademischen Grades eines
Doktors der Ingenieurwissenschaften (Dr.-Ing.)

von der KIT-Fakultät für Chemieingenieurwesen und Verfahrenstechnik des
Karlsruher Instituts für Technologie (KIT)
genehmigte

Dissertation

von
Lukas Fabian Wenger, M. Sc.
aus Ehingen (Donau)

Erstgutachter:	Prof. Dr. Jürgen Hubbuch
Zweitgutachter:	Prof. Dr.-Ing. Bastian E. Rapp

Tag der mündlichen Prüfung: 25.07.2022

„Science, my lad, is made up of mistakes, but they are mistakes which it is useful to make, because they lead little by little to the truth.“

— Jules Verne

Acknowledgements

This thesis is the product of a lot of sweat and time, but also of encouragement, support and successful team work. I would like to thank all those people who added the latter group of ingredients and made writing this thesis a journey worthwhile having.

First of all, I would like to thank Prof. Dr. Jürgen Hubbuch for the opportunity to do my PhD at the department of Biomolecular Separation Engineering. Thank you for your enthusiasm for new technologies, for your support and trust, for valuable scientific input and productive ideas, and for the freedom to pursue interesting topics that crossed my path.

I would also like to thank Prof. Dr.-Ing. Bastian Rapp for taking the time to attentively examine my thesis as a second reviewer and for his interest in the topic.

To Kersten Rabe from the Institute for Biological Interfaces 1, thank you for the great cooperation and the valuable scientific exchange about enzymes and enzyme kinetics.

For the successful and pleasant collaborations, I would like to express my gratitude to my colleagues Michael Wörner, Carsten Radtke and Svenja Strauß. Michael, your scientific input on the dark arts of chemistry was invaluable for our project and I enjoyed learning from you. Carsten, thank you for your initiative and drive to launch new projects together with me and for introducing me to the secrets of liquid handling stations. Svenja, I really enjoyed working with you and cannot thank you enough for never bringing our tennis-related rivalry to the lab.

My students André Bouché, Laura Kuger, Jacqueline Göpper, Eva Gerisch, Max Kollmann and Matthias Heusel deserve my special gratitude for their valuable work in the lab, their commitment and their intellectual contributions to the respective projects.

A special thank you to all the many colleagues and office mates I had the pleasure of meeting at the institute, you made my time at uni a unique and memorable chapter in my life through entertaining lunch and coffee breaks, delicious cakes, unforgettable seminars and conferences, on- and off-topic office discussions, numerous sports events and competitions, sweat-inducing gym sessions, and, of course, many (in-)famous Snablehouse Parties and pub visits. Thank you also for the outstanding work environment with smooth administration processes, reliable IT support, an excellent and well-maintained lab, fruitful scientific exchange and a great team spirit.

I would like to express a very cordial thank you to all my friends – at home, abroad and wherever – for making life outside university worth living and for demonstrating the true priorities in life. A very special thank you to the members of the Karlsruhe bioengineering gang (Christian, Anna, Eva, Ursula and Marina) with whom I spent countless studying sessions, power Thursdays and memorable nights and with whom I will hopefully spend many more nostalgic reunions.

Narmin, your company, support and chemistry advice have been an essential part of my life, both in and outside of university. I am deeply thankful for you being there and I am looking forward to what the future holds.

Finally, a most heartfelt thank you goes to my family for being the most reliable constant in my life. To my brother, thank you for your shaping influence on me and the great time I am having when I am at home. And to my parents, thank you for investing so much in me and always supporting me despite having barely any clue about what I was actually doing. May this thesis help you understand.

Abstract

In the last decade, Additive Manufacturing (AM) has evolved from a specialized niche application to a widely used standard tool that has become indispensable in many areas of research and industry. Due to new technologies and materials enabling the fabrication of high quality products, AM is not only relevant for Rapid Prototyping, but also in the fabrication of products for end users. Especially when a high degree of customization or geometrical complexity is involved, AM methods can be considered as viable options. In medicine and biochemical engineering, AM is typically employed for applications like the fabrication of dental implants and mouthguards or for customized lab equipment, microfluidic devices and even chromatography columns. The combination of biological materials and living cells with AM methods has resulted in the establishment of bioprinting as a separate field with new opportunities and challenges. Bioprinting methods allow the fabrication of soft, water-based materials suitable for the physical entrapment of enzymes. This allows biocatalytic reactors to be directly printed using enzyme-loaded inks.

The present thesis aims at extending the toolbox for the fabrication of biocatalytically active materials with a focus on extrusion-based bioprinting. Novel inks are established in combination with specifically adapted printing setups to achieve enhanced printability. To assess the performance of different materials regarding the resulting biocatalytic activity, microplate-based activity assays are established for two different enzymes. The inks and hydrogels are characterized using a range of additional analytical methods like rheology, mechanical testing or scanning electron microscopy. To determine the permeability of hydrogels for substrate molecules, a microfluidics-based method for the estimation of diffusion coefficients in hydrogels is developed. As a general contribution to the improvement of process monitoring and control in extrusion-based bioprinting, a PID-based pressure control is established to generate a constant and reproducible ink flow.

In an initial study, a novel material system for the printing of enzymatically active structures was established by employing high internal phase emulsions (HIPEs) as inks. HIPEs are emulsions that contain at least 74 % (v/v) of internal phase which corresponds to the densest possible packing of droplets before deformation occurs. Polymerizable oily monomers were used as the external phase of the HIPEs and poly(ethylene glycol) diacrylate and acrylic acid were added to the aqueous internal phase. Oil- and water-soluble photoinitiators were added to the respective phases, as well. Polymerizing these inks resulted in the formation of an open-porous polymer scaffold filled with an interconnected hydrogel. This approach enables the fabrication of composite materials with hydrogel-like properties like the diffusibility for substrate and product molecules, while exhibiting higher mechanical stability due to the supportive effect of the polymer scaffold. Also, the formulation

of inks as emulsion results in rheological properties favorable for extrusion-based printing. To allow the production of small HIPE batches, a customized setup was established based on a 3D-printed helical stirrer blade that allowed the production of HIPEs in 50 mL Falcon tubes. The small scale production allowed adding the enzyme β-galactosidase to the aqueous phase by minimizing material waste. Rheological measurements with a range of different HIPE compositions showed that HIPEs with a high amount of surfactant in the external phase and with a high volume fraction of inner phase displayed higher yield stress values which correlate with printability. In general, the produced HIPEs displayed excellent rheological properties. Electron scanning microscopy showed that both the external and internal phase of the HIPEs could be polymerized. A cure-on-dispense setup with four UV LEDs was developed to allow the polymerization of the inks during extrusion which reduced ink spreading and improved printing quality further. Hollow cylinders of enzyme-containing inks were printed to perform activity assays in 48-well microplates. The results showed that the HIPEs were more biocatalytically active when they contained high amounts of monomer in the aqueous phase and a high aqueous phase volume fraction. The presence of at least 7 % (w/w) monomer in the aqueous phase caused a more than fivefold increase in measured activity compared to HIPEs without monomer in the aqueous phase. The diameter of the printer nozzle could be identified as another important parameter influencing the resulting specific activity. This observation could be attributed to the mass transfer limitations caused by the matrix material which makes high surface-area-to-volume ratios favorable.

To cover a wider range of ink types, the second and third study of the thesis aimed at investigating inks based on agarose and agar. These inks demonstrated very different material properties compared to HIPEs, both in a fluid state as inks and in a solidified state as hydrogels. To adapt to the requirements of these inks, the hardware of the printing setup and the employed analytical techniques were again specifically adapted to the investigated inks. Diffusibility for substrate and product molecules was identified as one of the most important properties of the materials regarding their suitability for the immobilization of enzymes. Thus, a microfluidics-based method to estimate the diffusion coefficient of an analyte within transparent hydrogels was established. A microfluidic chip with three inlets and a y-junction was employed to create an interface between the hydrogel to be investigated and an analyte solution. For that purpose, liquid ink was injected at elevated temperature into the chip from one side, until it reached the y-junction. After the gelation of the ink, the analyte solution was injected through one of the other inlets and the diffusion of the analyte through the hydrogel was monitored using a UV area imaging system. Diffusion coefficients could be estimated by fitting the obtained analyte concentration profiles along the microfluidic channel with an analytical solution of Fick's second law of diffusion. As a case study, the diffusion coefficient of lysozyme was compared in a range of hydrogels made from different concentrations of unmodified agarose and low-melt hydroxyethyl agarose. It was found that the diffusion coefficient of 5(6)-carboxyfluorescein was slightly higher in unmodified agarose hydrogels compared to low-melt agarose hydrogels. This aligns well with the theoretical prediction that the polymer networks of low-melt agarose hydrogels exhibit smaller pore sizes. The same trend was found for polymer concentration where higher concentrations were associated with lower diffusion coefficients and smaller pores.

In a third study, inks based on low-melt agarose and agar were investigated as a less complex alternative to HIPE-based inks. The thermogelling behavior of agarose- and agar-based inks required a different printing setup than the photopolymerizable HIPEs. A heatable nozzle consisting of a 3D-printed metal body, a temperature sensor and a heating filament was implemented in the printer setup to ensure that the inks could be extruded in a liquid state at a defined temperature. The setup

also drastically reduced nozzle clogging. The inks were extruded onto a cooled substrate to accelerate the gelation process and reduce ink spreading. While the customized setup enhanced printability significantly compared to previous studies with agarose-based inks, it was still drastically inferior to the printability of HIPEs, both regarding strand thickness and achievable complexity like overhangs. Only basic grid structures without overhangs could be printed. A polymer concentration of at least 4.5 % (w/w) was found to be beneficial for printing and grid structures of 2 cm in height could be fabricated. Using rheological methods, the inks were analyzed for their flow properties and their melting and gelling behavior. The low-melt agarose showed drastically reduced gelling and melting temperatures compared to the agar inks. The solidified hydrogels were subjected to mechanical testing. A set of analytical methods established in the previous studies was reapplied to evaluate the agarose- and agar-based hydrogels with regards to their application in enzyme immobilization. For that purpose, the thermostable enzyme esterase 2 from *Alicyclobacillus acidocaldarius* was added to the liquid inks before printing. Microplate-based activity assays were used to analyze the enzymatic activity and leaching behavior of printed hydrogel samples, while the microfluidics-based method was employed to determine the diffusibility of the hydrogels for 5(6)-carboxyfluorescein, the product of the reaction catalyzed by esterase 2 in the employed activity assay. It was found that the agar-based hydrogels showed higher diffusibility and activity, but also increased enzyme leaching. The tendency for enzyme leaching not only demonstrated the lacking suitability of agar-based hydrogels for the employment in perfused reactors, it also explains the seemingly positive results in the performed activity assays, as leached enzyme is not exposed to the same mass transfer limitations as immobilized enzyme resulting in enhanced observed activity. Due to their low enzyme leaching and acceptable printability, agarose inks with a concentration of at least 4.5 % (w/w) were recommended as suitable inks for the application in biocatalytic reactors.

Independent of ink type, the previous studies revealed a general lack of reproducibility in pneumatically driven bioprinting caused by unsteady and poorly reproducible ink flow rates. Besides ink viscosity and extrusion pressure, additional factors like cartridge fill level, partial nozzle clogging and ink inhomogeneities were suspected to influence the extrusion flow rate and cause imperfections in the resulting prints. Batch-to-batch variations and temperature fluctuations influencing the ink viscosity posed additional challenges. In the study investigating agarose- and agar-based inks, every printed sample was weighed before being used for activity assays and discarded if it did not comply with the set target weight within a specified margin of error. When necessary, the extrusion pressure was manually adapted to ensure the comparability of the printed samples. As a consequence, a study was initiated to establish in-line process monitoring of the ink flow rate as an essential process parameter and to develop an automated and reproducible method to generate a constant target flow rate by continuously adapting the extrusion pressure based on real-time flow rate data. To obtain the required data in an in-line measurement, a liquid flow meter was integrated into the setup of a pneumatically driven bioprinter using a 3D-printed mount. A Python-based software tool was developed to communicate with the flow sensor and to process the data input. A PID loop was implemented and fed with the real-time flow rate data. Based on the data input, the software continuously adapted the extrusion pressure of the printer. Three different case studies were performed to assess the performance of the PID control setup:

a) Continuous dispensing: Several runs of continuous dispensing demonstrated the automatic pressure adjustment to consistently meet a specified target flow rate independently of the user. Compared to the constant pressure setting, the adaptive pressure control proved effective in compensating for environmental or system-related influences like nozzle clogging. b) Adaptation to ink inhomogeneities: A more realistic use case was investigated by printing hollow cylinders from

a cartridge filled with layers of two differently concentrated poloxamer 407 inks to simulate ink inhomogeneities. The adaptive pressure control was able to generate a constant flow rate by adapting the pressure appropriately during the printing process. As a result, relatively consistent cylinders could be printed, whereas the constant pressure setting resulted in cylinders with strongly deviating wall thicknesses. c) Process transfer to other nozzle types: To demonstrate the simple process transferability between different experimental setups, test prints were carried out with three different nozzle types with the same orifice diameter. The adaptive pressure control was able to generate the same constant flow rate with all three nozzle types within an adjustment phase of 30 to 60 s. The resulting cylinders were of consistent quality, independent of the nozzle. Prints with constant pressure setting suffered from a lack or abundance of extruded ink, if not performed with a pressure specifically determined for the corresponding nozzle type. The performance of the PID-regulated adaptive pressure control demonstrated that it can contribute to making extrusion-based bioprinting more reliable and reduce the need for extensive parameter screenings in process development.

Overall, the present work provides a toolbox for the printing of biocatalytically active materials. Novel inks with individually adapted printing methods and analytical techniques are presented. The application of emulsion-based inks demonstrates the wide range of materials that can be applied in combination with enzymes despite not being suitable matrices in tissue engineering. Material screenings can be accelerated by employing microplate-based activity assays and the adaptation of the printing setup specifically for each type of ink shows the need for fine-tuning between ink and printing method. The more universal approach to improve reproducibility in bioprinting using a PID-based pressure control could be valuable for applications outside the scope of biocatalysis.

Zusammenfassung

In den letzten zehn Jahren hat sich die Additive Fertigung (AM) von einer spezialisierten Nischenanwendung zu einem weit verbreiteten Standardwerkzeug entwickelt, das in vielen Bereichen der Forschung und Industrie unverzichtbar geworden ist. Dank neuer Technologien und Materialien, die die Herstellung hochwertiger Produkte ermöglichen, ist AM nicht nur für das schnelle Anfertigen von Prototypen relevant, sondern auch für die Herstellung von Produkten für Endverbraucher. Vor allem bei Produkten mit hohem Bedarf für kundenspezifische Anpassungen oder bei Produkten mit hoher geometrischer Komplexität können AM-Methoden als sinnvolle Alternative zu anderen Fertigungsverfahren in Betracht gezogen werden. In der Medizin und Bioverfahrenstechnik wird AM typischerweise für Anwendungen wie die Herstellung von Zahnimplantaten und Zahnschienen oder für maßgeschneiderte Laborgeräte, mikrofluidische Systeme und sogar Chromatographiesäulen eingesetzt. Die Kombination von biologischen Materialien und lebenden Zellen mit AM-Methoden hat dazu geführt, dass sich das Bioprinting als eigenständiger Bereich mit neuen Möglichkeiten und Herausforderungen etabliert hat. Bioprinting-Methoden ermöglichen die Herstellung von Objekten aus weichen, wasserbasierten Materialien, die sich für den physikalischen Einschluss von Enzymen eignen. Dadurch können biokatalytische Reaktoren direkt mit enzymhaltigen Tinten gedruckt werden.

Die vorliegende Arbeit zielt darauf ab, neue Werkzeuge für die Herstellung biokatalytisch aktiver Materialien zu schaffen, wobei der Schwerpunkt auf extrusionsbasiertem Bioprinting liegt. Neuartige Tinten werden in Kombination mit speziell angepassten Druckmethoden etabliert, um eine verbesserte Druckbarkeit zu erreichen. Um die Eignung der verschiedenen Materialien hinsichtlich der resultierenden biokatalytischen Aktivität zu bewerten, werden mikroplattenbasierte Aktivitätsassays mit zwei verschiedenen Enzymen und einer Reihe von 3D-gedruckten Materialien durchgeführt. Die Tinten und Hydrogele werden mit einer Reihe weiterer Analysemethoden wie Rheologie, mechanischen Tests oder Rasterelektronenmikroskopie charakterisiert. Um die Durchlässigkeit von Hydrogelen für Substratmoleküle zu bestimmen, wird eine auf Mikrofluidik basierende Methode zur Abschätzung von Diffusionskoeffizienten in Hydrogelen entwickelt. Als allgemeiner Beitrag zur Verbesserung der Prozessüberwachung und -steuerung beim extrusionsbasierten Bioprinting wird eine PID-basierte Drucksteuerung etabliert, um einen konstanten und reproduzierbaren Tintenfluss zu erzeugen.

In einer ersten Studie wurde ein neuartiges Materialsystem für das Drucken enzymatisch aktiver Strukturen etabliert, indem hochkonzentrierte Emulsionen (high internal phase emulsions – HIPEs) als Tinten verwendet wurden. HIPEs sind Emulsionen, die mindestens 74 % (v/v) an innerer Phase enthalten, was der dichtesten möglichen Packung von Tröpfchen entspricht, bevor

eine Verformung eintritt. Als äußere Phase der HIPEs wurden polymerisierbare ölige Monomere verwendet und der wässrigen inneren Phase wurden Poly(ethylenglycol)diacrylat und Acrylsäure zugesetzt. Auch öl- bzw. wasserlösliche Photoinitiatoren wurden den jeweiligen Phasen zugesetzt. Die Polymerisation der Tinten führte zur Bildung eines offenporigen Polymergerüsts, das mit untereinander vernetzten Hydrogeltröpfchen gefüllt ist. Dieser Ansatz ermöglicht die Herstellung von Kompositmaterialien mit hydrogelähnlichen Eigenschaften wie der Durchlässigkeit für Substrat- und Produktmoleküle bei gleichzeitig höherer mechanischer Stabilität aufgrund der stützenden Wirkung des Polymergerüsts. Tinten für den extrusionsbasierten 3D-Druck als Emulsionen zu formulieren bringt deutliche Vorteile hinsichtlich der rheologischen Eigenschaften der Tinten, da Emulsionen aufgrund ihrer Fließgrenze ideal für Extrusionsdruck geeignet sind. Um die Herstellung kleiner Volumina von HIPEs zu ermöglichen, wurde ein maßgeschneiderter Aufbau auf der Grundlage eines 3D-gedruckten spiralförmigen Rührblatts entwickelt, der die Herstellung von HIPEs in 50-mL-Falcon-Röhrchen ermöglichte. Durch die Minimierung von Materialverlust erlaubte die Produktion in kleinem Maßstab die Zugabe des Enzyms β-Galactosidase. Rheologische Messungen mit einer Reihe verschiedener HIPE-Zusammensetzungen zeigten, dass HIPEs mit einem hohen Anteil an Tensid in der äußeren Phase und mit einem hohen Volumenanteil an innerer Phase eine höhere Fließgrenze aufwiesen, was als Indikator für Druckbarkeit gilt. Im Allgemeinen wiesen die hergestellten HIPEs hervorragende rheologische Eigenschaften auf. Rasterelektronenmikroskopische Aufnahmen zeigten, dass sowohl die äußere, als auch die innere Phase der HIPEs polymerisiert werden konnte. Ein Versuchsaufbau mit vier um die Extrusionskanüle des Biodruckers herum angeordneten UV-LEDs wurde entwickelt, um die Polymerisation der Tinten während der Extrusion zu ermöglichen, was das Zerlaufen des Materials reduziert und so die Druckqualität weiter verbessert. Es wurden Hohlzylinder mit enzymhaltiger Tinte gedruckt, um Aktivitätsmessungen in 48-Well-Mikroplatten durchzuführen. Die Ergebnisse zeigten, dass die HIPEs biokatalytisch aktiver waren, wenn sie große Mengen an Monomer in der wässrigen Phase und einen hohen Volumenanteil an wässriger Phase enthielten. Die Anwesenheit von mindestens 7 % (v/v) Monomer in der wässrigen Phase führte zu einer mehr als fünffachen Steigerung der gemessenen Aktivität im Vergleich zu HIPEs ohne Monomer in der wässrigen Phase. Der Durchmesser der Extrusionskanüle konnte als weiterer wichtiger Parameter identifiziert werden, der die resultierende Aktivität beeinflusst. Diese Beobachtung könnte auf die durch das Trägermaterial bedingte Verringerung des Stofftransports zurückzuführen sein, die ein hohes Verhältnis von Oberfläche zu Volumen allgemein vorteilhaft macht.

Um ein breiteres Spektrum an Tintentypen abzudecken, wurden in der zweiten und dritten Studie dieser Arbeit Tinten auf der Basis von Agarose und Agar untersucht. Diese Tinten wiesen im Vergleich zu HIPEs deutlich andere Materialeigenschaften auf, sowohl im flüssigen Zustand als Tinte, als auch im verfestigten Zustand als Hydrogel. Um den Anforderungen dieser Tinten gerecht zu werden, wurden der Versuchsaufbau für den Druck und die eingesetzten Analyseverfahren speziell an die untersuchten Tinten angepasst. Die Durchlässigkeit für Substrat- und Produktmoleküle wurde als eine der wichtigsten Eigenschaften der Materialien hinsichtlich ihrer Eignung für die Immobilisierung von Enzymen identifiziert. Daher wurde eine auf Mikrofluidik basierende Methode zur Schätzung des Diffusionskoeffizienten eines Analyten in transparenten Hydrogelen entwickelt. Ein mikrofluidischer Chip mit drei Einlässen und einer Y-Verzweigung wurde verwendet, um eine Grenzfläche zwischen dem zu untersuchenden Hydrogel und einer Analytlösung zu schaffen. Zu diesem Zweck wurde flüssige Tinte bei erhöhter Temperatur von einer Seite in den Chip injiziert, bis sie die Y-Verzweigung erreichte. Nach dem Ausgelieren der Tinte wurde die Analytlösung durch einen der anderen Einlässe injiziert und die Diffusion des Analyten durch das Hydrogel wurde mit einem UV-Flächendetektor überwacht. Die Diffusionskoeffizienten konnten durch das Fitten

der gemessenen Konzentrationsprofile des Analyten entlang des mikrofluidischen Kanals mit einer analytischen Lösung des zweiten Fick'schen Diffusionsgesetzes geschätzt werden. In einer Fallstudie wurde der Diffusionskoeffizient von Lysozym in einer Reihe von Hydrogelen bestimmt und verglichen. Die untersuchten Hydrogele bestanden aus unterschiedlichen Konzentrationen von unmodifizierter Agarose bzw. modifizierter Hydroxyethylagarose mit niedrigem Schmelzpunkt. Es wurde festgestellt, dass der Diffusionskoeffizient von 5(6)-Carboxyfluorescein in unmodifizierten Agarosehydrogelen etwas höher war als in Agarosehydrogelen mit niedrigem Schmelzpunkt. Dies stimmt gut mit der theoretischen Vorhersage überein, dass das Polymernetzwerk von Hydrogelen aus Agarose mit niedrigem Schmelzpunkt kleinere Porengrößen aufweist. Der gleiche Trend wurde für die Polymerkonzentration festgestellt, wobei höhere Konzentrationen mit niedrigeren Diffusionskoeffizienten und kleineren Poren einhergingen.

In einer dritten Studie wurden Tinten auf Basis von Agarose mit niedrigem Schmelzpunkt und Agar als weniger komplexe Alternative zu Tinten auf HIPE-Basis untersucht. Das Gelierungsverhalten von Agarose- und Agarbasierten Tinten erforderte einen anderen Versuchsaufbau für den Druck als die photopolymerisierbaren HIPEs. Eine beheizbare Düse, bestehend aus einem 3D-gedruckten Metallkörper, einem Temperatursensor und einem Heizdraht, wurde in den Aufbau implementiert, um sicherzustellen, dass die Tinten in flüssigem Zustand bei einer definierten Temperatur extrudiert werden konnten. Die Tinten wurden auf ein gekühltes Substrat extrudiert, um den Gelierungsprozess zu beschleunigen und das Zerlaufen der Tinte zu reduzieren. Obwohl das individuell an die Tinten angepasste Equipment die Druckbarkeit im Vergleich zu früheren Studien mit agarosebasierten Tinten deutlich verbesserte, war sie der Druckbarkeit von HIPEs immer noch drastisch unterlegen, sowohl hinsichtlich der erzeugten Strangdicke, als auch bzgl. der erreichbaren geometrischen Komplexität. Es konnten nur einfache Gitterstrukturen ohne Überhänge gedruckt werden. Eine Polymerkonzentration von mindestens 4,5 % (w/w) erwies sich als vorteilhaft für den Druck, wobei Gitterstrukturen mit einer Höhe von 2 cm druckbar waren. Mit rheologischen Methoden wurden die Tinten auf ihre Fließeigenschaften sowie ihr Schmelz- und Gelierverhalten untersucht. Die Agarose mit niedrigem Schmelzpunkt zeigte im Vergleich zu den Agartinten wie erwartet deutlich reduzierte Gelier- und Schmelztemperaturen. Die verfestigten Hydrogele wurden einer mechanischen Prüfung unterzogen. Eine Reihe der in den vorherigen Studien etablierten Analysemethoden wurden erneut angewandt, um die Hydrogele auf Agarose- und Agarbasis im Hinblick auf ihre Anwendung für die Immobilisierung von Enzymen zu bewerten. Zu diesem Zweck wurde den Tinten vor dem Druck das thermostabile Enzym Esterase 2 aus *Alicyclobacillus acidocaldarius* zugegeben. Zur Messung der enzymatischen Aktivität und des Auswaschens von Enzym aus den gedruckten Hydrogelproben wurden mikrotiterplattenbasierte Aktivitätsassays verwendet. Die mikrofluidikbasierte Methode zur Bestimmung von Diffusionskoeffizienten wurde eingesetzt, um die Durchlässigkeit der Hydrogele für 5(6)-Carboxyfluorescein zu bestimmen. Es wurde festgestellt, dass die agarbasierten Hydrogele eine höhere Diffusionsfähigkeit und Aktivität aufwiesen, aber auch eine erhöhte Auswaschung von Enzym. Die Tendenz zum Auswaschen des Enzyms zeigte nicht nur die mangelnde Eignung von agarbasierten Hydrogelen für den Einsatz in durchströmten Reaktoren, sondern erklärt auch die scheinbar positiven Ergebnisse bei den durchgeführten Aktivitätsassays, da das ausgewaschene Enzym nicht mehr denselben Stofftransportbeschränkungen ausgesetzt ist wie immobilisiertes Enzym und dadurch eine höhere Aktivität aufweist. Aufgrund der geringen Auswaschung von Enzym und der akzeptablen Druckbarkeit wurden Agarosetinten mit einer Konzentration von mindestens 4,5 % (w/w) als geeignete Tinten für die Anwendung in biokatalytischen Reaktoren empfohlen.

Unabhängig vom Tintentyp zeigten die bisherigen Studien einen allgemeinen Mangel an Reproduzierbarkeit bei pneumatischen Bioprinting-Verfahren, der auf schwankende und schlecht

reproduzierbare Flussraten bei der Extrusion der Tinten zurückzuführen ist. Es wurde vermutet, dass neben der Viskosität der Tinte und dem Extrusionsdruck noch zusätzliche Faktoren wie der Füllstand der Kartusche, die teilweise Verstopfung der Düsen und Inhomogenitäten der Tinte die Extrusionsflussrate beeinflussen und Unregelmäßigkeiten in den Druckergebnissen verursachen. Unterschiede zwischen verschiedenen Tintenchargen und Temperaturschwankungen, die die Viskosität der Tinte beeinflussen, stellten eine zusätzliche Herausforderung dar. In der Studie zu agarose- und agarbasierten Tinten wurde jede gedruckte Probe gewogen, bevor sie für Aktivitätsmessungen verwendet wurde, und verworfen, wenn sie das vorgegebene Zielgewicht nicht innerhalb einer bestimmten Fehlertoleranz erreichte. Falls erforderlich, wurde der Extrusionsdruck manuell angepasst, um die Vergleichbarkeit der gedruckten Proben zu gewährleisten. Infolgedessen wurde eine Studie initiiert, um eine Inline-Prozessüberwachung für die Durchflussrate als wesentlichen Prozessparameter zu etablieren und eine automatisierte und reproduzierbare Methode zu entwickeln, um eine konstante Zielflussrate zu erzeugen, indem der Extrusionsdruck auf der Grundlage von Echtzeitflussdaten kontinuierlich angepasst wird. Um die benötigten Daten in einer Inline-Messung zu erhalten, wurde ein Durchflusssensor in den Aufbau eines pneumatischen Biodruckers mittels einer 3D-gedruckten Halterung integriert. Für die Kommunikation mit dem Flusssensor und die Verarbeitung der gemessenen Daten wurde ein auf Python basierendes Softwaretool entwickelt. Eine PID-Regelung wurde implementiert und mit den Echtzeit-Durchflussdaten gespeist. Auf Grundlage der eingespeisten Daten passte die Software den Extrusionsdruck des Druckers kontinuierlich an. Es wurden drei verschiedene Fallstudien durchgeführt, um die Leistung der PID-Regelung zu bewerten:

a) Kontinuierliche Extrusion: Mehrere Durchläufe mit kontinuierlicher Extrusion zeigten, dass die automatische Druckanpassung erfolgreich eine vorgegebene Zielflussrate unabhängig vom Benutzer einstellen konnte. Im Vergleich zur konstanten Druckeinstellung erwies sich die adaptive Druckregelung als effektiv bei der Kompensation von umwelt- oder systembedingten Einflüssen wie Verstopfungen der Extrusionskanüle. b) Anpassung an Tinteninhomogenitäten: Ein realistischerer Anwendungsfall wurde untersucht, indem Hohlzylinder mittels einer Kartusche gedruckt wurden, die mit Schichten aus zwei unterschiedlich konzentrierten Poloxamer-407-Tinten gefüllt war, um Tinteninhomogenitäten zu simulieren. Die adaptive Druckregelung erwies sich als wirksam, eine konstante Durchflussrate zu erzeugen, indem der Druck während des Druckvorgangs entsprechend angepasst wurde. Dadurch konnten relativ gleichmäßige Zylinder gedruckt werden, während die konstante Druckeinstellung zu Zylindern mit stark voneinander abweichenden Wandstärken führte. c) Prozessübertragung auf andere Düsentypen: Um die Übertragbarkeit von Prozessen zwischen verschiedenen Versuchsaufbauten zu demonstrieren, wurden Testdrucke mit drei verschiedenen Typen von Extrusionskanülen mit gleichem Öffnungsdurchmesser durchgeführt. Die adaptive Druckregelung war in der Lage, mit allen drei Extrusionskanülen innerhalb von 30 to 60 s die gewünschte Zielflussrate zu erzeugen. Die resultierenden Zylinder waren von gleichbleibender Qualität, unabhängig von der Kanüle. Beim Drucken mit konstanter Druckeinstellung wurde entweder zu wenig oder zu viel Tinte extrudiert, wenn der Druck nicht speziell für den entsprechenden Typ von Kanüle festgelegt wurde. Es wurde gezeigt, dass die PID-gesteuerte adaptive Druckregelung dazu beitragen kann, das extrusionsbasierte Bioprinting zuverlässiger zu machen und die Notwendigkeit umfangreicher Parameter-Screenings bei der Prozessentwicklung zu verringern.

Die vorliegende Arbeit demonstriert neue Methoden für das Drucken von biokatalytisch aktiven Materialien. Es werden neuartige Tinten mit individuell angepassten Druckverfahren und analytischen Techniken vorgestellt. Die Anwendung von emulsionsbasierten Tinten zeigt die große Bandbreite an Materialien, die in Kombination mit Enzymen eingesetzt werden können. Materialscreenings können durch den Einsatz von Aktivitätsassays im Mikrotiterplattenformat beschleunigt

werden. Die speziell für jede Tintenart angepassten Druckmethoden zeigen die Notwendigkeit einer Feinabstimmung zwischen Tinte und Druckverfahren. Der universelle Ansatz zur Verbesserung der Reproduzierbarkeit im pneumatischen Bioprinting unter Verwendung einer PID-basierten Druckregelung könnte auch für Anwendungen außerhalb der Biokatalyse von Nutzen sein.

Contents

1

Introduction

The disruptive nature of *Additive Manufacturing*, commonly called *3D printing*, has caused a substantial hype in manufacturing technology, especially over the last decade. A considerable amount of research and development effort has been invested to improve printing methods and materials and to find suitable fields of application to exploit the possibilities offered by the new technology. In a still continuing process of maturation, 3D printing has found its way into many fields of industry and research. It is mainly established as a flexible tool for Rapid Prototyping in research and for the production of specialized products with a low number of units or with complex geometries that are difficult or impossible to be produced using conventional methods [1]. With the more widespread commercial availability of 3D printing as a standard tool of fabrication, it has also found its way into sectors not directly related to the manufacturing industry. In medicine and life sciences like chemistry, biology or biotechnology, the amount of publications related to 3D printing has skyrocketed in the last decade. Figure 1.1 shows the number of results for the search term *3D printing* in the PubMed database[1] which contains abstracts of publications related to fields like medicine, life sciences or bioengineering. Between 2011 and 2021, the number of annual publications containing the term *3D printing* in the abstract increased from 13 to nearly 4000. A typical example of a practical application of 3D printing in medicine is the use of 3D-printed mouthguards [2, 3] or dental implants [4] which can be produced on the basis of intraoral 3D scans [5] and might even allow personalized oral drug delivery in the future [6].

Alongside the applications with conventional materials like plastics, metal and ceramics, a particular subbranch of 3D printing employing entirely different types of materials has emerged from the field of tissue engineering. The aim of this field is the fabrication of artificial substitute materials mimicking natural tissues. These materials contain living cells and can be used in lab-on-a-chip applications or as medical implants. To accommodate cells in an adequate aqueous environment, the use of hydrogels as matrix materials has been shown to be a suitable approach [7]. Hydrogels are polymer-based materials with a high water content [8] that allow the diffusion of oxygen and

[1] accessible via `https://pubmed.ncbi.nlm.nih.gov/`

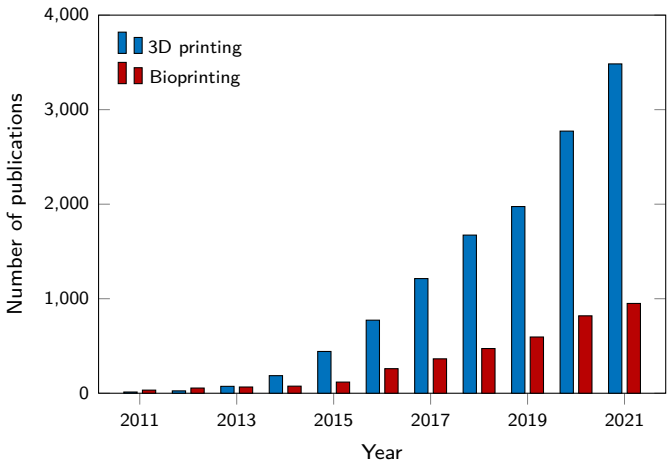

Figure 1.1 Number of entries in the PubMed database (`https://pubmed.ncbi.nlm.nih.gov/`) matching the search keywords *3D printing* and *bioprinting*. The PubMed database selectively lists abstracts of literature from the fields of biomedicine, life sciences, bioengineering and related disciplines.

nutrients and provide cell-friendly conditions similar to the extracellular matrix of natural tissues [9, 10]. The application of 3D printing methods specialized for hydrogel-based materials – summarized under the term *bioprinting* – allows the fabrication of constructs with customized geometries like simple grids or more complex structures imitating the vascularization of natural tissues. The presence of such three-dimensional (3D) structures is essential for the supply of the embedded cells with oxygen and nutrients. Analogous to 3D printing, there was a strong surge in new publications covering the topic of bioprinting, as represented by the number of search results in the PubMed data base which increased from 33 in 2011 to 950 in 2021 (see Figure 1.1).

Recently, bioprinting methods have been increasingly adopted for the fabrication of cell-free hydrogels which can be applied as smart materials or in biocatalysis. Smart materials exhibit certain special properties like shape memory or self-healing behavior. Due to the time-related aspect of these properties, the printing of smart materials is often referred to as *4D printing* [11]. The feasibility of applying bioprinting methods for the fabrication of biocatalytic reactors has been demonstrated before [12]. The present thesis aims at improving the employed printing methods, establishing novel inks for the immobilization of enzymes and developing suitable analytical techniques to assess the performance of the printed materials. The following sections provide a basic theoretical background on 3D (bio-)printing and biocatalysis.

1.1 Additive Manufacturing and 3D printing

3D printing has emerged in the 1980s as a new approach of manufacturing three-dimensional objects from virtual computer-aided design (CAD) models by sequentially adding layers of material to generate the desired three-dimensional shape. The term *Additive Manufacturing* (AM) has been established as a counterpart to subtractive manufacturing methods like drilling and machining and is mostly used synonymously to the more popular term *3D printing* [13]. Together with formative manufacturing (i. e. methods like casting and forging), additive and subtractive manufacturing form the three pillars of manufacturing technology [14]. Today, the available variety of materials and

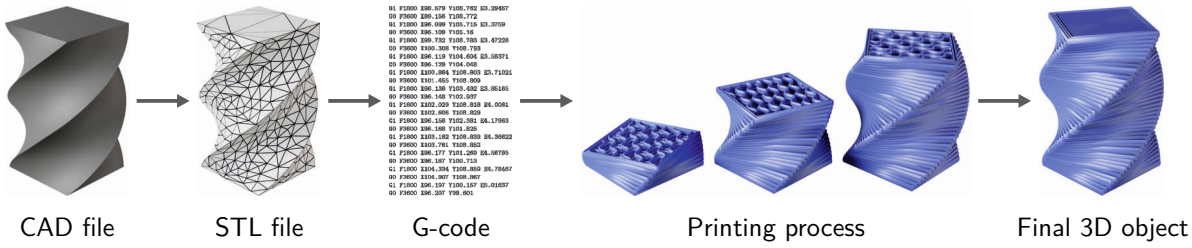

Figure 1.2 Typical workflow in 3D printing, shown exemplarily for FDM. An object is digitally modeled using CAD software and exported as an STL file. To provide the 3D printer with instructions, the object is sliced into layers and tool paths in the form of G-code are generated. The G-code is executed by the 3D printer to fabricate the final object.

printing methods has allowed AM to become a standard tool in research and industry. An overview of the field of AM with a focus on bioprinting is given in the following sections.

1.1.1 Concept, history and economic implications

The basic principle of AM is the automated stacking and merging of thin layers of material to generate physical objects from virtual 3D models which can be obtained from 3D scans or created by computer-aided design (CAD) [13–15]. This process requires several steps that can vary depending on the employed software and equipment. A typical workflow is exemplarily represented for fused deposition modeling (see Section 1.1.3.1) in Figure 1.2. First, the 3D CAD model is converted to an STL file, a file format that approximates the surface of the model by triangles and can be regarded as an unofficial industry standard [14]. Several different meanings of the abbreviation STL are reported, e. g. *standard transformation language* [14], *standard tessellation language* [15] or *stereolithography language* [14]. The 3D printing process is prepared using computer-aided manufacturing (CAM) software. The STL model is digitally sliced into layers with even thickness. To enable the 3D printer to fabricate and stack the single layers, appropriate instructions for the movements of the 3D printer are generated, e. g. in the form of G-code [4, 16]. Finally, the 3D printer executes the generated instructions to build up the desired structure.

The first report of a functional Rapid Prototyping technique using a photopolymerizable resin and selective curing dates back to a publication by Hideo Kodama in 1981 [17, 18]. A patent application from 1980 expired without completing the Japanese patent process [19]. Instead, Charles „Chuck“ Hull invented stereolithography (SLA) in 1984 and was issued a patent in 1986 [20] which led to the foundation of the company 3D Systems and the first commercial SLA printer in the world in 1988 [19]. Worldwide developments in the area of 3D printing followed and more patents were issued for other 3D printing techniques like selective laser sintering (SLS) [21] or fused deposition modeling (FDM) [22]. The expiration of the FDM patent around 2005 allowed the emergence of open source 3D printer projects like RepRap and Fab@Home which led to a range of affordable FDM printers like the Prusa Mendel or MakerBot Thing-O-Matic being widely available to private consumers. Crowd-funded printers like the B9Creator based on digital light processing (DLP) technology or the Form 1 stereolithography printer followed [19].

The potentially disruptive nature of AM [23] and its rapid spread in the industrial and private sector caused a significant hype within the manufacturing industry resulting in often unrealistic expectations and predictions like the full replacement of mass manufacturing with mass customization [24]. Despite potential benefits of AM compared to traditional manufacturing like reduced waste

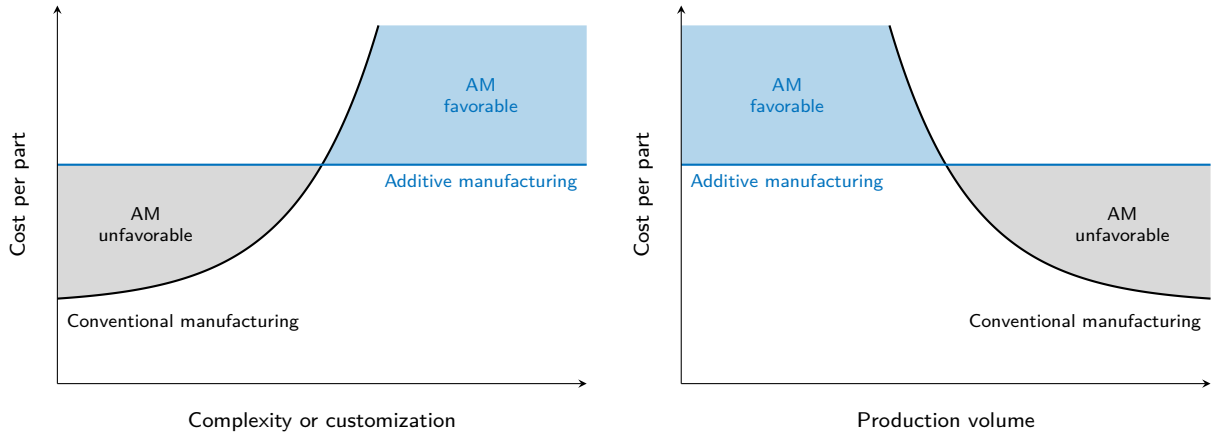

Figure 1.3 Qualitative depiction of the cost per part in dependence of complexity, customization and production volume for Additive Manufacturing (AM) compared to conventional manufacturing. Using Additive Manufacturing methods is more cost-efficient than conventional methods for parts with a high degree of complexity or customization and for parts with low production volumes. Figure adapted from [25, 26].

and increased flexibility [13], the reality of economic constraints still determines reasonable use cases for AM. The fabrication of custom-made parts or small series parts are typical applications where the use of AM can be economically viable because high investments for molds are not necessary [13]. High production volumes are mostly cheaper and faster to produce by conventional methods. This relationship is qualitatively represented in Figure 1.3 which depicts the cost per part to be constant for AM while for conventional manufacturing, it increases with complexity and degree of customization and decreases with production volume [25].

1.1.2 Advantages and limitations

Besides the unmatched flexibility offered by AM which makes it ideal for Rapid Prototyping and customization, it also offers a range of other potential benefits over conventional manufacturing. Processes like injection molding are subjected to a range of design limitations like the need for release angles, cooling channels or injection optimization by flow simulation. AM usually allows the fabrication of parts with complex geometries in one piece and with few restrictions regarding the freedom of design [1, 14].

Unlike subtractive manufacturing methods, AM does not inherently produce waste material, making it potentially advantageous from a sustainability viewpoint. However, additional factors like energy consumption and different raw materials have to be considered. Paris *et al.* [27] performed an environmental impact analysis for the fabrication of an aeronautic turbine made from a titanium alloy. AM using electron beam melting (EBM) was compared to conventional milling. The study found EBM to be more environmentally friendly for parts that require a lot of material removal in milling, but milling was favorable for parts with lower complexity and need for material removal. In general, the ecological footprint of AM compared to conventional manufacturing has to be evaluated for each specific use case.

A major limitation of AM is the build speed which is very low compared to mass manufacturing methods like injection molding. This is why AM is only economically viable for certain applications

like customized manufacturing [13]. However, new methods like continuous liquid interface production (CLIP) that allow a massively increased fabrication speed may shift the balance between AM and conventional manufacturing [28].

Inferior material properties are one of the main challenges of AM compared to conventional manufacturing. The reasons for limited material quality depend on the respective AM method. Products made by the fusion of powders exhibit process-related porosity resulting in a weakened material [13, 29]. The rough surfaces of these materials can be desirable or undesirable depending on the application [30]. FMD-made products are prone to anisotropy, i. e. different mechanical strength depending on the spatial direction. This behavior can be influenced by certain process parameters like object orientation, infill patterns or extrusion temperature [31, 32].

The achievable spatial resolution is another aspect to consider in AM that depends strongly on the employed method. 3D-printed objects typically exhibit stair step surfaces as a result of the material deposition in layers (see Figure 1.2). Accordingly, layer thickness is one parameter determining the resolution. Other parameters are the filament thickness in FDM or the size of the powder particles in powder-based methods. Typical feature resolutions are 100 to 150 µm for FDM, 50 to 100 µm for powder-based methods and 25 to 100 µm for methods based on photopolymerization [13]. Specialized methods like multiphoton lithography can reach very high resolutions of 0.1 to 5 µm but are restricted to the fabrication of very small objects [13, 33].

1.1.3 Available techniques

AM encompasses a wide range of different methods with specific advantages and disadvantages. The following section gives a short overview of the most relevant techniques.

1.1.3.1 Fused deposition modeling (FDM) or fused filament fabrication (FFF)

Due to its low cost and simple operation, fused deposition modeling (FDM) or fused filament fabrication (FFF) is one of the most popular AM methods with a wide range of applications from the aerospace industry to creative gifts [34, 35]. The principle of FDM is to heat up a plastic filament and extrude it through a nozzle in a semi-solid state. The extruded plastic is deposited layer-by-layer on a build platform to produce the desired shape [36]. FDM-printed parts show strong anisotropic properties due to the suboptimal bonding between the interfaces of extruded strands [34]. To optimize the resulting material quality, a range of approaches have been suggested, e. g. using a laser to locally heat up the already extruded material where new interfaces are to be formed [37]. Another major limitation of FDM is the rather poor resolution of 100 to 150 µm [13].

1.1.3.2 Stereolithography and related methods

Methods based on the polymerization of photosensitive resins are widely spread in both the consumer and professional area. Layers are formed by selectively polymerizing the resin contained in a vat by exposure with a laser (SLA) or a selectively masked light source like an LCD display or projector (digital light processing – DLP) [13]. Stereolithography can provide fine prints with a lateral resolution of usually 10 to 50 µm and a vertical resolution adjustable by light adsorbing additives [13]. After decades of development, many different types and systems of stereolithography have evolved and new developments have massively improved the technology in many areas [38]. This includes the improvement of production rate using CLIP [28], the expansion of the range of printable

materials enabling the fabrication of parts made from ceramics [39] or glass [40], and the enhancement of resolution to the sub-micrometer level using multiphoton lithography [33].

1.1.3.3 Selective laser sintering and selective laser melting

In selective laser sintering (SLS), solid layers are created by selectively fusing material in a bed of powder using a laser beam. After a layer is finished, a new layer of powder is spread over the surface of a build cylinder [41]. Laser sintering can be applied with a large variety of materials like polymers, metals, ceramics and their composites [42, 43]. Objects made by laser sintering exhibit a certain porosity and a variety of post-processing methods have been established to obtain products with higher density. This includes different infiltration methods and isostatic pressing [43]. Selective laser melting (SLM) operates with higher laser powers allowing the full melting of the powder. In general, SLM is more difficult to control and may cause surface tension-driven issues, but it can reduce the stair-step effect resulting in higher accuracy [41].

1.1.3.4 Binder jetting

In binder jetting, powder particles are selectively joined to form layers by spraying a liquid binding agent onto the powder bed similarly to conventional ink-jet printing. This technique is applicable for a range of materials like metals, polymer and ceramics [30, 44]. To obtain a more stable product, the printed objects are typically post-processed by sintering which causes shrinkage and has to be considered when designing the model [45].

1.1.4 Applications in medicine and research

Conventional AM methods have already been widely applied in medical fields, e. g. for the fabrication of dental implants [4] or mouthguards [2, 3]. In chemical engineering, 3D-printed flow microreactors and micromixers [46] and metal columns for capillary liquid chromatography [47] are reported. Microfluidic devices for the capturing of bacteria [48] and 3D-printed ion exchange chromatography columns for protein purification [49] are examples for applications in biotechnology.

1.2 3D Bioprinting

With the increasing proliferation of 3D printing in research and the diversification of printing methods, applications involving the use of 3D printing methods started to emerge in biochemical engineering and biotechnology. While conventional 3D printing methods can be used to fabricate laboratory hardware [50], microfluidic devices [51, 52] or chromatography columns [49, 53], the involvement of biologically active molecules or living cells opens up a whole new field of applications. At the same time, the exploration of this new field requires entirely different materials and printing methods to adequately accommodate the biological entities in a biocompatible aqueous environment. The subbranch of 3D printing dedicated to the investigation and development of such materials and methods is called *bioprinting*.

The term *bioprinting* was defined by Guillemot *et al.* as „the use of computer-aided transfer processes for patterning and assembling living and non-living materials with a prescribed 2D or 3D organization in order to produce bio-engineered structures serving in regenerative medicine, pharmacokinetic and basic cell biology studies“ [54]. As such, bioprinting is part of the larger

field of *biofabrication* which is „the automated generation of biologically functional products with structural organization from living cells, bioactive molecules, biomaterials, cell aggregates such as micro-tissues, or hybrid cell-material constructs, through Bioprinting or Bioassembly and subsequent tissue maturation processes“ [55]. To arrange cells and biomolecules in a spatially structured and organized formation, matrix materials are required that provide structural integrity and at the same time a suitable aqueous environment. In practice, hydrogels have been shown to be suitable materials to accommodate both cells [56, 57] and biomolecules [58, 59]. Due to their cell-friendly and highly biocompatible properties [60] and their ability to allow the diffusion of gas and nutrients [9], hydrogels are widely employed in tissue engineering which aims at the fabrication of tissue replacements containing living cells. The application of bioprinting expands the capabilities of tissue engineering, as it allows the fabrication of hydrogels in customized shapes like vascularized structures which are essential for nutrient and oxygen supply [61]. The following sections provide an overview of hydrogels and specialized 3D printing methods in the context of bioprinting.

1.2.1 Hydrogels and bioinks

Hydrogels are gel-like materials with a high water content whose structural integrity is maintained by a network of polymer chains with hydrophilic functional groups which allow them to retain large amounts of water, while cross-links between the chains prevent the polymer to simply be dissolved in water [8].

1.2.1.1 Types of hydrogels

Hydrogels can be classified in a number of ways, a few of which are named here [8]:

- Based on source: The polymers forming the hydrogel can either be of natural (e. g. agarose, alginate, collagen and gelatin [62]) or synthetic origin (e. g. poly(ethylene glycol) diacrylate and poloxamers [63, 64]). The advantages of natural hydrogels are biocompatibility and biodegradability, but they may lack the desired mechanical properties. Synthetic hydrogels can be designed to exhibit certain mechanical or other favorable properties, but do not show inherent bioactivity [63].
- Based on polymeric composition: Homopolymeric hydrogels contain polymers made from a single species of monomer [65], copolymeric hydrogels contain polymers made from at least two different types of monomer [66] and multipolymer hydrogels contain at least two independent, interpenetrating polymer networks [67].
- Based on the type of cross-linking: The junctions between polymer chains can either be permanent covalent bonds or transient physical junctions caused by polymer chain entanglement, ionic interactions, hydrogen bonds or hydrophobic interactions [8].

1.2.1.2 Requirements for bioinks

To fabricate solid hydrogel structures using bioprinting, a suitable starting material is needed. These starting materials are typically referred to as *bioinks*. Unlike the final hydrogels, these inks are fluid hydrogel precursor solutions that can be purposefully solidified during or after the printing process. Hence, these materials have to fulfill certain requirements before, during and after the printing process [68]. Before the printing process, the main focus is cell survival which requires the

bioink to be cytocompatible. During the printing process, an additional aspect becomes relevant, namely the rheological properties. Depending on the employed printing method, bioinks with very different flow behavior can be desirable. Extrusion-based bioprinting (EBB), also called robotic dispensing, requires bioinks with shear-thinning behavior and a high viscosity or a yield point. Typically, additives like methylcellulose [69] or nanosilicates [12] are added to bioinks to obtain the required rheological properties. This allows the ink to maintain its shape after extrusion. For inkjet printing, lower viscosities are suitable, as the ink has to pass a narrow orifice and form small droplets [68, 70]. After the printing process, it is important to preserve the shape of the printed object permanently by crosslinking the bioink to obtain a mechanically stable hydrogel. Different strategies are available to achieve this goal, ranging from radical photopolymerization to thermal or ionic crosslinking [71]. After crosslinking, the hydrogel should allow the cells to migrate, proliferate and differentiate [70]. The main challenge in the design of bioinks is to find compositions that fulfill the whole range of opposing requirements sufficiently at the same time. The spot where both shape fidelity and cytocompatibility are acceptable is referred to as the *biofabrication window* [70].

1.2.2 Bioprinting methods

Bioprinting methods can be categorized in three main groups: laser-induced forward transfer (LIFT), inkjet printing and extrusion-based bioprinting. Each of these methods has highly specific requirements for the properties of the employed inks, especially regarding rheological properties and curing mechanisms [70].

1.2.2.1 Laser-induced forward transfer

The principle of laser-induced forward transfer is to transfer small droplets of cell-containing bioink from a donor slide to a collector slide using a laser. Underneath a layer of bioink, the donor slide is covered by a laser-absorbing material that evaporates suddenly when hit by a laser pulse. The resulting high gas pressure accelerates a bioink droplet towards the collector slide. Advantages of this method are the cell-friendliness and the lack of a nozzle which eliminates the problem of clogging [70].

1.2.2.2 Inkjet printing

Inkjet printers use either acoustic waves created by piezoelectric crystals or pressure pulses created by short heat pulses to generate microdroplets of bioink that are deposited in the specified spots on a substrate. After depositing, different mechanisms of gelation like photocrosslinking can be applied. Nozzle clogging can be an issue with inkjet printing and low-viscosity bioinks are required. Very fine resolutions in the micrometer range (10 to 50 µm) can be achieved [68]. The use of commercially available inkjet printers optimized for 2D printing is challenging, as orifice diameters are often not much wider than the cells to be printed which has restrained inkjet printing from becoming more relevant in 3D bioprinting [70].

1.2.2.3 Extrusion-based bioprinting

Extrusion-based bioprinting (EBB) is the probably most common and most widely applied method in tissue engineering and biofabrication [68]. Instead of creating bioink droplets, the principle of EBB is to extrude a highly viscous bioink from a syringe or cartridge through a nozzle and to

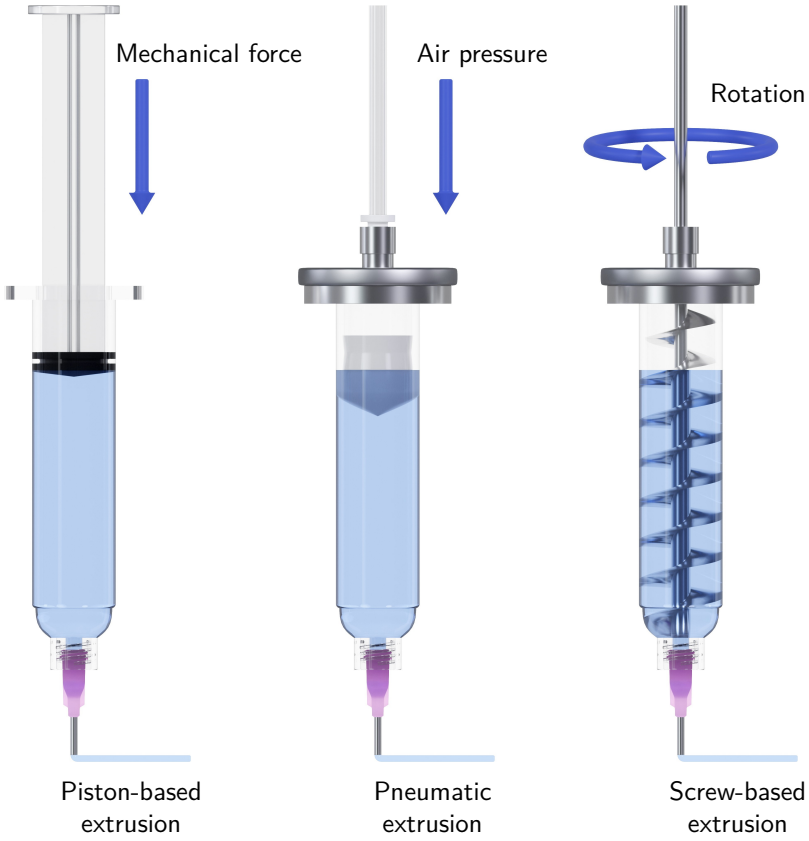

Figure 1.4 Different extrusion methods employed in bioprinting. Piston-based, pneumatic and screw-based extrusion can be used to dispense viscous inks from a cartridge in 3D printers.

deposit the resulting hydrogel filament on a substrate [68]. EBB can be categorized by the employed dispensing system into three subgroups: pneumatically driven, piston-driven and screw-driven EBB, as schematically represented in Figure 1.4.

Each of these methods has specific advantages and disadvantages [72, 73]. For screw-driven and piston-driven EBB, there is a direct correlation between the movement of the piston or screw and the extruded volume. For pneumatically driven EBB, the resulting ink flow does not only depend on the applied pressure, but also on the viscosity of the ink and other factors, making it harder to control. Piston-driven EBB has the tendency that a certain amount of ink unintentionally leaks at the end of the extrusion process. Several approaches have been suggested to counteract this behavior lik retracting the piston or adding a valve [74, 75]. Screw-based systems offer the best control of the extruded volume but come with the drawback of tedious cleaning and high dead volume [76] which can be problematic when working with costly material. Regarding the printing of cells, the shear forces induced by the screw can lead to unintended cell damage [77]. Due to the approach of extruding filaments instead of small droplets, EBB only provides inferior resolution (200 to 1000 µm) and nozzle clogging can be problematic. After extrusion, different crosslinking mechanisms can be applied to solidify the bioink [68]. Approaches to perform gelation *in situ* have also been reported, e. g. employing a coaxial nozzle setup with an alginate ink being extruded through the inner nozzle while $CaCl_2$ solution is extruded through the outer nozzle to immediately

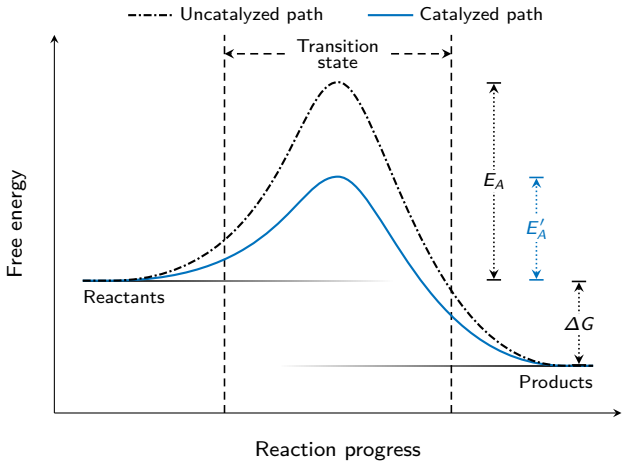

Figure 1.5 Energy diagram illustrating the mechanism of catalysis. The activation energy of the uncatalyzed path E_A is compared to the activation energy of the catalyzed path E'_A. ΔG is the change of free energy of the reaction. Adapted from [80].

induce gelation of the alginate ink [78]. This concept can also be inverted by extruding alginate ink through the outer and $CaCl_2$ solution through the inner nozzle to create hollow alginate microfibres [79].

1.3 Biocatalysis

Biochemical reactions are the basis of the metabolism of all living organisms. Many of these reactions have to be catalyzed in order to proceed at an appropriate rate. Catalysts selectively accelerate chemical reactions by reducing the energy barrier required to initiate the reaction by temporarily forming an activated transition state with the substrate, as depicted in Figure 1.5. The catalyst emerges unchanged from the reaction and can theoretically convert substrate indefinitely. Enzymes are protein-based catalysts that have evolved to catalyze specific reactions under mild conditions. They show a high degree of specificity, generate high turnover numbers, are biodegradable and considered natural products. However, they may be costly and are intrinsically susceptible to inactivation [80, 81].

1.3.1 Enzyme kinetics

The Michaelis-Menten equation is one of the fundamental models in enzyme kinetics. It describes the irreversible conversion of a substrate into a product. Michaelis and Menten proposed two sequential steps as the mechanism of enzyme catalysis. First, the substrate binds to the active site of the enzyme. Second, the amino acid residues of the active site interact with the substrate in a way that transforms the substrate into a product which is released, leaving the enzyme available for the next catalytic reaction [80]. This process is represented in Equation 1.1.

$$E + S \underset{k_{off}}{\overset{k_{on}}{\rightleftharpoons}} ES \xrightarrow{k_{cat}} E + P \tag{1.1}$$

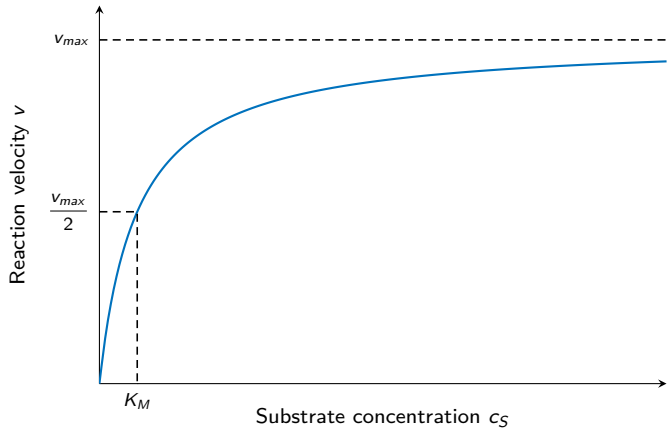

Figure 1.6 Graphical representation of the Michaelis-Mention equation (see Equation 1.2).

Kinetic parameters can be determined experimentally. Typically, the initial reaction rate is determined at different substrate concentrations. Plotting the reaction rates over the substrate concentration results in the characteristic shape of a Michaelis-Menten diagram as shown in Figure 1.6 [82].

The respective equation is given as follows:

$$v = \frac{v_{max} \cdot c_S}{K_M + c_S} \tag{1.2}$$

with the maximum reaction rate v_{max}, the substrate concentration c_S and the Michaelis constant K_M which combines the three rate constants k_{on}, k_{off} and k_{cat}.

As indicated in Figure 1.6, v_{max} is the maximum turnover rate which can theoretically be achieved in a state of abundance of substrate. K_M is the substrate concentration at $\frac{1}{2}v_{max}$. The parameters K_M and v_{max} are typically derived from linearized plots like the Lineweaver-Burk plot [80].

1.3.2 Model enzymes

Esterase 2 from the thermophilic organism *Alicyclobacillus acidocaldarius* (AaEst2) is a thermostable enzyme with a molecular mass of 34.89 kDa, an optimum temperature of approximately 70 °C and an optimum pH of 7.10 ± 0.15. It is classified as a carboxylesterase in enzyme class (EC) 3.1.1.1. The hydrolysis of 5(6)-carboxyfluorescein dihexylester catalyzed by AaEst2 results in the formation of 5(6)-carboxyfluorescein which can be detected using fluorescence measurements at an excitation wavelength $\lambda_{excitation} = 485\,\text{nm}$ and an emission wavelength of $\lambda_{emission} = 528\,\text{nm}$ [83–86].

β-Galactosidase from *Aspergillus oryzae* has a molecular weight of 120.15 kDa and is able to hydrolyze lactose. Accordingly, a typical industrial application of β-galactosidase is the production of lactose-free milk. β-Galactosidase is a hydrolase and part of EC 3.2.1.23. A suitable reaction for the detection of β-galactosidase activity is the cleavage of *ortho*-nitrophenyl-β-D-galactopyranoside (ONPG) into β-D-galactose and *ortho*-nitrophenol (ONP) which can be detected by UV-Vis spectroscopy at a wavelength of $\lambda_{absorption} = 420\,\text{nm}$ [87–89].

Table 1.1 Side-by-side comparison of β-galactosidase from *Aspergillus oryzae* (β-gal) and esterase 2 from *Alicyclobacillus acidocaldarius* (AaEst2).

	β-Galactosidase (β-gal)	Esterase 2 (AaEst2)
Organism	*Aspergillus oryzae*	*Alicyclobacillus acidocaldarius*
Enzyme class	3.2.1.23	3.1.1.1
Molecular weight	120.15 kDa	34.89 kDa
Model substrate	*ortho*-nitrophenyl-β -D-galactopyranoside (ONPG)	5(6)-carboxyfluorescein dihexylester

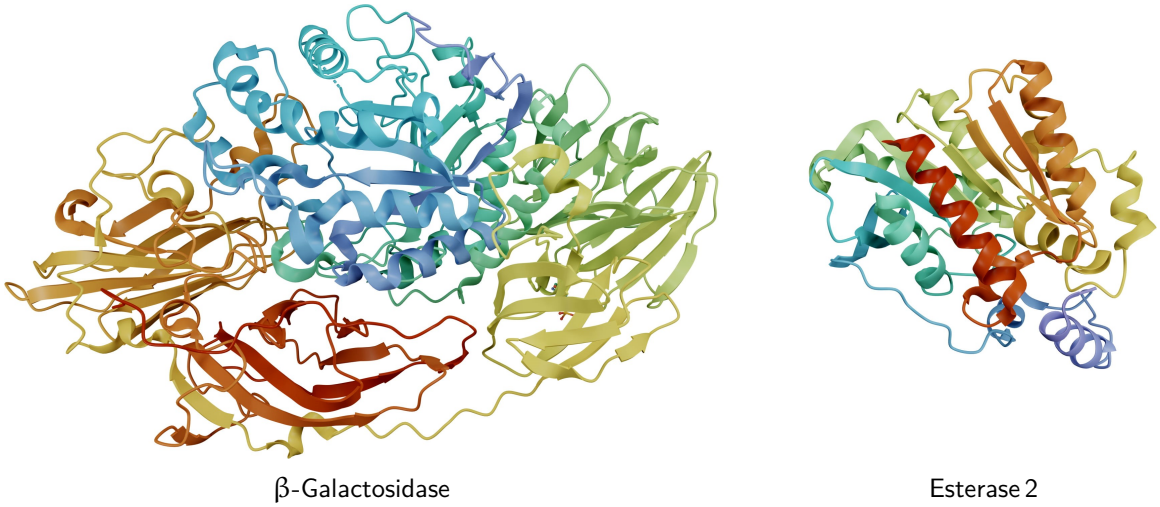

Figure 1.7 3D visualizations of β-galactosidase from *Aspergillus oryzae* (β-gal, 3D models obtained from [87, 88]) and esterase 2 from *Alicyclobacillus acidocaldarius* (AaEst2, 3D models obtained from [84, 86]).

A summary of the properties of both enzymes is given in Table 1.1 and 3D models of the enzymes are shown side-by-side in Figure 1.7. The chemical equations of the reactions used for activity assays are illustrated in Figure 1.8.

1.3.3 Enzyme immobilization

The immobilization of enzymes is a widely established method to simplify downstream processing, increase reusability and improve operational stability. There are a range of different immobilization techniques, as exemplarily shown in Figure 1.9. The simplest method is the adsorption of enzymes to a surface. However, this method suffers from a strong susceptibility to changes in pH and temperature and from a high amount of enzyme loss due to the weak interactions between enzyme and support [90].

The attachment to the solid support can be strongly enhanced by using covalent bonding. Due to its reliability, it is one of the most widely used immobilization methods. However, the enzymatic activity can be impaired if amino acids from the active center are involved in the binding to the support [90]. A very simple method for enzyme immobilization is the physical entrapment within a hydrogel network [91]. Usually, there is no need to adapt the method to a specific enzyme.

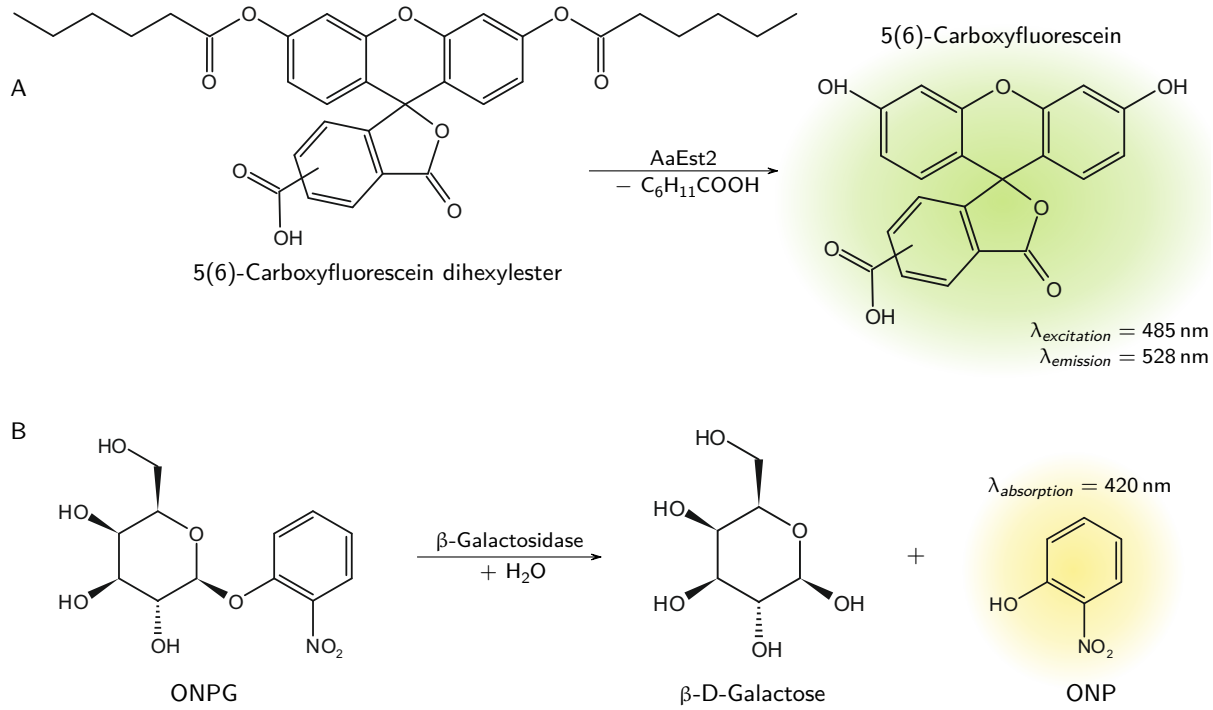

Figure 1.8 Reactions catalyzed by (A) AaEst2 and (B) β-galactosidase, as used for the determination of enzymatic activiy in colorimetric assays. Figure adapted from [85] and [89].

The principle of this method is to entrap the relatively large enzyme within a polymer network while the substrate and product molecules are still able to diffuse within the hydrogel due to their much smaller size [92]. The choice of a suitable support material with an appropriate pore size is paramount to minimize diffusion limitations for substrate and product molecules while ensuring the retention of the enzyme within the hydrogel [90]. The usually reduced mass transfer of substrate and product is the main disadvantage of immobilization by physical entrapment [12, 92]. Maximizing the surface-area-to-volume ratio of the hydrogel is a way to counteract this limitation.

A method for the irreversible immobilization of enzymes without the need for a solid support is enzyme crosslinking, e. g. in the form of crosslinked enzyme aggregates (CLEA). The main limitation of this method is the reduced substrate and product diffusion with increasing aggregate size [81, 90].

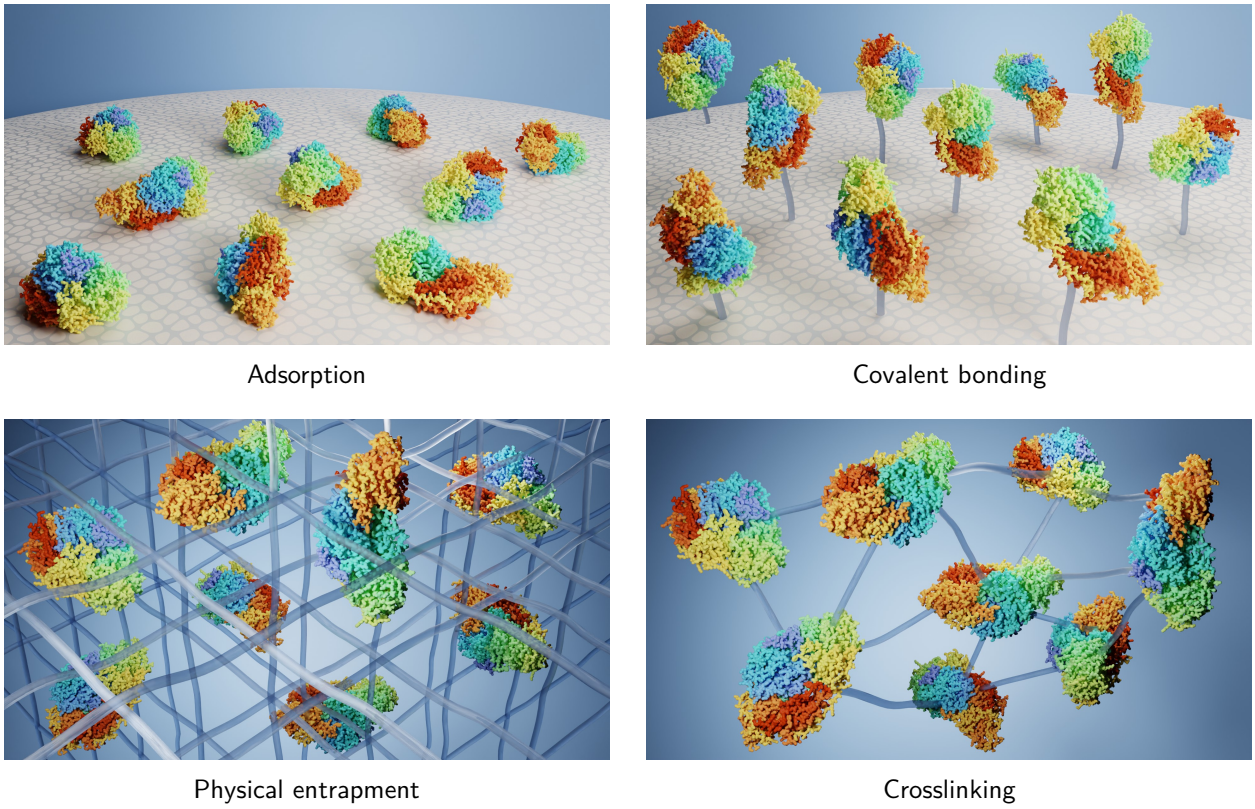

Figure 1.9 Different enzyme immobilization methods in side-by-side comparison. The shown protein represents β-galactosidase from *Aspergillus oryzae* (β-gal, 3D model obtained from [87, 88]).

Chapter references

[1] T. D. Ngo, A. Kashani, G. Imbalzano, K. T. Nguyen, and D. Hui, „Additive manufacturing (3D printing): A review of materials, methods, applications and challenges“, *Composites Part B: Engineering*, vol. 143, no. February, pp. 172–196, 2018.

[2] A. M. Sousa, A. C. Pinho, and A. P. Piedade, „Mechanical properties of 3D printed mouthguards: Influence of layer height and device thickness“, *Materials and Design*, vol. 203, p. 109 624, 2021.

[3] J. Saunders, M. Lißner, D. Townsend, N. Petrinic, and J. Bergmann, „Impact behaviour of 3D printed cellular structures for mouthguard applications“, *Scientific Reports*, vol. 12, no. 1, pp. 1–12, 2022.

[4] U. B. Sheela, P. G. Usha, M. M. Joseph, J. S. Melo, S. T. Thankappan Nair, and A. Tripathi, *3D printing in dental implants*. Elsevier (Singapore) Pte Ltd, 2020, pp. 83–104.

[5] A. Dawood, B. M. Marti, V. Sauret-Jackson, and A. Darwood, „3D printing in dentistry“, *British Dental Journal*, vol. 219, no. 11, pp. 521–529, 2015.

[6] K. Liang, S. Carmone, D. Brambilla, and J. C. Leroux, „3D printing of a wearable personalized oral delivery device: A first-in-human study“, *Science Advances*, vol. 4, no. 5, pp. 1–12, 2018.

[7] K. Y. Lee and D. J. Mooney, „Hydrogels for Tissue Engineering“, *Chemical Reviews*, vol. 101, no. 7, pp. 1869–1879, 2001.

[8] E. M. Ahmed, „Hydrogel: Preparation, characterization, and applications: A review“, *Journal of Advanced Research*, vol. 6, no. 2, pp. 105–121, 2015.

[9] E. Eisenbarth, „Biomaterials for Tissue Engineering“, *Advanced Engineering Materials*, vol. 9, no. 12, pp. 1051–1060, 2007.

[10] S. Hinderer, S. L. Layland, and K. Schenke-Layland, „ECM and ECM-like materials - Biomaterials for applications in regenerative medicine and cancer therapy“, *Advanced Drug Delivery Reviews*, vol. 97, pp. 260–269, 2016.

[11] J. Choi, O. C. Kwon, W. Jo, H. J. Lee, and M. W. Moon, „4D Printing Technology: A Review“, *3D Printing and Additive Manufacturing*, vol. 2, no. 4, pp. 159–167, 2015.

[12] B. Schmieg, A. Schimek, and M. Franzreb, „Development and performance of a 3D-printable poly(ethylene glycol) diacrylate hydrogel suitable for enzyme entrapment and long-term biocatalytic applications“, *Engineering in Life Sciences*, vol. 18, no. 9, pp. 659–667, 2018.

[13] S. C. Ligon, R. Liska, J. Stampfl, M. Gurr, and R. Mülhaupt, „Polymers for 3D Printing and Customized Additive Manufacturing“, *Chemical Reviews*, vol. 117, no. 15, pp. 10 212–10 290, 2017.

[14] A. Gebhardt, *Understanding Additive Manufacturing*. Munich: Hanser Publishers, 2011.

[15] I. Gibson, D. Rosen, B. Stucker, and M. Khorasani, *Additive Manufacturing Technologies*. 2021.

[16] K. Rajaguru, T. Karthikeyan, and V. Vijayan, „Additive manufacturing - State of art“, *Materials Today: Proceedings*, vol. 21, no. 1, pp. 628–633, 2020.

[17] H. Kodama, „Automatic method for fabricating a three-dimensional plastic model with photo-hardening polymer“, *Review of Scientific Instruments*, vol. 52, no. 11, pp. 1770–1773, 1981.

[18] J. J. Beaman, J. W. Barlow, D. L. Bourell, R. H. Crawford, H. L. Marcus, and K. P. McAlea, *Solid Freeform Fabrication: A New Direction in Manufacturing*. New York: Springer Science + Business Media, LLC, 1997.

[19] A. Su and S. J. Al'Aref, „History of 3D printing“, in *3D Printing Applications in Cardiovascular Medicine*, Elsevier Inc., 2018, pp. 1–10.

[20] C. W. Hull, *Apparatus for production of three-dimensional objects by stereolithography*, 1986.

[21] C. R. Deckard, *Apparatus for producing parts by selective sintering*, 1997.

[22] S. S. Crump, *Modeling apparatus for three-dimensional objects*, 1994.

[23] B. Panda, M. J. Tan, I. Gibson, and C. K. Chua, „The disruptive evolution of 3D printing“, *Proceedings of the International Conference on Progress in Additive Manufacturing*, vol. Part F1290, pp. 152–157, 2016.

[24] J. B. Roca, P. Vaishnav, J. Mendoṇa, and M. G. Morgan, „Getting Past the Hype about 3-D Printing“, *MIT Sloan Management Review*, vol. 58, no. 3, pp. 57–62, 2017.

[25] B. P. Conner, G. P. Manogharan, A. N. Martof, L. M. Rodomsky, C. M. Rodomsky, D. C. Jordan, and J. W. Limperos, „Making sense of 3-D printing: Creating a map of additive manufacturing products and services“, *Additive Manufacturing*, vol. 1, pp. 64–76, 2014.

[26] N. Hopkinson and P. Dickens, „Analysis of rapid manufacturing - Using layer manufacturing processes for production“, *Proceedings of the Institution of Mechanical Engineers, Part C: Journal of Mechanical Engineering Science*, vol. 217, no. 1, pp. 31–40, 2003.

[27] H. Paris, H. Mokhtarian, E. Coatanéa, M. Museau, and I. F. Ituarte, „Comparative environmental impacts of additive and subtractive manufacturing technologies“, *CIRP Annals - Manufacturing Technology*, vol. 65, no. 1, pp. 29–32, 2016.

[28] J. R. Tumbleston, D. Shirvanyants, N. Ermoshkin, R. Janusziewicz, A. R. Johnson, D. Kelly, K. Chen, R. Pinschmidt, J. P. Rolland, A. Ermoshkin, E. T. Samulski, and J. M. DeSimone, „Continuous liquid interface production of 3D objects“, *Science*, vol. 347, no. 6228, pp. 1349–1352, 2015.

[29] J. P. Kruth, G. Levy, F. Klocke, and T. H. Childs, „Consolidation phenomena in laser and powder-bed based layered manufacturing“, *CIRP Annals - Manufacturing Technology*, vol. 56, no. 2, pp. 730–759, 2007.

[30] Z. X. Low, Y. T. Chua, B. M. Ray, D. Mattia, I. S. Metcalfe, and D. A. Patterson, „Perspective on 3D printing of separation membranes and comparison to related unconventional fabrication techniques“, *Journal of Membrane Science*, vol. 523, no. May 2016, pp. 596–613, 2017.

[31] J. M. Chacón, M. A. Caminero, E. García-Plaza, and P. J. Núñez, „Additive manufacturing of PLA structures using fused deposition modelling: Effect of process parameters on mechanical properties and their optimal selection“, *Materials and Design*, vol. 124, pp. 143–157, 2017.

[32] D. Syrlybayev, B. Zharylkassyn, A. Seisekulova, M. Akhmetov, A. Perveen, and D. Talamona, „Optimisation of strength properties of FDM printed parts - A critical review“, *Polymers*, vol. 13, no. 10, 2021.

[33] D. M. Zuev, A. K. Nguyen, V. I. Putlyaev, and R. J. Narayan, „3D printing and bioprinting using multiphoton lithography“, *Bioprinting*, vol. 20, no. May, e00090, 2020.

[34] Z. Liu, Y. Wang, B. Wu, C. Cui, Y. Guo, and C. Yan, „A critical review of fused deposition modeling 3D printing technology in manufacturing polylactic acid parts“, *International Journal of Advanced Manufacturing Technology*, vol. 102, no. 9-12, pp. 2877–2889, 2019.

[35] O. A. Mohamed, S. H. Masood, and J. L. Bhowmik, „Optimization of fused deposition modeling process parameters: a review of current research and future prospects“, *Advances in Manufacturing*, vol. 3, no. 1, pp. 42–53, 2015.

[36] P. K. Penumakala, J. Santo, and A. Thomas, „A critical review on the fused deposition modeling of thermoplastic polymer composites“, *Composites Part B: Engineering*, vol. 201, no. May, p. 108 336, 2020.

[37] A. K. Ravi, A. Deshpande, and K. H. Hsu, „An in-process laser localized pre-deposition heating approach to inter-layer bond strengthening in extrusion based polymer additive manufacturing“, *Journal of Manufacturing Processes*, vol. 24, pp. 179–185, 2016.

[38] J. Huang, Q. Qin, and J. Wang, „A Review of Stereolithography: Processes and Systems“, *Processes*, vol. 8, no. 9, 2020.

[39] R. Felzmann, S. Gruber, G. Mitteramskogler, P. Tesavibul, A. R. Boccaccini, R. Liska, and J. Stampfl, „Lithography-based additive manufacturing of cellular ceramic structures“, *Advanced Engineering Materials*, vol. 14, no. 12, pp. 1052–1058, 2012.

[40] F. Kotz, K. Arnold, W. Bauer, D. Schild, N. Keller, K. Sachsenheimer, T. M. Nargang, C. Richter, D. Helmer, and B. E. Rapp, „Three-dimensional printing of transparent fused silica glass“, *Nature*, vol. 544, no. 7650, pp. 337–339, 2017.

[41] A. Mazzoli, „Selective laser sintering in biomedical engineering“, *Medical and Biological Engineering and Computing*, vol. 51, no. 3, pp. 245–256, 2013.

[42] S. L. Sing, W. Y. Yeong, F. E. Wiria, B. Y. Tay, Z. Zhao, L. Zhao, Z. Tian, and S. Yang, „Direct selective laser sintering and melting of ceramics: A review“, *Rapid Prototyping Journal*, vol. 23, no. 3, pp. 611–623, 2017.

[43] A.-N. Chen, J.-M. Wu, K. Liu, J.-Y. Chen, H. Xiao, P. Chen, C.-H. Li, and Y.-S. Shi, „High-performance ceramic parts with complex shape prepared by selective laser sintering: a review“, *Advances in Applied Ceramics*, vol. 117, no. 2, pp. 100–117, 2017.

[44] N. Shahrubudin, T. C. Lee, and R. Ramlan, „An Overview on 3D Printing Technology: Technological, Materials, and Applications“, *Procedia Manufacturing*, vol. 35, pp. 1286–1296, 2019.

[45] Y. Wang and Y. F. Zhao, „Investigation of Sintering Shrinkage in Binder Jetting Additive Manufacturing Process“, *Procedia Manufacturing*, vol. 10, pp. 779–790, 2017.

[46] C. Parra-Cabrera, C. Achille, S. Kuhn, and R. Ameloot, „3D printing in chemical engineering and catalytic technology: structured catalysts, mixers and reactors“, *Chemical Society Reviews*, vol. 47, pp. 209–230, 2018.

[47] S. Sandron, B. Heery, V. Gupta, D. A. Collins, E. P. Nesterenko, P. N. Nesterenko, M. Talebi, S. Beirne, F. Thompson, G. G. Wallace, D. Brabazon, F. Regan, and B. Paull, „3D printed metal columns for capillary liquid chromatography“, *The Analyst*, vol. 139, no. 24, pp. 6343–6347, 2014.

[48] F. Krujatz, A. Lode, J. Seidel, T. Bley, M. Gelinsky, and J. Steingroewer, „Additive Biotech—Chances, challenges, and recent applications of additive manufacturing technologies in biotechnology“, *New Biotechnology*, vol. 39, no. September, pp. 222–231, 2017.

[49] U. Simon and S. Dimartino, „Direct 3D printing of monolithic ion exchange adsorbers“, *Journal of Chromatography A*, vol. 1587, pp. 119–128, 2019.

[50] A. J. Capel, R. P. Rimington, M. P. Lewis, and S. D. Christie, „3D printing for chemical, pharmaceutical and biological applications“, *Nature Reviews Chemistry*, vol. 2, no. 12, pp. 422–436, 2018.

[51] W. G. Patrick, A. A. Nielsen, S. J. Keating, T. J. Levy, C. W. Wang, J. J. Rivera, O. Mondragón-Palomino, P. A. Carr, C. A. Voigt, N. Oxman, and D. S. Kong, „DNA Assembly in 3D Printed Fluidics“, *PLoS ONE*, vol. 10, no. 12, pp. 1–18, 2015.

[52] F. Kotz, M. Mader, N. Dellen, P. Risch, A. Kick, D. Helmer, and B. E. Rapp, „Fused Deposition Modeling of Microfluidic Chips in Polymethylmethacrylate“, *Micromachines*, vol. 11, no. 9, pp. 5–8, 2020.

[53] U. Simon, L. C. Scorza, S. Teworte, A. J. McCormick, and S. Dimartino, „Demonstration of protein capture and separation using three-dimensional printed anion exchange monoliths fabricated in one-step“, *Journal of Separation Science*, pp. 1078–1088, 2020.

[54] F. Guillemot, V. Mironov, and M. Nakamura, „Bioprinting is coming of age: Report from the International Conference on Bioprinting and Biofabrication in Bordeaux (3B'09)“, *Biofabrication*, vol. 2, no. 1, 2010.

[55] J. Groll, T. Boland, T. Blunk, J. A. Burdick, D. W. Cho, P. D. Dalton, B. Derby, G. Forgacs, Q. Li, V. A. Mironov, L. Moroni, M. Nakamura, W. Shu, S. Takeuchi, G. Vozzi, T. B. Woodfield, T. Xu, J. J. Yoo, and J. Malda, „Biofabrication: Reappraising the definition of an evolving field“, *Biofabrication*, vol. 8, no. 1, pp. 1–5, 2016.

[56] T. Billiet, E. Gevaert, T. De Schryver, M. Cornelissen, and P. Dubruel, „The 3D printing of gelatin methacrylamide cell-laden tissue-engineered constructs with high cell viability“, *Biomaterials*, vol. 35, no. 1, pp. 49–62, 2014.

[57] A. G. Tabriz, M. A. Hermida, N. R. Leslie, and W. Shu, „Three-dimensional bioprinting of complex cell laden alginate hydrogel structures“, *Biofabrication*, vol. 7, no. 4, 2015.

[58] C. A. Mandon, L. J. Blum, and C. A. Marquette, „Adding Biomolecular Recognition Capability to 3D Printed Objects“, *Analytical Chemistry*, vol. 88, no. 21, pp. 10 767–10 772, 2016.

[59] C. D. Devillard, C. A. Mandon, S. A. Lambert, L. J. Blum, and C. A. Marquette, „Bioinspired Multi-Activities 4D Printing Objects: A New Approach Toward Complex Tissue Engineering“, *Biotechnology Journal*, vol. 13, no. 12, 2018.

[60] C. D. Spicer, „Hydrogel scaffolds for tissue engineering: The importance of polymer choice“, *Polymer Chemistry*, vol. 11, no. 2, pp. 184–219, 2020.

[61] D. Richards, J. Jia, M. Yost, R. Markwald, and Y. Mei, „3D Bioprinting for Vascularized Tissue Fabrication“, *Annals of Biomedical Engineering*, vol. 45, no. 1, pp. 132–147, 2017.

[62] W. Zhao, X. Jin, Y. Cong, Y. Liu, and J. Fu, „Degradable natural polymer hydrogels for articular cartilage tissue engineering“, *Journal of Chemical Technology and Biotechnology*, vol. 88, no. 3, pp. 327–339, 2013.

[63] U. S. Madduma-Bandarage and S. V. Madihally, „Synthetic hydrogels: Synthesis, novel trends, and applications“, *Journal of Applied Polymer Science*, vol. 138, no. 19, pp. 1–23, 2021.

[64] M. C. Hacker and A. G. Mikos, *Synthetic Polymers*, Second Edi. Elsevier Inc., 2011, pp. 587–622.

[65] T. Iizawa, H. Taketa, M. Maruta, T. Ishido, T. Gotoh, and S. Sakohara, „Synthesis of Porous Poly(N-isopropylacrylamide) Gel Beads by Sedimentation Polymerization and Their Morphology“, *Journal of Applied Polymer Science*, vol. 104, pp. 842–850, 2007.

[66] L. Yang, J. S. Chu, and J. A. Fix, „Colon-specific drug delivery: New approaches and in vitro/in vivo evaluation“, *International Journal of Pharmaceutics*, vol. 235, no. 1-2, pp. 1–15, 2002.

[67] Z. Maolin, L. Jun, Y. Min, and H. Hongfei, „The swelling behavior of radiation prepared semi-interpenetrating polymer networks composed of polyNIPAAm and hydrophilic polymers“, *Radiation Physics and Chemistry*, vol. 58, no. 4, pp. 397–400, 2000.

[68] K. Hölzl, S. Lin, L. Tytgat, S. Van Vlierberghe, L. Gu, and A. Ovsianikov, „Bioink properties before, during and after 3D bioprinting“, *Biofabrication*, vol. 8, no. 3, pp. 1–19, 2016.

[69] H. Rastin, R. T. Ormsby, G. J. Atkins, and D. Losic, „3D Bioprinting of Methylcellulose/Gelatin-Methacryloyl (MC/GelMA) Bioink with High Shape Integrity“, *ACS Applied Bio Materials*, vol. 3, no. 3, pp. 1815–1826, 2020.

[70] J. Malda, J. Visser, F. P. Melchels, T. Jüngst, W. E. Hennink, W. J. A. Dhert, J. Groll, and D. W. Hutmacher, „25th Anniversary Article: Engineering Hydrogels for Biofabrication“, *Advanced Materials*, vol. 25, no. 36, pp. 5011–5028, 2013.

[71] A. GhavamiNejad, N. Ashammakhi, X. Y. Wu, and A. Khademhosseini, „Crosslinking Strategies for 3D Bioprinting of Polymeric Hydrogels“, *Small*, vol. 16, no. 35, pp. 1–30, 2020.

[72] S. V. Murphy and A. Atala, „3D bioprinting of tissues and organs“, *Nature biotechnology*, vol. 32, no. 8, pp. 773–785, 2014.

[73] I. T. Ozbolat, W. Peng, and V. Ozbolat, „Application areas of 3D bioprinting“, *Drug Discovery Today*, vol. 21, no. 8, pp. 1257–1271, 2016.

[74] L. R. Darwish, M. T. El-Wakad, and M. M. Farag, „Towards an Ultra-Affordable Three-Dimensional Bioprinter: A Heated Inductive-Enabled Syringe Pump Extrusion Multifunction Module for Open-Source Fused Deposition Modeling Three-Dimensional Printers“, *Journal of Manufacturing Science and Engineering*, vol. 143, no. 12, 2021.

[75] D. Bociaga, M. Bartniak, K. Sobczak, and K. Rosinska, „An Integration of a Peristaltic Pump-Based Extruder Into a 3D Bioprinter Dedicated to Hydrogels“, *Materials*, vol. 13, no. 19, 2020.

[76] P. Fisch, M. Holub, and M. Zenobi-Wong, „Improved accuracy and precision of bioprinting through progressive cavity pump-controlled extrusion“, *Biofabrication*, vol. 13, no. 2021, pp. 1–18, 2021.

[77] L. Ning, B. Yang, F. Mohabatpour, N. Betancourt, M. D. Sarker, P. Papagerakis, and X. Chen, „Process-induced cell damage: pneumatic versus screw-driven bioprinting“, *Biofabrication*, vol. 12, no. 2, 2020.

[78] C. Colosi, S. R. Shin, V. Manoharan, S. Massa, M. Costantini, A. Barbetta, M. R. Dokmeci, M. Dentini, and A. Khademhosseini, „Microfluidic Bioprinting of Heterogeneous 3D Tissue Constructs Using Low-Viscosity Bioink“, *Advanced Materials*, vol. 28, no. 4, 677–684a, 2016.

[79] W. Liu, Z. Zhong, N. Hu, Y. Zhou, L. Maggio, A. K. Miri, A. Fragasso, X. Jin, A. Khademhosseini, and Y. S. Zhang, „Coaxial extrusion bioprinting of 3D microfibrous constructs with cell-favorable gelatin methacryloyl microenvironments“, *Biofabrication*, vol. 10, no. 2, 2018.

[80] A. Illanes, Ed., *Enzyme Biocatalysis - Principles and Applications*. Springer Science + Business Media B.V., 2008, pp. 15–24.

[81] K.-E. Jaeger, A. Liese, and C. Syldatk, Eds., *Einführung in die Enzymtechnologie*. Berlin: Springer Spektrum, 2018.

[82] H. Bisswanger, *Enzyme Kinetics - Principles and Methods*, 3rd ed. Weinheim: Wiley-VCH Verlag GmbH, 2017.

[83] G. Manco, E. Adinolfi, F. M. Pisani, G. Ottolina, G. Carrea, and M. Rossi, „Overexpression and properties of a new thermophilic and thermostable esterase from Bacillus acidocaldarius with sequence similarity to hormone-sensitive lipase subfamily“, *Biochemical Journal*, vol. 332, no. 1, pp. 203–212, 1998.

[84] G. De Simone, S. Galdiero, G. Manco, D. Lang, M. Rossi, and C. Pedone, „A snapshot of a transition state analogue of a novel thermophilic esterase belonging to the subfamily of mammalian hormone-sensitive lipase“, *Journal of Molecular Biology*, vol. 303, no. 5, pp. 761–771, 2000.

[85] M. Maier, C. P. Radtke, J. Hubbuch, C. M. Niemeyer, and K. S. Rabe, „On-demand production of flow reactor cartridges by 3D printing of thermostable enzymes“, *Angewandte Chemie International Edition*, vol. 57, no. 19, pp. 5539–5543, 2018.

[86] RCSB Protein Data Bank, *PDB ID 1EVQ (carboxylesterase Est2 from Alicyclobacillus acidocaldarius)*, `https://www.rcsb.org/structure/1EVQ`, Accessed: 2022-03-15.

[87] M. M. Maksimainen, A. Lampio, M. Mertanen, O. Turunen, and J. Rouvinen, „The crystal structure of acidic β-galactosidase from Aspergillus oryzae“, *International Journal of Biological Macromolecules*, vol. 60, pp. 109–115, 2013.

[88] RCSB Protein Data Bank, *PDB ID 4IUG (β-galactosidase from Aspergillus oryzae)*, `https://www.rcsb.org/structure/4IUG`, Accessed: 2022-03-15.

[89] K. Labus, *Effective detection of biocatalysts with specified activity by using a hydrogel-based colourimetric assay - β-galactosidase case study*, 2018.

[90] E. Górecka and M. Jastrz bska, „Review article: Immobilization techniques and biopolymer carriers“, *Biotechnology and Food Science*, vol. 75, no. 1, pp. 65–86, 2011.

[91] S. Krishnamoorthi, A. Banerjee, and A. Roychoudhury, „Immobilized Enzyme Technology: Potentiality and Prospects“, *Journal of Enzymology and Metabolism*, vol. 1, no. 1, pp. 1–11, 2015.

[92] S. Nisha, S. Arun Karthick, and N. Gobi, „A Review on Methods, Application and Properties of Immobilized Enzyme“, *Chemical Science Review and Letters*, vol. 1, no. 3, pp. 148–155, 2012.

2

Thesis Outline

2.1 Research Proposal

The emergence of bioprinting has opened up new possibilities for the fabrication of complex three-dimensional hydrogel structures. These soft materials exhibit a high water content and provide a suitable environment for living cells and biomolecules. Bioprinting as a useful tool in tissue engineering allows the combination of biological functionality with complex geometries. Living cells can be embedded in the printed hydrogels to create vascularized tissues for transplantations or lab-on-a-chip devices. While applications in the field of tissue engineering involving living cells remain the predominant focus of bioprinting, other areas of biotechnology have started to adopt the approach of printing soft materials in complex shapes. Smart hydrogels with the ability to react to external stimuli and with features like shape memory or self-healing capabilities have been reported. Cell-free materials with a biological functionality have been created by embedding enzymes in the printed hydrogels. Due to their enzymatic activity, these materials can be employed in biocatalytic reactors. 3D bioprinting potentially enables the fabrication of perfusable grid structures with a high degree of freedom in design and without the need for molds which allows fast iteration cycles. The most common method in bioprinting is extrusion-based bioprinting which is the spatially controlled deposition of a bioink through a nozzle onto a substrate. Bioinks are fluid hydrogel precursor solutions that can be solidified after extrusion to form a stable hydrogel.

While the general feasibility of fabricating biocatalytic reactors using extrusion-based bioprinting has been demonstrated, the approach is still in the early stages of development. Typical limitations are low printing quality, limited reproducibility and missing analytical techniques. The main focus of the present thesis is to tackle these challenges by identifying parameters relevant for the successful printing of biocatalytic materials and by providing adapted printing methods, improved inks and suitable analytical techniques.

The first study of the thesis (Chapter 3) focuses on establishing a novel type of inks based on high internal phase emulsions (HIPEs), emulsions with an internal phase volume fraction of at least 74 %.

Both the oily external and the aqueous internal phase of the inks contain polymerizable monomers to allow them to be polymerized after extrusion. For improved printability, a cure-on-dispense setup is established that allows polymerization during the extrusion process. The resulting material consists of an open-porous polymeric scaffold filled with hydrogel. β-Galactosidase is added to the aqueous phase as a model enzyme to generate biocatalytically active materials. A microplate-based batch activity assay method is established to quantify the enzymatic activity of printed samples in an automated, fast and reproducible way. Enzyme leaching from the samples is investigated using a similar method based on activity assays. Other analytical methods like rheology and (environmental) scanning electron microscopy are applied to characterize the properties of the liquid inks and polymerized samples.

Due to the importance of the diffusibility of the employed matrix materials for the effective activity of entrapped enzymes, a microfluidics-based method for the estimation of diffusion coefficients in hydrogels is established in a second study (Chapter 4). The channel of a microfluidic chip is partially filled with hydrogel which is brought into contact with an analyte solution. The diffusion of the analyte through the material is monitored using a UV area imaging system. Image and data processing tools are applied to generate analyte concentration profiles along the channel. Diffusion coefficients are estimated by fitting the concentration profiles with an analytical solution of Fick's second law of diffusion. In a case study, the diffusion coefficient of lysozyme is determined in hydrogels made from different concentrations of either unmodified agarose or agarose with a low melting and gelling point.

The third study (Chapter 5) evaluates alternative types of inks based on either agarose or agar. Due to the inks' thermosensitivity, a customized printing setup including a heatable nozzle and a cooled substrate is established to improve printing quality and reduce nozzle clogging. The thermostable enzyme esterase 2 from *Alicyclobacillus acidocaldarius* (AaEst2) is added to the inks to print enzymatically active materials. Besides rheological measurements, the previously established analytical methods are employed to determine the activity and leaching behavior of the embedded enzyme (Chapter 3) and the diffusibility of the agarose- and agar-based hydrogels (Chapter 4).

The lack of process monitoring and control in extrusion-based bioprinting is addressed in the last study of this thesis (Chapter 6). To monitor the extrusion flow rate in real time, a liquid flow meter is integrated into the printing setup and a Python-based software tool is established to record and process the acquired flow rate data. A proportional-integral-derivative (PID) feedback loop is implemented to continuously adapt the extrusion pressure of the bioprinter in order to generate a constant target flow rate. The performance of the setup is evaluated with several exemplary use cases.

In summary, this work addresses several aspects of printing biocatalytically active materials, explicitly the development of suitable inks in combination with specifically adapted printing methods and analytical techniques.

2.2 Manuscript Overview

An overview of the research manuscripts written within the scope of this thesis is given here. Chapter 3 establishes the 3D printing of enzymatically active materials from emulsion-based inks and introduces a batch-based method in a microplate format to assess the enzymatic activity of these materials. Chapter 4 presents a method for the determination of diffusion coefficients of analytes in hydrogels. Chapter 5 applies the already established methods for the quantification of enzymatic activity and diffusion coefficients to agarose- and agar-based hydrogels. Chapter 6 introduces an approach for process monitoring and control in bioprinting based on the integration of a liquid flow meter and a Python-based software tool.

In the following, the conducted research projects are placed within the context of the thesis and presented as short summaries and overview flowcharts. A short overview of the entire thesis is given in Figure 2.1. Detailed statements about the specific contributions of the listed authors are given at the end of the respective chapters.

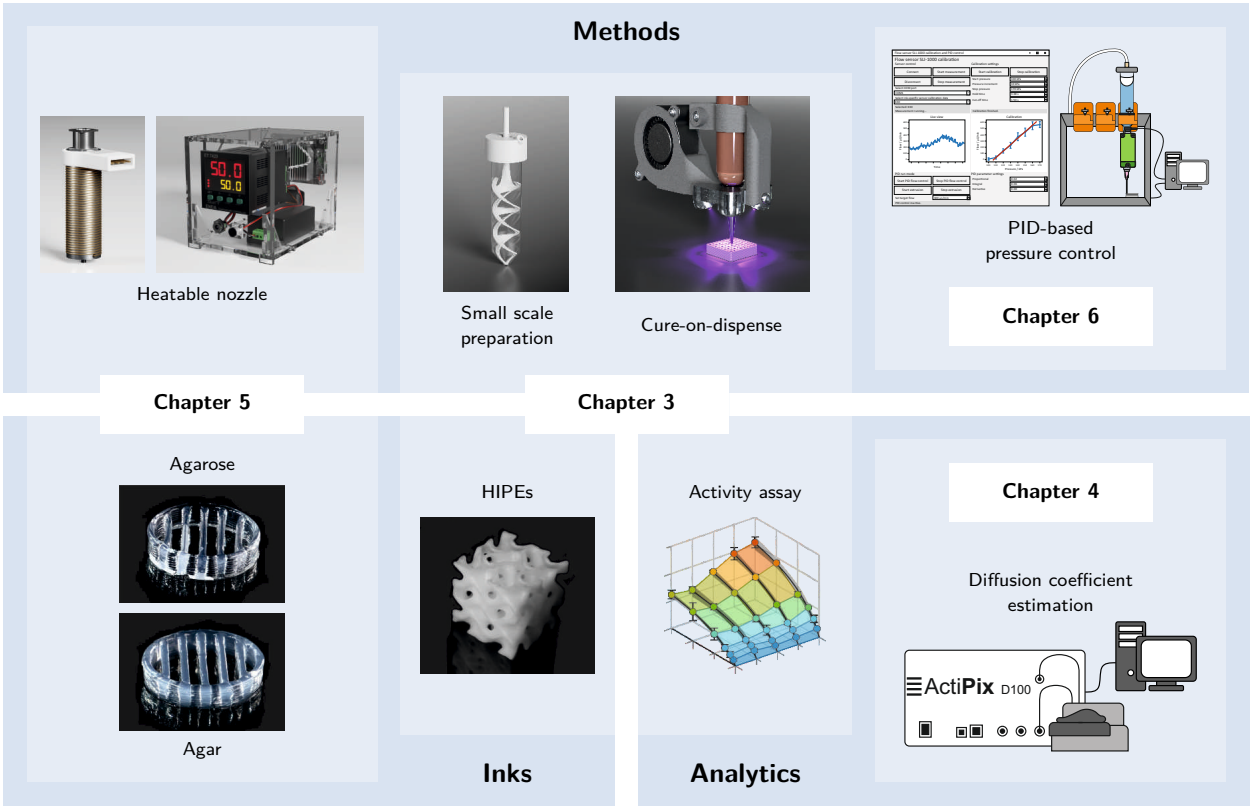

Figure 2.1 Visual overview of the scientific output generated in the scope of the thesis. The graph represents the positioning of different projects in the interconnected areas of methods, inks and analytics.

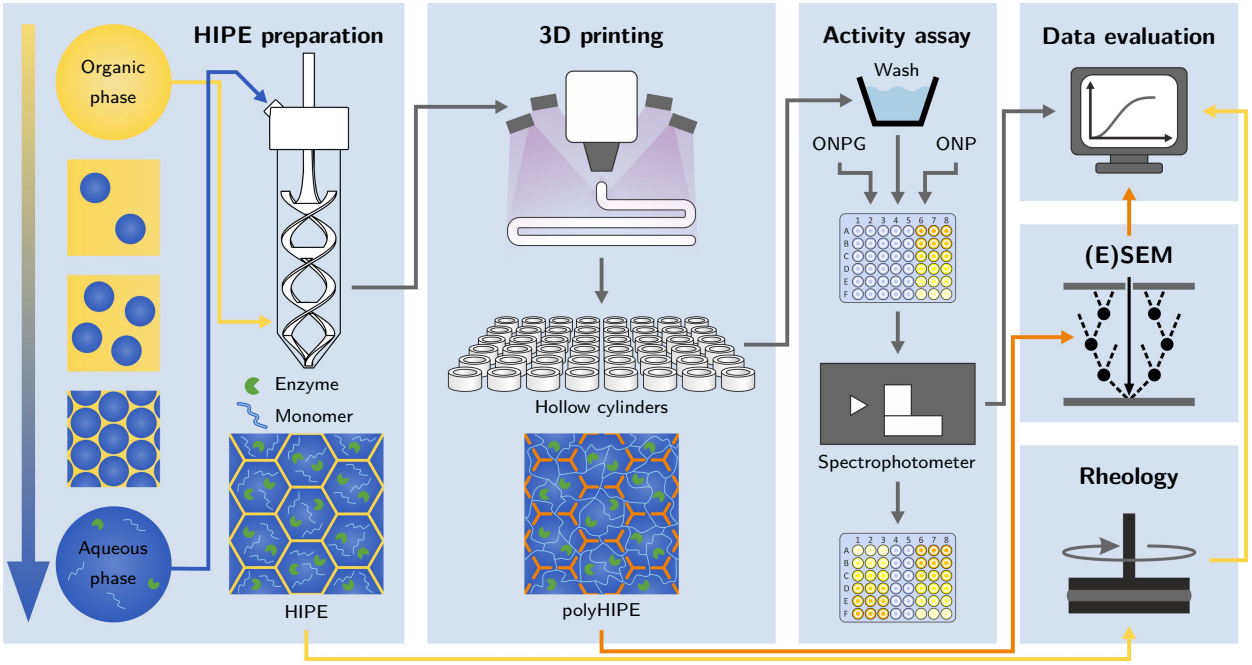

Chapter 3

Lukas Wenger, Carsten P. Radtke, Jacqueline Göpper, Michael Wörner and Jürgen Hubbuch

published in Frontiers in Bioengineering and Biotechnology, Volume 8, 2020, Article 713
https://doi.org/10.3389/fbioe.2020.00713

This study presents an approach of using high internal phase emulsions (HIPEs) as inks for the 3D printing of biocatalytically active materials. The established HIPE formulations can be photopolymerized resulting in composite materials consisting of a polymeric, porous scaffold filled with hydrogel. To allow the preparation of HIPEs on a small scale, a tailor-made stirrer blade design is established. A customized printer setup is presented that allows the photopolymerization of the extruded ink during the printing process (cure-on-dispense). The favorable rheological properties of the HIPEs in combination with the cure-on-dispense setup are shown to result in excellent printability. The enzyme β-galactosidase is embedded in the aqueous phase of the inks to generate enzymatically active materials. A range of different HIPE compositions is investigated using rheological methods and (environmental) scanning electron microscopy ((E)SEM). Most importantly, batch-based activity assays are performed in a microplate format to evaluate the residual enzymatic activity of printed samples with varying material compositions. The influence of printing with different nozzle diameters is investigated as an example of a process-related parameter. The study demonstrates a novel type of ink in combination with a specifically adapted printing method and provides insight into the relevance of different material and process parameters for the fabrication of biocatalytic reactors by 3D printing.

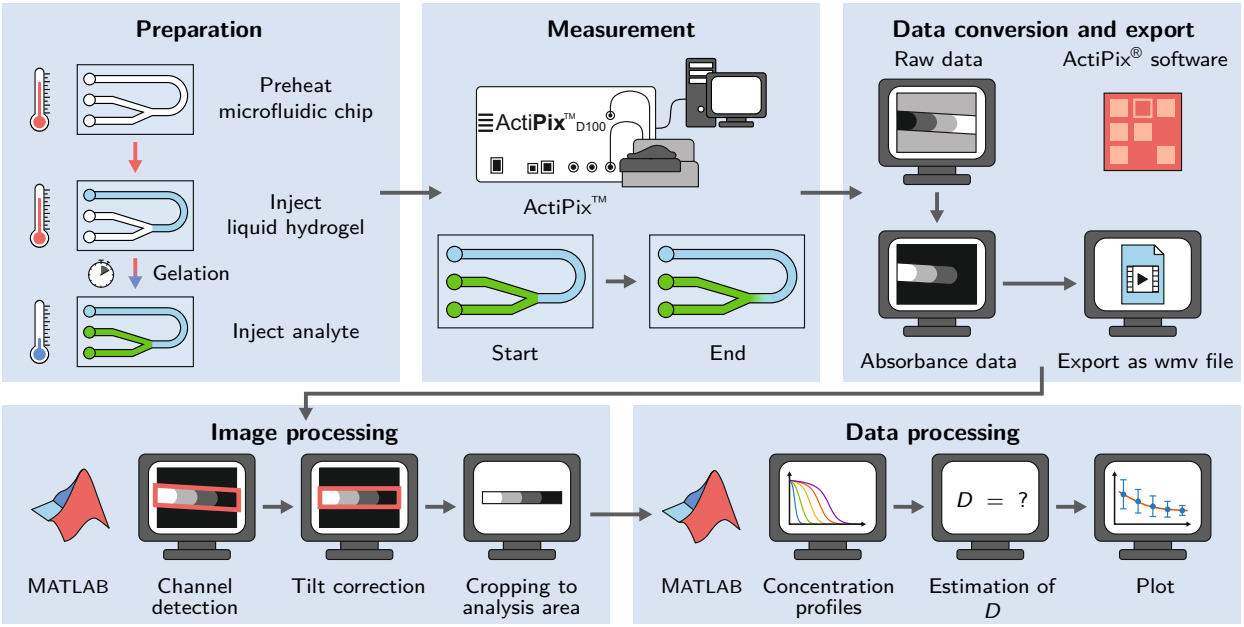

Chapter 4

Lukas Wenger and Jürgen Hubbuch

published in Frontiers in Bioengineering and Biotechnology, Volume 10, 2022, Article 849271
https://doi.org/10.3389/fbioe.2022.849271

Diffusibility is a crucial parameter for the application of hydrogels in the immobilization of enzymes. In this study, a photometric method for the determination of diffusion coefficients of UV-detectable analytes within transparent hydrogels is established. To obtain measurement data, the channel of a microfluidic chip is partially filled with hydrogel and an analyte solution is injected through another inlet of the chip to create an interface between hydrogel and analyte solution. The diffusion of the analyte through the hydrogel is monitored using a UV area imaging system. Employing automated image processing and data evaluation tools, the diffusion coefficient of the analyte is estimated by fitting analyte concentration profiles along the microfluidic channel with an analytical solution of Fick's second law of diffusion. As a case study, the diffusion of lysozyme in differently concentrated hydrogels based on an unmodified and a low-melt agarose is investigated. The presented method is only applicable for optically transparent hydrogels in combination with analytes that can be detected at a suitable wavelength. In a subsequent study (see Chapter 5), the method is applied to analyze the diffusion of 5(6)-carboxyfluorescein within agarose- and agar-based hydrogels.

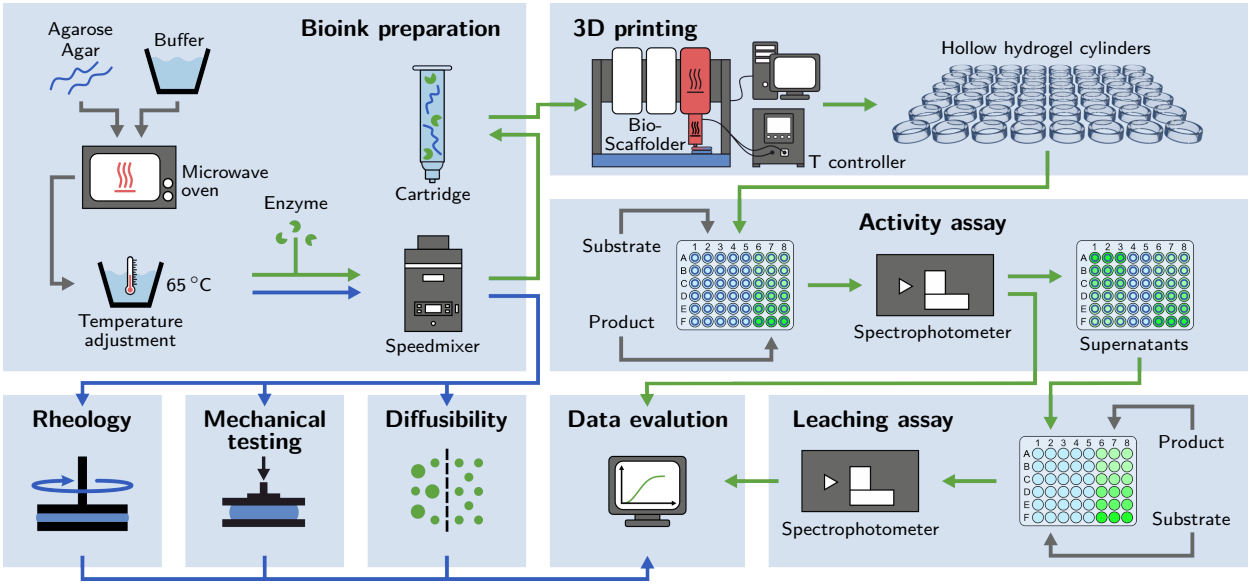

Chapter 5

Lukas Wenger, Carsten P. Radtke, Eva Gerisch, Max Kollmann, Christof M. Niemeyer, Kersten S. Rabe and Jürgen Hubbuch

submitted to Frontiers in Bioengineering and Biotechnology

Previous studies have shown the feasibility of using extrusion-based 3D printing methods for the fabrication of agarose-based hydrogel grids with embedded enzymes that can be employed in biocatalytic reactors. To improve the printing quality of thermosensitive hydrogels and reduce nozzle clogging, this study presents a refined experimental setup including a heatable nozzle and a cooled substrate. A systematic evaluation of the employed material system is provided by covering a range of differently concentrated agarose- and agar-based inks that are investigated with several analytical methods. Rheological measurements are applied to study the flow behavior of the liquid inks at different temperatures, as well as their melting and gelling behavior. The stability of the solidified hydrogels is examined using mechanical tests and their diffusibility is investigated by applying the previously established microfluidics-based UV imaging approach (see Chapter 4). The thermostable enzyme esterase 2 from *Alicyclobacillus acidocaldarius* (AaEst2) is added to the inks to produce enzymatically active hydrogel samples. To quantify the activity of the different materials and the amount of enzyme leaching, the batch-based activity assay method established for emulsion-based inks (see Chapter 3) is applied with appropriate adaptations. The study demonstrates an improved printing method for agarose- and agar-based hydrogels and identifies several parameters crucial for the successful immobilization of enzymes within these hydrogels.

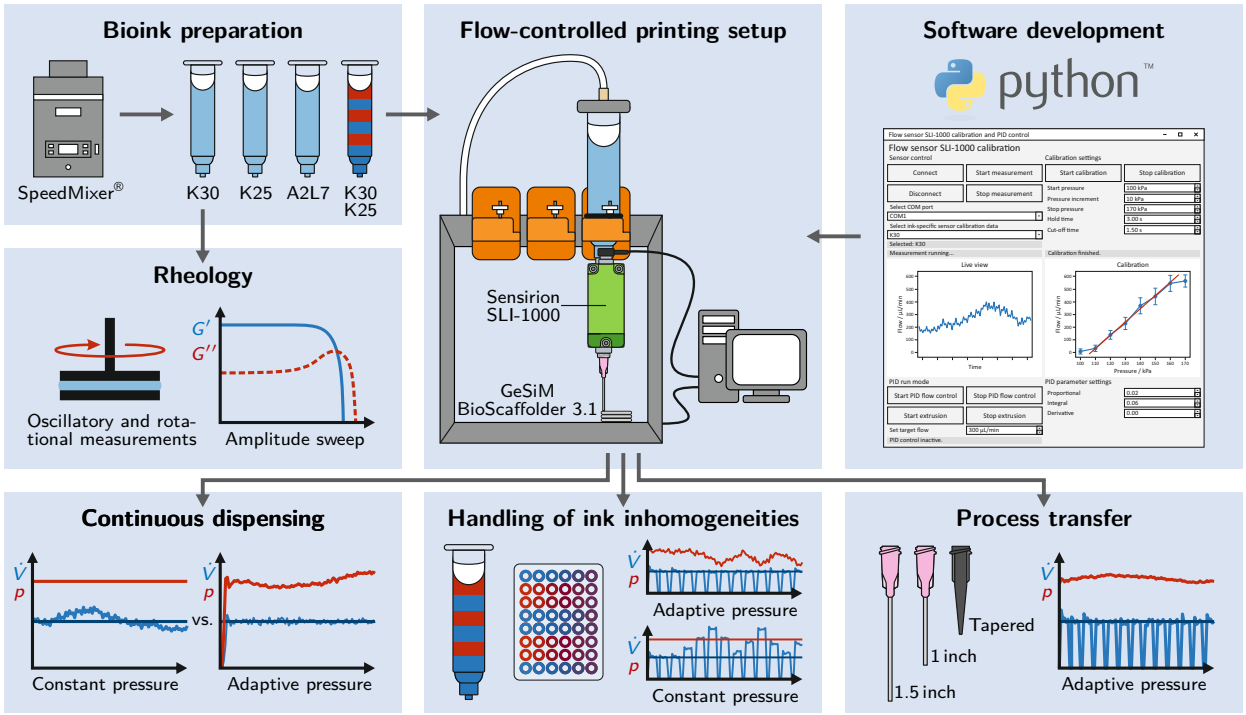

Chapter 6

Automated and Dynamic Extrusion Pressure Adjustment Based on Real-Time Flow Rate Measurements for Precise Ink Dispensing in 3D Bioprinting 99

Lukas Wenger*, Svenja Strauß* and Jürgen Hubbuch *contributed equally

published in Bioprinting, Volume 28, 2022, e00229
https://doi.org/10.1016/j.bprint.2022.e00229

Tedious parameter screenings, non-constant ink flow and poor reproducibility are typical limitations of extrusion-based bioprinting. The common lack of process monitoring poses an additional obstacle. To overcome these challenges, the study presents a customized printing setup incorporating a liquid flow meter to provide real-time flow measurement data. A Python-based software tool is established to allow flow rate monitoring and to dynamically adapt the extrusion pressure of the bioprinter in order to generate a constant flow rate. The recorded flow rate measurements are fed into a proportional-integral-derivative (PID) feedback loop that controls the pressure of the employed bioprinter. The performance of the established setup is evaluated with three different model inks in three application examples. The general ability of the setup to generate a constant ink flow is tested by continuously dispensing ink from a cartridge. The handling of ink inhomogeneities is tested by printing from a cartridge with a deliberately inhomogeneous ink. To assess whether the presented approach can facilitate process transfer and development, test prints with different nozzle geometries are performed. The study demonstrates a way to introduce process monitoring into bioprinting processes and to apply it in real time to automatically control the extrusion pressure of the bioprinter. The approach enhances reproducibility, improves the handling of non-constant process parameters like ink viscosity or cartridge fill level and facilitates process transfer and development.

3

3D-Printable and Enzymatically Active Composite Materials Based on Hydrogel-Filled High Internal Phase Emulsions

Lukas Wenger[1,2], Carsten P. Radtke[1], Jacqueline Göpper[1], Michael Wörner[1] and Jürgen Hubbuch[1,2]

[1] Institute of Engineering in Life Sciences, Section IV: Biomolecular Separation Engineering, Karlsruhe Institute of Technology (KIT), Karlsruhe, Germany

[2] Institute of Functional Interfaces, Karlsruhe Institute of Technology (KIT), Eggenstein-Leopoldshafen, Germany

Abstract

The immobilization of enzymes in biocatalytic flow reactors is a common strategy to increase enzyme reusability and improve biocatalytic performance. Extrusion-based 3D bioprinting has recently emerged as a versatile tool for the fabrication of perfusable hydrogel grids containing entrapped enzymes for the use in such reactors.

This study demonstrates the suitability of water-in-oil high internal phase emulsions (HIPEs) as 3D-printable bioinks for the fabrication of composite materials with a porous polymeric scaffold (polyHIPE) filled with enzyme-laden hydrogel. The prepared HIPEs exhibited excellent printability and are shown to be suitable for the printing of complex three-dimensional structures without the need for sacrificial support material. An automated activity assay method for the systematic screening of different material compositions in small-scale batch experiments is presented. The monomer mass fraction in the aqueous phase and the thickness of printed objects were found to be the most important parameters determining the apparent activity of the immobilized enzyme. Mass transfer limitations and enzyme inactivation were identified as probable factors reducing the apparent activity.

The presented HIPE-based bioinks enable the fabrication of flow-optimized and more efficient biocatalytic reactors while the automated activity assay method allows the rapid screening of materials to optimize the biocatalytic efficiency further without time-consuming flow-through experiments involving whole printed reactors.

3.1 Introduction

Biocatalysis is the key to a variety of biotechnological applications, ranging from large-scale industrial processes like the production of high fructose corn syrup [93] to more sophisticated analytical methods like biosensors [94, 95]. Enzymes act as catalysts even at mild reaction conditions. Due to their high chemo- and regioselectivity, they are suitable for the production of high-value products like enantiomerically pure chiral compounds [96]. Their usually high cost makes it desirable to immobilize enzymes in order to enhance their stability and shelf life and improve reusability by preventing enzyme-loss [91]. Immobilized enzymes can be efficiently employed in continuous processes, e. g. using perfusable fixed-bed reactors [97–99]. While a large variety of immobilization methods like covalent bonding to particles or monolithic support materials does exist, the entrapment of enzymes in hydrogels offers a very straight-forward, effective and universally applicable route [91, 100]. Hydrogels are hydrophilic polymer networks with a high water content that are well suited to accommodate cells and proteins in an aqueous environment [101]. The mesh size of the hydrogel polymer network can be tuned [102, 103] in order to ensure the retention of the usually relatively large enzymes while still allowing the diffusion of smaller substrate and product molecules through the material [91]. Besides increased cost efficiency, the immobilization of enzymes offers a way to realize processes combining different spatially separated reactions. These compartmentalized enzymatic cascades may prevent undesirable effects like product inhibition or cross-reactivities. [104] A drawback of entrapping enzymes in hydrogels is the reduced mass transfer through the hydrogel matrix which lowers the apparent biocatalytic activity as compared to the freely dissolved enzyme [12, 91]. This limitation can be counteracted by increasing the surface-area-to-volume ratio of the hydrogel structures [12].

Extrusion-based bioprinting methods can be used as a simple tool to produce hydrogel structures in customized 3D shapes, typically laden with living cells or bioactive molecules [55, 73]. The so-called bioink, a hydrogel precursor formulation blended with the biological component, is dispensed layer-by-layer from a cartridge through a nozzle and usually cross-linked after extrusion in order to retain a stable 3D shape [68, 105]. Extrusion-based printing is widely employed in biofabrication but resolutions are usually low with extruded strand widths of typically 200 to 1000 µm [68]. Achievable strand widths and hence printing quality and resolution depend largely on the rheological properties of the bioink. Shear-thinning behavior is desirable to facilitate the material flow through the nozzle and allow dispensing at lower pressure [106]. After extrusion, the ink should preserve its shape without spreading until fixation is achieved by cross-linking. This is ensured by a sufficiently high viscosity or the presence of a yield stress. [68, 70, 107] However, many hydrogel precursor solutions are low-viscosity liquids that lack the necessary rheological properties. Strategies to enhance printability include improving the rheological properties of the ink by the addition of viscosity-enhancing additives [12, 108] or by pre-crosslinking [109, 110]. Other approaches aim at improving shape preservation after extrusion by printing into a support bath [111, 112] or minimizing the time between extrusion and final fixation of the shape in order to reduce spreading of the material. Depending on the crosslinking machanism, this can be achieved by co-extruding a crosslinking agent through a coaxial nozzle [78, 113] or by *in situ* photopolymerization using a cure-on-dispense setup [114–116].

High internal phase emulsions (HIPEs) are paste-like emulsions containing more than 74 % (v/v) of internal phase [117]. Below the yield stress, they act as a solid retaining their shape. Applying a force above the yield stress initiates the flow of the material [118]. This property makes HIPEs ideal candidates for extrusion-based 3D printing, as shown by Sears *et al.* [115, 119]. The external phase of HIPEs can be polymerized creating so-called polyHIPEs, a monolithic and porous polymer scaffold with void sizes typically in the range of one to several hundred micrometers [120–122] and interconnecting pores between the voids [122]. There are two approaches towards formulating low-viscosity hydrogel precursor solutions as printable HIPE-based inks: Using oil-in-water HIPEs with a polymerizable external phase [119] or using water-in-oil HIPEs with both phases being polymerizable [123–125]. The first approach yields a hydrogel filled with droplets of liquid oil, while the second approach yields a typical open-cell polyHIPE scaffold filled with hydrogel.

In (bio-)chemical engineering, 3D printing methods can enable the fabrication of highly sophisticated, geometrically optimized reactors not producible by conventional methods [46], as has been shown for bed geometries of chromatography columns [126], heat exchangers [127] or microfluidic reactors [128]. 3D printing can also dramatically speed up the production of prototypes [1], allowing the iterative testing of different designs. Kazenwadel *et al.* used a commercial inkjet 3D printer to manufacture biocatalytic flow reactors based on a 3D-printed grid of synthetic material. Glucose oxidase and horseradish peroxidase were covalently immobilized on the surface of the grid in a subsequent step [129]. This concept has been developed further by directly printing enzyme-containing hydrogel grids in a single step using extrusion-based 3D bioprinters [12, 85, 130]. Enzymatically active printed hydrogels with living yeast cells have been reported as well [131].

The reported methods and inks for extrusion-based 3D printing of enzyme-containing hydrogels are limited to the fabrication of very basic geometries comprising only a few layers and exhibiting relatively high wall thicknesses, thereby limiting mass transfer and reducing efficiency. Furthermore, a systematic investigation of the influence of material parameters on the resulting apparent activity

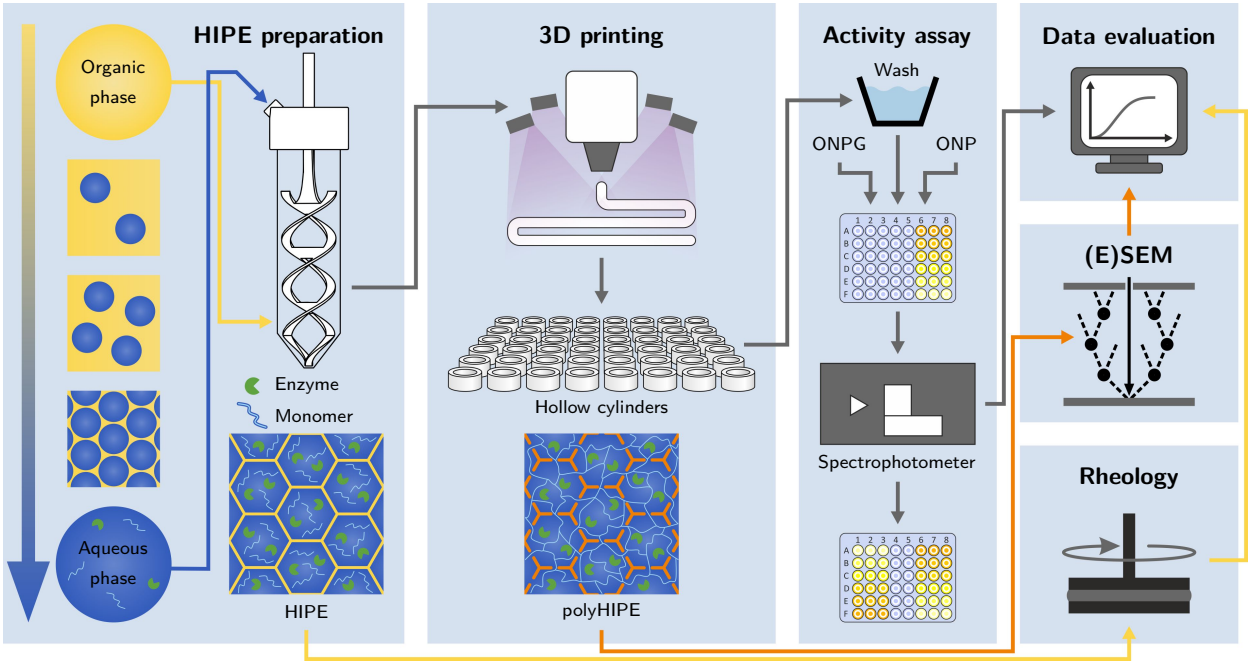

Figure 3.1 Schematic of the workflow applied in this study. After preparation, HIPEs are printed and photopolymerized *in situ* using a cure-on-dispense setup. The resulting hydrogel-filled polyHIPE cylinders are analyzed in automated activity assays in a 48-well microtiter plate format. Samples of liquid HIPEs are analyzed using rheological measurements. (Environmental) scanning electron micrographs of polyHIPEs are taken to analyze their morphology and confirm the presence of hydrogel inside the polyHIPE voids.

of the printed hydrogels is missing. The study presented here investigates the approach to enhance the printability of low-viscosity hydrogel precursor solutions using water-in-oil HIPEs as bioinks with excellent printability enabling the fabrication of more complex structures. Scanning electron microscopy techniques are used to analyze the scaffold morphology and confirm the formation of hydrogel inside the polyHIPE voids. The enzyme β-galactosidase is entrapped in the hydrogel-filled polyHIPEs and an automated activity assay method is presented to determine the influence of different HIPE compositions on the apparent activity of the produced materials. A workflow of the presented study is shown in Figure 3.1.

3.2 Materials and Methods

3.2.1 Chemicals

All chemicals were purchased from Sigma Aldrich and used as received. For the organic phase of the HIPEs, 2-ethylhexyl acrylate (EHA), isobornyl acrylate (IBOA), trimethylolpropane triacrylate (TMPTA), poly(ethylene glycol)-block-poly(propylene glycol)-block-poly(ethylene glycol) (Pluronic® L-121) and diphenyl(2,4,6-trimethylbenzoyl)phosphine oxide (Darocur® TPO) were used. The aqueous phase contained acrylic acid (AA), poly(ethylene glycol) diacrylate with an average molar mass of M_n = 700 g/mol (PEG-DA 700), lithium phenyl-2,4,6-trimethylbenzoylphosphinate (LAP) and β-galactosidase from *Aspergillus oryzae* (EC 3.2.1.23, 10.9 units/mg). Activity assays were con-

ducted using 2-nitrophenyl β-D-galactopyranoside (ONPG) as the substrate and calibration curves of the reaction product were determined from serial dilutions of 2-nitrophenol (ONP). All buffers and solutions were prepared with ultrapure water from a Purelab Ultra water purification system (Elga, High Wycombe, UK) and filtered through an 0.2 µm cellulose acetate filter (Sartorius AG).

3.2.2 Stock solutions

20 % (w/w) AA and 20 % (w/w) PEG-DA 700 were prepared as stock solutions for the aqueous phase, both buffered with 100 mM phosphate and adjusted to pH 7. A stock solution of 1.6 kU/mL β-galactosidase was prepared in 100 mM phosphate (pH 7). Serial dilutions of ONPG for the activity assays and ONP for the calibration curves were prepared in 100 mM phosphate, pH 7. The stock solutions of β-galactosidase, ONPG and ONP were frozen in aliquots at −30 °C and thawed directly before use.

3.2.3 Preparation of HIPEs

A series of preliminary experiments resulted in the selection of a set of suitable chemicals for HIPE preparation. The external organic phase of the HIPEs was prepared from the monomers EHA, IBOA and TMPTA, the surfactant Pluronic® L-121 and the photoinitiator Darocur® TPO. For all HIPEs, the mass ratio between EHA, IBOA and TMPTA was kept constant at 2.3:4.2:1 while the amount of Pluronic® L-121 in the organic phase was varied between 6 and 12 % (w/w). The Darocur® TPO concentration was 0.5 % (w/w) for all HIPEs. All compositions of organic phase are listed in Table A3.1 in the supplementary material. The internal aqueous phase was always freshly prepared from buffered stock solutions of AA, PEG-DA 700, LAP and β-galactosidase. The resulting aqueous phase had constant concentrations of LAP (1 mg/mL) and β-galactosidase (40 units/mL) with varying total monomer mass fractions and a constant molar ratio of AA:PEG-DA 700 = 10:1. In HIPEs with a lower monomer content in the aqueous phase than 14 % (w/w), a corresponding amount of AA stock solution was replaced by a buffered solution of 100 mM phosphate at pH 7 that was adjusted to the same conductivity as the AA stock solution by adding NaCl. The corresponding amount of PEG-DA 700 solution was replaced by 100 mM phosphate buffer, pH 7. All HIPE variations prepared in this study, as listed in Table 3.1, are derived from HIPE A, a HIPE with 14 % (w/w) monomer in the aqueous phase, 12 % (w/w) surfactant in the organic phase, 87.5 % aqueous phase volume fraction and printed using a 250 µm nozzle.

Emulsification of the HIPEs was performed in 50 mL Falcon tubes (Corning, Inc.) using an overhead stirrer (Velp Scientifica DLS) and a specifically designed, 3D-printed, helical stirrer blade made from nylon, as depicted in Figure 3.2A. For HIPEs with a percentage of 87.5 % (v/v) of aqueous phase, 2.5 mL of organic phase were added to a Falcon tube. Under continuous stirring, 17.5 mL of aqueous phase were continuously added at a rate of 1.25 mL/min using a syringe pump (Cetoni neMESYS 290N). The stirring rate was initially set to 600 rpm and increased to 800 rpm after 2 min and 1000 rpm after 7 min. After addition of the aqueous phase, agitation was maintained for another 5 min at 1000 rpm. For HIPEs with a percentage of aqueous phase different from 87.5 %, the amounts of organic phase and aqueous phase were adjusted to always produce 20 mL of HIPE in total. The addition rate and time points of stirring rate changes were adjusted relative to the amount of organic phase, as shown in Table A3.2 in the supplementary material.

Table 3.1 Overview of the HIPEs prepared and printed in this study. The table shows the mass fraction of monomer in the internal aqueous phase, the surfactant mass fraction in the external organic phase, the aqueous phase volume fraction and the nozzle diameter used for printing hollow cylinders for activity assays. All variations are derived from HIPE A (blue). Parameters deviating from HIPE A are highlighted in orange.

	Varied parameter	Monomer in aqueous phase (% (w/w))	Surfactant in organic phase (% (w/w))	Aqueous phase volume fraction (% (v/v))	Nozzle diameter (µm)
HIPE A	—	14	12	87.5	250
HIPE variations	Monomer	10.5	12	87.5	250
		7	12	87.5	250
		3.5	12	87.5	250
		1.75	12	87.5	250
		0	12	87.5	250
	Surfactant	14	9	87.5	250
		14	6	87.5	250
	Aqueous phase	14	12	90	250
		14	12	85	250
		14	12	82.5	250
		14	12	80	250
	Nozzle diameter	14	12	87.5	840
		14	12	87.5	110

3.2.4 Rheology

Rheological measurements of HIPEs were performed using an MCR 301 rheometer (Anton Paar GmbH). A measurement geometry with profiled parallel plates with a diameter of 25 mm and a gap width of 150 µm was used to perform shear stress-controlled rotational tests. Yield stress values were determined by plotting deformation over shear stress in a log-log graph, fitting the two linear regions of the plot with tangents and calculating their point of intersection.

Using the same experimental setup, oscillatory measurements with controlled shear stress in a range of 1 to 1000 Pa were performed at an angular frequency of $\omega = 10\,/\mathrm{s}$. The storage modulus G' and loss modulus G'' were recorded. All measurements were carried out as technical triplicates.

3.2.5 (Environmental) scanning electron microscopy (ESEM and SEM)

For sample preparation, HIPEs were polymerized on microscope slides in a frame of 2 mm in height. The polymerization was carried out for 1 min from each side at an intensity of approximately 25 $\mathrm{mW/cm^2}$ and a peak wavelength of 365 nm.

Samples for environmental scanning electron microscopy (ESEM) were stored in 100 mM phosphate buffer (pH 7) and cut immediately before analysis to investigate the cross-section. ESEM micrographs were taken using an FEI Quanta 650 FEG (Thermo Fisher Scientific, Inc.) in a water-saturated atmosphere at a pressure between 704 Pa and 823 Pa, a working distance between 6.8 mm and 8.1 mm, a 2000-fold magnification and an acceleration voltage of 15 kV.

For scanning electron microscopy (SEM), samples were freeze-dried, cut and the cross-section coated with platinum. Analysis was carried out on a Tescan Vega 3 SBU at an acceleration voltage of 8 kV and a working distance of 14 mm.

3.2.6 3D printing

HIPEs were 3D-printed employing two different extrusion-based printers: a piston-driven, previously described modified Ultimaker Original+, introduced as *Biomaker* by Radtke *et al.* [132], and a pneumatically driven Gesim BioScaffolder 3.1. Both printers were equipped with a cure-on-dispense setup similar to a system reported by Sears *et al.* [115], based on four high-power UV LEDs emitting at a peak wavelength of 365 nm (LEDengin, San Jose, USA). The setup employed in combination with the BioScaffolder is depicted in Figure 3.2B.

For activity assays, simple hollow cylinders with a diameter of 8 mm and a height of 2.4 mm were printed, designed to fit into the wells of 48-well microtiter plates (Figure 3.5C). The *Biomaker* was used in combination with conical nozzles with an inner diameter of 250 and 840 µm to print 300 µm layers while curing at an intensity of approximately 3.5 mW/cm^2. The BioScaffolder was equipped with Micron-S nozzles (Vieweg GmbH) with an inner diameter of 110 µm and 100 µm layers were printed while curing at an intensity of approximately 13 mW/cm^2. In order to prevent clogging, aluminium foil was wrapped around the end of the nozzle to shield the nozzle opening from UV irradiation. All printing parameters are summarized in Table 3.2. After the printing process, all cylinders were post-cured at an intensity of approximately 25 mW/cm^2 for 2 min.

Table 3.2 Printing parameters employed in the fabrication of polyHIPE cylinders and exemplary prints.

Printer	Printing speed (mm/s)	Nozzle diameter (µm)	Nozzle type —	Layer height (µm)	Extrusion pressure (kPa)	Extrusion rate (EU[a]/mm)	UV intensity (mW/cm^2)
Biomaker	9	840	conical	300	—	9×10^{-4}	3.5
Biomaker	9	250	conical	300	—	6×10^{-4}	3.5
Bioscaffolder	9	110	Micron-S	100	30 ± 10	—	13.0

[a]EU = extrusion unit, an arbitrary unit to adjust the extrusion rate on the Biomaker

3.2.7 Activity assays with printed polyHIPEs

PolyHIPE cylinders, printed as described above, were washed three times for 5 min: once in 30 % (v/v) ethanol in 100 mM phosphate (pH 7) and twice in 100 mM phosphate (pH 7). The washed cylinders were transferred into a 48-well microtiter plate, one cylinder per well. ONPG solutions at concentrations between 1 mM and 30 mM in 100 mM phosphate (pH 7) were added using a Tecan Freedom Evo pipetting platform and the conversion from ONPG to ONP catalyzed by β-galactosidase was monitored online at a wavelength of 460 nm for 90 min using a Tecan infinite M200 pro spectrophotometer (Figure 3.3A). All activity assays were carried out at 25 °C. Employing calibration curves, ONP concentrations were calculated from the absorbance signal and the maximum volumetric activity per well was calculated by determining the maximum slope of each curve which occured after a variable delay time t_{delay} (Figure 3.3B). The specific activity of each sample was determined by dividing the volumetric activity by the amount of enzyme in one polyHIPE cylinder.

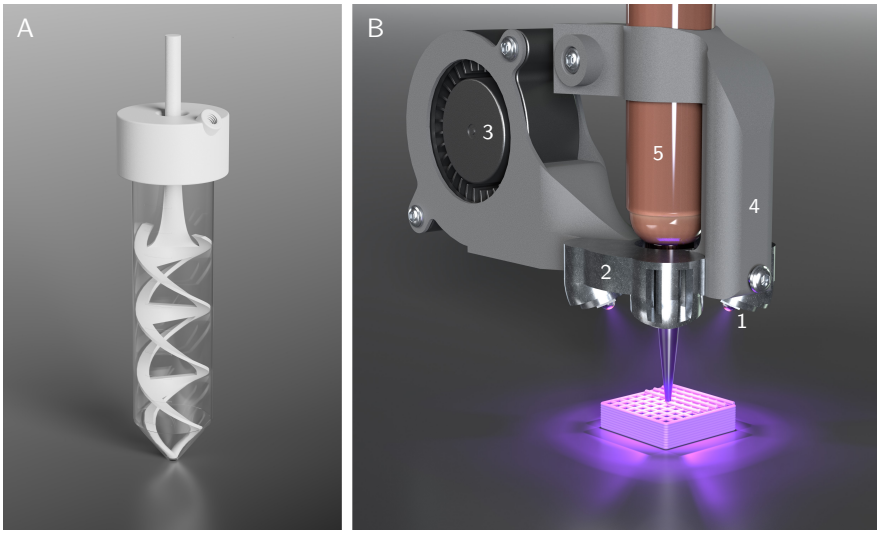

Figure 3.2 Illustrations of custom-made equipment used for HIPE preparation and printing. (A) Setup used for HIPE emulsification. The helical stirrer blade and the lid were custom-made for 50 mL Falcon tubes. The lid offers an opening for the stirrer blade and a threaded hole to connect tubing and allow the continuous addition of aqueous phase using a syringe pump. (B) Cure-on-dispense setup used in combination with a Gesim BioScaffolder 3.1. Four high power UV LEDs (1) are attached to a metal heatsink (2) which is perfused by air from a fan (3) for active cooling. The mount (4) allows the direct attachment to 10 mL cartridges (5).

Plots of the specific activity over the substrate concentration were fitted with Michaelis-Menten kinetics (Figure 3.3C). Combining several of these kinetics resulted in 3D plots showing the influence of both substrate concentration and a second varied parameter on the specific activity (Figure 3.3D).

3.2.8 Calibration curves and equilibration time

Data for ONP calibration curves for the polyHIPE activity assays were collected following the same procedure as applied for the activity assays, only adding solutions of up to 25 mM ONP instead of ONPG before monitoring the absorbance at 460 nm for 90 min. Due to diffusion and evaporation effects, the observed absorbance was not constant over time but showed an exponential decay at the beginning, turning into a linear decay after a certain time. The recorded data for the calibration curves of HIPE A are shown as an example in the supplementary material (Figure A3.1).

Linear calibration curves were determined from the end points of the measurements where an equilibrium between polyHIPE cylinder and supernatant was already reached. Triplicates of five different ONP concentrations (2.5 to 20 mM) were used as the calibration points. To determine the equilibration time as a measure of diffusion limitations, an algorithm was employed that calculated the earliest point of time at which the slopes of the measured absorbance curves were within 20 % of the end slope of the curves. The time span from the addition of ONP until this time point was defined as the equilibration time (see Figure A3.1 in the supplementary material).

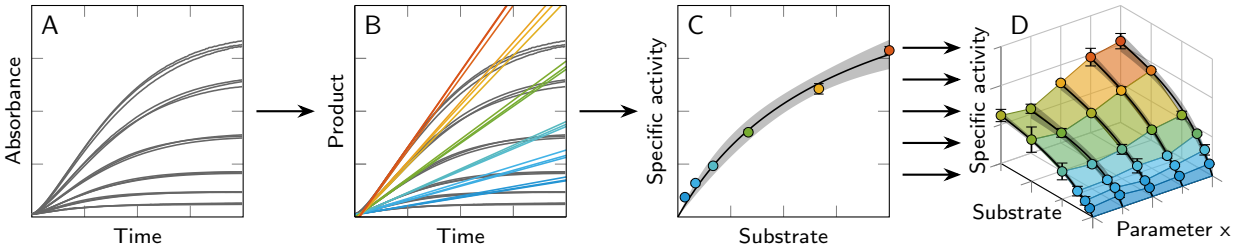

Figure 3.3 Overview of the data processing steps used for the evaluation of activity assays with polyHIPE cylinders. The example shows data from the analysis of different aqueous phase volume fractions. (A) The product formation was monitored by measuring the absorbance at 460 nm in a spectrophotometer. The curves show triplicates of six different substrate concentrations. (B) Using calibration curves, the product concentration was calculated from the absorbance signal and the maximum slope of the resulting curves was calculated to determine the maximum volumetric activity. Due to diffusion limitations, the maximum slope does not occur at the start of the reaction but after an initial delay time t_{delay}. (C) The specific activity was calculated from the volumetric activity and the resulting data points were plotted over the substrate concentration and fitted with a Michaelis-Menten equation (95 % confidence intervals shown in gray). (D) Several kinetics curves were combined with a surface plot to compare different conditions.

3.2.9 Enzyme leaching

To determine the amount of leached enzyme during different process steps, activity assays were performed with the supernatants of the polyHIPE cylinder wash procedure described above. Also, single polyHIPE cylinders were incubated with 300 µL phosphate buffer (100 mM, pH 7) for 90 min mimicking the polyHIPE activity assay to analyze the amount of leached enzyme during the whole incubation period. The supernatant activity assays were carried out in 96-well microtiter plates by adding 150 µL 30 mM ONPG in 100 mM phosphate (pH 7) to a 50 µL sample of supernatant (dilution factor $f = 4$) and recording the conversion of ONPG to ONP at a wavelength of 460 nm for 20 min. In order to account for samples from different wash solutions (30 % ethanol and 100 mM phosphate), separate calibration curves with a range of ONP and β-galactosidase concentrations were recorded for the respective samples and used to calculate the volumetric activity of the samples and the amount of active enzyme leached from the polyHIPE cylinders. For error analysis of the polyHIPE activity assays (see following section), the volumetric activity of the supernatant samples after a 90 min incubation period ($v_{leached,\,90\,\mathrm{min}}$) was determined taking into account the dilution factor f.

3.2.10 Error analysis of polyHIPE activity assays

An error analysis was performed in order to estimate the influence of leached enzyme on the activity assays performed with printed polyHIPEs. The maximum error E_{max} and minimum error E_{min} were calculated by introducing a best-case and a worst-case scenario. These scenarios assume that the total apparent volumetric activity $v_{apparent}$ observed in the polyHIPE activity assays is composed

of a proportion caused by the enzyme immobilized in the polyHIPEs ($v_{immobilized}$) and a proportion caused by leached enzyme ($v_{leached}$). The error E is defined as

$$E = \frac{v_{leached}}{v_{apparent}}. \tag{3.1}$$

The worst-case scenario assumes that $v_{leached,\,max}$ equals the volumetric activity in the supernatant after a 90 min incubation period ($v_{leached,\,90\,\mathrm{min}}$).

$$v_{leached,\,max} = v_{leached,\,90\,\mathrm{min}} \tag{3.2}$$

The best-case scenario assumes that enzyme is leaching from the polyHIPE at a constant rate over 90 min and accumulates in the supernatant of the polyHIPE cylinders. As the maximum volumetric activity of the polyHIPE cylinders occurs after an initial delay time t_{delay} (see Figure 3.3, the amount of leached enzyme that has accumulated during this time period determines $v_{leached,\,min}$.

$$v_{leached,\,min} = \frac{t_{delay}}{90\,\mathrm{min}} \cdot v_{leached,\,90\,\mathrm{min}} \tag{3.3}$$

These scenarios result in the following definitions of maximum and minimum error.

$$E_{max} = \frac{v_{leached,\,90\,\mathrm{min}}}{v_{apparent}} \tag{3.4}$$

$$E_{min} = \frac{t_{delay} \cdot v_{leached,\,90\,\mathrm{min}}}{90\,\mathrm{min} \cdot v_{apparent}} \tag{3.5}$$

3.2.11 Statistical analysis

The statistical significance of data was tested employing a one-way analysis of variance (ANOVA) and the Tukey method for multiple comparisons.

3.3 Results

3.3.1 Rheology

Rheological measurements were performed in order to investigate the influence of changing HIPE compositions on yield stress and storage and loss moduli as important parameters for printability. Figure 3.4 shows both yield stress and storage and loss moduli for HIPEs with a varying monomer mass fraction in the aqueous phase (A), surfactant mass fraction in the organic phase (B) and aqueous phase volume fraction (C). Yield stress values could be determined for all prepared HIPEs. The different formulations of aqueous phase not formulated as HIPEs did not exhibit a yield point. Of all parameters tested, the surfactant concentration in the organic phase had the largest impact on yield stress with a 10-fold increase between 6 % and 12 % (w/w) surfactant. Increasing the aqueous phase volume fraction from 80 % to 90 % (v/v) led to a 3.5-fold increase in yield stress. For different monomer concentrations in the aqueous phase, the yield stress fluctuated between (123.1 ± 2.1) Pa and (148.2 ± 4.4) Pa without any clear trend.

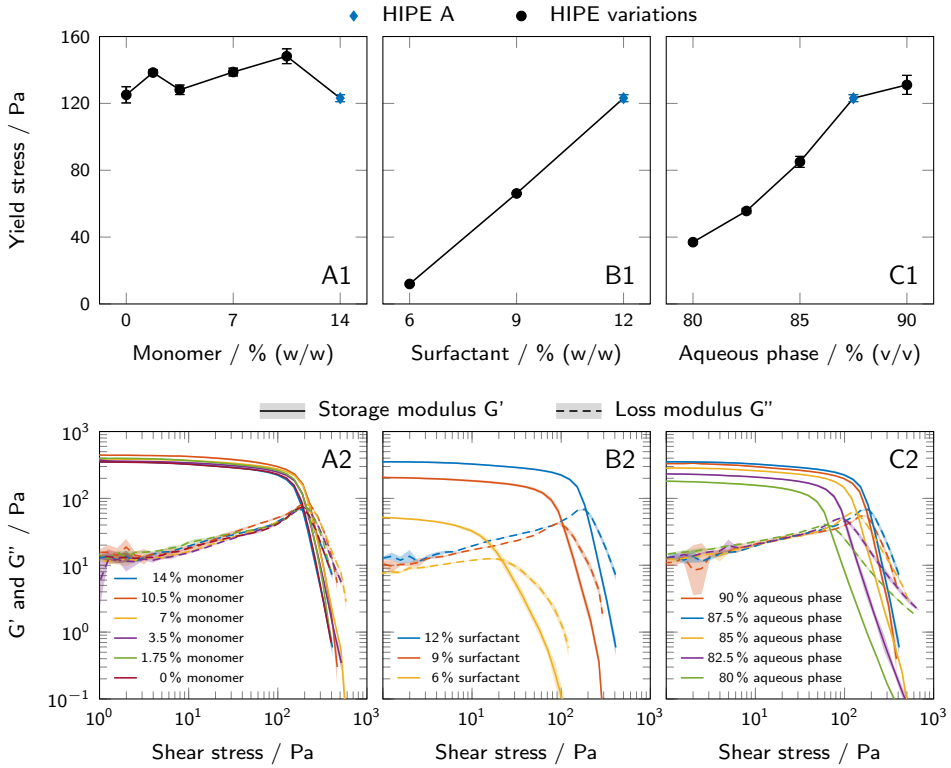

Figure 3.4 (A1-C1) Yield stress of all prepared HIPEs, as determined by rotational tests and the tangent fit method. The results are presented as mean values ± standard deviation ($n = 3$, technical triplicates). (A2-C2) Shear stress-controlled oscillatory measurements showing storage and loss moduli of all prepared HIPEs. The results are presented as mean values and standard deviations are indicated by shaded areas ($n = 3$, technical triplicates). All variations are derived from HIPE A (depicted in blue in each graph). The influence of (A) monomer mass fraction in the aqueous phase, (B) surfactant mass fraction in the organic phase and (C) aqueous phase volume fraction is shown.

Similar trends could be observed for the loss and storage moduli in shear stress-controlled oscillatory measurements. All samples showed a higher storage than loss modulus at low shear stress, i. e. a loss factor $tan(\delta) < 1$, indicating a gel-like nature of the HIPEs.

3.3.2 Printability

Hollow cylinders of different HIPE compositions, as depicted in Figure 3.5C, were printed for batch activity assays using the *Biomaker*. Samples of printed cylinders made from HIPEs with five different compositions ($n = 5 \times 5 = 25$) representing the whole measured yield stress range were weighed to assess how reproducibly cylinders could be printed using identical printing parameters with different HIPEs. ANOVA showed no significant differences between the analyzed groups ($p = 0.68$). The overall mean weight of the printed cylinders was (45.7 ± 0.9) mg. To illustrate the excellent printability of HIPE inks, more complex structures were printed from HIPE A using a pneumatically driven Gesim BioScaffolder 3.1. Figure 3.5A shows a grid with a 10 mm edge length and a height of 5 mm consisting of 100 µm layers. All inter-strand spaces are free of obstructing artefacts making the

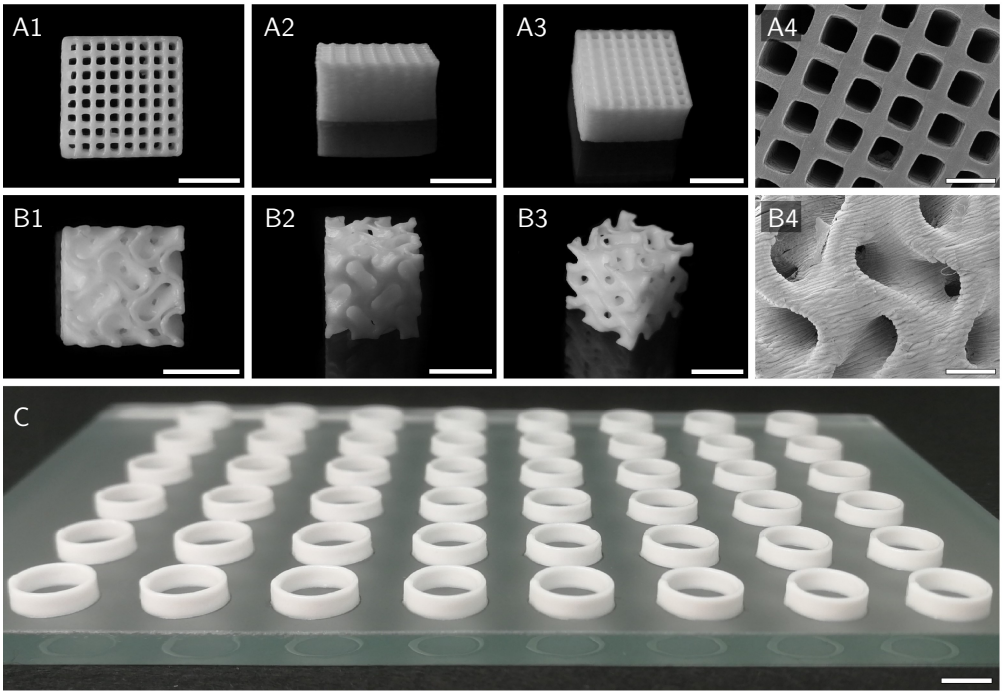

Figure 3.5 Various scaffolds printed with HIPE A to demonstrate printability. (A1-A4) Top, side, angled and SEM view of a cuboid grid structure with an edge length of 10 mm and a height of 5 mm. (B1-B4) Top, side, angled and SEM view of a cubic gyroid structure with an edge length of 8 mm. Model adapted from [133]. (C) 48 hollow cylinders, as used for activity assays, printed on a glass plate in microtiter plate format. Scale bars represent 5 mm (A1-A3, B1-B3, C) and 1 mm (A4, B4), respectively.

grid entirely perfusable. The gyroid structure depicted in Figure 3.5B demonstrates the applicability of HIPEs as inks for prints of more complex reactor geometries including overhangs without the need for sacrificial material. While the printability of all prepared HIPEs was sufficient to print the simple hollow cylinders needed for the activity assays, a certain yield stress was essential for prints of more complex structures as shown in Figure 3.5.

3.3.3 PolyHIPE morphology

SEM and ESEM micrographs of polyHIPE cross-sections were taken to investigate the scaffold morphology and the presence of polymerized hydrogel in the voids of the scaffolds. PolyHIPEs with different surfactant mass fractions in the organic phase and no monomers in the aqueous phase (Figure 3.6A-C) were compared to the corresponding polyHIPEs containing 14 % (w/w) monomer in the aqueous phase (Figure 3.6D-F and G-I). HIPEs without monomers in the aqueous phase resulted in samples exhibiting typical polyHIPE morphologies with empty voids and interconnecting pores between the voids (Figure 3.6A-C). Increasing the surfactant mass fraction in the organic phase resulted in smaller voids. SEM micrographs of polyHIPEs with 14 % (w/w) monomer in the aqueous phase are represented in Figure 3.6D-F. Here, the typical polyHIPE scaffold is only visible in the samples with 6 and 9 % (w/w) surfactant in the organic phase. Some of the voids are filled with hydrogel spheres slightly smaller than the surrounding voids. It is noticeable that the interconnecting pores of these samples are smaller and less frequent compared to the samples

without monomers in the aqueous phase, resulting in a lower degree of openness of the scaffold. The SEM micrograph of the sample with 12 % (w/w) surfactant in the organic phase shows a collapsed scaffold structure (Figure 3.6F) indicating a reduced mechanical stability of the porous scaffold. As a comparison, the samples containing monomers in the aqueous phase were also analyzed by ESEM (Figure 3.6G-I) which does not require the samples to be freeze-dried before analysis. Here, not only a few but most voids were filled with hydrogel spheres and even at a surfactant concentration of 12 % (w/w) in the organic phase, the ESEM micrographs show an intact polyHIPE scaffold, implying the freeze-drying step to be the cause for the collapsed scaffold obvserved in SEM. Despite the preparation of the ESEM samples in a hydrated state, the hydrogel spheres were smaller than the surrounding voids implying a certain degree of shrinkage.

In order to analyze the effect of the printing process on the material morphology, additional SEM micrographs were taken of polyHIPEs printed with a 250 µm nozzle and with different surfactant concentrations (see Figure A3.2 in the supplementary material). The cross-sections of these samples showed intact polyHIPE scaffolds indicating that the printing process did not impair the structure of the resulting material. Furthermore, micrographs of the surface of these printed samples revealed an open-porous surface potentially suitable for the penetration of the material by substrate solutions. Micrographs of a printed cylinder of HIPE A at a lower magnification showed a homogeneous cross-section without any visible interfaces between different printed layers (see Figure A3.3 in the supplementary material).

3.3.4 Equilibration time

The equilibration time when adding ONP solutions to polyHIPE cylinders was determined from calibration data as a measure of diffusion limitations. Data for calibration curves were generated by adding serial dilutions of ONP to printed polyHIPE cylinders and recording the absorbance at 460 nm for 90 min. The observed signals showed an exponential decay at the beginning, turning into a linear decay after a certain time span depending on the polyHIPE composition and the thickness of the cylinder. The linear decay of the absorbance signal was caused by evaporation of ONP, as confirmed experimentally. The time span until a steady slope was reached was defined as the equilibration time. It was determined for all measured samples and is shown in Figure 3.7. The mass fraction of monomer in the aqueous phase was found to have no significant effect within the analyzed range (Figure 3.7A). Both a higher mass fraction of surfactant in the organic phase and a higher aqueous phase volume fraction correlated with a decrease in equilibration time (Figure 3.7B and 3.7C). The highest impact of all tested parameters was observed for the nozzle diameter where the equilibration time increased from (6.6 ± 3.1) min to (52.0 ± 0.9) min when changing nozzle diameters from 110 µm to 840 µm.

3.3.5 Enzyme leaching

In order to quantify the amount of active enzyme leached from the polyHIPE cylinders during the three wash steps and a 90 min incubation period, activity assays were conducted with the supernatants of the wash and incubation steps (Figure 3.8). The most remarkable result was found for wash step 1 of the polyHIPE sample with a monomer concentration of 0 % (w/w) in the aqueous phase. Here, the determined amount of leached active enzyme is only a sixth of the second lowest value determined for step 1. Furthermore, this was the only sample exhibiting a similar amount of leached active enzyme for all three wash steps. For all other conditions, the amount of active

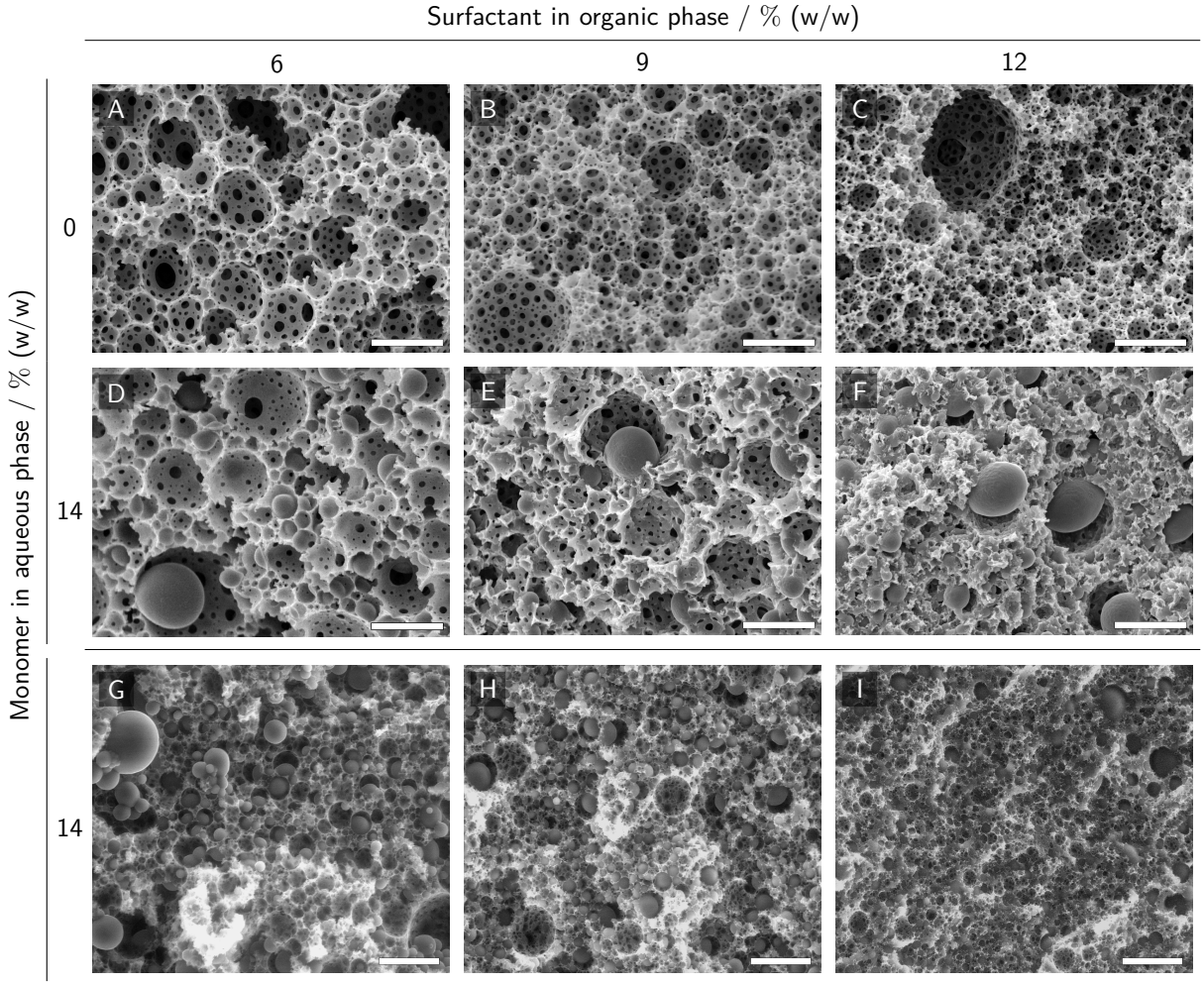

Figure 3.6 (E)SEM micrographs of polyHIPE cross-sections with 0 % and 14 % (w/w) monomer in the aqueous phase and 6 % to 12 % (w/w) surfactant in the organic phase. (A-C) SEM micrographs of polyHIPEs without monomer in the aqueous phase display a typical polyHIPE morphology with empty voids and interconnecting pores between the voids. (D-F) SEM micrographs of polyHIPEs with monomers in the aqueous phase. (G-I) ESEM micrographs of polyHIPEs with monomers in the aqueous phase. The scale bars represent 10 µm (A-F) and 25 µm (G-I), respectively.

enzyme leached during the first step was at least fourfold higher than for the two subsequent steps. A clear trend could be observed for the volume fraction of aqueous phase where a higher volume fraction correlated with a higher amount of active leached enzyme in the supernatant of wash step 1. The relative loss of enzyme during the first wash step was also inversely correlated with the nozzle diameter. However, with a maximum deviation of 6 % between the samples, the absolute amount of leached enzyme was nearly identical for all three nozzle diameters. Regarding the supernatants of the 90 min incubation samples, only two showed more than 0.5 % leached enzyme: (1.8 ± 0.2) % for samples with 90 % aqueous phase volume fraction and (8.0 ± 0.9) % for samples printed with 110 µm nozzles.

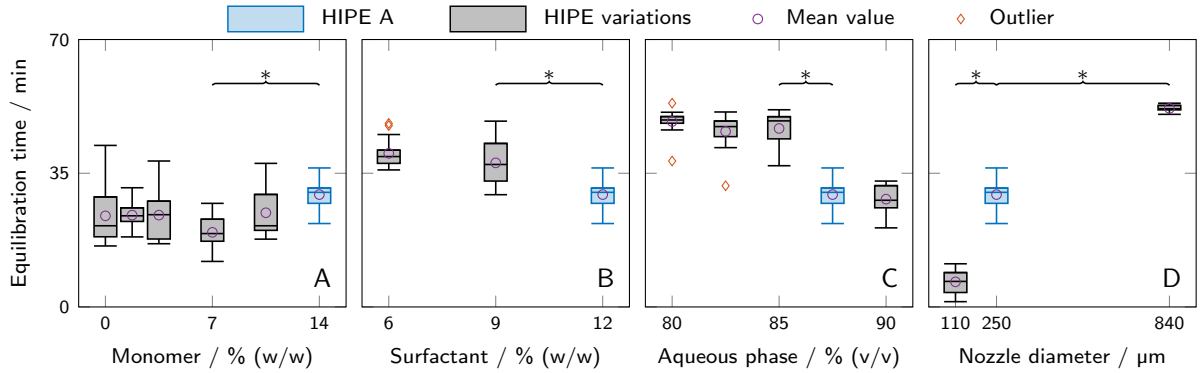

Figure 3.7 Equilibration time as determined from measurements for ONP calibration curves with different polyHIPE cylinders. All variations are derived from HIPE A printed with a 250 µm nozzle (depicted in blue in each graph). The box plots represent the median and the upper and lower quartile. The whiskers represent the most extreme value still within a 1.5-fold interquartile range (IQR) from the upper and lower quartile, respectively. All data points outside the 1.5-fold IQR are depicted as outliers. Each box represents triplicates of six different ONP concentrations ($n = 6 \times 3 = 18$). For clarity, only significant differences to the nearest significantly different data points are highlighted by asterisks ($p < 0.05$). The compared parameters are (A) monomer mass fraction in the aqueous phase, (B) surfactant mass fraction in the organic phase, (C) aqueous phase volume fraction and (D) nozzle diameter.

3.3.6 Activity assays

Activity assays with printed hydrogel-filled polyHIPE cylinders containing β-galactosidase in the aqueous phase were performed to investigate the influence of various parameters on the resulting enzymatic activity. All values discussed here are specific activity values calculated per mg of β-galactosidase crude cell extract from *Aspergillus oryzae*. Figure 3.3 shows the typical evolution of absorbance (A) and product concentration (B) over time for different substrate concentrations. Unlike in assays with freely dissolved enzyme, the maximum turnover rates did not occur immediately after substrate addition but after a delay of several minutes with steadily increasing turnover rates. The maximum turnover rate of each sample was determined and the specific activity calculated to ensure comparability between experiments with different amounts of enzyme. Plotting the specific activities over substrate concentration resulted in curves resembling Michaelis-Menten kinetics which were fitted accordingly (Figure 3.3C). Combining different kinetics curves with a 3D surface plot allows depicting variations in activity over substrate concentration and a second parameter (Figure 3.3D).

The resulting kinetics of all performed activity assays are presented in Figure 3.9. Of the three HIPE composition parameters being varied, the monomer mass fraction in the aqueous phase had the highest impact on specific activity. An increase in monomer mass fraction from 0 % to 7 % correlated with a more than fivefold increase in specific activity at 30 mM substrate concentration (Figure 3.9A). Increasing the amount of monomer further to 14 % (w/w) had no significant additional effect. PolyHIPEs with 12 % (w/w) surfactant in the organic phase showed a 1.5 times higher specific activity at 30 mM substrate than polyHIPEs with 9 % or 6 % (w/w) surfactant (Figure 3.9B). The aqueous phase volume fraction had an influence on the specific activity at 30 mM substrate in the range between 82.5 % and 87.5 % (v/v) with a 1.7-fold increase (Figure 3.9C). Below 82.5 %

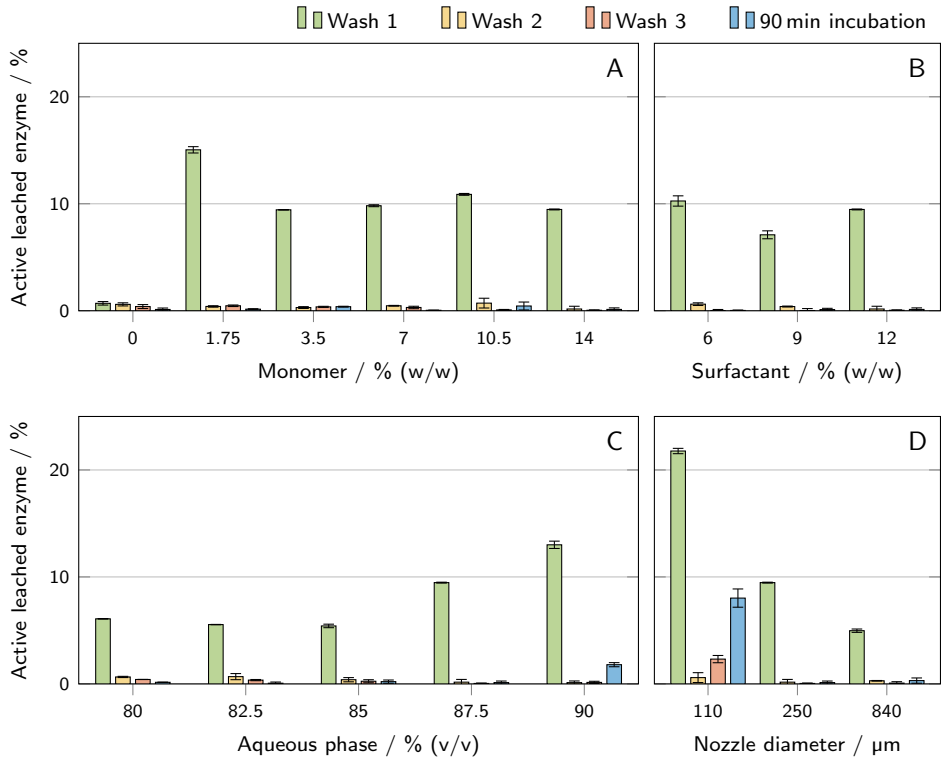

Figure 3.8 Determination of the amount of active enzyme leached from the printed polyHIPE cylinders during the wash procedure and a 90 min incubation in a microtiter plate. The results are presented as mean values ± standard deviation ($n = 3$). The influence of (A) monomer mass fraction in the aqueous phase, (B) surfactant mass fraction in the organic phase, (C) aqueous phase volume fraction and (D) nozzle diameter is shown.

and above 87.5 %, no further significant changes could be observed. Besides the variations of HIPE composition, HIPE A was printed using nozzles with different diameters in order to evaluate the influence of cylinder thickness on the resulting specific activity (Figure 3.9D). The lowest activity at 30 mM substrate was determined for a nozzle diameter of 840 µm with a value of (1.1 ± 0.1) mM/(min · mg). In comparison, cylinders printed with a 250 µm nozzle showed a nearly twofold increase in specific activity and a nearly fourfold increase was determined for the 110 µm nozzle. This was also the highest specific activity of all analyzed samples, more than two times higher than any other condition.

3.3.7 Error analysis of polyHIPE activity assays

An error estimation with a worst-case scenario (error E_{max}) and a best-case scenario (error E_{min}) was performed in order to estimate the proportion of activity observed in the polyHIPE activity assays that was caused by leached rather than immobilized enzyme, as described in section 3.2.10. The highest E_{max} of 12.79 % was found for polyHIPEs printed with 110 µm nozzles, E_{min} was 1.28 %. PolyHIPEs with 90 % (v/v) aqueous phase volume fraction showed the second highest E_{max} with 5.85 %. All other samples showed values between 0.14 % and 2.30 % for E_{max} and between 0.03 % and 1.74 % for E_{min}, as listed in Table A3.3 in the supplementary material.

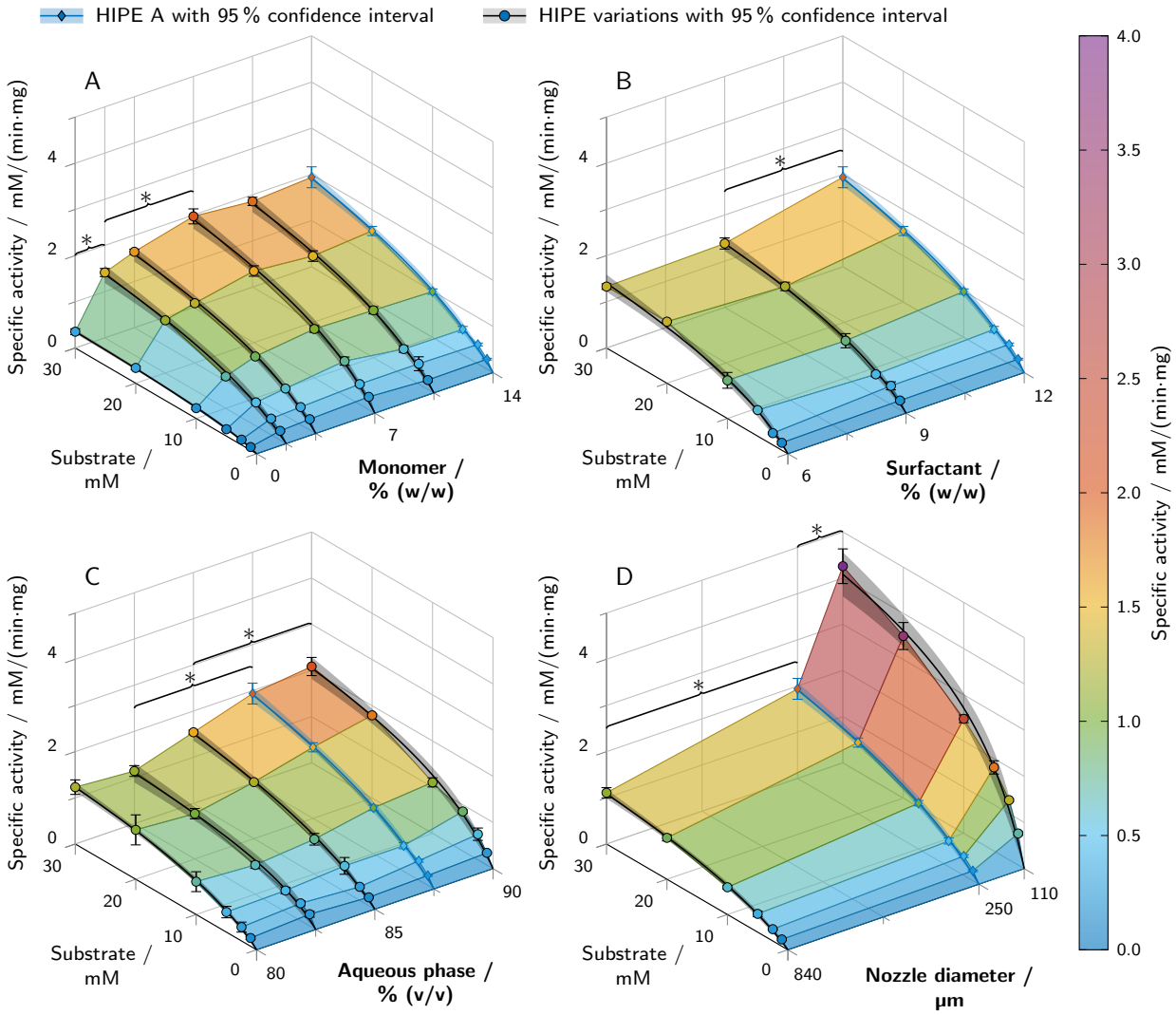

Figure 3.9 Results of batch activity screenings of printed polyHIPE cylinders containing β-galactosidase. The apparent specific activity is shown over the substrate concentration and a second varied parameter. All variations are derived from HIPE A printed with a 250 µm nozzle (depicted in blue in each graph). Varied parameters were (A) the monomer mass fraction in the aqueous phase, (B) the surfactant mass fraction in the organic phase, (C) the aqueous phase volume fraction and (D) the nozzle diameter. Data points are represented as mean ± standard deviation ($n = 3$). The black and blue lines represent Michaelis-Menten fits with 95 % confidence intervals in semi-transparent shading. For clarity, only significant differences to the nearest significantly different data points at 30 mM substrate are highlighted by asterisks ($p < 0.05$).

3.4 Discussion

This study aims at formulating aqueous solutions of AA and PEG-DA 700 as the internal phase of HIPEs in order to enhance printability and allow the 3D printing of composite materials consisting of porous polymeric scaffolds filled with enzyme-laden hydrogels. Different HIPE compositions were systematically characterized to assess rheological and morphological properties, equilibration time as a measure of diffusion behavior, leaching and enzymatic activity.

3.4.1 Rheology and printability

Yield stress is an essential predictor of printability, especially for structures involving overhangs, as it substantially determines the bridging and shape retention capabilities of the material after extrusion [119]. While the aqueous phase volume fraction and the surfactant concentration in the organic phase were found to strongly influence the yield stress, the monomer concentration in the aqueous phase had a minor effect (Figure 3.4). This indicates that little or no adverse effects on the printability of HIPEs are to be expected from the addition of AA and PEG-DA 700 to the aqueous phase. However, high surfactant concentrations and high aqueous phase volume fractions are desirable to enhance printing quality and allow the fabrication of more complex geometries. Shear stress-controlled oscillatory measurements indicated a gel-like character for all samples and could confirm the trends observed for yield stress.

The void size of the prepared polyHIPEs was found to be inversely correlated to the surfactant concentration in the organic phase (Figure 3.6). These results are in accordance with results described by Princen *et al.* who showed that the yield stress of HIPEs is a function of aqueous phase volume fraction, droplet size and interfacial tension [134, 135]. HIPE A, one of the HIPEs with a high yield stress, exhibited excellent printability, as demonstrated by the printed grid and gyroid structures shown in Figure 3.5. High-quality prints are essential to reduce mass transfer limitations in biocatalytic reactors, as they enable the fabrication of flow-optimized geometries with thin walls [100].

3.4.2 PolyHIPE morphology

It was expected that the addition of AA and PEG-DA 700 as monomers and LAP as a photoinitiator to the aqueous phase of the HIPEs would result in polyHIPE scaffolds filled with hydrogel. This was intended in order to retain the enzyme within the material and prevent it from leaching through the interconnecting pores of the polyHIPE while still allowing the diffusion of the relatively small substrate and product molecules. ESEM micrographs (Figure 3.6G-I) revealed that most voids of samples with 14 % (w/w) monomer in the aqueous phase were indeed filled, while the control samples with 0 % (w/w) monomer showed empty voids. This implies a successful formation of hydrogel inside the voids. Previous studies about hydrogel-filled polyHIPEs have addressed aspects like monomer content in the aqueous phase and locus of initiation [123], pre-polymerization of the organic phase [124], degree of cross-linking [125] or shape-memory properties [136]. These studies mostly used scanning electron microscopy (SEM) micrographs of dried samples for morphology analysis and typically found bi-continuous systems with an interconnected hydrogel that collapsed onto the polyHIPE walls covering the interconnecting pores of the polyHIPE scaffold. Also, depending on locus of initiation and monomer content in the aqueous phase, hydrogels covering only the polyHIPE walls while leaving the interconnecting pores open were described [123]. However, all of

the cited studies were conducted with styrene-based organic phases, thermal initiators and different surfactants than used here, so comparability is limited. The SEM and ESEM micrographs of the samples prepared in this study show mostly separate hydrogel spheres, not connected with the hydrogel in neighboring voids or the surrounding polyHIPE scaffold. This may imply the presence of a liquid interface layer between hydrogel and surrounding polyHIPE which could be beneficial for mass transport, as it offers an alternative route through the composite material avoiding passage through the hydrogel phase. The high number of empty voids found in SEM as opposed to ESEM micrographs can probably be attributed to the sample preparation method which in the case of SEM involves a freeze-drying step causing the hydrogel to shrink and dry out which may promote the detachment of the hydrogel from the scaffold. ESEM samples were prepared in a hydrated state which may have caused an increased adherence of the hydrogel to the polyHIPE scaffold and hence a reduced loss. The observed shrinkage of hydrogel spheres in ESEM samples can be attributed to a drying effect due to the exposure to air directly after sample preparation.

The decreased stability of the polyHIPE scaffold with 12 % (w/w) surfactant in the organic phase and 14 % (w/w) monomer in the aqueous phase may be caused by the incorporation of water-soluble monomers into the external scaffold which has been reported to have a destabilizing effect leading to the collapse of the scaffold upon drying [123, 124]. The intact polyHIPE morphology of printed samples (see Figure A3.2 in the supplementary material) shows the suitability of HIPEs for the application in extrusion-based 3D printing.

3.4.3 Mass transfer limitations

Immobilizing enzymes in hydrogel-filled polyHIPEs may result in two main disadvantages: reduced mass transfer caused by the hydrogel and the polyHIPE scaffold and stress-induced enzyme inactivation due to harsh conditions during HIPE preparation. As a measure of mass transfer limitations, ONP solutions were added to the printed polyHIPE cylinders and the equilibration time was determined (Figure 3.7). A shorter equilibration time can be attributed to a higher mass transfer through the material or a shorter path length due to a thinner cylinder. Both enable the embedded enzyme to work more efficiently due to an improved substrate supply.

No clear influence on equilibration time was found for the monomer mass fraction in the aqueous phase. However, both a higher surfactant mass fraction in the organic phase and a higher aqueous phase volume fraction correlated with a shorter equilibration time. Assuming that all cylinders had approximately identical dimensions, it can be concluded that polyHIPEs with a higher amount of surfactant or internal phase allow a higher mass transfer through the material. This may be caused by an increased degree of openness of the polyHIPE scaffold. The degree of openness is the ratio of open surface to total surface of a scaffold cavity and typically increases with both surfactant concentration and aqueous phase volume fraction [137]. Assuming that substrate and product molecules are able to diffuse through the internal hydrogel phase but not through the polyHIPE scaffold itself, a high degree of openness would allow for a less tortuous and hence shorter path through the material. This may explain the decreased equilibration time for samples with high amounts of surfactant and aqueous phase observed in this study.

As discussed in section 3.4.2, a second pathway through a liquid-filled interface between hydrogel and polyHIPE scaffold may be available for a more efficient mass transport. Due to the absence of hydrogel, this pathway would offer a higher rate of diffusion for both substrate and product but a higher tortuosity due to the necessity of bypassing the hydrogel. Mass transport via this pathway

would benefit from a smaller void size and hence decreased tortuosity. As has been shown here (Figure 3.6) and in other studies [138, 139], smaller void sizes can be achieved by higher amounts of surfactant.

The lowest equilibration time was determined for cylinders printed with a 110 µm instead of a 250 µm nozzle. Here, the low equilibration time can be attributed to a lower path length through the cylinder which demonstrates the importance of printing fine structures to reduce mass transfer limitations.

3.4.4 Apparent enzymatic activity, leaching and enzyme inactivation

The main focus of this work was to establish printable HIPE formulations as bioinks for enzymes and to evaluate the effect of different HIPE compositions and nozzle diameters on the apparent enzymatic activity of the printed and polymerized material. Besides mass transfer limitations, stress-induced enzyme inactivation and leaching during the wash steps may cause a reduced apparent activity. Potential sources of stress-induced enzyme inactivation in the applied process are the contact with highly hydrophobic organic compounds in the organic phase [140] or monomer species in the aqueous phase, high shear forces during the emulsification process [141] or UV irradiation [142, 143], free radicals [144] and increased temperature [145] during the exothermic photo-crosslinking reaction. The measured activities alone cannot give any indication about the predominant aspect leading to reduced apparent activity. However, in combination with the determined equilibration time (Figure 3.7) as a measure of mass transfer limitations and the amount of active enzyme leached during the wash procedure (Figure 3.8), certain conclusions can be drawn about the causes for activity differences of different samples.

For both surfactant mass fraction in the organic phase and aqueous phase volume fraction, a decline in equilibration time (Figure 3.7B and C) correlated with an increase in apparent activity (Figure 3.9B and C). This indicates that the change in apparent activity for these parameters can at least partly be explained by differences in mass transfer limitations of the polyHIPE compositions. In contrast, the monomer mass fraction in the aqueous phase had no significant effect on the equilibration time while still influencing the apparent activity between 0 % and 14 % (w/w) monomer by a factor of 5. In this case, the reduced activity at 0 % monomer cannot be attributed to mass transfer limitations. A reasonable assumption would be that the enzyme is lost during the wash steps due to the lack of a retaining hydrogel, but analysis of the wash solutions showed a decreased rather than increased amount of leached active enzyme in these samples (see Figure 3.8). This eliminates the leaching of active enzyme as a cause for the decrease in apparent activity at lower amounts of monomer in the aqueous phase and leaves enzyme inactivation as the most probable explanation. Depending on concentration and chain length, PEG is known to stabilize proteins in aqueous solutions [146], so the presence of PEG-DA 700 might preserve the enzymatic activity of the β-galactosidase during the emulsification and polymerization process.

A very simple and efficient way to reduce mass transfer limitations is to decrease diffusion path lengths by increasing the surface-area-to-volume ratio of the printed material [12], as demonstrated here by the equilibration time analysis of cylinders printed with different nozzles (Figure 3.7D). In an enzymatic reactor, this can be realized in the form of finer grids. Hence, the influence of printing with different nozzle diameters was investigated to determine the achievable increase in apparent specific activity. It should be noted that the nozzle diameter does not correspond to the thickness of the printed strand but is also dependent on printing parameters like extrusion rate and

layer height. Using 110 µm instead of 840 µm nozzles caused a 5-fold increase in apparent activity at 30 mM ONPG for an identical polyHIPE composition (see Figure 3.9). This demonstrates that decreasing the diffusion path length and increasing the surface-area-to-volume ratio is an essential prerequisite for efficient biocatalytical processes.

Regarding leaching behavior, all polyHIPEs containing hydrogel lost a significant amount of enzyme, especially during the first wash step (see Figure 3.8). To avoid this, enzymes could be covalently incorporated into the hydrogel with appropriate linker molecules. During the 90 min incubation period following the wash steps, most samples lost less than 0.5 % of enzyme. However, the cylinders printed with a 110 µm nozzle lost an amount of enzyme several times higher than all other samples. Due to their thin strands, these cylinders were more flexible than others and underwent higher mechanical deformations during the wash process and transfer to microtiter plates. This stress may have caused defects in the polyHIPE scaffold leading to increased leaching of enzyme or enzyme-containing hydrogel particles. The influence of leached enzyme on the results of the polyHIPE activity assays is discussed in the following section.

3.4.5 Error analysis of polyHIPE activity assays

Results of activity assays with enzyme immobilized in polyHIPEs could be influenced by leached enzyme. An error estimation with a worst-case scenario (error E_{max}) and a best-case scenario (error E_{min}) was performed in order to estimate the proportion of the observed activity that was caused by leached rather than immobilized enzyme. The calculation is based on the volumetric activity of supernatant samples incubated for 90 min with a polyHIPE cylinder. The worst-case scenario assumes the leached enzyme to be present from the beginning of the activity assay reaction while the best-case scenario assumes a linear release profile over 90 min, as described in section 3.2.10. Hence, E_{max} only depends on the volumetric activity of the supernatant after a 90 min incubation and the maximum activity occuring during the polyHIPE activity assay, while E_{min} is also proportional to the time delay until the maximum activity occurs.

Due to the high amount of leached enzyme during the 90 min incubation, a high E_{max} of 12.79 % was found for polyHIPEs printed with 110 µm nozzles. The high discrepancy between E_{max} and E_{min} (1.28 %) can be attributed to the short diffusion path lengths in these samples allowing the maximum activity to occur after a short time delay of 9 min after substrate addition. For all other samples, E_{max} was below 6 % and E_{min} below 2 %. Further experiments would be necessary to determine a realistic release profile instead of a best- and worst-case scenario. However, even assuming the worst-case scenario, errors can be neglected for most samples and all trends observed in the polyHIPE activity assays (Figure 3.9) can be confirmed. The observed differences in activity can indeed be attributed to the polyHIPE material properties, not different amounts of leached enzyme in the supernatant.

3.4.6 Conclusion

This study demonstrates the applicability of HIPEs as enzyme-containing bioinks for the extrusion-based 3D printing of enzymatically active composite materials to be employed in biocatalytic reactors. Most prepared HIPEs exhibited excellent printability allowing the fabrication of complex 3D structures without the need for sacrificial support material. The inks could be polymerized employing a cure-on-dispense setup resulting in polyHIPE scaffolds filled with hydrogel, as confirmed

by (E)SEM micrographs. Automated activity assays showed that β-galactosidase could be preserved within the polyHIPEs in an active state and that it could be supplied with the substrate ONPG. The presented activity assay method allows the time-efficient screening of a large variety of materials, printing parameters and reaction conditions enabling a systematic optimization with regard to apparent activity. Mass transfer limitations and enzyme inactivation were identified as the most important factors limiting the apparent activity. While not significantly affecting the mass transfer of the material, the presence of monomer in the aqueous phase was found to be essential for the preservation of enzymatic activity: PolyHIPEs with 14 % (w/w) monomer showed a more than fivefold higher apparent activity than polyHIPEs with 0 % (w/w) monomer in the aqueous phase. Printing thin structures was shown to reduce diffusion path lengths and hence mass transfer limitations, causing a nearly fourfold increase in specific apparent activity for prints from 110 µm nozzles, as compared to 840 µm nozzles. The surfactant mass fraction in the organic phase and the aqueous phase volume fraction were found to have a less pronounced but still significant effect on mass transfer and hence apparent activity. Due to their excellent printability, the presented bioinks are suitable for the additive manufacturing of more sophisticated and finer resolved biocatalytic reactor designs with reduced mass transfer limitations.

In order to reduce mass transfer limitations even further, oil-in-water instead of water-in-oil HIPEs could be produced with an external enzyme-laden hydrogel phase and an internal phase consisting of inert oil droplets. However, these materials are likely to exhibit relatively low mechanical stability and may require time-consuming wash steps in order to remove the internal phase. An alternative field of use for the materials presented in this study could be sustained release applications with tunable release kinetics by altering both HIPE composition and the geometry of the print.

Conflict of interest

The authors declare that the research was conducted in the absence of any commercial or financial relationships that could be construed as a potential conflict of interest.

Author contributions

LW, MW and JH conceptualized the research. LW developed the employed lab ware, established automated data evaluation tools, conducted all shown experiments and wrote the manuscript. CPR provided expertise on automated activity assays and bioprinting, MW expertise on HIPEs. JG established workflows for HIPE preparation and printing. JG and LW established the activity assay procedure. CR, MW and JH proofread the manuscript. All authors contributed to the article and approved the submitted version.

Acknowledgments

We would like to thank Volker Zibat for the preparation of ESEM micrographs and André Bouché and Laura Kuger for their work with HIPEs leading on to this project. The authors bear the complete responsibility for the content of this publication. We acknowledge support by the KIT-Publication Fund of the Karlsruhe Institute of Technology.

Data availability statement

The raw data supporting the conclusions of this article will be made available by the authors, without undue reservation.

Chapter references

[1] T. D. Ngo, A. Kashani, G. Imbalzano, K. T. Nguyen, and D. Hui, „Additive manufacturing (3D printing): A review of materials, methods, applications and challenges“, *Composites Part B: Engineering*, vol. 143, no. February, pp. 172–196, 2018.

[12] B. Schmieg, A. Schimek, and M. Franzreb, „Development and performance of a 3D-printable poly(ethylene glycol) diacrylate hydrogel suitable for enzyme entrapment and long-term biocatalytic applications“, *Engineering in Life Sciences*, vol. 18, no. 9, pp. 659–667, 2018.

[46] C. Parra-Cabrera, C. Achille, S. Kuhn, and R. Ameloot, „3D printing in chemical engineering and catalytic technology: structured catalysts, mixers and reactors“, *Chemical Society Reviews*, vol. 47, pp. 209–230, 2018.

[55] J. Groll, T. Boland, T. Blunk, J. A. Burdick, D. W. Cho, P. D. Dalton, B. Derby, G. Forgacs, Q. Li, V. A. Mironov, L. Moroni, M. Nakamura, W. Shu, S. Takeuchi, G. Vozzi, T. B. Woodfield, T. Xu, J. J. Yoo, and J. Malda, „Biofabrication: Reappraising the definition of an evolving field“, *Biofabrication*, vol. 8, no. 1, pp. 1–5, 2016.

[68] K. Hölzl, S. Lin, L. Tytgat, S. Van Vlierberghe, L. Gu, and A. Ovsianikov, „Bioink properties before, during and after 3D bioprinting“, *Biofabrication*, vol. 8, no. 3, pp. 1–19, 2016.

[70] J. Malda, J. Visser, F. P. Melchels, T. Jüngst, W. E. Hennink, W. J. A. Dhert, J. Groll, and D. W. Hutmacher, „25th Anniversary Article: Engineering Hydrogels for Biofabrication“, *Advanced Materials*, vol. 25, no. 36, pp. 5011–5028, 2013.

[73] I. T. Ozbolat, W. Peng, and V. Ozbolat, „Application areas of 3D bioprinting“, *Drug Discovery Today*, vol. 21, no. 8, pp. 1257–1271, 2016.

[78] C. Colosi, S. R. Shin, V. Manoharan, S. Massa, M. Costantini, A. Barbetta, M. R. Dokmeci, M. Dentini, and A. Khademhosseini, „Microfluidic Bioprinting of Heterogeneous 3D Tissue Constructs Using Low-Viscosity Bioink“, *Advanced Materials*, vol. 28, no. 4, 677–684a, 2016.

[85] M. Maier, C. P. Radtke, J. Hubbuch, C. M. Niemeyer, and K. S. Rabe, „On-demand production of flow reactor cartridges by 3D printing of thermostable enzymes“, *Angewandte Chemie International Edition*, vol. 57, no. 19, pp. 5539–5543, 2018.

[91] S. Krishnamoorthi, A. Banerjee, and A. Roychoudhury, „Immobilized Enzyme Technology: Potentiality and Prospects“, *Journal of Enzymology and Metabolism*, vol. 1, no. 1, pp. 1–11, 2015.

[93] O. Kirk, T. V. Borchert, and C. C. Fuglsang, „Industrial enzyme applications“, *Current Opinion in Biotechnology*, vol. 13, no. 4, pp. 345–351, 2002.

[94] A. Hasan, M. Nurunnabi, M. Morshed, A. Paul, A. Polini, T. Kuila, M. Al Hariri, Y. K. Lee, and A. A. Jaffa, „Recent advances in application of biosensors in tissue engineering“, *BioMed Research International*, vol. 2014, 2014.

[95] G. Rocchitta, A. Spanu, S. Babudieri, G. Latte, G. Madeddu, G. Galleri, S. Nuvoli, P. Bagella, M. I. Demartis, V. Fiore, R. Manetti, and P. A. Serra, „Enzyme biosensors for biomedical applications: Strategies for safeguarding analytical performances in biological fluids“, *Sensors (Switzerland)*, vol. 16, no. 6, pp. 1–21, 2016.

[96] B. M. Nestl, S. C. Hammer, B. A. Nebel, and B. Hauer, „New Generation of Biocatalysts for Organic Synthesis“, *Angewandte Chemie - International Edition*, vol. 53, no. 12, pp. 3070–3095, 2014.

[97] S. C. Mohapatra and J. T. Hsu, „Immobilization of α-chymotrypsin for use in batch and continuous reactors“, *Journal of Chemical Technology and Biotechnology*, vol. 75, no. 7, pp. 519–525, 2000.

[98] B. Rodriguez-Colinas, L. Fernandez-Arrojo, P. Santos-Moriano, A. O. Ballesteros, and F. J. Plou, *Continuous Packed Bed Reactor with Immobilized β-Galactosidase for Production of Galactooligosaccharides (GOS)*, 2016.

[99] C. Zhao, N. Zhang, H. Zheng, Q. Zhu, M. Utsumi, and Y. Yang, „Effective and long-term continuous bio-hydrogen production by optimizing fixed-bed material in the bioreactor“, *Process Biochemistry*, vol. 83, no. April, pp. 55–63, 2019.

[100] B. Schmieg, J. Döbber, F. Kirschhöfer, M. Pohl, and M. Franzreb, „Advantages of Hydrogel-Based 3D-Printed Enzyme Reactors and Their Limitations for Biocatalysis“, *Frontiers in Bioengineering and Biotechnology*, vol. 6, no. January, pp. 1–12, 2019.

[101] A. S. Hoffman, „Hydrogels for biomedical applications“, *Advanced Drug Delivery Reviews*, vol. 64, no. SUPPL. Pp. 18–23, 2012.

[102] M. S. Rehmann, K. M. Skeens, P. M. Kharkar, E. M. Ford, E. Maverakis, K. H. Lee, and A. M. Kloxin, „Tuning and Predicting Mesh Size and Protein Release from Step Growth Hydrogels“, *Biomacromolecules*, vol. 18, no. 10, pp. 3131–3142, 2017.

[103] V. Hagel, T. Haraszti, and H. Boehm, „Diffusion and interaction in PEG-DA hydrogels“, *Biointerphases*, vol. 8, no. 36, pp. 1–9, 2013.

[104] K. S. Rabe, J. Müller, M. Skoupi, and C. M. Niemeyer, „Cascades in Compartments: En Route to Machine-Assisted Biotechnology“, *Angewandte Chemie - International Edition*, vol. 56, no. 44, pp. 13 574–13 589, 2017.

[105] A. Panwar and L. P. Tan, „Current status of bioinks for micro-extrusion-based 3D bioprinting“, *Molecules*, vol. 21, no. 6, pp. 1–26, 2016.

[106] F. P. W. Melchels, W. J. A. Dhert, D. W. Hutmacher, and J. Malda, „Development and characterisation of a new bioink for additive tissue manufacturing“, *Journal of Materials Chemistry B*, vol. 2, p. 2282, 2014.

[107] V. H. M. Mouser, F. P. W. Melchels, J. Visser, W. J. A. Dhert, D. Gawlitta, and J. Malda, „Yield stress determines bioprintability of hydrogels based on gelatin-methacryloyl and gellan gum for cartilage bioprinting.“, *Biofabrication*, vol. 8, no. 3, p. 035 003, 2016.

[108] K. Markstedt, A. Mantas, I. Tournier, H. Martínez Ávila, D. Hägg, and P. Gatenholm, „3D bioprinting human chondrocytes with nanocellulose-alginate bioink for cartilage tissue engineering applications“, *Biomacromolecules*, vol. 16, no. 5, pp. 1489–1496, 2015.

[109] A. L. Rutz, K. E. Hyland, A. E. Jakus, W. R. Burghardt, and R. N. Shah, „A multimaterial bioink method for 3D printing tunable, cell-compatible hydrogels“, *Advanced Materials*, vol. 27, no. 9, pp. 1607–1614, 2015.

[110] A. Skardal, J. Zhang, L. McCoard, X. Xu, S. Oottamasathien, and G. D. Prestwich, „Photocrosslinkable hyaluronan-gelatin hydrogels for two-step bioprinting“, *Tissue Engineering - Part A*, vol. 16, no. 8, pp. 2675–2685, 2010.

[111] W. Wu, A. Deconinck, and J. A. Lewis, „Omnidirectional printing of 3D microvascular networks“, *Advanced Materials*, vol. 23, no. 24, pp. 178–183, 2011.

[112] T. J. Hinton, Q. Jallerat, R. N. Palchesko, J. H. Park, M. S. Grodzicki, H. J. Shue, M. H. Ramadan, A. R. Hudson, and A. W. Feinberg, „Three-dimensional printing of complex biological structures by freeform reversible embedding of suspended hydrogels“, *Science Advances*, vol. 1, no. 9, 2015.

[113] W. Jia, P. S. Gungor-Ozkerim, Y. S. Zhang, K. Yue, K. Zhu, W. Liu, Q. Pi, B. Byambaa, M. R. Dokmeci, S. R. Shin, and A. Khademhosseini, „Direct 3D bioprinting of perfusable vascular constructs using a blend bioink“, *Biomaterials*, vol. 106, pp. 58–68, 2016.

[114] L. A. Hockaday, K. H. Kang, N. W. Colangelo, P. Y. C. Cheung, B. Duan, E. Malone, J. Wu, L. N. Girardi, L. J. Bonassar, H. Lipson, C. C. Chu, and J. T. Butcher, „Rapid 3D printing of anatomically accurate and mechanically heterogeneous aortic valve hydrogel scaffolds“, *Biofabrication*, vol. 4, no. 3, p. 035 005, 2012.

[115] N. A. Sears, P. S. Dhavalikar, and E. M. Cosgriff-Hernandez, „Emulsion Inks for 3D Printing of High Porosity Materials“, *Macromolecular Rapid Communications*, vol. 37, no. 16, pp. 1369–1374, 2016.

[116] W. Y. Maeng, J. B. Lee, Y. H. Koh, and H. E. Kim, „Innovative in situ photocuring-assisted 3D plotting technique for complex-shaped ceramic architectures with high shape retention“, *Ceramics International*, vol. 45, no. 7, pp. 8440–8447, 2019.

[117] N. R. Cameron, P. Krajnc, and M. S. Silverstein, „Colloidal Templating“, in *Porous Polymers*, M. S. Silverstein, N. R. Cameron, and M. A. Hillmyer, Eds., Hoboken, NJ, USA: John Wiley & Sons, Inc., 2011, pp. 119–172.

[118] R. Foudazi, S. Qavi, I. Masalova, and A. Y. Malkin, „Physical chemistry of highly concentrated emulsions“, *Advances in Colloid and Interface Science*, vol. 220, pp. 78–91, 2015.

[119] N. A. Sears, T. S. Wilems, K. A. Gold, Z. Lan, S. N. Cereceres, P. S. Dhavalikar, R. Foudazi, and E. M. Cosgriff-Hernandez, „Hydrocolloid Inks for 3D Printing of Porous Hydrogels“, *Advanced Materials Technologies*, vol. 4, no. 2, p. 1 800 343, 2019.

[120] A. Y. Sergienko, H. Tai, M. Narkis, and M. S. Silverstein, „Polymerized high internal-phase emulsions: Properties and interaction with water“, *Journal of Applied Polymer Science*, vol. 84, no. 11, pp. 2018–2027, 2002.

[121] P. Hainey, I. M. Huxham, B. Rowatt, D. C. Sherrington, and L. Tetley, „Synthesis and Ultrastructural Studies, of Styrene-Divinylbenzene Polyhipe Polymers“, *Macromolecules*, vol. 24, no. 1, pp. 117–121, 1991.

[122] M. S. Silverstein, „Emulsion-templated polymers: Contemporary contemplations“, *Polymer (United Kingdom)*, vol. 126, pp. 261–282, 2017.

[123] T. Gitli and M. S. Silverstein, „Bicontinuous hydrogel–hydrophobic polymer systems through emulsion templated simultaneous polymerizations“, *Soft Matter*, vol. 4, no. 12, p. 2475, 2008.

[124] T. Gitli and M. S. Silverstein, „Emulsion templated bicontinuous hydrophobic-hydrophilic polymers: Loading and release“, *Polymer*, vol. 52, no. 1, pp. 107–115, 2011.

[125] S. Kovačič, K. Jeřabek, and P. Krajnc, „Responsive poly(acrylic acid) and poly(N-isopropylacrylamide) monoliths by high internal phase emulsion (HIPE) templating“, *Macromolecular Chemistry and Physics*, vol. 212, no. 19, pp. 2151–2158, 2011.

[126] C. Fee, S. Nawada, and S. Dimartino, „3D printed porous media columns with fine control of column packing morphology“, *Journal of Chromatography A*, vol. 1333, pp. 18–24, 2014.

[127] C. Fee, „3D-printed porous bed structures“, *Current Opinion in Chemical Engineering*, vol. 18, pp. 10–15, 2017.

[128] M. Konarova, W. Aslam, L. Ge, Q. Ma, F. Tang, V. Rudolph, and J. N. Beltramini, „Enabling Process Intensification by 3D Printing of Catalytic Structures“, *ChemCatChem*, vol. 9, no. 21, pp. 4132–4138, 2017.

[129] F. Kazenwadel, E. Biegert, J. Wohlgemuth, H. Wagner, and M. Franzreb, „A 3D-printed modular reactor setup including temperature and pH control for the compartmentalized implementation of enzyme cascades“, *Engineering in Life Sciences*, vol. 16, no. 6, pp. 560–567, 2016.

[130] M. Peng, E. Mittmann, L. Wenger, J. Hubbuch, M. K. M. Engqvist, C. M. Niemeyer, and K. S. Rabe, „3D-Printed Phenacrylate Decarboxylase Flow Reactors for the Chemoenzymatic Synthesis of 4-Hydroxystilbene“, *Chemistry – A European Journal*, vol. 25, pp. 15 998–16 001, 2019.

[131] A. Saha, T. G. Johnston, R. T. Shafranek, C. J. Goodman, J. G. Zalatan, D. W. Storti, M. A. Ganter, and A. Nelson, „Additive Manufacturing of Catalytically Active Living Materials“, *ACS Applied Materials & Interfaces*, vol. 10, no. 16, pp. 13 373–13 380, 2018.

[132] C. P. Radtke, N. Hillebrandt, and J. Hubbuch, „The Biomaker: an entry-level bioprinting device for biotechnological applications“, *Journal of Chemical Technology & Biotechnology*, vol. 93, no. 3, pp. 792–799, 2017.

[133] Vitroid, *Gyroid surface*, `https://www.thingiverse.com/thing:3091246`, Accessed: 2019-09-01, 2018.

[134] H. Princen, „Rheology of foams and highly concentrated emulsions. I. Elastic properties and yield stress of a cylindrical model system“, *Journal of Colloid and Interface Science*, vol. 91, no. 1, pp. 160–175, 1983.

[135] H. M. Princen, „Rheology of foams and highly concentrated emulsions. II. Experimental study of the yield stress and wall effects for concentrated oil-in-water emulsions“, *Journal of Colloid And Interface Science*, vol. 105, no. 1, pp. 150–171, 1985.

[136] C. Warwar Damouny and M. S. Silverstein, „Hydrogel-filled, semi-crystalline, nanoparticle-crosslinked, porous polymers from emulsion templating: Structure, properties, and shape memory“, *Polymer*, vol. 82, pp. 262–273, 2016.

[137] I. Pulko and P. Krajnc, „High internal phase emulsion templating - a path to hierarchically porous functional polymers“, *Macromolecular rapid communications*, vol. 33, no. 20, pp. 1731–46, 2012.

[138] J. M. Williams, A. J. Gray, and M. H. Wilkerson, „Emulsion Stability and Rigid Foams from Styrene or Divinylbenzene Water-in-Oil Emulsions“, *Langmuir*, vol. 6, no. 2, pp. 437–444, 1990.

[139] T. Zhang, R. A. Sanguramath, S. Israel, and M. S. Silverstein, „Emulsion Templating: Porous Polymers and beyond“, *Macromolecules*, vol. 52, no. 15, pp. 5445–5479, 2019.

[140] P. V. Iyer and L. Ananthanarayan, „Enzyme stability and stabilization - Aqueous and non-aqueous environment“, *Process Biochemistry*, vol. 43, no. 10, pp. 1019–1032, 2008.

[141] I. B. Bekard, P. Asimakis, J. Bertolini, and D. E. Dunstan, „The effects of shear flow on protein structure and function“, *Biopolymers*, vol. 95, no. 11, pp. 733–745, 2011.

[142] R. A. Luse and A. D. McLaren, „Mechamisn of Enzyme Inactivation by Ultraviolet Light and the Photochemistry of Amino Acids“, *Photochemistry and Photobiology*, vol. 2, no. 3, pp. 343–360, 1963.

[143] Y. A. Vladimirov, D. I. Roshchupkin, and E. E. Fesenko, „Photochemical Reactions in Amino Acid Residues and Inactivation of Enzymes During U.V.-Irradiation. A Review“, *Photochemistry and Photobiology*, vol. 11, no. 4, pp. 227–246, 1970.

[144] I. F. Dumitru and M. T. Nechifor, „Decrease in yeast glucose-6-phosphate dehydrogenase activity due to oxygen free radicals“, *International Journal of Biochemistry*, vol. 26, no. 2, pp. 229–233, 1994.

[145] F. I. Ustok, C. Tari, and S. Harsa, „Biochemical and thermal properties of β-galactosidase enzymes produced by artisanal yoghurt cultures“, *Food Chemistry*, vol. 119, no. 3, pp. 1114–1120, 2010.

[146] W. Wang, *Instability, stabilization, and formulation of liquid protein pharmaceuticals*. 1999, vol. 185, pp. 129–188.

4

Investigation of Lysozyme Diffusion in Agarose Hydrogels Employing a Microfluidics-Based UV Imaging Approach

Lukas Wenger[1] and Jürgen Hubbuch[1]

[1] Institute of Engineering in Life Sciences, Section IV: Biomolecular Separation Engineering, Karlsruhe Institute of Technology (KIT), Karlsruhe, Germany

Abstract

Hydrogels are polymer-based materials with a high water content. Due to their biocompatible and cell-friendly nature, they play a major role in a variety of biotechnological applications. For many of these applications, diffusibility is an essential property influencing the choice of material. We present an approach to estimate diffusion coefficients in hydrogels based on absorbance measurements of a UV area imaging system. A microfluidic chip with a y-junction was employed to generate a fluid-hydrogel interface and the diffusion of lysozyme from the fluid into the hydrogel phase was monitored. Employing automated image and data processing, analyte concentration profiles were generated from the absorbance measurements and fits with an analytical solution of Fick's second law of diffusion were applied to estimate diffusion coefficients. As a case study, the diffusion of lysozyme in hydrogels made from different concentrations (0.5 to 1.5 % (w/w)) of an unmodified and a low-melt agarose was investigated. The estimated diffusion coefficients for lysozyme were between $(0.80 \pm 0.04) \times 10^{-10}\,\mathrm{m^2\,s^{-1}}$ for 1.5 % (w/w) low-melt agarose and $(1.14 \pm 0.02) \times 10^{-10}\,\mathrm{m^2\,s^{-1}}$ for 0.5 % (w/w) unmodified agarose. The method proved sensitive enough to resolve significant differences between the diffusion coefficients in different concentrations and types of agarose. The microfluidic approach offers low consumption of analyte and hydrogel and requires only relatively simple instrumentation.

4.1 Introduction

Hydrogels are polymer-based materials with a high water content [8]. They are employed in a variety of medical and biotechnological applications like the immobilization of enzymes [147, 148], tissue engineering [60, 149] or as bioinks in bioprinting [150, 151]. Both synthetic polymers like poly(ethylene glycol)-diacrylate [152] or poly(vinyl alcohol) [153, 154] and natural polymers like agarose [155], alginate [156] or gelatin [157] can serve as the base material of hydrogels. The aqueous matrices of hydrogels mimic native soft tissues and provide a cell-friendly and highly biocompatible environment [60] that is ideally suited to accommodate living cells or stress-sensitive biomolecules like enzymes. An essential property of hydrogels that is relevant for many applications is their diffusibility. In tissue engineering, cells embedded in or growing on top of hydrogels rely on the diffusional transport of oxygen, nutrients and waste products through the hydrogel to sustain their metabolism [158]. In biocatalytic applications involving physically entrapped enzymes, the hydrogel should ensure the retention and immobilization of the relatively large enzyme within the hydrogel, while allowing the diffusion of small substrate and product molecules [91]. The diffusion of a molecule through a hydrogel depends mainly on the size of the molecule, the crosslinking density of the hydrogel polymer network [159] and potential physical interactions between the diffusing molecule and the polymer chains of the hydrogel. This includes van der Waals forces [159] and electrostatic interactions [160, 161].

Precise knowledge about the diffusional behavior of compounds in hydrogels is essential for many applications. A large variety of methods for the determination of diffusion coefficients has been described. Methods like fluorescence recovery after photobleaching (FRAP) [103, 162, 163], dual-focus fluorescence correlation spectroscopy (FCS) [164] or the tracking of diffusing molecules using a fluorescence microscope [165] are only applicable to fluorescent compounds or require fluorescent tagging of the target molecule which may alter the compound's behavior and requires additional conjugation and purification steps [166]. Holographic laser interferometry (HLI) [167, 168], electron

speckle pattern interferometry (ESPI) [169] and pulsed-field-gradient nuclear magnetic resonance (PFG-NMR) [170, 171] require specialized and costly equipment not typically available in most laboratories. Other methods like Taylor dispersion analysis (TDA) [172, 173], refractive index methods [174] or certain spectrophotometric methods [175, 176] may suffer from limitations like requiring relatively large sample volumes or being only applicable for liquid samples.

UV area imaging systems have been employed for the spatial observation of diffusion processes in hydrogels to estimate diffusion coefficients. Studies with several different compounds and hydrogels have been conducted, e. g. addressing the diffusion of human serum albumin and piroxicam in Pluronic F127 hydrogels [177], piroxicam in subcutaneous tissue models based on agarose and Pluronic F127 [178], insulin in agarose hydrogels [173] and lysozyme and several other proteins in different agarose-based cartilage models [161]. The described methods consume relatively large amounts of sample due to the use of quartz cells requiring hydrogel sample volumes between 310 to 600 µL. The high amount of material consumption may prevent these methods from being applied with cost-intensive materials or materials with limited availability, as scaling effects caused by high numbers of experiments and replicates may render the methods prohibitively expensive. Even commercially available bioinks may cost more than a hundred dollars for 1 mL of hydrogel. Even more challenging may be the often very limited availability of novel, custom-made materials only synthesized on a small lab scale.

We present a modified approach employing a microfluidic chip to observe the diffusion of an analyte within a hydrogel-filled microchannel using an ActiPix™ UV area imaging system. The presented technique reduces both hydrogel and analyte consumption down to 40 µL and 25 µL, respectively. Automated image processing and data evaluation is employed to analyze the acquired raw absorbance data provided by the imaging system. Diffusion coefficients are estimated by fitting a solution of Fick's second law with obtained analyte concentration profiles along the channel. The applicability of the method is demonstrated by a case study involving lysozyme as the analyte and hydrogels made from different concentrations (0.5 to 1.5 % (w/w)) of an unmodified and a low-melt agarose. The applied workflow of the study is schematically summarized in Figure 4.1.

4.2 Materials and Methods

4.2.1 Manufacturing of the microfluidic chip

A simple microfluidic chip with three inlets and a y-junction was custom-made using a silicone molding technique as described by Waldbaur *et al.* [179]. In short, a specific replication master made by stereolithography was kept in place by a molding tool and a spacer to allow the casting of the top part of the microfluidic chip. To achieve a smooth and clear surface suitable for absorbance measurements, a spacer made from polished stainless steel was used [180]. Elastosil®RT 601 (Wacker Chemie AG), a pourable, two-component silicone rubber that cures at room temperature was used as the base material for the chip. After curing, the silicone part was bonded with a second, planar silicone part to seal the channels. To achieve bonding, the silicone surface was activated by plasma treatment with a hand-held corona treater (BD-20AC, Electro-Technic Products Inc.) [181]. The channels were 1000 µm in width and 500 µm in height. A scheme of the employed microfluidic chip is shown in Figure 4.2A, a 3D rendering in Figure 4.2B and photographs in Figure 4.2C.

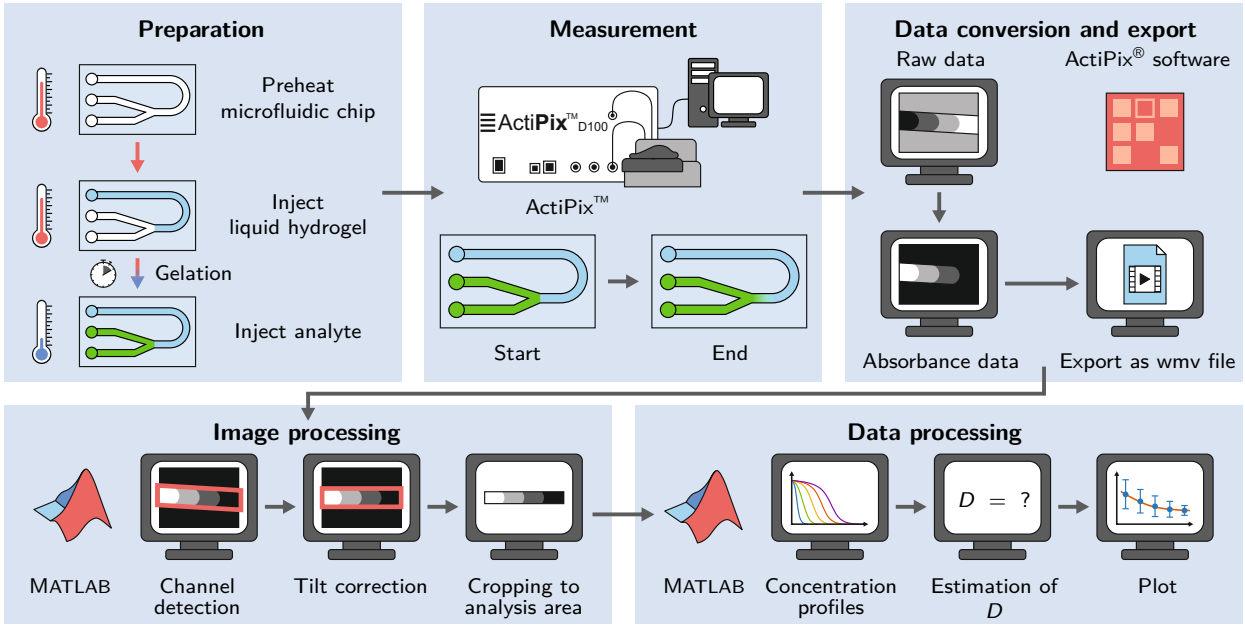

Figure 4.1 Schematic of the workflow applied in this study. The microfluidic chip is preheated to allow the injection of liquid agarose into the channel and ensure the controlled gelation by cooling at room temperature. The diffusion measurement is started right after the injection of the analyte. The acquired data is converted and exported using the ActiPix™ software. Image and data processing for the estimation of diffusion coefficients is done in MATLAB.

4.2.2 Chemicals and buffer preparation

Unmodified agarose (Roti®garose for DNA/RNA electrophoresis) and low-melt agarose (Roti®garose with low melting and gelling temperature) were obtained from Carl Roth GmbH & Co. KG. Lysozyme (lyophilized, from chicken egg white, Hampton Research) was used for the analyte solution. The hydrogels and lysozyme solutions were prepared with phosphate buffered saline (PBS), pH 7.4. Sodium chloride (NaCl), potassium chloride (KCl), disodium hydrogen phosphate dihydrate ($Na_2HPO_4 \cdot 2\,H_2O$) and potassium dihydrogenphosphate (KH_2PO_4) were purchased from Merck KGaA. The PBS buffers were prepared with ultrapure water from a Purelab Ultra water purification system (ELGA LabWater) and filtered through an 0.2 µm cellulose acetate filter (Sartorius AG).

4.2.3 Hydrogel preparation

Agarose hydrogels were prepared at different concentrations (0.5 %, 1.0 %, and 1.5 % (w/w)) in PBS buffer, pH 7.4. Appropriate amounts of agarose powder were dissolved in PBS buffer by heating up the mixtures several times to boiling point using a microwave oven (WP800L20-5, Hanseatic). The resulting solutions were transferred to preheated syringes, sealed and stored at 60 °C until use in a drying oven (T 6120, Heraeus Instruments) to avoid gelation.

4.2.4 Preparation of the microfluidic chip for the measurement

The microfluidic chip was preheated at 60 °C in a drying oven (T 6120, Heraeus Instruments) for 10 min. Liquid agarose solution (∼40 µL) was injected into the preheated chip using a blunt needle

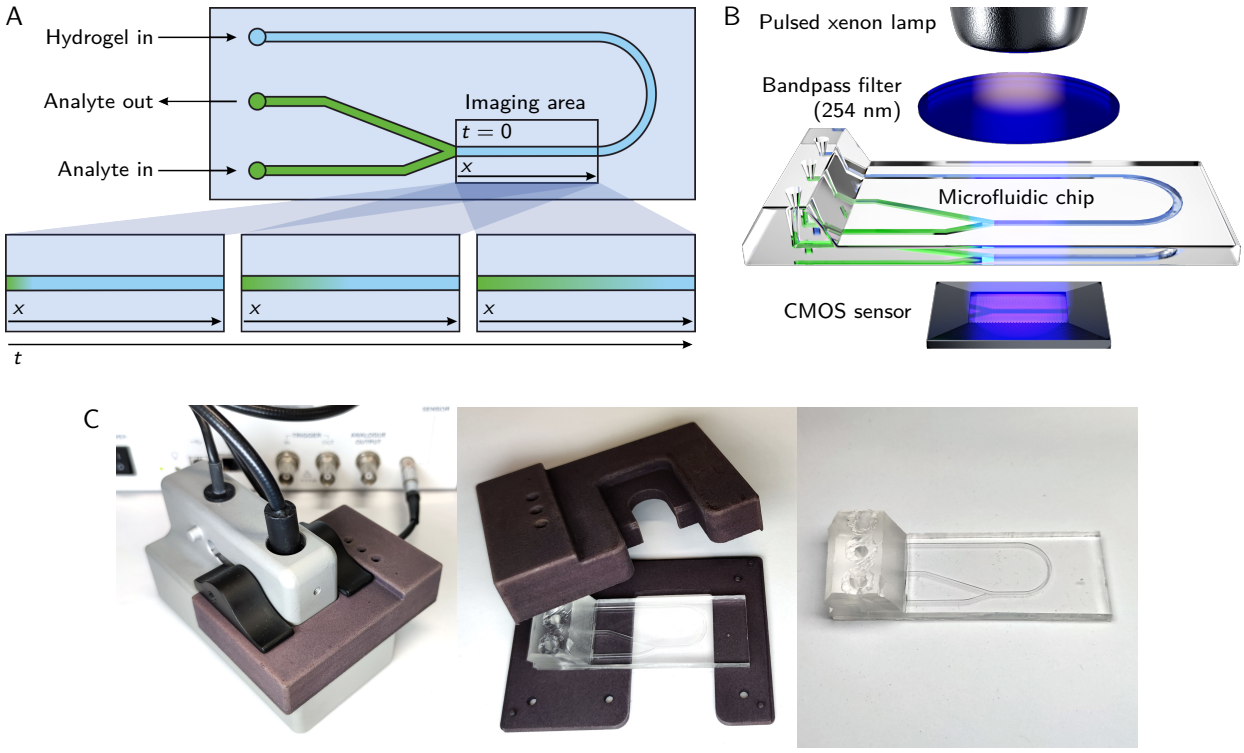

Figure 4.2 (A) Schematic of the microfluidic chip. The imaging area being observed by the ActiPix™ is roughly indicated with a rectangle. The bottom part of the subfigure shows the observed diffusion of the analyte through the hydrogel over time. (B) Overview of the essential components of the employed setup. The illustration demonstrates the integration of the microfluidic chip within the Actipix™ imaging system. Absorbance area measurements are generated by guiding light from a pulsed xenon lamp through a 254 nm bandpass filter and the microfluidic chip before being detected by a CMOS sensor. (C) Photographs of the microfluidic chip with the casing.

(Sterican® MIX, 1.2 × 40 mm, B. Braun SE), until it reached the Y-junction of the channel, as shown in Figure 4.2A. The chip was left at room temperature for 10 min to cool down and allow the gelation of the hydrogel. This duration was chosen based on experiments with 0.5 % (w/w) low-melt agarose where a gelling time of 5 min was found to be sufficient to avoid dissolving the gel when injecting buffer into the other inlets of the chip. After gelation, the analyte solution (∼25 µL) was injected into the chip through one of the other inlets immediately before the start of the measurement, generating an interface between analyte solution and hydrogel at the y-junction. The y-junction design was chosen to allow the air contained in the microfluidic channel to escape during the injection of the analyte solution.

4.2.5 Diffusion measurements: UV imaging and data export

An ActiPix™ D100 UV area imaging system (Paraytec Ltd.) was employed to observe the propagation of the analyte through the hydrogel over time. It was equipped with a pulsed xenon lamp, a 254 nm bandpass filter and a complementary metal-oxide-semiconductor (CMOS) sensor for detection. A simplified schematic of the parts of the setup is shown in Figure 4.2B. The microfluidic chip was

positioned in the appropriate location using a custom-made, 3D-printed casing which provided access to the channel inlets and shielded the chip from external light sources. To reduce the potential influence of stray light further, all measurements were performed in a darkened room and the inlets of the chip were sealed with aluminium foil. With the employed setup, the imaging area (9×7 mm, 1280×1024 pixels) was limited to the region of the microfluidic chip immediately after the y-junction, as indicated in Figure 4.2A.

Each measurement was started immediately after the injection of the analyte solution. After dark images and reference images were collected for 60 s each, imaging data were collected for 4 h at a frame rate of $0.18\,s^{-1}$. All measurements were performed at an ambient temperature of (22 ± 2) °C. Using the ActiPix™ software version 1.5 (Paraytec Ltd.), the acquired data were converted to absorbance data and exported as wmv (Windows Media Video) files for further processing.

4.2.6 Image processing

The exported wmv files containing the collected absorbance data were processed in MATLAB R2020a (The MathWorks®, Inc.) using an automated script. The raw video files were read in and converted to grayscale. Due to the flexibility of the microfluidic silicone chip and some clearance between the chip and the casing, the orientation of the channel deviated from a perfect horizontal alignment in most measurements. This deviation was constant during the measurement, hence the last frame of each measurement was evaluated to provide a suitable correction. The channel was detected using a thresholding function and its orientation was determined. Each frame of the measurement was rotated by the appropriate angle to obtain a horizontally aligned channel. To reduce the image size to the relevant minimum, each frame was cropped to an area of 100 pixels in height containing the middle of the channel over the whole observed channel length. This extracted part of the frame served as the analysis area that provided the data for the generation of analyte concentration profiles along the channel over time (see section 4.2.8.1). The described image processing steps are exemplarily illustrated in Figure 4.3.

4.2.7 Calibration curves

Calibration curves with different lysozyme concentrations (0 to 10 mg/mL) were prepared by filling the channel of the microfluidic chip with the respective analyte solution and recording the absorbance for 5 min. Measurement, data export and image processing steps were performed in the same way as for the diffusion measurements (section 4.2.5 and 4.2.6). To obtain a value for the calibration curve, a mean pixel intensity value was calculated from a part of the analysis area (100×100 pixels) of the last frame of each measurement. PBS buffer (0 mg/mL lysozyme) served as a blank. All data points of the calibration were in the linear range of Beer's law.

4.2.8 Data processing

4.2.8.1 Determination of concentration profiles

The extracted and corrected image data of the analysis area were further processed in MATLAB R2020a. A blank value was obtained from the end part of the analysis area of the first valid data frame. This area (100×100 pixels) covered a part of the channel that only contained hydrogel, but no analyte ($c_{lysozyme} = 0$). The mean of the pixel intensities of this region served as a blank value and was subtracted from the image data of all frames. From each 240 min long measurement,

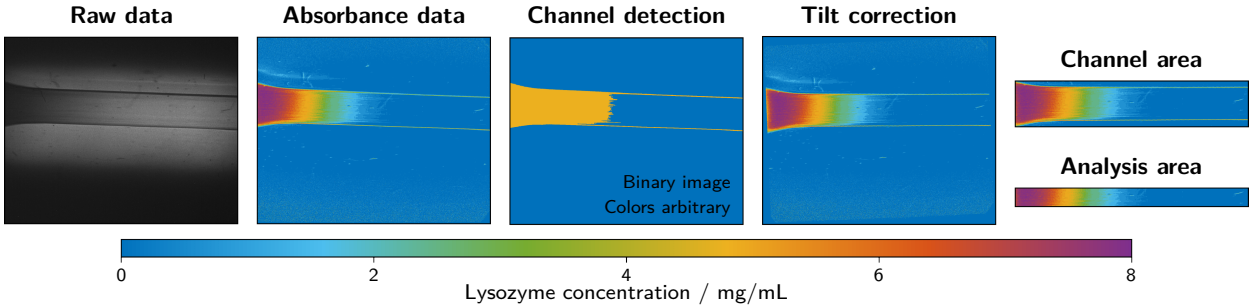

Figure 4.3 Image processing steps as performed with the ActiPix™ software and MATLAB. The example shows the last frame of a measurement with 10 mg/mL lysozyme as the analyte solution and 1.5 % (w/w) low-melt agarose as the hydrogel. Raw data files were converted to absorbance data using the ActiPix™ software. In MATLAB, the channel was detected based on the last frame of the measurement to correct for inaccuracies in positioning and alignment. Based on the channel detection, the tilt was corrected and the channel area extracted. An area of 100 pixels in height was taken from the middle of the channel and used as the analysis area.

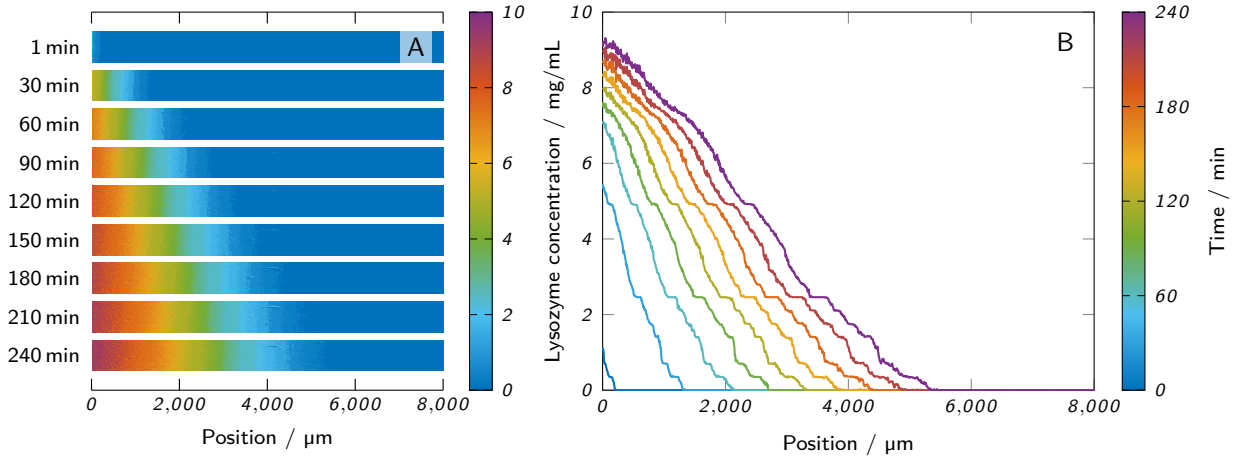

Figure 4.4 (A) The observed analysis area of a measurement at different time points shows the propagation of the lysozyme through the hydrogel. (B) The lysozyme concentration profiles of the same measurement were obtained from the analysis area by column-wise calculation of mean values. The shown measurement was performed with 0.5 % (w/w) low-melt agarose as the hydrogel and 10 mg/mL lysozyme as the analyte solution.

a frame was extracted every 15 min, starting at 30 min. All absorbance values were converted to lysozyme concentration values using the obtained calibration curves. Figure 4.4A exemplarily shows the extracted and converted analysis areas of a measurement with 0.5 % low-melt agarose at different time points. To create lysozyme concentration profiles along the channel length, column-wise mean values were calculated with one column corresponding to 7 µm of channel length. Figure 4.4B shows the resulting lysozyme concentration profiles of the extracted frames of the same measurement.

4.2.8.2 Estimation of diffusion coefficients using Fick's second law

To estimate diffusion coefficients from the recorded concentration profiles, diffusion in one dimension (along the microfluidic channel) according to Fick's second law of diffusion was assumed [182]:

$$\frac{\partial C}{\partial t} = D\frac{\partial^2 C}{\partial x^2} \tag{4.1}$$

where C is the analyte concentration, t is the time, x is the distance along the channel and D is the diffusion coefficient of the analyte in the medium. Different analytical solutions for Fick's second law exist, depending on the assumed boundary and initial conditions [182]. To find a solution suitable to describe the observed concentration profiles, three different solutions were applied in this study, all assuming a system of two phases (in the present case fluid and hydrogel phase) with different analyte concentrations. The diffusion coefficient D is assumed to stay constant during the measurement. The initial ($t = 0$) concentration of analyte is C_0 in the fluid phase ($x < 0$) and zero in the hydrogel phase ($x > 0$). The phases are in contact at a boundary layer at $x = 0$. The solutions assume either both the fluid-containing and the hydrogel-containing channel as infinitely long (infinite system) or only the hydrogel-containing channel (semi-infinite system) with a constant analyte concentration C_0 at the boundary layer. The assumption of infinity demands the condition $t \ll L^2/D$ to be met, with the duration of the measurement t and the length of the hydrogel-filled channel L. This assumption implies that the analyte concentration at the end of the measurement is still zero at the end of the hydrogel-filled channel and still C_O at the end of the fluid-filled channel [178].

The first applied solution assumes a composite system composed of two phases with different diffusion coefficients. Assuming no accumulation of the analyte at the boundary layer ($x = 0$), the boundary condition can be expressed as follows [178, 182]:

$$D_{hydrogel}\frac{\partial C_{hydrogel}}{\partial x} = D_{fluid}\frac{\partial C_{fluid}}{\partial x} \tag{4.2}$$

with the diffusion coefficients and concentrations of the analyte in the hydrogel ($D_{hydrogel}$ and $C_{hydrogel}$) and in the fluid, respectively (D_{fluid} and C_{fluid}). From this, a solution for the analyte concentration in the hydrogel phase ($x > 0$) can be derived [178]:

$$C\left(x,t\right) = \frac{C_0\sqrt{\frac{D_{fluid}}{D_{hydrogel}}}}{1 + K\sqrt{\frac{D_{fluid}}{D_{hydrogel}}}}\left(1 - \mathrm{erf}\left(\frac{x}{2\sqrt{D_{hydrogel}t}}\right)\right) \tag{4.3}$$

with the equilibrium ratio of analyte concentration between the two phases $K = C_{fluid}/C_{hydrogel}$.

The other two applied solutions do not assume a composite system with two different values for D, but a constant D within the whole system. The second solution assumes a semi-infinite medium with a boundary layer that is kept at a constant analyte concentration C_0 throughout the whole

measurement ($t > 0$). The analyte concentration in the hydrogel-filled channel over time t and distance x is then given by [182]:

$$C\left(x,t\right) = C_0\left(1 - \mathrm{erf}\left(\frac{x}{2\sqrt{Dt}}\right)\right) \tag{4.4}$$

The third applied solution of Fick's second law assumes an infinite system with the fluid phase ($x < 0$) acting as an extended analyte source of infinite extent. With the initial conditions $C = C_0$ in the fluid phase and $C = 0$ in the hydrogel phase ($x > 0$), the analyte concentration is given by [182]:

$$C\left(x,t\right) = C_0\left(\frac{1}{2} - \frac{1}{2}\,\mathrm{erf}\left(\frac{x}{2\sqrt{Dt}}\right)\right) \tag{4.5}$$

In this case, the concentration at the boundary layer is $\frac{1}{2}C_0$ throughout the measurement and diffusion processes take place on both sides of the boundary layer.

As mentioned before, all equations assume a fixed boundary layer at the position $x = 0$. In practice, the employed experimental setup did not allow a precise and reproducible positioning of the hydrogel-fluid interface at $x = 0$ for each measurement. Differences in positioning of the microfluidic chip and slightly varying hydrogel fill levels introduced a variability that was accounted for by introducing an additional parameter x_0. This allowed expressing the Equations (4.3), (4.4) and (4.5) with a variable position of the boundary layer at $x = x_0$ [177]:

$$\text{infinite composite system: } C\left(x,t\right) = \frac{C_0\sqrt{\frac{D_{fluid}}{D_{hydrogel}}}}{1 + K\sqrt{\frac{D_{fluid}}{D_{hydrogel}}}}\left(1 - \mathrm{erf}\left(\frac{x - x_0}{2\sqrt{D_{hydrogel}t}}\right)\right) \tag{4.6}$$

$$\text{semi-infinite system: } C\left(x,t\right) = C_0\left(1 - \mathrm{erf}\left(\frac{x - x_0}{2\sqrt{Dt}}\right)\right) \tag{4.7}$$

$$\text{infinite system: } C\left(x,t\right) = C_0\left(\frac{1}{2} - \frac{1}{2}\,\mathrm{erf}\left(\frac{x - x_0}{2\sqrt{Dt}}\right)\right) \tag{4.8}$$

To estimate diffusion coefficients, the observed concentration profiles of all samples were fitted with the presented solutions of Fick's second law using MATLAB. For Equation (4.6), a diffusion coefficient for lysozyme in the fluid phase $D_{fluid} = 1.2 \times 10^{-10}\,\mathrm{m^2/s}$ (lysozyme in 67 mM phosphate, pH 7.4 at 25 °C) was assumed [161]. In the course of the manuscript, Equation (4.8) was finally chosen for further analysis. For a clearer overview, the assumptions and boundary conditions of the three equations are summarized in Table 4.1.

4.2.9 Influence of temperature

All measurements were performed at an ambient temperature of (22 ± 2) °C. The actual temperature within the microfluidic chip could not be determined, but it can be estimated that the employed setup involving the ActiPix™ UV imaging system generates a temperature gradient of up to 5 °C compared to ambient temperature [173]. Due to the high uncertainty with regards to the actual experimental

Table 4.1 Summary of the general assumptions and the boundary and initial conditions of the applied equations.

General assumptions	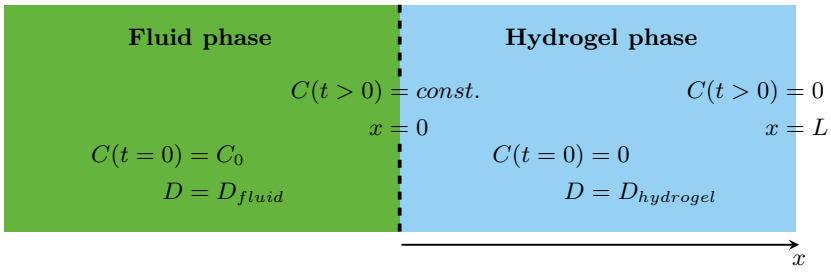	
Infinite composite system	$D_{fluid} \neq D_{hydrogel}$	$C(x=0) = \frac{C_0\sqrt{\frac{D_{fluid}}{D_{hydrogel}}}}{1+K\sqrt{\frac{D_{fluid}}{D_{hydrogel}}}}$
Semi-infinite system	$D_{fluid} = D_{hydrogel}$	$C(x=0) = C_0$
Infinite system		$C(x=0) = \frac{1}{2}C_0$

temperature (ambient temperature ±2 °C, unknown temperature gradient), no corrections of the estimated D values were implemented, but an error estimation was performed.

The influence of temperature on the diffusion coefficient can be estimated using the Stokes-Einstein equation:

$$D = \frac{k_B \cdot T}{6\pi \cdot \eta \cdot r} \tag{4.9}$$

with Boltzmann's constant k_B, the absolute temperature T, the viscosity of the surrounding solution η and the hydrodynamic radius of the analyte r. Assuming a temperature difference $\Delta T = 5\,\mathrm{K}$ with the two temperatures $T_1 = 22\,^\circ\mathrm{C} = 295\,\mathrm{K}$ and $T_2 = 27\,^\circ\mathrm{C} = 300\,\mathrm{K}$ and a constant r, the ratio of the corresponding diffusion coefficients D_1 and D_2 is given by:

$$\frac{D_1}{D_2} = \frac{T_1\eta_2}{T_2\eta_1} \tag{4.10}$$

with the viscosities of the solution η_1 at T_1 and η_2 at T_2. The viscosities of the solution were estimated using an empirical model for water [183]:

$$\eta = exp\left(A + \frac{B}{T} + CT + DT^2\right)\,\mathrm{mPa}\cdot\mathrm{s} \tag{4.11}$$

with the constants $A = -24.71$, $B = 4209\,\mathrm{K}$, $C = 0.045\,27\,\mathrm{K}^{-1}$ and $D = -3.376 \times 10^{-5}\,\mathrm{K}^{-2}$. Combining Equation (4.10) with Equation (4.11) yields:

$$\frac{D_1}{D_2} = 0.88 \tag{4.12}$$

The result implies an error of 12 % for D assuming $\Delta T = 5\,\mathrm{K}$.

4.2.10 Statistical analysis

The statistical significance of data was tested employing one-way analysis of variance (ANOVA) and the Tukey method for multiple comparisons. Differences between data points were considered statistically significant when $p < 0.05$.

4.3 Results and Discussion

An ActiPix™ UV imaging system was used to observe the diffusion of lysozyme through agarose hydrogels contained in the channel of a microfluidic chip. The acquired absorbance data were exported as video files and processed in MATLAB to generate lysozyme concentration profiles along the length of the microfluidic channel. The diffusion coefficient of lysozyme within the agarose hydrogels was estimated by fitting the concentration profiles with three analytical solutions of Fick's second law.

4.3.1 Choice of an appropriate equation for the estimation of diffusion coefficients

The analytical solutions for Fick's second law presented in section 4.2.8.2 are based on certain assumptions like a constant diffusion coefficient D and boundary and initial conditions. These assumptions as simplifications of reality should represent the experimental setting as accurately as possible, but it is not always obvious which assumptions match a given case best. For the presented experimental setup, the boundary layer is given by the interface between fluid phase and hydrogel phase. The analyte is dissolved in the fluid phase and starts to diffuse into the hydrogel phase at the beginning of the experiment. Assuming a large and well-mixed reservoir of fluid phase or a large reservoir in combination with a diffusion coefficient that is considerably higher in the fluid phase than in the hydrogel phase ($D_{fluid} \gg D_{hydrogel}$), the assumption of a constant analyte concentration at the boundary as in Equation (4.7) seems valid. Assuming $D_{fluid} \approx D_{hydrogel}$ and a stagnant fluid phase, Equation (4.8) seems more appropriate, as this equation assumes diffusion processes on both sides of the boundary layer and requires a constant D throughout both phases. In reality, both scenarios will not ideally match the presented experimental setup, because D_{fluid} is likely to be higher than $D_{hydrogel}$, although this difference has been reported to be only marginal or non-existent for the diffusion of insulin [173] and lysozyme [161] in low-concentration agarose gels. Equation (4.6) assumes a composite system of two materials with different diffusion coefficients and should theoretically resemble the given case best.

In order to empirically evaluate the suitability of the equations to fit the observed data, the concentration profiles of all recorded samples were fitted with all three equations at an analysis time of 240 min. The coefficient of determination R^2 and the root-mean-square error $RMSE$ of all

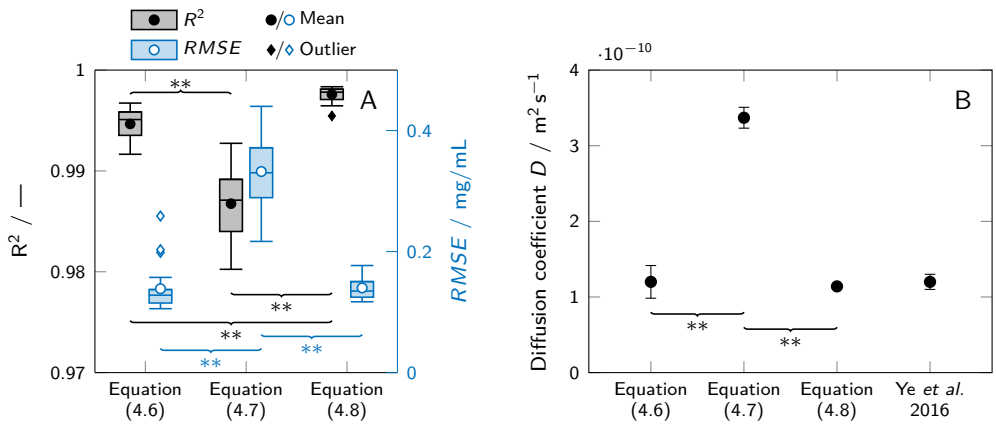

Figure 4.5 Evaluation of the suitability of different fits to describe the observed concentration profiles. (A) Observed R^2 values when fitting observed concentration profiles after 240 min with different analytical solutions of Fick's second law (Equation (4.6), (4.7) and (4.8)). The box plots represent the median and the upper and lower quartile. The whiskers represent the most extreme value still within a 1.5-fold interquartile range (IQR) from the upper and lower quartile. All data points outside the 1.5-fold IQR are depicted as outliers. Each box represents 18 samples ($n = 18$). (B) Comparison of the obtained D estimates for lysozyme in 0.5 % (w/w) agarose with each other and a value from literature [161] for lysozyme in 0.5 % (w/v) agarose at 21–24 °C. Significant differences between the equations are highlighted by asterisks ($^*p < 0.05$, $^{**}p < 0.005$).

fits were determined, as depicted in Figure 4.5A. The fits with Equation (4.7) (semi-infinite system) only showed a mean value of 0.987 ± 0.003 for R^2, while R^2 was significantly higher at 0.995 ± 0.002 for Equation (4.6) (composite system) and even higher at 0.998 ± 0.001 for fits with Equation (4.8) (infinite system). The $RMSE$ was (0.332 ± 0.060) mg/mL for Equation (4.7). The $RMSE$ values for fits with Equation (4.6) and (4.8) were about 60 % lower and not significantly different from each other with (0.139 ± 0.039) mg/mL and (0.140 ± 0.018) mg/mL, respectively. However, the $RMSE$ values for fits with Equation (4.6) showed more outliers. This could be due to the fitting of the additional parameter K which may increase the likelihood of finding local instead of global fit optima.

Besides the indicators for fit quality, the suitability of the equations to describe the observed data was judged by comparing the absolute values of the determined diffusion coefficients to a literature value obtained by Ye *et al.* [161]. Figure 4.5B shows the values obtained with the different equations in comparison to the literature value. It is clear that Equation (4.7) agrees least with the reported literature value and is higher by a factor of about 3. The other two equations align well with the value from Ye *et al.*

The results identify Equation (4.7) as the least suitable to describe the observed concentration profiles (low R^2, high $RMSE$) and to estimate diffusion coefficients (poor agreement with literature value). The assumption of a constant analyte concentration C_0 does obviously not match the experimental conditions. Perfusing the analyte channel with a constant flow of analyte solution could change this, but would require a massively increased complexity of the experimental setup and cause a higher analyte consumption.

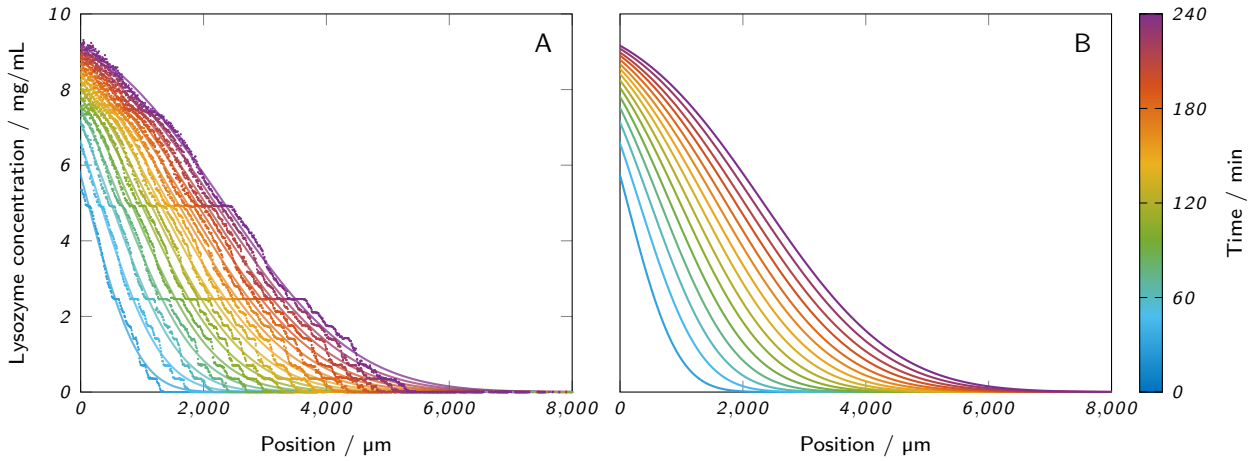

Figure 4.6 (A) Lysozyme concentration profiles along the microfluidic channel at the analyzed time points, as obtained from an ActiPix™ measurement. The scattered raw data are underlaid with the corresponding fits with Equation (4.8). The example shows a measurement with 0.5 % low-melt agarose as the hydrogel and 10 mg/mL lysozyme as the analyte solution. (B) Separate visualization of the same fits for better visibility.

The Equations (4.6) and (4.8) performed very similarly. The obtained diffusion coefficient values were in very good agreement with data reported by Ye *et al.* [161] for both equations, but Equation (4.8) generated slightly higher R^2 values and less outliers in the $RMSE$ analysis indicating more robust fits. Consequently, Equation (4.8) was chosen for further analysis.

Figure 4.6A shows the raw data of the recorded concentration profiles of an exemplary sample (0.5 % low-melt agarose as hydrogel, 10 mg/mL lysozyme as analyte solution) at all analyzed time points. The raw data are underlaid with the corresponding fits with Equation (4.8) which are also separately presented in Figure 4.6B. The graph visualizes the progression of lysozyme through the hydrogel and allows to draw conclusions about the analyte concentration at different penetration depths and time points. However, the observed concentration profiles clearly contradict an assumption of Equation (4.8) which requires a stationary boundary layer at $x = x_0$ with a constant analyte concentration of $\frac{1}{2}C_0$ which corresponds to 5 mg/mL lysozyme in this case. In the observed data, the concentration of 5 mg/mL moves along the x-axis over time implying a moving boundary. Post-measurement observations could rule out the possibility that the hydrogel-fluid interface was actually moving along the channel during the measurement due to shrinkage or other effects. Hence, the observed data suggest that Equation (4.8) does not ideally represent the experimental setup. One cause for this could be the difference of the lysozyme diffusion coefficients in the fluid and the hydrogel phase. However, the same effect of a moving boundary was observed for fits with Equation (4.6) which assumes a composite system with two different diffusion coefficients. Other potential reasons for the moving boundary could be undesired side-effects like capillary action, protein adsorption [182] or a change of the diffusion coefficient over time due to a temperature increase caused by heat dissipation from the ActiPix™ device, as reported before [173].

4.3.2 Case study and influence of analysis time on diffusion coefficient estimation

As a case study for the application of the presented method, the diffusion of lysozyme in agarose hydrogel samples was analyzed. Two different kinds of agarose, an unmodified agarose and a low-melt hydroxyethyl agarose at three different concentrations (0.5 %, 1 %, and 1.5 % (w/w)) were examined in triplicates for 4 h per measurement. The diffusion coefficient of lysozyme in the hydrogel was estimated for each sample by fitting the measured concentration profiles with Equation (4.8). To evaluate whether the apparent moving boundary had negative effects on the estimation of D like strongly deviating values depending on the analysis time, an investigation of the influence of analysis time was carried out. Specifically, concentration profiles were fitted and the diffusion coefficient estimated at different time points of the measurement. Figure 4.7A shows the results for the unmodified agarose, the corresponding standard deviations of the triplicates are plotted in Figure 4.7D. At an analysis time of 30 min, the standard deviations were relatively high (between 2.9 and $6.1 \times 10^{-11}\,\mathrm{m^2\,s^{-1}}$) compared to the remaining time points, indicating a lack of significant data points to perform reproducible and robust fits for several replicates. Between 45 and 240 min, the standard deviations were considerably lower ($< 2 \times 10^{-11}\,\mathrm{m^2\,s^{-1}}$) with a slight downward trend over the whole time period. As can be derived from Figure 4.6, the fits became more precise and more reproducible with increasing analysis time due to the increased coverage of data points over the whole course of the sigmodal-shaped concentration profile. An additional factor could be that with increasing analysis time, the imperfections of the fluid-gel interface like a meniscus or other irregularities become less relevant relatively to diffusion distance. The absolute values of the diffusion coefficients were slightly erratic until an analysis time of 60 min (see Figure 4.7A). Afterwards, they showed a moderately decreasing trend with only minor changes ($< 9\,\%$) happening after 120 min. As shown in Figure 4.7B and E, very similar trends could be observed for low-melt agarose with the absolute values of the diffusion coefficients being about 15 % lower than in unmodified agarose.

To determine the statistical significance of differences between the diffusion coefficients of different agarose concentrations, a one-was analysis of variance (ANOVA) was performed for each time point and the resulting p-values plotted in Figure 4.7C. The ANOVA tested the null hypothesis that there was no significant difference between the mean values of D in hydrogels of different agarose concentrations. For $p < 0.05$, the null hypothesis can be rejected. This was the case for most data points of both modified and unmodified agarose beyond an analysis time of 180 min. The already described erratic nature of the first data points determined with low analysis times is also reflected in the corresponding p-values which fluctuate considerably until an analysis time of 105 min, where a continuous downward trend sets in resulting in overall minimum p-values at an analysis time of 240 min. As a consequence, an analysis time of 240 min was chosen for the final data evaluation.

The results show that despite the apparent moving boundary, the analysis time did not strongly affect the results of the diffusion coefficient estimation when the analysis time exceeded a certain minimum. However, the p-values at different analysis times imply that longer analysis times allow a more precise estimation of the diffusion coefficient which increases the statistical significance and hence relevance of the data.

The comparison of lysozyme diffusion coefficients in Figure 4.7F between the two types of agarose hydrogels and different agarose concentrations clearly shows the influence of the two analyzed parameters. For every concentration, the mean diffusion coefficient was higher in hydrogels from unmodified agarose than low-melt agarose, although the difference was only statistically significant

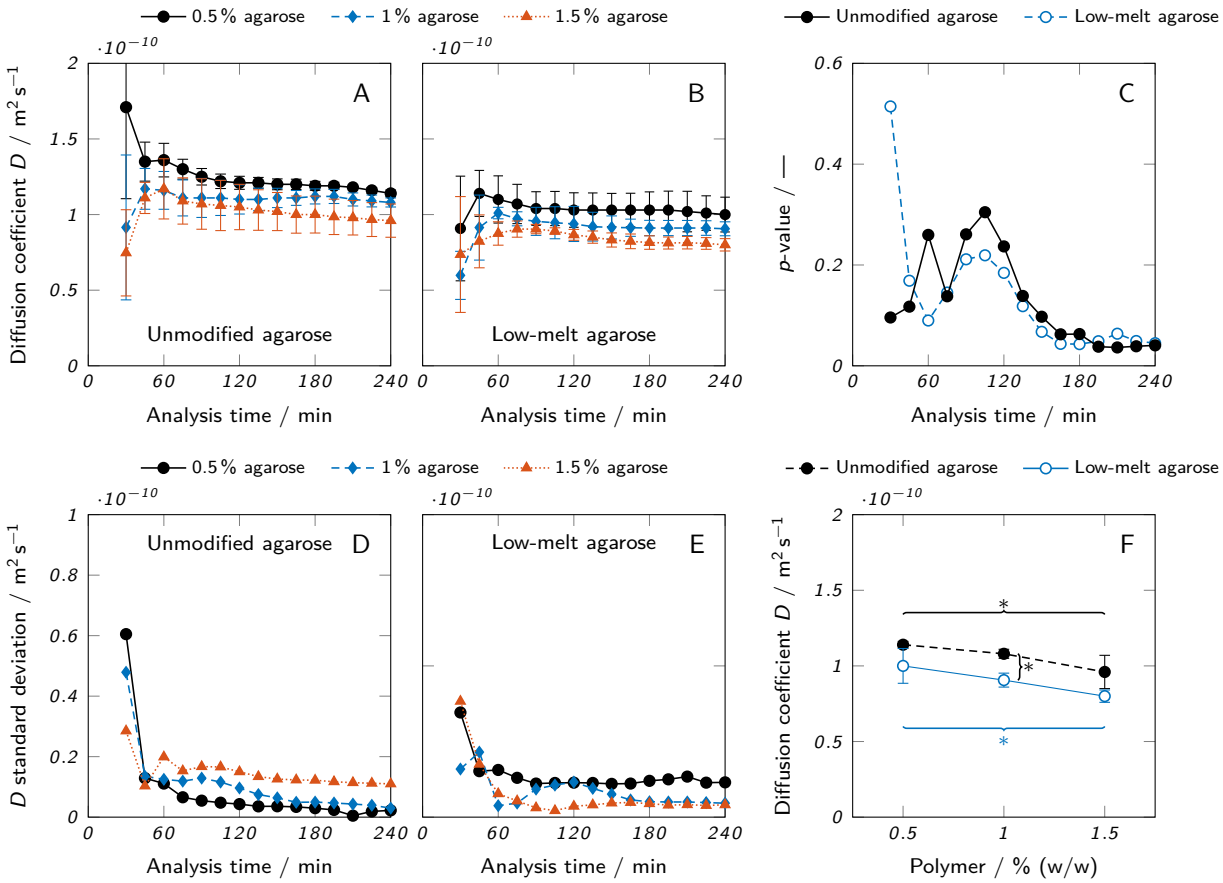

Figure 4.7 Diffusion coefficient estimates at different analysis times for (A) unmodified agarose and (B) low-melt agarose hydrogels. (C) p-values of a one-way ANOVA testing the null hypothesis that there is no difference among the mean values of D for samples of different agarose concentrations. (D and E) Standard deviations for (D) unmodified and (E) low-melt agarose hydrogels resulting from the D estimates which were carried out as triplicates ($n = 3$). (F) Diffusion coefficients for different concentrations of unmodified and low-melt agarose hydrogels obtained at an analysis time of 240 min. The results are presented as mean values ± standard deviation ($n = 3$). Significant differences between the Equations are highlighted by asterisks ($^*p < 0.05$, $^{**}p < 0.005$).

for a concentration of 1.0 % (w/w). There was also a clear trend of a decreasing D with increasing agarose concentration. For both unmodified and low-melt agarose, the difference of D between 0.5 % and 1.5 % (w/w) was statistically significant. These trends align well with data reported in literature. The diffusion coefficients of lysozyme and bovine serum albumin have been shown to decrease with increasing agarose concentration (0.5 to 3 % (w/w)) [174]. Higher concentrations of agarose lead to the formation of polymer networks with reduced mesh size and hence reduced diffusibility [174]. The observation that the diffusion coefficient was higher in hydrogels of unmodified agarose than of low-melt agarose can be attributed to the structure of the respective polymer networks. Hydroxyethylation reduces the number of intrastrand hydrogen bonds [184], leading to the formation of a tighter polymer mesh with smaller pores for the low-melt agarose, depending on the degree of substitution [185].

The absolute values for the estimated diffusion coefficients were between $(0.80 \pm 0.04) \times 10^{-10}\,\mathrm{m^2\,s^{-1}}$ for 1.5 % low-melt agarose and $(1.14 \pm 0.02) \times 10^{-10}\,\mathrm{m^2\,s^{-1}}$ for 0.5 % unmodified agarose. In good accordance with this, Ye *et al.* reported a value of $(1.2 \pm 0.1) \times 10^{-10}\,\mathrm{m^2\,s^{-1}}$ for the diffusion coefficient of lysozyme in an 0.5 % agarose hydrogel at 21 to 24 °C [161]. These results demonstrate the suitability of the presented method to provide diffusion coefficient estimates aligning well with previously reported literature values. The method is sensitive enough to allow the detection of statistically significant differences ($p < 0.05$) of the diffusion coefficient of lysozyme between samples of different agarose concentration (0.5 to 1.5 % (w/w)). Also, the samples of unmodified agarose were found to be higher than the samples of low-melt agarose for every analyzed concentration (difference only statistically significant at 1.0 % (w/w)), demonstrating the suitability to detect differences between slightly different material types.

The present study only investigated one analyte and a range of relatively similar hydrogels. The transferability of the method to other use cases and its applicability in a more general context should be investigated further. Hydrogel-analyte combinations with a very different rate of diffusion than observed here may require adaptations of the evaluation method or may not be suitable to be investigated with the presented setup at all. The use of hydrogels with smaller pores could reduce diffusion rates to an extent that the method is not sensitive enough for a valid diffusion coefficient estimation. The use of smaller analyte molecules with increased diffusion rate may allow shorter analysis times. In general, it is important to always consider possible interactions between analyte and hydrogel that could influence the observed diffusion rate.

4.3.3 Experimental considerations

Previously reported methods for the determination of diffusion coefficients using UV area imaging sensors [161, 173, 177, 178] employed large quartz cells requiring correspondingly large sample volumes. The high material consumption may be problematic in certain contexts like high-cost materials or during early-stage development when the amount of available material is very limited. The presented method requires only about 40 µL of hydrogel and 25 µL of analyte solution for one measurement which could be further reduced by optimizing the microfluidic chip design. The possibility of introducing variable channel heights for different analyte concentrations or investigating alternative chip materials, tailored to the requirements of the hydrogels and analytes to be investigated, adds to the appeal of employing microfluidic chips for this purpose.

However, several aspects of the applied experimental setup could be optimized. The error estimation (section 4.2.9) demonstrated the importance of temperature regarding diffusional processes. The

current setup did not allow any control over the temperature inside the microfluidic chip. Replacing the employed plastic casing for the microfluidic chip by a temperature-controlled metal casing (e. g. employing a Peltier element) could improve the reliability of the acquired data.

The employed microfluidic chip was designed to allow the observation of the hydrogel phase only. Shifting the imaging area would allow a direct investigation of the fluid-hydrogel interface and the observation of diffusional effects in the fluid phase. This could provide further insights into the effects of interface imperfections and the validity of boundary assumptions. In general, it is desirable to improve the quality and positioning of the hydrogel-fluid interface. The method of filling the channel with hydrogel, as employed in this study, produced non-straight and non-reproducible boundary layers due to the formation of a meniscus and slightly different fill levels. This could be resolved by using a chip consisting of two separate parts for the hydrogel and fluid phase. The part for the hydrogel could be overfilled and the hydrogel trimmed to form an appropriate interface, before the second part of the chip is attached and filled with the analyte solution. A chip-casing combination with less manufacturing tolerance could improve the alignment of the chip within the UV imaging system.

4.4 Conclusion

The method established in this study allows the estimation of diffusion coefficients for UV-absorbing analytes in transparent hydrogels. The diffusion of lysozyme through agarose hydrogels was observed using an ActiPix™ UV imaging system. To minimize material consumption, a microfluidic chip was employed, that reduced the required amount of hydrogel to 40 µL. Employing automated image and data processing in MATLAB, the obtained raw absorbance data contained in video files were corrected and processed to generate lysozyme concentration profiles along the microfluidic channel. The concentration profiles were fitted with a solution of Fick's second law to estimate diffusion coefficients. As a case study, the diffusion of lysozyme in hydrogels with different concentrations (0.5 to 1.5 %) of unmodified and low-melt agarose was analyzed. The obtained diffusion coefficients allowed the detection of significant differences between the different types and concentrations of agarose. Generally, the diffusion coefficients were higher in unmodified agarose and at lower concentrations of agarose. The estimated diffusion coefficient of lysozyme in 0.5 % (w/w) agarose was in accordance with data reported by Ye *et al.* [161]. Refinements of the experimental setup, especially regarding temperature control, could enhance the reliability of the obtained data further.

Conflict of interest

The authors declare that the research was conducted in the absence of any commercial or financial relationships that could be construed as a potential conflict of interest.

Author contributions

LW and JH conceptualized the research. LW conducted the experiments, established the image and data processing tools and wrote the manuscript. JH proofread the manuscript.

Acknowledgments

We thank Carsten Radtke for providing the microfluidic chip and valuable expertise about the UV imaging device.

Data availability statement

The raw data supporting the conclusions of this article will be made available by the authors, without undue reservation.

Chapter references

[8] E. M. Ahmed, „Hydrogel: Preparation, characterization, and applications: A review“, *Journal of Advanced Research*, vol. 6, no. 2, pp. 105–121, 2015.

[60] C. D. Spicer, „Hydrogel scaffolds for tissue engineering: The importance of polymer choice“, *Polymer Chemistry*, vol. 11, no. 2, pp. 184–219, 2020.

[91] S. Krishnamoorthi, A. Banerjee, and A. Roychoudhury, „Immobilized Enzyme Technology: Potentiality and Prospects“, *Journal of Enzymology and Metabolism*, vol. 1, no. 1, pp. 1–11, 2015.

[103] V. Hagel, T. Haraszti, and H. Boehm, „Diffusion and interaction in PEG-DA hydrogels“, *Biointerphases*, vol. 8, no. 36, pp. 1–9, 2013.

[147] R. J. Russell, M. V. Pishko, A. L. Simonian, and J. R. Wild, „Poly(ethylene glycol) Hydrogel-Encapsulated Fluorophore-Enzyme Conjugates for Direct Detection of Organophosphorus Neurotoxins“, *Analytical Chemistry*, vol. 71, no. 21, pp. 4909–4912, 1999.

[148] J. Kunkel and P. Asuri, „Function, Structure, and Stability of Enzymes Confined in Agarose Gels“, *PLOS ONE*, vol. 9, no. 1, pp. 1–6, 2014.

[149] X. Zhao, Q. Lang, L. Yildirimer, Z. Y. Lin, W. Cui, N. Annabi, K. W. Ng, M. R. Dokmeci, A. M. Ghaemmaghami, and A. Khademhosseini, „Photocrosslinkable Gelatin Hydrogel for Epidermal Tissue Engineering“, *Advanced Healthcare Materials*, vol. 5, no. 1, pp. 108–118, 2016.

[150] F. You, B. F. Eames, and X. Chen, „Application of Extrusion-Based Hydrogel Bioprinting for Cartilage Tissue Engineering“, *International Journal of Molecular Sciences*, vol. 18, no. 7, pp. 8–14, 2017.

[151] P. Rastogi and B. Kandasubramanian, „Review of alginate-based hydrogel bioprinting for application in tissue engineering“, *Biofabrication*, vol. 11, no. 4, 2019.

[152] F. Tan, X. Xu, T. Deng, M. Yin, X. Zhang, and J. Wang, „Fabrication of positively charged poly(ethylene glycol)-diacrylate hydrogel as a bone tissue engineering scaffold“, *Biomedical Materials*, vol. 7, no. 5, pp. 1–10, 2012.

[153] H. Zhang, H. Xia, and Y. Zhao, „Poly(vinyl alcohol) Hydrogel Can Autonomously Self-Heal“, *ACS Macro Letters*, vol. 1, no. 11, pp. 1233–1236, 2012.

[154] I. Gibas and H. Janik, „Review: Synthetic Polymer Hydrogels for Biomedical Applications“, *Chemistry & Chemical Technology*, vol. 4, no. 4, pp. 297–304, 2010.

[155] B. Rahfoth, J. Weisser, F. Sternkopf, T. Aigner, K. Von Der Mark, and R. Bräuer, „Transplantation of allograft chondrocytes embedded in agarose gel into cartilage defects of rabbits“, *Osteoarthritis and Cartilage*, vol. 6, no. 1, pp. 50–65, 1998.

[156] W.-H. Tan and S. Takeuchi, „Monodisperse Alginate Hydrogel Microbeads for Cell Encapsulation“, *Advanced Materials*, vol. 19, no. 18, pp. 2696–2701, 2007.

[157] G. Sheelu, G. Kavitha, and N. W. Fadnavis, „Efficient Immobilization of Lecitase in Gelatin Hydrogel and Degumming of Rice Bran Oil Using a Spinning Basket Reactor“, *JAOCS, Journal of the American Oil Chemists' Society*, vol. 85, no. 8, pp. 739–748, 2008.

[158] M. Lovett, K. Lee, A. Edwards, and D. L. Kaplan, „Vascularization Strategies for Tissue Engineering“, *Tissue Engineering: Part B*, vol. 15, no. 3, pp. 353–370, 2009.

[159] L. M. Weber, C. G. Lopez, and K. S. Anseth, „Effects of PEG hydrogel crosslinking density on protein diffusion and encapsulated islet survival and function“, *Journal of Biomedical Materials Research. Part A*, vol. 90, no. 3, pp. 720–729, 2008.

[160] N. Hirota, Y. Kumaki, T. Narita, J. P. Gong, and Y. Osada, „Effect of Charge on Protein Diffusion in Hydrogels“, *Journal of Physical Chemistry B*, vol. 104, no. 42, pp. 9898–9903, 2000.

[161] F. Ye, S. Baldursdottir, S. Hvidt, H. Jensen, S. W. Larsen, A. Yaghmur, C. Larsen, and J. Østergaard, „Role of Electrostatic Interactions on the Transport of Druglike Molecules in Hydrogel-Based Articular Cartilage Mimics: Implications for Drug Delivery“, *Molecular Pharmaceutics*, vol. 13, no. 3, pp. 819–828, 2016.

[162] A. Pluen, P. A. Netti, R. K. Jain, and D. A. Berk, „Diffusion of Macromolecules in Agarose Gels: Comparison of Linear and Globular Configurations“, *Biophysical Journal*, vol. 77, no. 1, pp. 542–552, 1999.

[163] H. Deschout, J. Hagman, S. Fransson, J. Jonasson, M. Rudemo, N. Lorén, and K. Braeckmans, „Straightforward FRAP for quantitative diffusion measurements with a laser scanning microscope“, *Optics Express*, vol. 18, no. 22, p. 22 886, 2010.

[164] C. B. Müller, A. Loman, V. Pacheco, F. Koberling, D. Willbold, W. Richtering, and J. Enderlein, „Precise measurement of diffusion by multi-color dual-focus fluorescence correlation spectroscopy“, *EPL*, vol. 83, no. 4, pp. 1–5, 2008.

[165] M. H. Hettiaratchi, A. Schudel, T. Rouse, A. J. García, S. N. Thomas, R. E. Guldberg, and T. C. McDevitt, „A rapid method for determining protein diffusion through hydrogels for regenerative medicine applications“, *APL Bioengineering*, vol. 2, no. 2, 2018.

[166] C. A. Teske, M. Schroeder, R. Simon, and J. Hubbuch, „Protein-Labeling Effects in Confocal Laser Scanning Microscopy“, *Journal of Physical Chemistry B*, vol. 109, no. 28, pp. 13 811–13 817, 2005.

[167] N. O. Gustafsson, B. Westrin, A. Axelsson, and G. Zacchi, „Measurement of Diffusion Coefficients in Gels Using Holographic Laser Interferometry“, *Biotechnology Progress*, vol. 9, no. 4, pp. 436–441, 1993.

[168] C. Mattisson, P. Roger, B. Jönsson, A. Axelsson, and G. Zacchi, „Diffusion of lysozyme in gels and liquids A general approach for the determination of diffusion coefficients using holographic laser interferometry“, *Journal of Chromatography B: Biomedical Sciences and Applications*, vol. 743, no. 1-2, pp. 151–167, 2000.

[169] D. Karlsson, G. Zacchi, and A. Axelsson, „Electronic Speckle Pattern Interferometry: A Tool for Determining Diffusion and Partition Coefficients for Proteins in Gels“, *Biotechnology Progress*, vol. 18, no. 6, pp. 1423–1430, 2002.

[170] S. J. Gibbs, E. N. Lightfoot, and T. W. Root, „Protein Diffusion in Porous Gel Filtration Chromatography Media Studied by Pulsed Field Gradient NMR Spectroscopy“, *Journal of Physical Chemistry*, vol. 96, no. 18, pp. 7458–7462, 1992.

[171] J. Harmon, C. Coffman, S. Villarrial, S. Chabolla, K. A. Heisel, and V. V. Krishnan, „Determination of Molecular Self-Diffusion Coefficients Using Pulsed-Field-Gradient NMR: An Experiment for Undergraduate Physical Chemistry Laboratory“, *Journal of Chemical Education*, vol. 89, no. 6, pp. 780–783, 2012.

[172] F. Ye, H. Jensen, S. W. Larsen, A. Yaghmur, C. Larsen, and J. Østergaard, „Measurement of drug diffusivities in pharmaceutical solvents using Taylor dispersion analysis“, *Journal of Pharmaceutical and Biomedical Analysis*, vol. 61, pp. 176–183, 2012.

[173] S. S. Jensen, H. Jensen, C. Cornett, E. H. Møller, and J. Østergaard, „Insulin diffusion and self-association characterized by real-time UV imaging and Taylor dispersion analysis“, *Journal of Pharmaceutical and Biomedical Analysis*, vol. 92, pp. 203–210, 2014.

[174] S. Liang, J. Xu, L. Weng, H. Dai, X. Zhang, and L. Zhang, „Protein diffusion in agarose hydrogel in situ measured by improved refractive index method“, *Journal of Controlled Release*, vol. 115, no. 2, pp. 189–196, 2006.

[175] E. N. Dunmire, A. M. Plenys, and D. F. Katz, „Spectrophotometric analysis of molecular transport in gels“, *Journal of Controlled Release*, vol. 57, no. 2, pp. 127–140, 1999.

[176] M. P. Di Cagno, F. Clarelli, J. Vabenø, C. Lesley, S. D. Rahman, J. Cauzzo, E. Franceschinis, N. Realdon, and P. C. Stein, „Experimental Determination of Drug Diffusion Coefficients in Unstirred Aqueous Environments by Temporally Resolved Concentration Measurements“, *Molecular Pharmaceutics*, vol. 15, no. 4, pp. 1488–1494, 2018.

[177] F. Ye, A. Yaghmur, H. Jensen, S. W. Larsen, C. Larsen, and J. Østergaard, „Real-time UV imaging of drug diffusion and release from Pluronic F127 hydrogels“, *European Journal of Pharmaceutical Sciences*, vol. 43, no. 4, pp. 236–243, 2011.

[178] F. Ye, S. W. Larsen, A. Yaghmur, H. Jensen, C. Larsen, and J. Østergaard, „Real-time UV imaging of piroxicam diffusion and distribution from oil solutions into gels mimicking the subcutaneous matrix“, *European Journal of Pharmaceutical Sciences*, vol. 46, no. 1-2, pp. 72–78, 2012.

[179] A. Waldbaur, J. Kittelmann, C. P. Radtke, J. Hubbuch, and B. E. Rapp, „Microfluidics on liquid handling stations (μF-on-LHS): An industry compatible chip interface between microfluidics and automated liquid handling stations“, *Lab on a Chip*, vol. 13, no. 12, pp. 2337–2343, 2013.

[180] C. P. Radtke, M.-T. Schermeyer, Y. C. Zhai, J. Göpper, and J. Hubbuch, „Implementation of an analytical microfluidic device for the quantification of protein concentrations in high-throughput format“, *Engineering in Life Sciences*, vol. 16, no. 6, pp. 515–524, 2016.

[181] K. Haubert, T. Drier, and D. Beebe, „PDMS bonding by means of a portable, low-cost corona system“, *Lab on a Chip*, vol. 6, no. 12, pp. 1548–1549, 2006.

[182] J. Crank, *The Mathematics of Diffusion*, 2nd. Oxford: Oxford University Press, 1975.

[183] R. C. Reid, J. M. Prausnitz, and B. E. Poling, *The Properties of Gases & Liquids*, 4th, B. Sun and G. H. Fleck, Eds. New York: McGraw-Hill, Inc., 1987, pp. 22–46.

[184] N. Zhang, J. Wang, J. Ye, P. Zhao, and M. Xiao, „Oxyalkylation modification as a promising method for preparing low-melting-point agarose“, *International Journal of Biological Macromolecules*, vol. 117, no. 2017, pp. 696–703, 2018.

[185] R. B. Cook, *Derivatized agarose and method of making and using same*, 1982.

5

Systematic Evaluation of Agarose- and Agar-Based Bioinks for Extrusion-Based Bioprinting of Enzymatically Active Hydrogels

Lukas Wenger[1], Carsten P. Radtke[1], Eva Gerisch[1], Max Kollmann[1], Christof M. Niemeyer[2], Kersten S. Rabe[2] and Jürgen Hubbuch[1]

[1] Institute of Engineering in Life Sciences, Section IV: Biomolecular Separation Engineering, Karlsruhe Institute of Technology (KIT), Karlsruhe, Germany

[2] Institute for Biological Interfaces 1, Karlsruhe Institute of Technology (KIT), Eggenstein-Leopoldshafen, Germany

Abstract

Extrusion-based 3D bioprinting enables the production of customized hydrogel structures that can be employed in flow reactors when printing with enzyme-containing inks. The present study compares inks based on either low-melt agarose or agar at different concentrations (3 to 6 %) and loaded with the thermostable enzyme esterase 2 from the thermophilic organism *Alicyclobacillus acidocaldarius* (AaEst2) with regard to their suitability for the fabrication of such enzymatically active hydrogels. A customized printer setup including a heatable nozzle and a cooled substrate was established to allow for clean and reproducible prints. The inks and printed hydrogel samples were characterized using rheological measurements and compression tests. All inks were found to be sufficiently printable to create lattices without overhangs, but printing quality was strongly enhanced at 4.5 % polymer or more.

The produced hydrogels were characterized regarding mechanical strength and diffusibility. For both properties, a strong correlation with polymer concentration was observed with highly concentrated hydrogels being more stable and less diffusible. Agar hydrogels were found to be more stable and show higher diffusion rates than comparable agarose hydrogels. Enzyme leaching was identified as a major drawback of agar hydrogels, while hardly any leaching from agarose hydrogels was detected. The poor ability of agar hydrogels to permanently immobilize enzymes indicates their limited suitability for their employment in perfused biocatalytic reactors. Batch-based activity assays showed that the enzymatic activity of agar hydrogels was roughly twice as high as the activity of agarose hydrogels which was mostly attributed to the increased amount of enzyme leaching.

Agarose bioinks with at least 4.5 % polymer were identified as the most suitable of the investigated inks for the printing of biocatalytic reactors with AaEst2. Drawbacks of these inks are limited mechanical and thermal stability, not allowing the operation of a reactor at the optimum temperature of AaEst2 which is above the melting point of the employed low-melt agarose.

5.1 Introduction

Additive manufacturing (AM) – or 3D printing – is a dynamically evolving field offering versatile and highly adaptive fabrication methods that are useful for a wide range of applications [1]. It is based on the stacking of layers to gradually build three-dimensional objects. While initially mostly applied for visualization models and rapid prototyping, the advancement of printing technologies and materials has made 3D printing a more commonly applied method for the fabrication of working prototypes and even functional parts for end use [15]. This can be mainly attributed to the availability of AM methods allowing the fabrication of parts with excellent mechanical stability, e. g. made from metal [186] or ceramics [187], that can be employed in demanding applications. Many fields, ranging from the aerospace [188], automotive [189] and construction [190] industry to the chemical engineering [46] and biotechnology [48] sector, are investigating how to exploit the new possibilities provided by 3D printing. In (bio-)chemical engineering, two general fields can be distinguished based on the employed types of material. On one side, conventional materials like glass [191], metal [192] or water-free polymers [53] are used in the production of microfluidic devices or chromatography columns. On the other side, soft and biocompatible, water-based materials like hydrogels are employed with the purpose of accommodating cells [56, 57] or biomolecules [58, 59] in a suitable aqueous environment.

This discipline, often referred to as *bioprinting* as a branch of *biofabrication* [55], is mainly focused on the development of new methods, tools and materials for tissue engineering [73]. Recently, those tools were increasingly adopted for the fabrication of biocatalytic flow reactors based on cells [131] or enzymes [12, 85, 130, 193]. Such reaction systems, both on a microfluidic and macroscopic scale, play an important role in biocatalytic applications like compartmentalized catalytic cascades which can be realized by employing spatially separated reaction chambers [104].

Hydrogels can serve as a matrix for the immobilization of enzymes by physical entrapment, thereby avoiding the loss of the catalyst and enhancing cost-efficiency [91]. This method offers a simple way of immobilization, usually without the need to adapt it to a specific enzyme. The immobilization of enzymes in hydrogels is based on the entrapment of the relatively large enzyme within a polymer network while allowing small substrate and product molecules to diffuse in and out of the hydrogel [92]. Choosing a support material with an appropriate pore size is required to maximize the diffusion of substrate and product while minimizing the leaching of enzyme [90]. A drawback of the method is limited mass transfer of substrate and product and hence decreased activity [12, 92]. In order to compensate for this limitation, it is paramount to maximize the surface-area-to-volume ratio of the hydrogel [193].

Bioprinting enables the rapid and flexible fabrication of appropriate hydrogel structures with a high surface-area-to-volume ratio and perfusable geometries like simple grids [85, 130] or more complex gyroid structures [193] that can be employed in microreactors. To achieve high surface-area-to-volume ratios and complex geometric shapes, it is paramount to optimize the printability of the employed materials. Unlike molding methods, bioprinting allows quick adaptations to new geometries without the need to fabricate new molds and enables the fabrication of certain geometries like gyroid structures that are not manufacturable using common molding techniques. Spatially separated or compartmentalized enzymatic reactions can be realized by employing multiple print heads that allow the deposition of different enzymes in a spatially controlled manner. Overall, the flexible and fast fabrication of biocatalytically active constructs by additive manufacturing can accelerate iterative optimization processes and contribute to the advancement of the field [104].

One of the most common techniques in biofabrication is extrusion-based bioprinting, a simple method based on the deposition of fluid materials from a cartridge through a nozzle onto a substrate [105]. It requires the use of (bio-)inks that can be printed in a fluid state and be solidified after deposition, forming stable hydrogels. Suitable rheological properties like a high viscosity or high yield stress [107] are vital factors to ensure good printability [68]. Typically, water-soluble polymers like gelatin [194], hyaluronic acid [195] or alginate [57, 196] are used, often accompanied by additives like methyl cellulose [197, 198] or nanosilicates [199, 200] to enhance and adapt rheological properties.

Unlike cells, enzymes do not require any nutrient supply and can often handle harsher environments, opening up new options regarding bioprinting methods and materials. Current approaches include the use of poly(ethylene glycol) diacrylate-based hydrogels [12] or emulsion-based hybrid materials [193] to print catalytically active materials containing β-galactosidase. Both these approaches rely on UV curing, introducing the potential of enzyme inactivation due to the presence of free radicals. As an alternative material system based on natural polymers, agarose and agar hydrogels are potential candidates. Agarose and agar can be dissolved in water at elevated temperature and form stable hydrogels upon cooling [201, 202] which makes them interesting materials to be employed in bioprinting. Agarose is a naturally occuring polymer that is the main component of agar which can be extracted from red algae (*Rhodophyceae*) [203]. Hydrogels based on modified low-melt

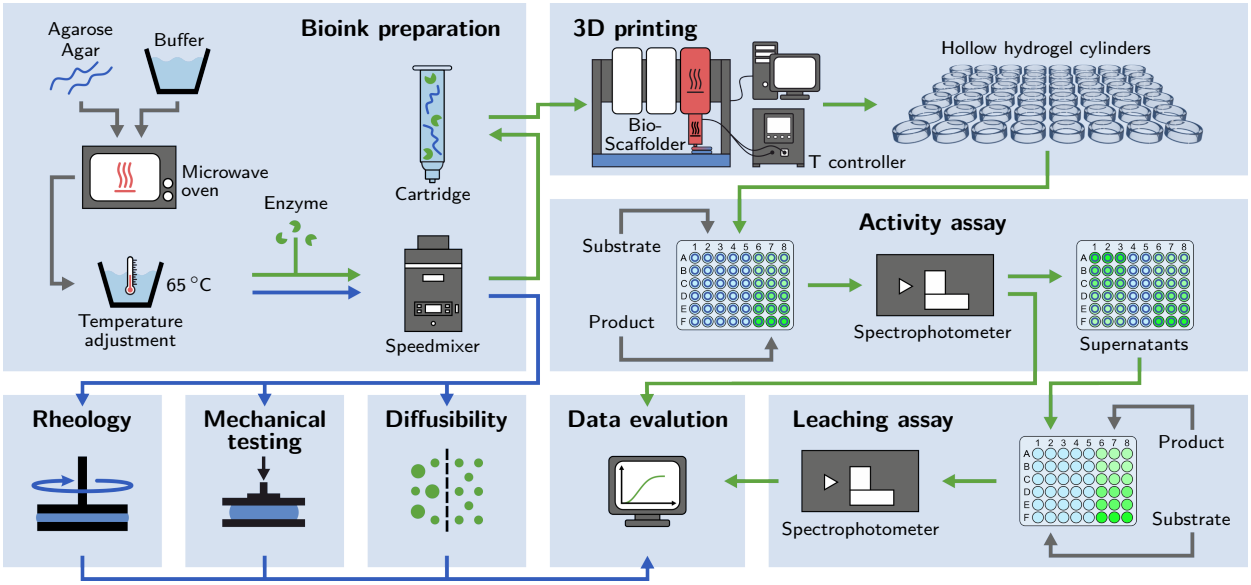

Figure 5.1 Schematic of the applied workflow. Bioinks based on different concentrations of low-melt agarose and agar are prepared. Enzyme-loaded hydrogel cylinders are printed to perform activity assays. The supernatants are used for leaching assays. Enzyme-free bioinks and hydrogels are examined with rheological analysis, mechanical testing and diffusibility measurements.

hydroxyethyl agarose have been shown to be applicable for the printing of thermostable enzymes [85, 130]. The demonstrated process includes a step to reliquefy the low-melt agarose hydrogel at 60 °C making this approach viable for thermostable enzymes only. In the published studies, 3 % (w/v) low-melt hydroxyethyl agarose has been used [85, 130] to print modules for perfusable biocatalytic reactors. So far, no systematic optimization of the printing setup and procedure and no screening of different bioink compositions has been performed. The present study shows the further development of the printing setup by introducing a heatable nozzle that allows for a more precise control of the bioink temperature upon extrusion to achieve more reproducible and robust prints. Furthermore, we assess bioinks prepared from two different materials (low-melt hydroxyethyl agarose and unmodified agar) at different concentrations to explore the potential for optimizing printability and catalytic activity using adapted ink compositions. The liquid inks are assessed for rheological properties and gelation behavior. The solidified hydrogels are investigated regarding mechanical stability and diffusibility. Enzyme-containing hydrogel samples are printed and analyzed for enzyme leaching and biocatalytic activity using microplate-based batch activity assays. The screening of a range of inks with slightly different compositions with regard to multiple performative aspects demonstrates the importance of adapting inks specifically for certain applications. A schematic overview of the applied workflow of the study is presented in Figure 5.1.

5.2 Materials and Methods

5.2.1 Chemicals and buffers

Agar (bacteriology grade) was purchased from AppliChem GmbH, low-melt agarose (Roti®garose with low melting and gelling temperature) from Carl Roth GmbH & Co. KG. All hydrogels were prepared with phosphate buffered saline (PBS), pH 7.4. Sodium chloride (NaCl), potassium chloride (KCl), disodium hydrogen phosphate dihydrate ($Na_2HPO_4 \cdot 2\,H_2O$) and potassium dihydrogenphosphate (KH_2PO_4) were purchased from Merck KGaA. The PBS buffers were prepared with ultrapure water from a Purelab Ultra water purification system (ELGA LabWater) and filtered through an 0.2 µm cellulose acetate filter (Sartorius AG) before use. 5(6)-carboxyfluorescein dihexylester was synthesized at the Institute for Biological Interfaces 1 and used as a substrate for activity assays.

5.2.2 Enzyme expression and purification

As a model enzyme, esterase 2 from the thermophilic organism *Alicyclobacillus acidocaldarius* (AaEst2, EC 3.1.1.1) containing a His-tag was heterologously expressed in *Escherichia coli* and purified as reported earlier [85, 204]. Aliquots were stored at −80 °C until use.

5.2.3 Bioink preparation

Aqueous solutions of agar and low-melt agarose (3 to 6 % (w/w)) were prepared by adding appropriate amounts of agar or agarose powder to PBS buffer and heating the mixture in a microwave oven (WP800L20-5, Hanseatic) several times to boiling point, until a homogeneous solution was obtained. The solution was transferred into a 25 mL SpeedMixer® cup (Hauschild GmbH & Co. KG) and the temperature was adapted to 65 °C in a water bath. If required, the appropriate amount of AaEst2 stock solution was added to obtain the desired enzyme concentration of 100 nM. Due to its limited availability, no enzyme was added, if the bioink was intended for rheological analysis, mechanical testing or diffusibility measurements. It was assumed that the low concentrations of enzyme used (100 nM) did not significantly influence the evaluated material properties. The bioink was mixed and degassed in a dual asymmetric centrifuge (DAC) SpeedMixer® DAC 150.1 FVZ-K (Hauschild GmbH & Co. KG) at 3500 rpm for 90 s. Before the mixing step, the cup holder of the SpeedMixer® was pre-heated to 65 °C to avoid gelation during the mixing step. Bioinks intended for printing were transferred into pre-heated 10 mL printing cartridges, sealed with an outlet cap and a piston (all purchased from Nordson EFD) and used directly. Bioinks intended for enzyme-free analytics were filled into 10 mL syringes and stored at 65 °C until use.

5.2.4 Rheology

The flow properties and gelation behavior of the bioinks were analyzed using an MCR 301 rheometer (Anton Paar GmbH). To prepare a measurement, liquid bioink was applied to the pre-heated rheometer plate at 60 °C. The top plate was moved to the measurement position and the sample was trimmed. To avoid air exposure and prevent the sample from drying out during the measurement, paraffin oil (Fluka Analytical) was applied to the measurement gap. The temperature was set to the required start temperature of the measurement and the sample was left to equilibrate for at least 5 min.

5.2.4.1 Gelation behavior

Temperature hysteresis curves were recorded to investigate the melting and gelling behavior of the bioinks. The measurements were performed with profiled parallel plates with a diameter of 25 mm and a gap width of 500 µm. The measurement was started at 70 °C. Gelation was induced by steadily decreasing the temperature to 15 °C at a rate of 1 °C min^{-1}. To remelt the sample, the temperature was increased at the same rate to 80 °C for low-melt agarose and to 100 °C for agar. During the whole process, the storage modulus G' and the loss modulus G were recorded applying an oscillatory measurement with a shear strain (deformation) amplitude $\gamma_A = 3\,\%$ and an angular frequency $\omega = 20\,\mathrm{s}^{-1}$. Each data point was averaged over a period of 30 s. All measurements were carried out as triplicates ($n = 3$).

To determine the melting temperature (T_{melt}) and gelling temperature (T_{gel}), an inflection point method derived from Bonino *et al.* [205] was applied. The descending and ascending part of the G' measurement were separately fitted with a sigmoidal curve and the inflection point of the curve was defined as T_{melt} and T_{gel}, respectively.

5.2.4.2 Flow behavior

Flow curves of the bioinks were recorded at different temperatures to gather information about the behavior of the inks during extrusion. A cone-plate setup with a diameter of 60 mm was employed. The viscosity was determined using shear rate-controlled rotational measurements. All inks were analyzed in triplicates ($n = 3$) at a comparison temperature $T_c = 70\,°\mathrm{C}$ and the specific nozzle temperature T_{nozzle} of the respective ink, as shown in Table 5.1. To observe the influence of temperature on flow behavior in the range relevant during the printing process, the same measurement was performed in the range from 40 to 25 °C for low-melt agarose and from 50 to 35 °C for agar, both in 1 °C steps with one measurement per temperature ($n = 1$). The measurements were performed with a variable measuring time per data point, ranging from 10 s at a shear rate of $\dot{\gamma} = 0.1\,\mathrm{s}^{-1}$ to 1 s at $\dot{\gamma} = 0.1\,\mathrm{s}^{-1}$.

5.2.5 3D bioprinting

5.2.5.1 Customized experimental setup

All bioinks were printed using a BioScaffolder 3.1 (GeSiM – Gesellschaft für Silizium-Mikrosysteme mbH) with a specifically adapted setup including a custom-made heatable nozzle and a water-cooled microplate carrier. A scheme of the setup is shown in Figure 5.2A. The custom-made heatable nozzle is depicted in Figure 5.2B as a cross-section and in Figure 5.2D as a 3D illustration. A commercially available 2 inch steel dispensing tip (Vieweg GmbH) with an inner diameter of 0.35 mm and a length of 25 mm was the basis of the heatable nozzle. It was placed inside a 3D printed metal jacket that contained a Pt 100 element (L220, Heraeus Deutschland GmbH & Co. KG) to measure the nozzle temperature. Heating was achieved with a resistance wire coiled around the metal jacket. The components of the heatable nozzle were joined with thermo-conductive epoxy resin (Omegabond 200, Omega Engineering GmbH). The temperature sensor and resistance wire were coupled with a control box containing a 12 V, 60 W power supply (IRM-60-12ST, Mean Well Enterprises Co., Ltd.), a MOSFET board and a PID controller (ET 7420, ENDA GmbH & Co. KG). The output from the temperature sensor was processed by the PID controller to operate the MOSFET board which regulated the current flow in the resistance wire. This allowed the metal

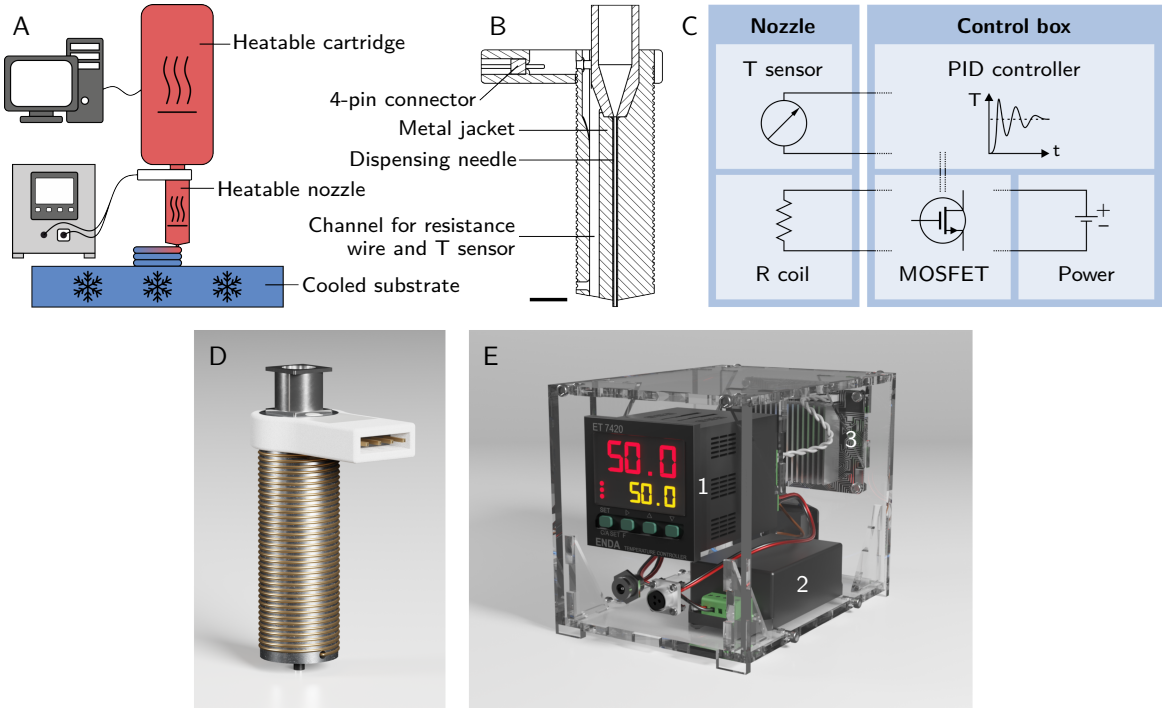

Figure 5.2 (A) Scheme of the printing setup with a heatable cartridge, a customized heatable nozzle and a cooled substrate. (B) Cross-section of the metal jacket of the heatable nozzle before the assembly of resistance wire and temperature sensor (the scale bar represents 5 mm). (C) Simplified circuit layout of the setup showing the interaction of the nozzle containing a temperature sensor and a resistance coil with the control box containing a PID controller, a power supply and a MOSFET control board. (D) 3D illustration of the heatable nozzle used for the printing process. The assembled nozzle consists of a 3D-printed steel body containing a commercially available 2 inch steel dispensing tip with an inner diameter of 0.35 mm and a Pt 100 element as a temperature sensor. A resistance wire is coiled around the body of the nozzle for heating. (E) Control box containing a PID controller (1), a 12 V power supply (2) and a MOSFET control board (3) to regulate the temperature of the heatable nozzle.

body of the nozzle to be kept at the set temperature. A simplified circuit layout of the setup is shown in Figure 5.2C, a 3D illustration of the control box in Figure 5.2E. Sand-blasted glass plates were used as the printing substrate. To accelerate the gelation process, the plates were cooled to 5 °C by a water-cooled microplate carrier connected to a F12-MP cooling aggregate (Julabo GmbH).

5.2.5.2 Printing process

Immediately after the preparation process, the temperature of the bioink cartridges was adjusted to the final printing temperature by incubation in the heating jacket of the BioScaffolder for 20 min at the temperature appropriate for the corresponding bioink. The pre-heated nozzle was mounted onto the cartridge, calibrated for height and purged with bioink. Prints were always carried out at a fixed layer height of 300 µm, all other printing parameters were individually adjusted to the corresponding inks as shown in Table 5.1.

Table 5.1 Printing parameters employed in the fabrication of activity assay cylinders and exemplary prints made from inks based on low-melt agarose and agar.

Polymer type	Polymer concentration (% (w/w))	Printing speed (mm/s)	Extrusion pressure[a] (kPa)	Cartridge temperature[b] (°C)	Nozzle temperature (°C)
Agar	3	5	30	52	47
	4.5	7	120	60	55
	6	7	300	65	57
Agarose	3	5	40	38	30
	4.5	7	160	39	32
	6	7	380	40	35

[a]The extrusion pressure was continuously adapted to produce cylinders of the specified target weight.

[b]The actual (measured) temperature inside the cartridge was roughly 3 °C lower than the set value.

Hollow, enzyme-loaded hydrogel cylinders were printed to perform activity assays with different hydrogel compositions and substrate concentrations in multiwell plates (see section 5.2.8.1). For mechanical tests (section 5.2.6), identical cylinders were printed without added enzyme. The cylinder diameter of 10 mm, the total height of 3 mm and the layer height of 300 µm were kept identical for all prints, independent of the used ink. In order to produce comparable cylinders, every printed cylinder was weighed and the extrusion pressure was continuously adapted in order to yield a target weight of 100 mg per cylinder. Cylinders not meeting the specified target weight within a ±3 % tolerance window were discarded. Cylinders matching the defined specifications were stored in multiwell plates (CellStar® 48 well suspension culture plate, Greiner Bio-One GmbH) sealed with self-adhesive plastic foil (polypropylene, for PCR plates, Brand GmbH & Co. KG).

5.2.6 Assessment of cylinder height and mechanical properties of hydrogels

A ZwickiLine Z0.5TN universal testing machine (ZwickRoell GmbH & Co. KG) equipped with a 100 N load cell (Xforce HP) and stainless steel compression plates with a diameter of 30 mm was used to determine the height and maximum tolerable force of printed hydrogel cylinders with uniaxial compression tests. These measurements can provide valuable information about the mechanical stability of the hydrogels which determines the degree of stress they can tolerate during handling. All measurements were controlled employing the software testXpert III, V. 1.4 (ZwickRoell GmbH & Co. KG). For the measurement, a sample was placed on the bottom plate of the device. Every measurement was started at a gap width of 3.5 mm and the top plate with the load cell was moved down at a speed of 2 mm/min. The measurement gap at a load of 0.01 N was defined as the cylinder height. The maximum achievable compression force before a rupture of the sample occured was defined as F_{max}. As a comparison with non-printed samples, the maximum force measurement was also performed with solid hydrogel cylinders punched out of a 3 mm thick layer of cast hydrogel. Twelve samples were measured for each data point ($n = 12$).

5.2.7 Diffusion properties

The diffusion coefficient of 5(6)-carboxyfluorescein in different hydrogels was estimated employing a microfluidics-based UV imaging method reported previously [206]. A solution of 1 mg/mL 5(6)-carboxyfluorescein (Acros Organics, part of Fisher Scientific Co. LLC) in 6.25 % (v/v) dimethyl sulfoxide (DMSO, purchased from Fisher Scientific Co. LLC) in PBS was prepared by dissolving the appropriate amount of 5(6)-carboxyfluorescein in pure DMSO and then diluting it with the appropriate amount of 3.125 % DMSO in PBS. The microfluidic chip was pre-heated to 70 °C in a drying oven (T 6120, Heraeus Instruments GmbH & Co. KG), filled with liquid bioink and left at room temperature for 10 min to allow gelation. The 1 mg/mL 5(6)-carboxyfluorescein solution was filled into the chip through one of the other inlets to create an interface between solution and hydrogel. The diffusion of the 5(6)-carboxyfluorescein through the hydrogel was monitored using an ActiPix™ D100 imaging system (Paraytec Ltd.). The resulting raw data were transformed to absorbance data and exported as wmv files using the ActiPix™ software (version 1.5). Matlab R2020a (The MathWorks®, Inc.) was used to import the files, detect the channel area and rotate the frames in order to achieve a horizontal alignment of the channel. Using a calibration curve, the image data at 120 min were converted to 5(6)-carboxyfluorescein concentration data. To obtain a value for the diffusion coefficient D, the concentration profiles along the microfluidic channel were fitted with an analytical solution of Fick's second law [206]:

$$C(x,t) = C_0 \left(\frac{1}{2} - \frac{1}{2} \operatorname{erf} \left(\frac{x - x_0}{2\sqrt{Dt}} \right) \right) \tag{5.1}$$

with the position along the microfluidic channel x, the time t, the initial concentration of 5(6)-carboxyfluorescein in the fluid phase C_0, the position of the boundary layer x_0 and the diffusion coefficient D. All measurements were performed as triplicates ($n = 3$).

5.2.8 Activity assays

5.2.8.1 Enzyme immobilized in hydrogels

Printed hydrogel cylinders were assessed for their enzymatic activity in a 48-well microplate format using a Tecan Freedom Evo pipetting platform (Tecan Group AG). Each well of a 48-well microplate (for suspension culture, Greiner Bio-One GmbH) contained one printed hydrogel cylinder loaded with 100 nM esterase 2 (AaEst2). For the measurement, 320 µL of substrate solution (10 to 150 µM 5(6)-carboxyfluorescein dihexylester in PBS, pH 7.4) were added to each cylinder using the Tecan Freedom Evo pipetting robot. To avoid evaporation effects, 300 µL of light mineral oil (Sigma-Aldrich, part of Merck KGaA) were added manually using a multichannel pipette. Calibration samples of 5(6)-carboxyfluorescein (0 to 150 µM) were prepared in the same way on the same plate to allow the transformation of fluorescence measurements to concentration values. The fluorescence signal ($\lambda_{excitation} = 485$ nm, $\lambda_{emission} = 528$ nm) was recorded for 2 h in a Tecan infinite M200 pro spectrophotometer. Using the obtained calibration curves, the resulting fluorescence measurements were converted to concentration values and the curves of 5(6)-carboxyfluorescein concentration over time were fitted with sigmoidal fits. To determine the maximum activity of a sample, the maximum slope of the fits was determined. The activity assays were performed in triplicates ($n = 3$) at 25 °C with different hydrogel compositions (3 %, 4.5 %, and 6 % (w/w) low-melt agarose and agar).

5.2.8.2 Freely dissolved enzyme leached from hydrogels

During the activity assays with enzyme-loaded hydrogel cylinders, six cylinders were incubated with only PBS buffer (substrate-free). At the end of the measurement after 2 h, the supernatants were sampled and stored for later analysis of their catalytic activity as an indicator of leaching. The activity assays were conducted in the same way as with the printed hydrogel cylinders, i. e. employing a Tecan Freedom pipetting platform and 48-well microplates. 320 µL of 50 µM substrate solution were added to 100 µL of supernatant to induce the catalytic reaction. 300 µL of light mineral oil (Sigma-Aldrich) were added manually to avoid evaporation effects. Calibration samples of 5(6)-carboxyfluorescein (0 to 150 µM) were prepared in the same way on the same plate to allow the transformation of fluorescence measurements to concentration values. The fluorescence signal ($\lambda_{excitation}$ = 485 nm, $\lambda_{emission}$ = 528 nm) was recorded for 20 min at 25 °C. The resulting data were converted to product concentrations using calibration curves. The volumetric activity was determined from the initial slope (over 5 min) of the product-over-time curve. All measurements were performed as triplicates ($n = 3$).

5.2.9 Statistical analysis

The statistical significance of data was tested employing one-way analysis of variance (ANOVA) and the Tukey method for multiple comparisons. Differences between data points were considered statistically significant when $p < 0.05$. Normality was assessed for large data sets ($n = 12$) applying the Anderson-Darling test. For small data sets ($n = 3$), normality was assumed.

5.3 Results and discussion

5.3.1 Rheology and printability

The print fidelity of extrusion-based 3D printing mainly depends on the extent of ink spreading after extrusion which is primarily influenced by two parameters: the rheological properties of the liquid bioink, namely the viscosity or the presence of a yield point, and the time delay, until the ink is solidified after extrusion [207]. For thermosensitive materials like agarose- or agar-based inks, both properties are substantially influenced by temperature. Excessively high printing temperatures may reduce the viscosity and prolong the period of ink spreading, while too low temperatures may allow premature gelation to occur within the nozzle resulting in the extrusion of distorted or currugated filaments [107, 208], nozzle clogging [73, 208] and reduced inter-layer adhesion [209, 210]. Hence, the thermal regulation of both cartridge and nozzle is paramount in order to achieve the desired ink properties upon extrusion. For this purpose, a customized printer setup with a heatable nozzle and a heatable cartridge jacket was employed. Rheological methods were used to study the thermo-dependent behavior of agarose and agar inks. In particular, the gelling and melting behavior and the influence of temperature on flow properties were analyzed.

5.3.1.1 Gelling and melting behavior

Gelling and melting temperatures of the bioinks were determined using oscillatory measurements in combination with temperature sweeps, as shown in Figure 5.3. Liquid bioink samples were applied to the pre-heated rheometer plate at 60 °C and solidified by cooling below the gel point T_{gel}, indicated by a sudden increase in storage modulus G' and loss modulus G''. The samples were

reliquefied by increasing the temperature above the melting point T_{melt}, accompanied by a decrease in G' and G''. The gel point is commonly determined by calculating the cross-over of G' and G'' [56, 211, 212]. In the given case, some samples displayed $G' > G''$ over the whole analyzed range and there was no cross-over despite the obviously liquid nature of the samples at 70 °C. Mao *et al.* found that incorrectly high values of G' may be caused by oxidation effects on the surface of the metallic measuring plates or by a partial invasion of the measurement gap by oil that is used to protect the sample from evaporation [212]. This invasion may be further promoted by thermal expansion and contraction effects during the temperature sweep. Hence, an alternative approach reported by Bonino *et al.* [205] was applied to estimate the gelling and melting temperatures from the inflection points of the G' curves as indicated in Figure 5.3A and B. The final estimations of T_{melt} and T_{gel} are shown in Figure 5.3C.

Agarose bioinks exhibited a very sharp increase in G' upon gelation, while the change occured more gradually with agar bioinks. Both agarose and agar inks exhibited a strong thermal hysteresis, i. e. a large difference between T_{gel} and T_{melt}. While the polymer concentration was found to have a relatively low impact on T_{gel} and T_{melt} with a maximum difference of 2 °C between 3 % and 6 % polymer, there was a strong influence of the material system. In general, agar bioinks gelled and melted at higher temperatures ($T_{gel,mean} = (37.0 \pm 0.8)$ °C and $T_{melt,mean} = (92.5 \pm 0.9)$ °C) than agarose bioinks ($T_{gel,mean} = (29.3 \pm 0.9)$ °C and $T_{melt,mean} = (65.1 \pm 1.0)$ °C). The determined values for agarose were in good accordance with manufacturer's data ($T_{gel} \leq 28$ °C and $T_{melt} \leq 65.5$ °C for a 1.5 % gel).

The determined gelling and melting temperatures were used as a basis to select suitable temperatures for printing. Commonly, thermosensitive hydrogels are printed in a partially cross-linked state at a temperature close to the cross-over point of G' and G'' in order to reduce spreading after extrusion but still allow for a smooth dispensing process [213]. We found that operating at temperatures too close to T_{gel} resulted in a time-dependent increase in viscosity and finally nozzle clogging due to slow gelation within the cartridge, especially with agar inks. Thus, the final adjustments of nozzle and cartridge temperatures were done in an iterative process. Higher temperatures were chosen for the cartridge than for the nozzle to avoid time-dependent gelation and to ensure constant extrusion conditions. The tendency of agar to gel prematurely increased strongly with growing concentration resulting in a high temperature difference between different agar concentrations, while different low-melt agarose inks were printed at relatively similar temperatures (see Table 5.1). Also, it was found that the actual ink temperature within the cartridge was roughly 3 °C lower than the set value which was considered, as well. The selected temperatures are listed in Table 5.1.

The recorded temperature sweeps also allow an assessment of the possible application temperatures for biocatalytic reactions with enzymes immobilized in the printed hydrogels. The chosen temperature should allow the enzyme to work as efficiently as possible while not impairing the mechanical integrity of the hydrogel. AaEst2 shows an activity maximum at a temperature of approximately 70 °C [83]. At a temperature of 25 °C, as employed for all experiments in this study, the activity is lower by a factor of approximately 4.5 [83]. To avoid a weakening of the hydrogel, the reaction should be performed at a temperature below the onset of the melting process which is around 50 °C for the agarose hydrogels and around 70 °C for the agar hydrogels. Hence, the use of agar hydrogels would allow the AaEst2 to operate at its optimum temperature while reactors made from agarose hydrogels can only be operated at suboptimal temperatures. It should be noted that a modified

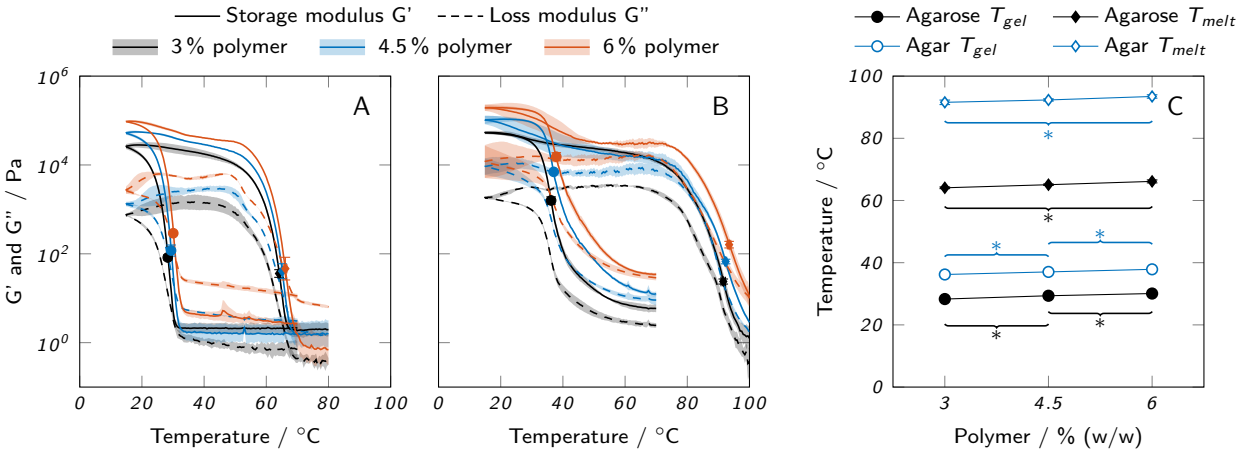

Figure 5.3 Thermal properties of low-melt agarose and agar hydrogels. Loss and storage modulus of (A) low-melt agarose and (B) agar hydrogels are shown over temperature. (C) Melting and gelling points of low-melt agarose and agar, as derived from the oscillatory measurements. All data are shown as mean values with the standard deviation as shaded areas or error bars ($n = 3$). For clarity, only significant differences to the nearest significantly different data points are highlighted by asterisks ($p < 0.05$).

agarose with low melting point was used in this study and higher operating temperatures could be realized with a different type of agarose.

5.3.1.2 Flow properties

The flow properties of liquid agarose and agar inks were analyzed using rotational tests. Figure 5.4 shows the viscosity over shear rate for both a comparison temperature $T_c = 70\,°C$ and the nozzle temperature T_{nozzle} which was specific for each bioink (see Table 5.1). The temperature range relevant for printing was covered in more detail by additional measurements, as represented in Figure 5.5. Here, the flow curves recorded at different temperatures are shown in the range of 40 to 25 °C for agarose inks and 50 to 35 °C for agar inks. In general, all inks showed a strong correlation between polymer concentration and viscosity. At T_c, agarose inks exhibited ideally viscous (Newtonian) behavior in the analyzed range, i. e. a constant viscosity, independent of the applied shear rate. Lowering the temperature to T_{nozzle} drastically changed the behavior of agarose inks with 3 % and 4.5 % polymer towards the shear-thinning behavior of a pseudo-plastic fluid. The 6 % agarose ink still showed Newtonian behavior at shear rates below $100\,s^{-1}$ with a viscosity plateau shifted up by a factor of 3 compared to T_c. The seemingly inconsistent behavior at T_{nozzle} can be attributed to the different nozzle temperatures used for different agarose concentrations. When reducing the temperature further, the same shear-thinning behavior was observed for 6 % agarose as for the other concentrations (see Figure 5.5A-C). The found shear-thinning behavior of most inks at T_{nozzle} is a favorable property for extrusion-based bioprinting, as it contributes to high-fidelity printing [214].

The measurements with variable temperature (Figure 5.5) confirm the observation of the oscillatory measurements that the change in material properties is more abrupt in agarose inks than in agar inks when approaching T_{gel}. This observed change of rheological behavior with the reduction

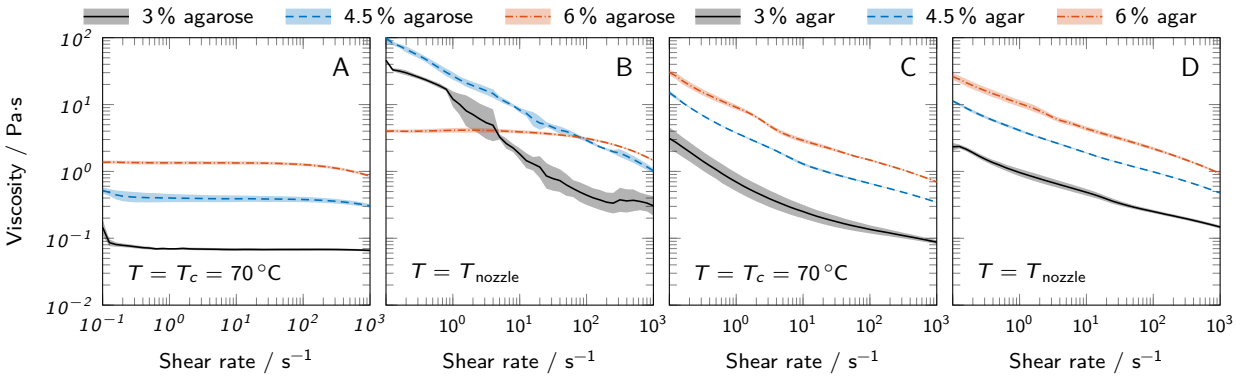

Figure 5.4 Viscosity curves of all prepared bioinks at 70 °C and the respective nozzle temperature T_{nozzle} used for printing. Low-melt agarose bioinks at (A) 70 °C and (B) T_{nozzle} are compared to agar bioinks at (C) 70 °C and (D) T_{nozzle}. All curves show mean values and the standard deviation as shaded areas ($n = 3$).

of temperature can be explained by the onset of gelation. At high temperatures, the agarose polysaccharide chains behave as random coils. During cooling, the chains start forming double-stranded helices stabilized by intramolecular hydrogen bonds. At further reduced temperatures, the helices start to aggregate due to intermolecular hydrogen bonds, forming microcrystalline junction zones [215–217]. The gelation continues with reduced temperature and leads to a sharp increase in viscosity when approaching the gel point [217] causing the observed shear-thinning behavior. Agar inks already showed shear-thinning behavior at 70 °C and only marginally changed their rheological properties upon temperature reduction to T_{nozzle} which can be attributed to the larger difference between T_{nozzle} and T_{gel} for agar inks.

5.3.1.3 Printability

The printability of different bioinks was compared by printing two standardized test objects, namely a hollow cylinder and a lattice structure. All prints were carried out at a layer height of 300 µm with a target height of 3 mm. Additionally, the lattice structure was printed with a target height of 20 mm only using inks with 6 % polymer. Figure 5.6 shows the resulting prints. For both agarose and agar inks, the printability was drastically enhanced at higher polymer concentrations, especially for the lattice structure. While at 3 % polymer, the circular outline merged almost entirely with the outermost transverse strands, there was a clear separation between outline and inner strands in prints with 4.5 and 6 % polymer and the extruded strands were thinner in general. The increased spreading of inks with 3 % polymer did not allow printing structures notably higher than 3 mm with the employed settings. Lowering the printing speed or the nozzle and cartridge temperature may reduce the spreading effect and allow the printing of higher objects. More efficient cooling, e. g. employing a fan, might also contribute, but comes with the drawback of accelerating the drying of the gel. Grid structures with more layers were printable only with inks containing 4.5 and 6 % polymer. Figure 5.6 shows grids with a height of 20 mm made from inks with 6 % agarose and agar. In general, the resolution of the printed objects was relatively low with a strand thickness of roughly 600 to 1000 µm which could be optimized by adding suitable additives like nanosilicates to enhance the viscosity of the inks. At large, the presented results are in accordance with the rheological analysis,

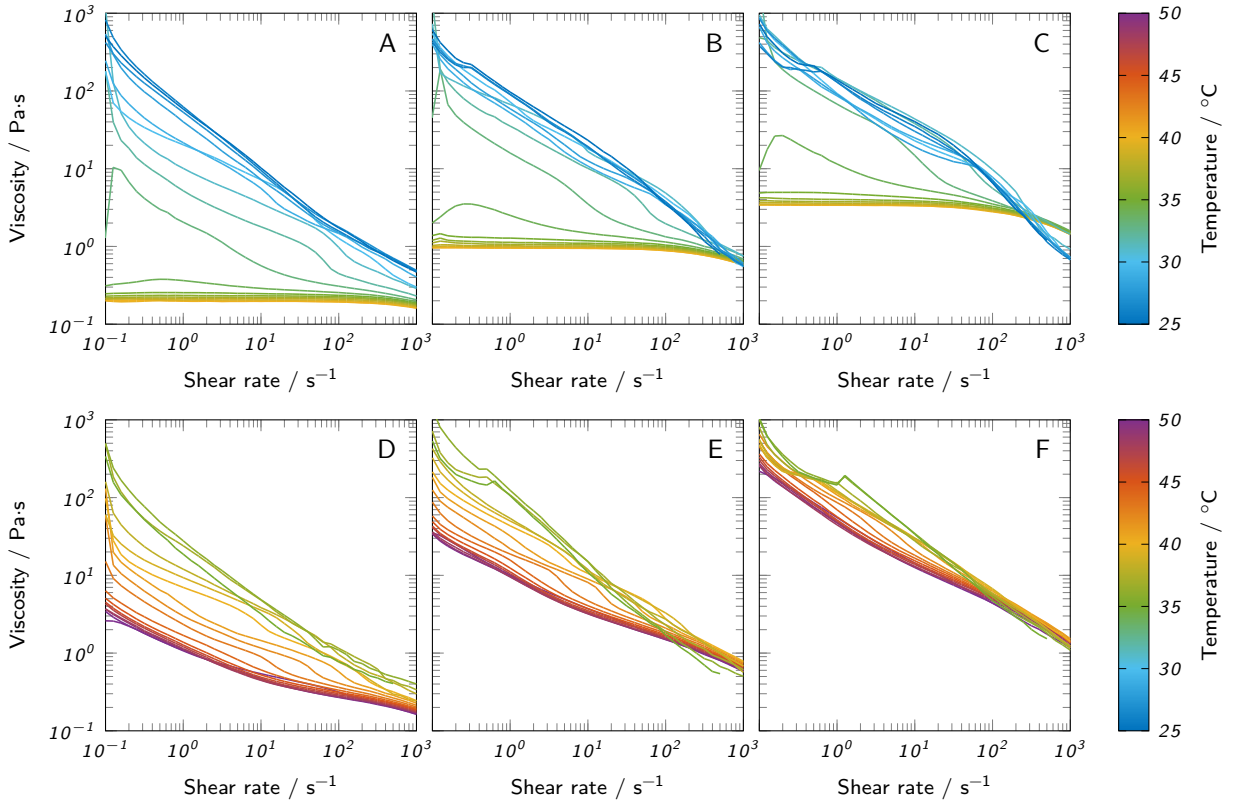

Figure 5.5 Flow curves of all prepared bioinks at different temperatures. (A) 3 % low-melt agarose, (B) 4.5 % low-melt agarose, (C) 6 % low-melt agarose, (D) 3 % agar, (E) 4.5 % agar and (F) 6 % agar.

as lower viscosities caused reduced printing quality due to increased ink spreading. Despite a lower measured viscosity at T_{nozzle} at low shear rates, the 6 % agarose ink showed superior printability compared to 3 % agarose. This behavior contradicts the rheological observations indicating that the actual extrusion temperature deviated from T_{nozzle}. The inks were stored in the cartridge at a slightly higher temperature ($T_{cartridge}$) to prevent time-dependent gelation effects. The residence time of ink within the nozzle was calculated to be between 1.1 to 1.5 s (see supplementary material) which may have been too short to cool the ink to T_{nozzle} resulting in a slightly higher extrusion temperature. Small temperature differences close to T_{gel} can cause strong variations in viscosity [217] and hence influence the printability significantly. Faster gelation kinetics of the high-polymer inks may play an additional role.

Compared to the lattice structures, the basic hollow cylinders only showed minor differences between different polymer concentrations. At 4.5 and 6 % polymer, the single layers were more visible in form of a ribbed surface, indicating a higher surface area available for mass exchange compared to inks with 3 % polymer, where the layers were more smoothly merged due to increased ink spreading before gelation. Excessive ink spreading can also cause a deviation of the actual object height from the target height defined by the executed gcode. Height measurements with a universal testing machine indeed revealed a positive correlation between polymer concentration and the height of printed cylinders, as shown in Figure 5.7A. The maximum difference in height of 14 % was found between

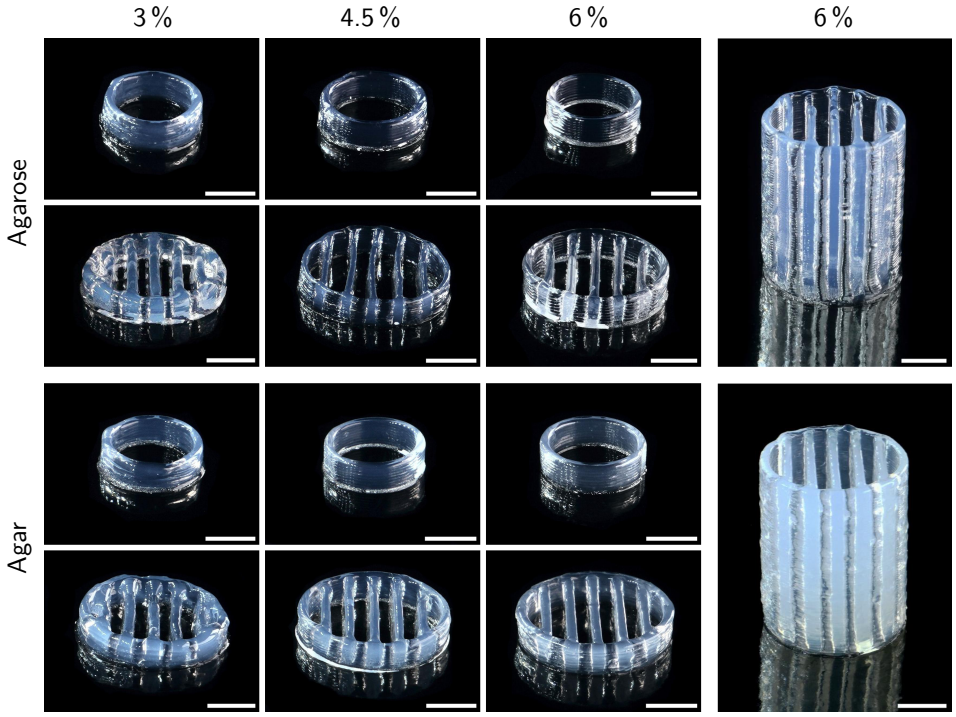

Figure 5.6 Exemplary prints of low-melt agarose and agar hydrogels with a target height of 3 mm (left side) and 20 mm (right side). All prints were carried out at a layer height of 300 µm. Scale bars represent 5 mm.

cylinders made from 3 and 6 % agarose. Assuming a perfect hollow cylinder, this corresponds to a difference of 8.7 % in surface area available for mass exchange (see supplementary material).

The presented photographs only allow a qualitative assessment of printability. For further studies with adapted ink compositions it would be desirable to apply more precise analysis methods that allow an objective assessment based on quantitative data.

5.3.2 Material properties of agarose and agar hydrogels

5.3.2.1 Mechanical strength

High mechanical strength is not a primary requirement for hydrogels employed in a biocatalytic reactor unless high operating pressures or shear forces are involved. However, weak hydrogels can massively impede the handling of printed objects and complicate processing steps like the reactor assembly or the removal of the printed hydrogel from the printing substrate. As a measure of mechanical strength, the maximum compression force F_{max} before rupture of the gels was determined using a universal testing machine. Printed hollow cylinders, as used for the printability and activity studies, were compared to solid cylinders punched out of a layer of cast hydrogel, as shown in Figure 5.7B and C. Due to the different geometries of the cast and printed samples (solid vs. hollow cylinders), only trends can be compared, not the absolute values of the measurements.

If extracted from the same source and used at the same concentration, agarose forms stronger gels than agar [139] due to the lack of non-gelling components like agaropectin [218]. Here, agar

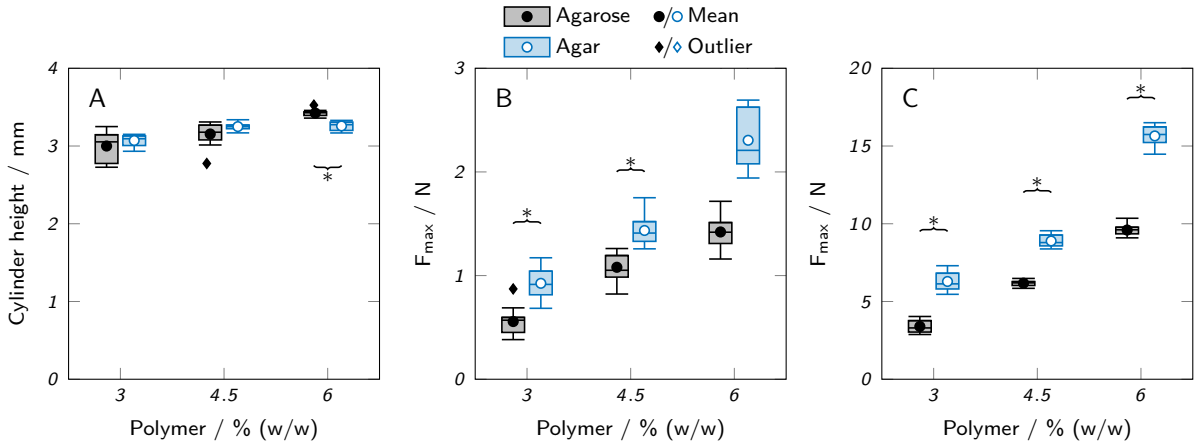

Figure 5.7 Mechanical testing of low-melt agarose and agar hydrogels. (A) Height of printed hydrogel cylinders. (B and C) Maximum applicable compression force F_{max} before rupture of (B) printed hollow hydrogel cylinders and (C) cast hydrogel samples. The box plots represent the median and the upper and lower quartile. The whiskers represent the most extreme value still within a 1.5-fold interquartile range (IQR) from the upper and lower quartile. All data points outside the 1.5-fold IQR are depicted as outliers. Each box represents twelve samples ($n = 12$). Significant differences between agarose and agar are highlighted by asterisks ($p < 0.05$).

hydrogels showed a higher tolerable compression force than the respective agarose gels by a factor of 1.3 to 1.9. This is probably due to the use of an agarose with low melting and gelling point, prepared by introduction of hydroxyethyl groups into the agarose skeleton which is associated with a reduction in gel strength [219]. The polymer concentration was positively correlated with F_{max} with a 2.5-fold increase between 3 % and 6 % (w/w) polymer for agar hydrogels, independent of the preparation method. An increased polymer concentration allows the formation of more junction zones between agarose chains and hence higher stability [220]. For agarose hydrogels, F_{max} increased by a factor of 2.8 for cast samples, but only by a factor of 2.5 for printed samples. This implies that differences in geometry play an additional role in the stability of the printed cylinders. Reduced contact areas in samples printed with high-viscosity inks may weaken the integrity of the printed object, while the increased layer merging of low-viscosity inks may be beneficial for the stability. In general, the measurements of the printed objects showed higher standard deviations than the samples punched-out from cast material. This indicates a lower reproducibility and larger deviations between theoretically identical printed samples which may be influenced by geometric irregularities due to an unsteady ink flow or material inhomogeneities caused by changing cooling patterns.

It is important to note that the mechanical testing was performed at room temperature and that employing the hydrogels at elevated temperatures to optimize the enzymatic activity may drastically reduce the mechanical stability, as discussed in Section 5.3.1.1. Another aspect of mechanical stability of printed objects is the adherence between layers which was not analyzed quantitatively. However, it was made sure that the printing temperatures were chosen in a way that guaranteed the ink to come in contact with the previous layer in a non-gelled state. This allowed the handling of the printed objects like the transfer from the printing substrate into microplates without any delamination. Also, the performed compression tests always caused a vertical rupture of the printed cylinders indicating that the interlayer bonding was not a particular weak spot.

5.3.2.2 Diffusion characteristics

The immobilization of enzymes by physical entrapment in hydrogels leads to reduced catalytic efficiency due to mass transfer limitations caused by the hydrogel [12, 193, 221]. To reduce this effect, a high diffusibility of the hydrogel itself and short path lengths due to appropriate geometries of the printed object are desirable. The diffusion coefficient of 5(6)-carboxyfluorescein in agarose and agar hydrogels was determined to assess the effect of different polymer types and concentrations on mass transfer limitations. 5(6)-carboxyfluorescein is the product of the cleavage of 5(6)-carboxyfluorescein dihexylester by AaEst2 and was chosen as the analyte, as it is readily available and can be detected using UV-Vis spectroscopy. Figure 5.8 shows the results of the measurements over a range of 1.5 to 7.5 % (w/w) polymer. A decrease of the diffusion coefficient with increasing polymer concentration could be observed for both hydrogel types. Over the whole analyzed range, the diffusion coefficient in agar hydrogels was higher than in agarose hydrogels by a factor of 1.4 to 1.7. For both, the diffusion coefficient dropped by roughly 30 % between 1.5 % and 7.5 % (w/w) polymer.

The observed higher diffusion coefficients in agar hydrogels can be attributed to the expected smaller pore size of low-melt agarose hydrogels. Both the lack of non-gelling components like agaropectin [218] in agarose and the chemically modified polymer chains of the low-melt agarose contribute to this effect [185]. The pore sizes of agarose hydrogels reported in literature are typically by orders of magnitude larger than small molecules like 5(6)-carboxyfluorescein ((289 ± 66) nm in 3 % agarose, (201 ± 36) nm in 5 % agarose [222]). However, increased path lengths due to steric obstruction by the polymer chains and hydrodynamic drag can reduce the diffusion coefficient [223]. Furthermore, not only the type of agarose, but also properties of the solvent like ionic strength and process parameters like cooling speed can strongly influence the molecular structure and hence diffusivity of the resulting hydrogel [222]. Specifically, low-melt hydroxyethyl agarose is known to form smaller pores than the unmodified starting product [185] and rapid cooling creates a more uniform agarose microstructure with thinner fibers and smaller average pore diameters than slow cooling [224]. In practice, the cooling process is hard to control and can even lead to a heterogeneous pore distribution within a single sample, as some parts will cool and gel more quickly due to contact with a cold surface, while other parts are cooled slower by the contact with air or because the core will cool slower than the surface. This leads to a limited comparability between the samples analyzed here and printed objects.

5.3.3 Enzyme immobilization within printed agar and agarose hydrogels

The achievable catalytic activity and the amount of enzyme leaching from the material are relevant criteria to assess the suitability of the studied hydrogels for the application in printed biocatalytic reactors. Both these properties were examined in microplate-based batch experiments with hollow printed hydrogel cylinders containing 100 nM AaEst2. In comparison to cast samples, printed hydrogel cylinders offer a more realistic representation of a printed reactor due to the identical production process and hence similar material properties. During the production process, the enzyme is exposed to a certain regime of temperature changes which cannot be replicated by using cast samples and which is especially relevant when using enzymes that are susceptible to thermal inactivation. Material properties determined by the production process include geometric differences caused by varying degrees of layer merging or differences in the polymer structure of the hydrogels as a result of printing temperature and cooling rate during gelation [222, 224, 225]. Thus, the results

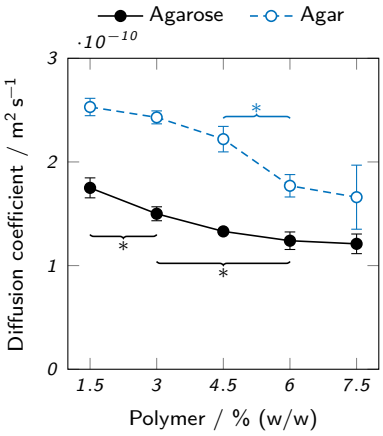

Figure 5.8 Diffusion coefficients of 5(6)-carboxyfluorescein in low-melt agarose and agar hydrogels. The data points represent mean values ± standard deviation ($n = 3$). For clarity, only significant differences to the nearest significantly different data points are highlighted by asterisks ($p < 0.05$).

presented here are to be interpreted as a function of not only polymer type and concentration but also various other process- and material-related parameters.

5.3.3.1 Leaching

Enzyme-laden hydrogel cylinders were immersed in buffer for 120 min and samples of the supernatants were analyzed for leached enzyme using activity assays. Figure 5.9 shows the acquired results. Only a low amount of enzymatic activity was observed in the supernatants of agarose hydrogels (below 0.03 µM/min), but values between 1.16 µM/min and 1.20 µM/min were determined for the supernatants of agar hydrogels. For both hydrogel types, no significant differences between different polymer concentrations were found. The substantial enzyme leaching observed for agar hydrogels indicates that no sufficient enzyme retention was achieved. In perfusable reactors, the degree of leaching would be even higher than in the static experiment performed here. This demonstrates the poor suitability of agar hydrogels in this context.

The immobilization of enzymes within hydrogels is based on the physical entrapment of the enzymes within the polymer fibre network and does typically not involve chemical or adsorptive interactions [226, 227]. Thus, the pore size of the polymer network is the main factor influencing the retention of the enzyme within the hydrogel. The minimum diameter of AaEst2, as calculated from its molecular weight of 34 kDa [83], is 4.3 nm [228], although the effective hydrodynamic diameter can be assumed to be substantially larger. Still, AaEst2 is considerably smaller than the typically reported pore sizes of agarose hydrogels (e. g. (201 ± 36) nm at 5 % agarose, determined by atomic force microscopy [222]) making an effective and permanent retention of AaEst2 by physical entrapment in standard agarose implausible. However, the actual pore size of agarose hydrogels depends strongly on a number of factors like gelation speed [224, 229] and expression organism, as agarose can be extracted from a variety of algae [218]. In the present study, the probably most relevant factor is that a chemically modified low-melt hydroxyethyl agarose was used which typically forms smaller pores, depending on the degree of substitution [185]. The hydroxyethyl substitution and the lack of

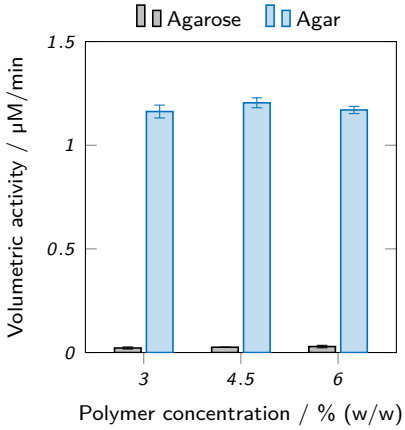

Figure 5.9 Activity assay of supernatants incubated with enzyme-laden hydrogel cylinders made from inks based on low-melt agarose and agar. Different amounts of leaching can be observed for different hydrogels. The data points represent mean values ± standard deviation ($n = 3$). Significant differences between polymer concentrations are marked by asterisks ($p < 0.05$).

non-gelling components in low-melt agarose are likely reasons for the observed low amount of leached enzyme compared to agar-based hydrogels. A previous study has shown that AaEst2 is washed out from hydrogels of 3 % (w/v) low-melt agarose over longer time periods when employed in perfused microreactors [85]. As the use of low-melt agarose has the disadvantage of limited applicability at high temperatures, alternatives with both high enzyme retention and temperature stability may be desirable. Agarose derivatives that can be crosslinked for higher temperature stability or that offer reaction sites for covalent attachment are potential candidates for this objective [227].

5.3.3.2 Enzymatic activity in hydrogels

Activity assays with hollow cylinders containing 100 nM AaEst2 were performed in order to compare the maximum enzymatic activity in different hydrogels. Figure 5.10 shows the results for agarose and agar at three different polymer concentrations and six different substrate concentrations. The resulting kinetics resemble the form of a Michaelis-Menten equation and were fitted accordingly. For both polymer types, there was a slight trend of reduced activity with increasing polymer concentration, as shown in a trend analysis in the supplementary material. This trend is attributable to the reduced diffusibility and hence higher mass transfer limitation of hydrogels with increased polymer concentration, as presented in Figure 5.8 and discussed above. Across all polymer concentrations, the measured maximum activity of agar hydrogels was roughly twice as high as the activity of the respective agarose samples. Here again, the higher diffusibility of agar hydrogels plays a role, as it allows a higher enzymatic activity due to higher mass transfer rates. However, the more important aspect is most likely the leaching of enzyme from agar hydrogels (Figure 5.9). The leached enzyme can accumulate in the supernatant and catalyze the reaction without the mass transfer limitations of the hydrogel, resulting in a higher activity of the sample. A quantification of the two effects is not possible with the available data, as the supernatant was only sampled after an incubation time of 2 h. Other possible, but probably minor influences include different surface areas and cylinder heights of the hydrogel samples caused by printing irregularities. Variable printing temperatures are unlikely to cause differences in activity, as AaEst2 is thermostable at 70 °C for at least several

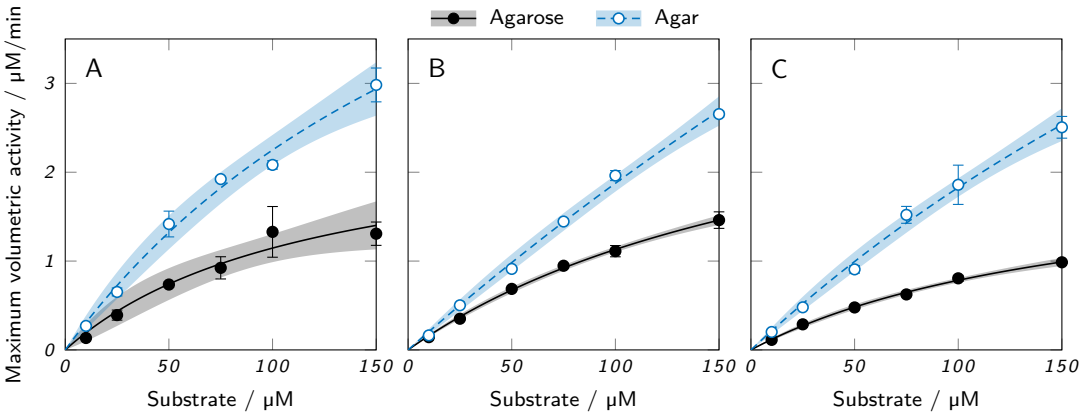

Figure 5.10 Activity assays of printed low-melt agarose and agar cylinders containing 100 nM AaEst2 and (A) 3 %, (B) 4.5 % and (C) 6 % polymer. The data points represent mean values ± standard deviation ($n = 3$) and were fitted with a Michaelis-Menten equation. 95 % confidence intervals are displayed as shaded areas.

hours [83]. At first glance, the results of the activity assays imply agar hydrogels to be the superior material due to the enhanced activity. However, taking enzyme leaching as the most probable reason for the obtained results into account, the enhanced activity is merely a symptom of the unsuitability of agar as an immobilization matrix for AaEst2. Applied in a perfusable reactor, these hydrogels would lose enzyme and hence catalytic activity quickly, failing to provide reusability which is the main advantage of enzyme immobilization. This shows that results of batch experiments cannot be considered alone, but have to be evaluated in the context of additional factors like enzyme leaching.

5.3.4 Further considerations

Besides the already analyzed and discussed aspects like diffusibility, leaching and enzymatic activity, several additional factors may be worth considering when choosing an appropriate ink.

The different viscosities of inks with varying polymer concentration do not only affect the printability, but can influence the handling and processability of these inks during preparation. Low viscosity inks with a low gelling point (e. g. 3 % agarose) can be easily transferred between different containers like the mixing vessel and the printing cartridge, even with pipettes. The handling of highly viscous inks with a high gelling point (e. g. 6 % agar) is more difficult and there may be a significant loss of material during preparation which is problematic when working with costly or scarcely available enzymes.

In previous studies, cartridges with enzyme-laden low-melt agarose-hydrogels were prepared for stock and reliquefied as needed [85, 130]. This approach allows a high flexibility of the printing process and rapid, on-demand production of enzymatically active hydrogel structures. The high temperatures required to reliquefy agar hydrogels would inactivate most enzymes, making this approach inapplicable in combination with agar-based inks.

For the operation of biocatalytic reactors, the working temperature is a crucial parameter to achieve high activities. The temperature stability of agar hydrogels allows higher working temperatures

than could be achieved with low-melt agarose hydrogels. For AaEst2 with its temperature optimum of 70 °C [83], only agar hydrogels allow an operation at ideal conditions.

All discussed advantages and disadvantages of hydrogels made from low-melt agarose and agar are qualitatively summarized in Table 5.2.

Table 5.2 Qualitative ratings of low-melt agarose and agar bioinks regarding a range of criteria determining their suitability for the printing of biocatalytically active hydrogels.

	Agarose			Agar		
	3 %	4.5 %	6 %	3 %	4.5 %	6 %
Printability	−	○	+	−	○	+
Mechanical stability	−−	−	+	−	+	++
Avoidance of leaching	++	++	++	−−	−−	−−
Enzymatic activity	○	○	○	+[1]	+[1]	+[1]
Handling and processability	++	+	−	○	−	−−
Reliquefaction with enzyme	+	+	+	−−	−−	−−
Temperature stability of hydrogel	−	−	−	+	+	+

[1]Determined enzymatic activity of agar hydrogels was increased due to enzyme leaching.

5.4 Conclusion and outlook

The present study compares bioinks with regard to their suitability for the extrusion-based 3D printing of enzymatically active hydrogels. Inks with different concentrations of either low-melt agarose or agar were investigated. A customized printer setup including a heatable nozzle and a cooled substrate was established. Compared to previous publications employing 3 % agarose inks and a nozzle without thermal control [85, 130], the newly established setup allowed cleaner and more defined prints without uncontrolled pre-gelation and nozzle clogging. The gel and melting points and the flow behavior of all inks were analyzed using rheological methods. Based on this, suitable printing parameters were determined individually. All bioinks were found to be sufficiently printable to create lattices without overhangs and a height of at least 3 mm with 300 µm layers, but the printing quality was strongly enhanced at 4.5 % polymer or more.

The produced hydrogels were characterized regarding mechanical strength and diffusibility. For both properties, a correlation with polymer concentration was observed with highly concentrated hydrogels being more stable and less diffusible. Agar hydrogels were found to be more stable and allow higher diffusion rates of 5(6)-carboxyfluorescein than comparable agarose hydrogels. Enzyme leaching was identified as a major drawback of agar hydrogels, while hardly any leaching from the agarose hydrogels was detected. The leached enzyme is most probably the dominant cause for the observed superiority of agar hydrogels in the performed batch activity assays. This indicates the limited suitability of agar hydrogels for perfused biocatalytic reactors, as the enzyme would be washed out over time. The activity assays showed a small effect of polymer concentration on enzymatic activity.

In summary, agarose inks with at least 4.5 % polymer were found to be the most suitable of the investigated inks for the printing of biocatalytic reactors with AaEst2 due to their superior printability

and leaching behavior. Drawbacks of the low-melt agarose hydrogels are limited mechanical and thermal stability, not allowing the operation of a reactor at the optimum temperature of AaEst2 which is above the melting point of the tested low-melt agarose.

The observed limitations of the inks could be addressed by a systematic optimization of the ink formulation. Rheological additives could enhance process robustness and printability and enable the manufacturing of more sophisticated geometries including overhangs. Quantitative fidelity measurements should be applied to assess and compare the printability of modified inks. Functionalization of the agarose with polymerizable groups or adding additional monomers would allow a post-curing step that may increase mechanical strength, reduce leaching even further and enable reactions at higher temperatures by enhancing the melting point. Such modifications should be finely tuned to minimize potential enzymatic inactivation by free radicals. Blends of low-melt agarose with agar or unmodified agarose could be used to create inks with defined melting and gelling properties. In order to improve the reaction conditions, systematic screenings of pH, ionic strength and temperature could be performed based on the presented activity assay method.

Conflict of interest

The authors declare that the research was conducted in the absence of any commercial or financial relationships that could be construed as a potential conflict of interest.

Author contributions

LW, CPR, CMN, KSR and JH conceptualized the research. LW, EG and MK established the experimental workflows and conducted the experiments. LW developed the employed lab ware, established automated data evaluation tools and wrote the manuscript. CPR supported the establishing of the experimental workflow and provided expertise on automated activity assays and bioprinting, KSR on enzymes and biocatalysis. CPR, KSR and JH proofread the manuscript.

Acknowledgments

CMN and KSR acknowledge financial support through the Helmholtz program „Materials Systems Engineering“ under the topic „Adaptive and Bioinstructive Materials Systems“. KSR acknowledges financial support by the German Bundesministerium für Bildung und Forschung (BMBF) under project number 161L0284A. The authors bear the complete responsibility for the content of this publication. We acknowledge support by the KIT-Publication Fund of the Karlsruhe Institute of Technology.

Data availability statement

The raw data supporting the conclusions of this article will be made available by the authors, without undue reservation.

Chapter references

[1] T. D. Ngo, A. Kashani, G. Imbalzano, K. T. Nguyen, and D. Hui, „Additive manufacturing (3D printing): A review of materials, methods, applications and challenges“, *Composites Part B: Engineering*, vol. 143, no. February, pp. 172–196, 2018.

[12] B. Schmieg, A. Schimek, and M. Franzreb, „Development and performance of a 3D-printable poly(ethylene glycol) diacrylate hydrogel suitable for enzyme entrapment and long-term biocatalytic applications“, *Engineering in Life Sciences*, vol. 18, no. 9, pp. 659–667, 2018.

[15] I. Gibson, D. Rosen, B. Stucker, and M. Khorasani, *Additive Manufacturing Technologies*. 2021.

[46] C. Parra-Cabrera, C. Achille, S. Kuhn, and R. Ameloot, „3D printing in chemical engineering and catalytic technology: structured catalysts, mixers and reactors“, *Chemical Society Reviews*, vol. 47, pp. 209–230, 2018.

[48] F. Krujatz, A. Lode, J. Seidel, T. Bley, M. Gelinsky, and J. Steingroewer, „Additive Biotech—Chances, challenges, and recent applications of additive manufacturing technologies in biotechnology“, *New Biotechnology*, vol. 39, no. September, pp. 222–231, 2017.

[53] U. Simon, L. C. Scorza, S. Teworte, A. J. McCormick, and S. Dimartino, „Demonstration of protein capture and separation using three-dimensional printed anion exchange monoliths fabricated in one-step“, *Journal of Separation Science*, pp. 1078–1088, 2020.

[55] J. Groll, T. Boland, T. Blunk, J. A. Burdick, D. W. Cho, P. D. Dalton, B. Derby, G. Forgacs, Q. Li, V. A. Mironov, L. Moroni, M. Nakamura, W. Shu, S. Takeuchi, G. Vozzi, T. B. Woodfield, T. Xu, J. J. Yoo, and J. Malda, „Biofabrication: Reappraising the definition of an evolving field“, *Biofabrication*, vol. 8, no. 1, pp. 1–5, 2016.

[56] T. Billiet, E. Gevaert, T. De Schryver, M. Cornelissen, and P. Dubruel, „The 3D printing of gelatin methacrylamide cell-laden tissue-engineered constructs with high cell viability“, *Biomaterials*, vol. 35, no. 1, pp. 49–62, 2014.

[57] A. G. Tabriz, M. A. Hermida, N. R. Leslie, and W. Shu, „Three-dimensional bioprinting of complex cell laden alginate hydrogel structures“, *Biofabrication*, vol. 7, no. 4, 2015.

[58] C. A. Mandon, L. J. Blum, and C. A. Marquette, „Adding Biomolecular Recognition Capability to 3D Printed Objects“, *Analytical Chemistry*, vol. 88, no. 21, pp. 10 767–10 772, 2016.

[59] C. D. Devillard, C. A. Mandon, S. A. Lambert, L. J. Blum, and C. A. Marquette, „Bioinspired Multi-Activities 4D Printing Objects: A New Approach Toward Complex Tissue Engineering“, *Biotechnology Journal*, vol. 13, no. 12, 2018.

[68] K. Hölzl, S. Lin, L. Tytgat, S. Van Vlierberghe, L. Gu, and A. Ovsianikov, „Bioink properties before, during and after 3D bioprinting“, *Biofabrication*, vol. 8, no. 3, pp. 1–19, 2016.

[73] I. T. Ozbolat, W. Peng, and V. Ozbolat, „Application areas of 3D bioprinting“, *Drug Discovery Today*, vol. 21, no. 8, pp. 1257–1271, 2016.

[83] G. Manco, E. Adinolfi, F. M. Pisani, G. Ottolina, G. Carrea, and M. Rossi, „Overexpression and properties of a new thermophilic and thermostable esterase from Bacillus acidocaldarius with sequence similarity to hormone-sensitive lipase subfamily“, *Biochemical Journal*, vol. 332, no. 1, pp. 203–212, 1998.

[85] M. Maier, C. P. Radtke, J. Hubbuch, C. M. Niemeyer, and K. S. Rabe, „On-demand production of flow reactor cartridges by 3D printing of thermostable enzymes“, *Angewandte Chemie International Edition*, vol. 57, no. 19, pp. 5539–5543, 2018.

[90] E. Górecka and M. Jastrz bska, „Review article: Immobilization techniques and biopolymer carriers“, *Biotechnology and Food Science*, vol. 75, no. 1, pp. 65–86, 2011.

[91] S. Krishnamoorthi, A. Banerjee, and A. Roychoudhury, „Immobilized Enzyme Technology: Potentiality and Prospects“, *Journal of Enzymology and Metabolism*, vol. 1, no. 1, pp. 1–11, 2015.

[92] S. Nisha, S. Arun Karthick, and N. Gobi, „A Review on Methods, Application and Properties of Immobilized Enzyme“, *Chemical Science Review and Letters*, vol. 1, no. 3, pp. 148–155, 2012.

[104] K. S. Rabe, J. Müller, M. Skoupi, and C. M. Niemeyer, „Cascades in Compartments: En Route to Machine-Assisted Biotechnology“, *Angewandte Chemie - International Edition*, vol. 56, no. 44, pp. 13 574–13 589, 2017.

[105] A. Panwar and L. P. Tan, „Current status of bioinks for micro-extrusion-based 3D bioprinting“, *Molecules*, vol. 21, no. 6, pp. 1–26, 2016.

[107] V. H. M. Mouser, F. P. W. Melchels, J. Visser, W. J. A. Dhert, D. Gawlitta, and J. Malda, „Yield stress determines bioprintability of hydrogels based on gelatin-methacryloyl and gellan gum for cartilage bioprinting.“, *Biofabrication*, vol. 8, no. 3, p. 035 003, 2016.

[130] M. Peng, E. Mittmann, L. Wenger, J. Hubbuch, M. K. M. Engqvist, C. M. Niemeyer, and K. S. Rabe, „3D-Printed Phenacrylate Decarboxylase Flow Reactors for the Chemoenzymatic Synthesis of 4-Hydroxystilbene“, *Chemistry – A European Journal*, vol. 25, pp. 15 998–16 001, 2019.

[131] A. Saha, T. G. Johnston, R. T. Shafranek, C. J. Goodman, J. G. Zalatan, D. W. Storti, M. A. Ganter, and A. Nelson, „Additive Manufacturing of Catalytically Active Living Materials“, *ACS Applied Materials & Interfaces*, vol. 10, no. 16, pp. 13 373–13 380, 2018.

[139] T. Zhang, R. A. Sanguramath, S. Israel, and M. S. Silverstein, „Emulsion Templating: Porous Polymers and beyond“, *Macromolecules*, vol. 52, no. 15, pp. 5445–5479, 2019.

[185] R. B. Cook, *Derivatized agarose and method of making and using same*, 1982.

[186] T. Blachowicz, G. Ehrmann, and A. Ehrmann, „Metal additive manufacturing for satellites and rockets“, *Applied Sciences*, vol. 11, no. 24, pp. 1–15, 2021.

[187] Z. Chen, Z. Li, J. Li, C. Liu, C. Lao, Y. Fu, C. Liu, Y. Li, P. Wang, and Y. He, „3D printing of ceramics: A review“, *Journal of the European Ceramic Society*, vol. 39, no. 4, pp. 661–687, 2019.

[188] S. C. Joshi and A. A. Sheikh, „3D printing in aerospace and its long-term sustainability“, *Virtual and Physical Prototyping*, vol. 10, no. 4, pp. 175–185, 2015.

[189] R. Leal, F. M. Barreiros, L. Alves, F. Romeiro, J. C. Vasco, M. Santos, and C. Marto, „Additive manufacturing tooling for the automotive industry“, *International Journal of Advanced Manufacturing Technology*, vol. 92, no. 5-8, pp. 1671–1676, 2017.

[190] P. Wu, J. Wang, and X. Wang, „A critical review of the use of 3-D printing in the construction industry“, *Automation in Construction*, vol. 68, pp. 21–31, 2016.

[191] E. Gal-Or, Y. Gershoni, G. Scotti, S. M. Nilsson, J. Saarinen, V. Jokinen, C. J. Strachan, G. Boije Af Gennäs, J. Yli-Kauhaluoma, and T. Kotiaho, „Chemical analysis using 3D printed glass microfluidics“, *Analytical Methods*, vol. 11, no. 13, pp. 1802–1810, 2019.

[192] V. Gupta, M. Talebi, J. Deverell, S. Sandron, P. N. Nesterenko, B. Heery, F. Thompson, S. Beirne, G. G. Wallace, and B. Paull, „3D printed titanium micro-bore columns containing polymer monoliths for reversed-phase liquid chromatography“, *Analytica Chimica Acta*, vol. 910, pp. 84–94, 2016.

[193] L. Wenger, C. P. Radtke, J. Göpper, M. Wörner, and J. Hubbuch, „3D-Printable and Enzymatically Active Composite Materials Based on Hydrogel-Filled High Internal Phase Emulsions“, *Frontiers in Bioengineering and Biotechnology*, vol. 8, no. July, pp. 1–17, 2020.

[194] J. Yin, M. Yan, Y. Wang, J. Fu, and H. Suo, „3D Bioprinting of Low-Concentration Cell-Laden Gelatin Methacrylate (GelMA) Bioinks with a Two-Step Cross-linking Strategy“, *ACS Applied Materials and Interfaces*, vol. 10, no. 8, pp. 6849–6857, 2018.

[195] L. Pescosolido, W. Schuurman, J. Malda, P. Matricardi, F. Alhaique, T. Coviello, P. R. Van Weeren, W. J. Dhert, W. E. Hennink, and T. Vermonden, „Hyaluronic acid and dextran-based semi-IPN hydrogels as biomaterials for bioprinting“, *Biomacromolecules*, vol. 12, no. 5, pp. 1831–1838, 2011.

[196] E. Axpe and M. L. Oyen, „Applications of alginate-based bioinks in 3D bioprinting“, *International Journal of Molecular Sciences*, vol. 17, no. 12, 2016.

[197] N. Contessi Negrini, L. Bonetti, L. Contili, and S. Farè, „3D printing of methylcellulose-based hydrogels“, *Bioprinting*, vol. 10, 2018.

[198] N. Law, B. Doney, H. Glover, Y. Qin, Z. M. Aman, T. B. Sercombe, L. J. Liew, R. J. Dilley, and B. J. Doyle, „Characterisation of hyaluronic acid methylcellulose hydrogels for 3D bioprinting“, *Journal of the Mechanical Behavior of Biomedical Materials*, vol. 77, pp. 389–399, 2018.

[199] C. W. Peak, J. Stein, K. A. Gold, and A. K. Gaharwar, „Nanoengineered Colloidal Inks for 3D Bioprinting“, *Langmuir*, vol. 34, no. 3, pp. 917–925, 2018.

[200] S. A. Wilson, L. M. Cross, C. W. Peak, and A. K. Gaharwar, „Shear-Thinning and Thermo-Reversible Nanoengineered Inks for 3D Bioprinting“, *ACS Applied Materials and Interfaces*, vol. 9, no. 50, pp. 43 449–43 458, 2017.

[201] D. W. Renn, „Agar and Agarose: Indispensable Partners in Biotechnology“, *Industrial and Engineering Chemistry Product Research and Development*, vol. 23, no. 1, pp. 17–21, 1984.

[202] A. Sassolas, A. Hayat, and J.-L. Marty, „Entrapment Within an Agarose Gel“, in *Immobilization of Enzymes and Cells*, J. M. Guisan, Ed., Third, Humana Press / Springer, 2013, ch. Enzyme Imm, pp. 229–240.

[203] R. Armisén, „Agar and agarose biotechnological applications“, *Hydrobiologia*, vol. 221, no. 1, pp. 157–166, 1991.

[204] R. Greifenstein, T. Ballweg, T. Hashem, E. Gottwald, D. Achauer, F. Kirschhöfer, M. Nusser, G. Brenner-Weiß, E. Sedghamiz, W. Wenzel, E. Mittmann, K. S. Rabe, C. M. Niemeyer, M. Franzreb, and C. Wöll, „MOF-hosted enzymes for continuous flow catalysis in aqueous and organic solvents“, *Angewandte Chemie International Edition*, 2022.

[205] C. A. Bonino, J. E. Samorezov, O. Jeon, E. Alsberg, and S. A. Khan, „Real-time in situ rheology of alginate hydrogel photocrosslinking“, *Soft Matter*, vol. 7, no. 24, pp. 11 510–11 517, 2011.

[206] L. Wenger and J. Hubbuch, „Investigation of lysozyme diffusion in agarose hydrogels employing a microfluidics-based UV imaging approach“, *Frontiers in Bioengineering and Biotechnology*, 2022.

[207] T. Jungst, W. Smolan, K. Schacht, T. Scheibel, and J. Groll, „Strategies and Molecular Design Criteria for 3D Printable Hydrogels“, *Chemical Reviews*, vol. 116, no. 3, pp. 1496–1539, 2016.

[208] Y. Gu, L. Zhang, X. Du, Z. Fan, L. Wang, W. Sun, Y. Cheng, Y. Zhu, and C. Chen, „Reversible physical crosslinking strategy with optimal temperature for 3D bioprinting of human chondrocyte-laden gelatin methacryloyl bioink“, *Journal of Biomaterials Applications*, vol. 33, no. 5, pp. 609–618, 2018.

[209] I. T. Ozbolat, H. Chen, and Y. Yu, „Development of 'Multi-arm Bioprinter' for hybrid biofabrication of tissue engineering constructs“, *Robotics and Computer-Integrated Manufacturing*, vol. 30, no. 3, pp. 295–304, 2014.

[210] B. MacCallum, E. Naseri, H. Butler, W. MacNevin, R. A. Tasker, and A. Ahmadi, „Development of a 3D bioprinting system using a Co-Flow of calcium chloride mist“, *Bioprinting*, no. August 2019, e00085, 2020.

[211] S. Wüst, M. E. Godla, R. Müller, and S. Hofmann, „Tunable hydrogel composite with two-step processing in combination with innovative hardware upgrade for cell-based three-dimensional bioprinting“, *Acta Biomaterialia*, vol. 10, no. 2, pp. 630–640, 2014.

[212] B. Mao, T. Divoux, and P. Snabre, „Normal force controlled rheology applied to agar gelation“, *Journal of Rheology*, vol. 60, no. 3, pp. 473–489, 2016.

[213] M. M. Laronda, A. L. Rutz, S. Xiao, K. A. Whelan, F. E. Duncan, E. W. Roth, T. K. Woodruff, and R. N. Shah, „A bioprosthetic ovary created using 3D printed microporous scaffolds restores ovarian function in sterilized mice“, *Nature Communications*, vol. 8, no. May, pp. 1–10, 2017.

[214] D. Chimene, K. K. Lennox, R. R. Kaunas, and A. K. Gaharwar, „Advanced Bioinks for 3D Printing: A Materials Science Perspective“, *Annals of Biomedical Engineering*, vol. 44, no. 6, pp. 2090–2102, 2016.

[215] M. Tako and S. Nakamura, „Gelation mechanism of agarose“, *Carbohydrate Research*, vol. 180, pp. 277–284, 1988.

[216] K. te Nijenhuis, „Advances in Polymer Science Thermoreversible Networks“, *Advances in Polymer Science*, vol. 130, pp. 194–202, 1997.

[217] E. Fernández, D. López, C. Mijangos, M. Duskova-Smrckova, M. Ilavsky, and K. Dusek, „Rheological and Thermal Properties of Agarose Aqueous Solutions and Hydrogels“, *Journal of Polymer Science, Part B: Polymer Physics*, vol. 46, pp. 322–328, 2007.

[218] H. H. Selby and R. L. Whistler, „Agar“, in *Industrial Gums: Polysaccharides and Their Derivatives: Third Edition*, R. L. Whistler and J. N. Bemiller, Eds., Third Edit, Academic Press, 1993, ch. Agar, pp. 87–103.

[219] N. Zhang, J. Wang, J. Ye, P. Zhao, and M. Xiao, „Oxyalkylation modification as a promising method for preparing low-melting-point agarose“, *International Journal of Biological Macromolecules*, vol. 117, no. 2017, pp. 696–703, 2018.

[220] S. Arnott, A. Fulmer, W. E. Scott, I. C. Dea, R. Moorhouse, and D. A. Rees, „The agarose double helix and its function in agarose gel structure“, *Journal of Molecular Biology*, vol. 90, no. 2, pp. 269–284, 1974.

[221] B. Schmieg, M. Nguyen, and M. Franzreb, „Simulative Minimization of Mass Transfer Limitations Within Hydrogel-Based 3D-Printed Enzyme Carriers“, *Frontiers in Bioengineering and Biotechnology*, vol. 8, no. April, pp. 1–13, 2020.

[222] M. Maaloum, N. Pernodet, and B. Tinland, „Agarose gel structure using atomic force microscopy: Gel concentration and ionic strength effects“, *Electrophoresis*, vol. 19, no. 10, pp. 1606–1610, 1998.

[223] B. Amsden, „Solute diffusion within hydrogels. Mechanisms and models“, *Macromolecules*, vol. 31, no. 23, pp. 8382–8395, 1998.

[224] N. Kusukawa, M. V. Ostrovsky, and M. M. Garner, „Effect of gelation conditions on the gel structure and resolving power of agarose-based DNA sequencing gels“, *Electrophoresis*, vol. 20, no. 7, pp. 1455–1461, 1999.

[225] Z. H. Mohammed, M. W. Hember, R. K. Richardson, and E. R. Morris, „Kinetic and equilibrium processes in the formation and melting of agarose gels“, *Carbohydrate Polymers*, vol. 36, no. 1, pp. 15–26, 1998.

[226] N. R. Mohamad, N. H. C. Marzuki, N. A. Buang, F. Huyop, and R. A. Wahab, „An overview of technologies for immobilization of enzymes and surface analysis techniques for immobilized enzymes“, *Biotechnology and Biotechnological Equipment*, vol. 29, no. 2, pp. 205–220, 2015.

[227] P. Zucca, R. Fernandez-Lafuente, and E. Sanjust, „Agarose and its derivatives as supports for enzyme immobilization“, *Molecules*, vol. 21, no. 11, pp. 1–25, 2016.

[228] H. P. Erickson, „Size and shape of protein molecules at the nanometer level determined by sedimentation, gel filtration, and electron microscopy“, *Biological Procedures Online*, vol. 11, no. 1, pp. 32–51, 2009.

[229] K. C. Labropoulos, D. E. Niesz, S. C. Danforth, and P. G. Kevrekidis, „Dynamic rheology of agar gels: Theory and experiments. Part II: Gelation behavior of agar sols and fitting of a theoretical rheological model“, *Carbohydrate Polymers*, vol. 50, no. 4, pp. 407–415, 2002.

6

Automated and Dynamic Extrusion Pressure Adjustment Based on Real-Time Flow Rate Measurements for Precise Ink Dispensing in 3D Bioprinting

Lukas Wenger[1*], Svenja Strauß[2*] and Jürgen Hubbuch[1,2]

[1] Institute of Engineering in Life Sciences, Section IV: Biomolecular Separation Engineering, Karlsruhe Institute of Technology (KIT), Karlsruhe, Germany

[2] Institute of Functional Interfaces, Karlsruhe Institute of Technology (KIT), Eggenstein-Leopoldshafen, Germany

[*] Contributed equally

Abstract

Extrusion-based printing relying on pneumatic dispensing systems is the most widely employed tool in bioprinting. However, standardized and reliable methods for process development, monitoring and control are still not established. Suitable printing parameters are often determined in a trial-and-error approach and neither process monitoring nor real-time adjustments of extrusion pressure to environmental and process-related changes are commonly employed.

The present study evaluates an approach to introduce flow rate as a main process parameter to monitor and control extrusion-based bioprinting. An experimental setup was established by integrating a liquid flow meter between the cartridge and nozzle of a pneumatically driven bioprinter to measure the actual flow of dispensed ink in real-time. The measured flow rate was fed to a Python-based software tool implementing a proportional-integral-derivative (PID) feedback loop that automatically and dynamically adapted the extrusion pressure of the bioprinter to meet a specified target flow rate.

The performance of the employed experimental setup was evaluated with three different model inks in three application examples. a) Continuous dispensing: Several runs of continuous dispensing showed that the PID-based pressure control was able to generate a steady flow rate more consistently and precisely than constant pressure settings. b) Adaptation to ink inhomogeneities: Deliberately created ink inhomogeneities were successfully compensated for by real-time pressure adjustments which profoundly enhanced the printing quality compared to printing without adaptive pressure. c) Process transfer to other nozzle types: Experiments with different nozzle types demonstrated the potential of the established setup to facilitate and accelerate process transfer and development.

The present study provides an alternative approach for process design, monitoring and control by introducing flow rate as a main process parameter. We propose bioprinting processes to be based on flow rate specifications instead of constant pressure settings. This approach has the potential to save time by avoiding tedious parameter screenings and to introduce an active, real-time control over the printing process. Subjective influences by individual users during process development can be reduced and the process transfer between different devices and experimental setups can be facilitated and accelerated.

6.1 Introduction

Additive manufacturing, or 3D printing, is a collective term for a variety of fabrication techniques to produce three-dimensional objects by gradually adding material in a layer-by-layer buildup process [15]. 3D printing is already established in areas like mechanical engineering and the aerospace industry and is increasingly spreading into other fields like biotechnology [46, 230–232]. Novel applications in disciplines such as tissue engineering [72], smart materials [233] or bioprocess engineering [100, 193] already show the potential of this technique. Tissue engineering aims at designing artificially made and functional substitutes to restore, maintain or support the function of natural tissues [234]. The fabrication of such substitutes requires the embedding of living cells within a supporting matrix material mimicking the natural environment of living tissue [101]. Hydrogels are typically chosen for that purpose due to their aqueous nature and high biocompatibility [101]. Another common application for hydrogels is the immobilization of enzymes by physical entrapment [91]. Hydrogels or hydrogel precursor solutions are often employed in bioprinting, an interdisciplinary

field combining 3D printing and biofabrication with the objective to print biologically functional constructs like living tissues [73]. In this context, the hydrogel precursor solutions are typically referred to as *bioinks* when containing living cells, or as *biomaterial inks* if they are cell-free [235]. Depending on the field of application and the printing method, bioinks need to meet certain criteria like cytocompatibility, specific rheological properties and the ability for crosslinking [73]. To meet these requirements, bioinks are often hybrid materials containing several components like polymers, rheological additives and crosslinkable components. The polymers can be synthetic, e. g. based on polyethylene glycol (PEG) or poloxamer, or naturally derived, e. g. based on agarose, alginate, chitosan, hyaluronic acid, fibrin, or collagen. Depending on the intended use, the polymers can be chemically modified and, for example, ligands for cell adhesion can be incorporated. The polymers can be crosslinked physically, chemically, thermally, enzymatically or by photopolymerization [70, 236]. Certain hydrogels, e. g. based on poloxamer, are also used as a sacrificial support material that is removed after printing [237].

In bioprinting, a variety of methods like inkjet-, laser- or stereolithography-based bioprinting is available. The most common method, especially in cell-based printing, is extrusion-based bioprinting (EBB) [73] which relies on a steady flow of material being dispensed from a cartridge. EBB methods can be classified by the employed dispensing system which can be based on pneumatic or mechanical extrusion, with each method having different advantages and disadvantages [72, 73]. Pneumatic systems use pressurized air to extrude material, while mechanical systems are driven by a piston or a screw [73]. Piston-based systems theoretically allow a more precise control of the extruded volume as the flow rate is directly correlated to the movement of the piston and the cartridge dimensions. The flow rate can be set independently of the material by defining the piston speed, but there is a tendency of lagging leakage at the end of an extrusion process which can be counteracted by retracting the piston or adding a valve [74, 75]. Screw-based systems allow excellent control of the extruded volume, but cleaning the system is tedious and often accompanied by a high loss of material due to dead volume [76]. This may be problematic when working with costly bioinks and slowly growing cells. The screw-driven mechanism induces higher shear forces which can result in increased cell damage, depending on the design of the screw and the printing conditions [77].

Pneumatic dispensing is widely employed due to its simplicity [72], but it is prone to delays due to the compression of gas volume within the cartridge which can reduce the printing precision [68, 70]. In pneumatic dispensing systems, the resulting flow rate cannot be controlled directly, as it is not only dependent on the applied pressure, but also on the rheological properties of the bioink and the components of the experimental setup like the nozzle. This makes the method susceptible to unintended variations of the experimental conditions. Therefore, environment-related parameters like temperature or humidity, system-related parameters like cartridge fill level, or material-related parameters, such as inhomogeneities or batch-to-batch variations of the bioinks, can have a relevant effect on the generated flow rate and hence the outcome of the printing process [238–242]. Compensating for such variations may require a change in extrusion pressure to achieve the desired flow rate. However, the most common approach to bioprinting process development is to define constant printing parameters or working windows either systematically or by trial and error [239, 242, 243]. These approaches are usually based on indirect parameters like rheological properties of inks [239] or qualitative aspects like filament formation [107]. Other methods include the analysis of strand widths [244] or filament fusion [242] by structural image analysis. In order to handle variations of bioink properties or environmental conditions, all these approaches may require parameter screenings before performing a printing run, depending on the robustness of

the process. An alternative approach is to reduce the environmental variations to a minimum by placing the bioprinter in a temperature- and humidity-controlled environment [245]. However, both strategies cannot equally handle both batch-to-batch variations of the bioink and time-dependent environmental changes.

Direct real-time monitoring of bioprinting processes is relatively uncommon, but previous studies have shown that liquid flow sensors can be employed to monitor the flow rate during bioprinting and to observe batch- and time-related changes in the relation of pressure and flow [246, 247]. Flow sensors are currently used for industrial applications in the automotive, oil and gas industry, but also in the food and beverage and pharmaceutical industry [248–254]. A range of different flow sensors are available which can be classified based on the employed measurement principle. Thermal flow sensors derive the flow rate from the travel time of heat pulses or the temperature profile around a heater [255]. Non-thermal sensors are based on other physical principles [255]. Today, very small flow meters can be produced with many advantages such as a lack of moving parts, better dynamic characteristics, low power consumption, low cost and easier integration into other systems [256]. Progress in the production of microelectromechanical systems allowed the development of micromachined thermal flow sensors which can be applied in the medical field to monitor blood and respiratory flow or drug delivery [252, 257, 258].

While it has been shown that flow sensors can be employed in bioprinting for process monitoring [247], there is still no demonstration of how to use the flow data obtained during extrusion in order to dynamically adapt the pressure and create a steady flow, independent of interference factors like temperature, cartridge fill level and other parameters. The present work introduces an experimental setup including a liquid flow sensor as a part of a feedback-loop controlling the pressure of a pneumatically driven bioprinter. A Python-based software tool is developed to read and record the sensor data and to generate a steady flow rate by continuously adapting the pressure based on on a proportional-integral-derivative (PID)-controlled feedback loop. The developed setup is tested with three different model inks, two of which are based on the synthetic polymer poloxamer 407 (also known as Pluronic®F-127 or Kolliphor®P407) in different concentrations. Poloxamer 407 inks are suitable model inks due to their excellent printability and simple preparation [237, 239, 259]. Additionally, an ink based on the natural polymer alginate and the additive Laponite® RD is investigated. Alginate is a very common component of bioinks due to its gelling properties [260–263] and Laponite® RD is typically employed as an inorganic filler to increase viscosity and enhance printability [100, 264, 265]. The performance of the employed adaptive pressure control setup was investigated in three application examples. a) Continuous dispensing: The general behavior of the flow sensor and the ability of the PID control to generate a constant flow were tested using continuous dispensing runs. b) Adaptation to ink inhomogeneities: The suitability for realistic printing applications was tested by printing from a cartridge with an intentionally inhomogeneous ink created by alternating layers of poloxamer 407 inks of different concentrations. c) Process transfer to other nozzle types: As an example for process transfer, the ability of the setup to adapt to different nozzle types was tested. An overview of the employed workflow is depicted in Figure 6.1.

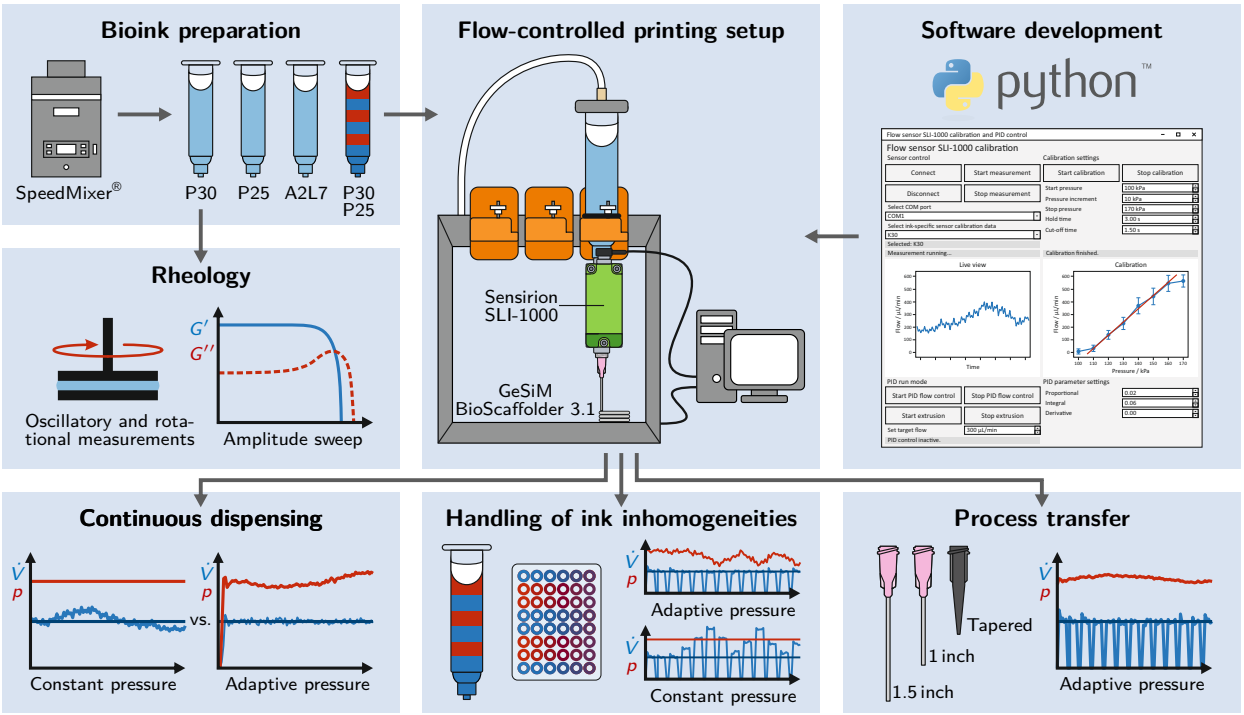

Figure 6.1 Schematic of the workflow applied in the present study. Three different inks are prepared and analyzed with rheological methods. A Python-based software tool is developed that implements a PID control loop to continuously adapt the extrusion pressure of a pneumatic bioprinter based on real-time data from a liquid flow meter. The integrated PID control setup is evaluated in three separate application examples.

6.2 Materials and methods

6.2.1 Ink preparation

Sodium alginate and poloxamer 407 were both obtained from Sigma Aldrich (St. Louis, USA) and Laponite® RD from BYK-Chemie GmbH (Wesel, Germany). Three different inks were prepared by dissolving the appropriate amounts of the respective components in ultrapure water (arium® pro VF, Satorius AG, Göttingen, Germany) and mixing at 3500 rpm in a SpeedMixer® (Hauschild GmbH & Co. KG, Hamm, Germany), until a homogenous mixture was obtained. Poloxamer-based inks were cooled in an ice bath between mixing steps to increase solubility. Three different ink compositions were prepared, the first one containing 30 % (w/w) poloxamer 407 (P30), the second one 25 % (w/w) poloxamer 407 (P25) and the third one 2 % (w/w) sodium alginate with 7 % (w/w) Laponite® RD (A2L7). An overview of the employed inks and their components is given in Table 6.1. The prepared inks were filled into 10 mL cartridges (Nordson Corporation Westlake, USA) and centrifuged at 600 g for 10 min to minimize the amount of entrapped air bubbles. The cartridges were sealed with pneumatic pistons (Nordson Corporation Westlake, USA) for printing.

Abbreviation	Poloxamer 407 (% (w/w))	Alginate (% (w/w))	Laponite® RD (% (w/w))	Extrusion pressure (kPa)
P30	30	—	—	436
P25	25	—	—	256
A2L7	—	2	7	329

Table 6.1 Ink compositions with the corresponding extrusion pressure, as employed for printing runs with a constant pressure setting. The pressure was determined from the first adaptive dispensing run with a 1 inch nozzle and a target flow rate of 300 µL/min by averaging the applied pressure over a period of 10 min.

6.2.2 Rheology

The rheological behavior of P30, P25, and A2L7 was investigated using the rheometer Physica MCR301 (Anton Paar GmbH, Graz, Austria). A setup with parallel stainless steel plates with a diameter of 25 mm was employed for all rheological experiments. The gap width was 150 µm and all measurements were performed at 20 °C as technical triplicates ($n = 3$).

Yield stress values were determined from shear stress-controlled rotational tests. The deformation was plotted against shear stress on a logarithmic scale. The yield stress was determined by fitting the two linear regions of the plot with tangents and calculating the shear stress at their point of intersection.

Oscillatory measurements were performed with controlled shear stress τ in a range of 1 to 1000 Pa at an angular frequency of $\omega = 10\,\mathrm{s}^{-1}$. For each measurement, the loss factor $\tan\delta = G''/G'$ was determined by averaging G' and G'' in the region from $\tau = 10$ Pa to $\tau = 100$ Pa which was within the linear viscoelastic (LVE) region and low in noise for each measurement.

6.2.3 Adaptive PID pressure control: hardware and software setup

The main objective of the present study was to establish a tool that enables flow-based process control for pneumatic extrusion-based bioprinting. The approach was to employ a software-based proportional-integral-derivative (PID) control that uses input data from a liquid flow meter to adapt the extrusion pressure of a pneumatic bioprinter in real-time. The components of the established setup and their interactions are described in the following sections.

6.2.3.1 Hardware configuration

All conducted dispensing and printing experiments were performed on a BioScaffolder 3.1 bioprinter (GeSiM mbH, Radeberg, Germany) with three pneumatic extrusion heads. An SLI-1000 liquid flow meter (Sensirion, Stäfa, Switzerland) was employed to measure the flow rate of inks during printing. The SLI-1000 contains a straight glass capillary with an inner diameter of 1 mm and is specified for flow rates up to 1000 µL/min with water. The sensor relies on calorimetric sensing, a measurement principle that derives flow rates from thermal profiles forming around a heating element depending on the current fluid flow [256]. In the case of the Sensirion SLI-1000, two thermal sensors are placed up- and downstream of the heating element to detect the thermal profile, as indicated in Figure 6.2A. The flow sensor was attached below one of the extrusion heads of the

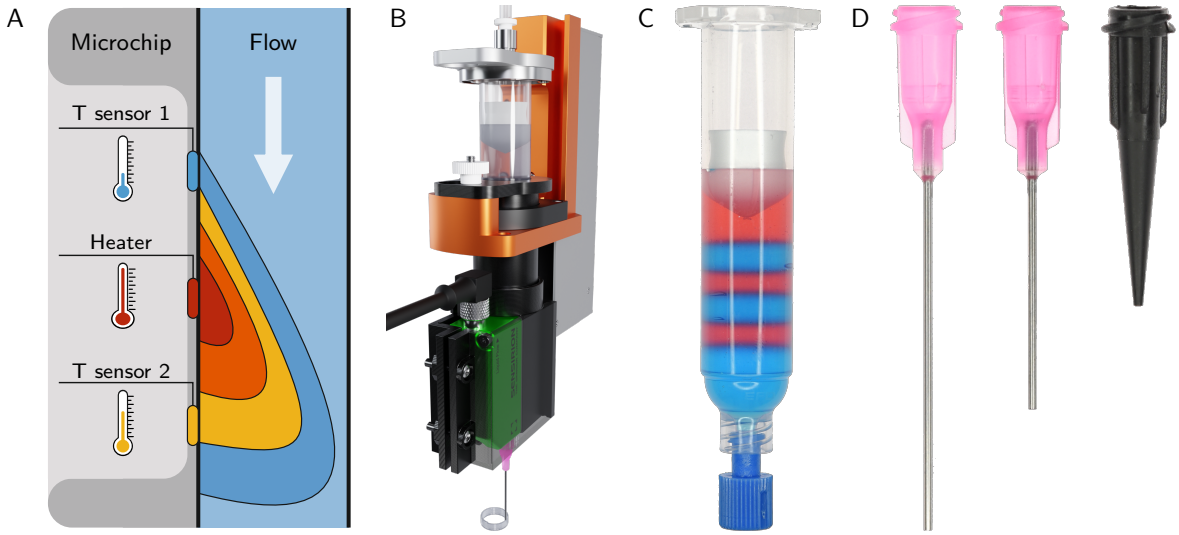

Figure 6.2 (A) Schematic representation of the thermal measuring principle of the liquid flow meter. Adapted from Schnell *et al.* [266] and Kuo *et al.* [256]. (B) 3D visualization of the arrangement of the hardware components of the PID control setup. The sensor is attached below the extrusion head of the bioprinter using a 3D-printed mount. The right part of the mount is shown as transparent to reveal the flow sensor. A cartridge is connected to the sensor inlet on the top, a nozzle to the outlet at the bottom. The CAD file of the sensor was obtained from Sensirion [267]. (C) Printer cartridge filled with alternating layers of P30 (blue) and P25 (red). The layered material served as a performance test for the PID-controlled printing setup. (D) Dispensing tips used in this study, from left to right: 1.5 inch straight nozzle, 1 inch straight nozzle, tapered nozzle. All nozzles had an orifice diameter of 0.58 mm. Depending on length and geometry, even dispensing tips with identical orifice diameter can generate massively different back pressures.

BioScaffolder using a customized, 3D-printed mount. A USB cable enabled the communication between flow sensor and computer via RS485 interface.

The arrangement of the components allowed a cartridge to be directly attached to the inlet on the upper side of the liquid flow meter and a nozzle to the outlet at the bottom side. The setup reduced the amount of available space in the z-direction, but otherwise enabled unrestricted printing. Figure 6.2B shows the employed setup while printing a hollow cylinder.

6.2.3.2 Software development

A software tool based on Python 3.8.5 (Python Software Foundation, Delaware, USA) was developed to integrate the liquid flow meter and the pneumatic extrusion bioprinter into a PID-controlled feedback loop that constantly adapts the extrusion pressure to keep the resulting ink flow at a constant target value. A scheme representing all the components involved in the PID control and their interactions is shown in Figure 6.3. In short, the user sets the target flow rate and PID parameters using a graphical user interface (GUI). The Python-based software receives real-time data from the liquid flow meter which is converted to flow rate values using imported calibration curves. To generate the desired target flow rate, the software-based PID control constantly adapts

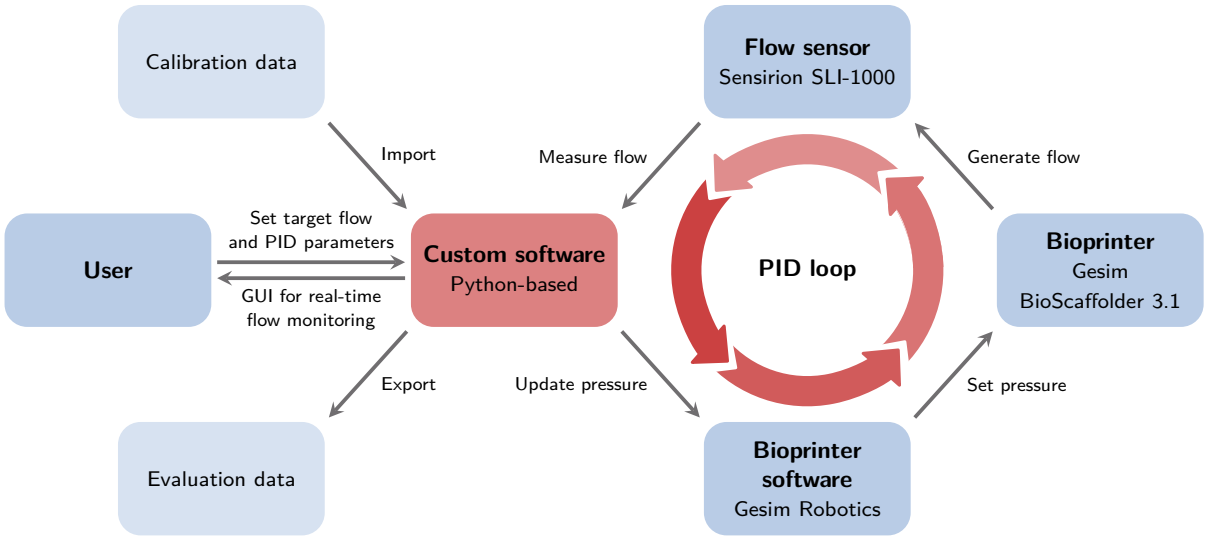

Figure 6.3 Schematic of the interactions between the relevant components of the PID control setup.

the pressure by sending commands to the GeSiM Robotics software which controls the GeSiM BioScaffolder. The flow rate and pressure settings are stored and exported for later evaluation.

Graphic user interface For easy interaction with the user, a graphical user interface (GUI) was developed that allowed controlling the flow sensor, performing calibrations and adjusting the PID control. Figure 6.4 shows the GUI of the developed Python tool with the GUI of the GeSiM Robotics software in the background. The GUI was split in several sections. The top left section provided the flow sensor control panel including buttons to connect and disconnect and to start and stop measurements. The COM port of the flow sensor and the appropriate ink calibration could be selected from drop-down menus. Depending on the selection, the ink-specific calibration data necessary to convert the sensor output to flow values were loaded from an external Excel file. Section 6.2.4.1 describes how the calibration data were generated using a syringe pump and an adapted version of the Python tool. Below the sensor control panel, the GUI showed a graph with a live view of the current flow measurement.

Another control panel to perform pressure-flow calibrations was located in the top right part of the GUI, accompanied by an additional graph showing the determined calibration points with the respective calibration curve. This feature allows determining the correlation between applied pressure and resulting flow rate for a specific ink and experimental setup. Within the scope of this paper, this feature was not applied but it may be used to characterize the flow behavior of inks under certain conditions. The bottom part of the GUI accommodated the PID control panel including buttons to start and stop the PID control and the extrusion process. Input fields allowed setting the target flow rate and the PID parameters.

Device communication Communication between the Sensirion SLI-1000 liquid flow meter and Python could be established by customizing code provided by Sensirion. The code was based on the *pySerial* package (version 3.5) which enables communication over the serial port. While running,

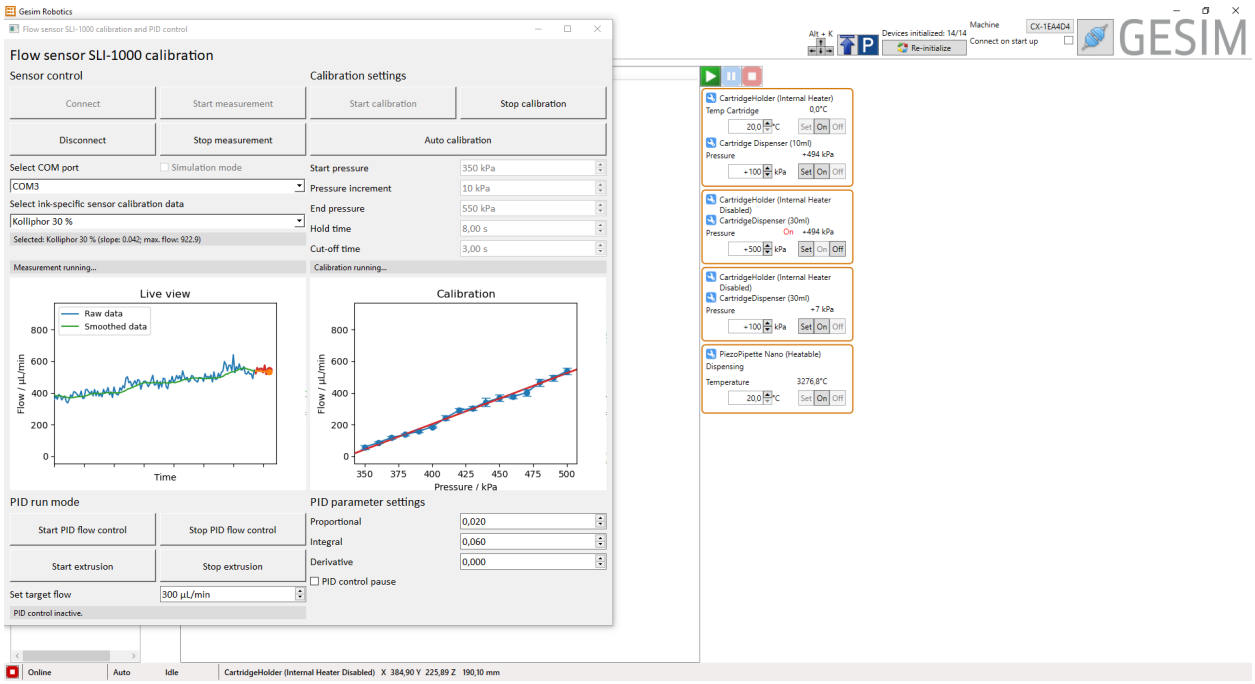

Figure 6.4 Screenshot of the graphical user interface of the Python-based PID control tool. The example shows the calibration of the ink P30. The left graph represents a live view of the flow measurement data, the right graph shows data points obtained during the calibration. The GeSiM Robotics software being automatically operated by the Python tool is visible in the background.

the software constantly read out the current flow from the liquid flow meter at a rate of roughly five readings per second. During printing processes, the pressure is frequently turned on and off when switching from one strand or layer to the next. These switching operations are accompanied by a drop in flow rate that is irrelevant to the PID control. To ignore these irrelevant data points, only flow rate values larger than 3 % of the sensor output limit were regarded as valid. To ignore spikes in flow rate that sometimes occurred with the switching operations, all data points deviating from the previous data point by more than 20 % relative to the sensor output limit were regarded as invalid. Besides the raw flow rate data, an additional curve with smoothed data was plotted in the live view of the GUI. The smoothed data was obtained by determining a rolling average over the last 15 valid data points.

Direct communication between Python and the BioScaffolder 3.1 allowing real-time changes in pressure could not be established. As a workaround, the GeSiM Robotics software controlling the BioScaffolder was automatically operated by Python to trigger pressure changes. For this purpose, the *PyAutoGUI* package (version 0.9.52) was employed that allows performing automated operations on third-party GUIs like clicking buttons or entering text into input fields. This workaround allowed controlling the extrusion pressure of the BioScaffolder indirectly via Python, even during an active printing process.

PID-based pressure control The software-based PID control loop was implemented in Python using the package *simple-pid* (version 0.2.4). In the active state, the PID loop was fed every

Table 6.2 Proportional, integral and derivative gain, as applied for all experiments involving the PID control for automatic pressure adjustment.

Gain parameter	Value
K_p (proportional)	0.02
K_i (integral)	0.06
K_d (derivative)	0.00

0.25 s with the last valid data point and the pressure in the Gesim Robotics software was updated every 0.5 s based on the output of the PID loop. Suitable PID control parameters (proportional, integral and derivative gain) were determined iteratively by trial-and-error and kept constant for all performed experiments, as shown in Table 6.2.

The applied PID algorithm of the *simple-pid* package is based on the controller output function

$$u(t) = K_p e(t) + K_i \int_0^t e(t)dt + K_d \frac{de(t)}{dt} \tag{6.1}$$

with the gain parameters K_p (proportional), K_i (integral) and K_d (derivative) and the error term

$$e(t) = r(t) - y(t) \tag{6.2}$$

where $r(t)$ is the reference input and $y(t)$ is the process variable [268, 269]. In the given case, $u(t)$ is used as an input variable for the printer to set the current extrusion pressure, $r(t)$ is the set point of the flow rate for the PID control and $y(t)$ is the flow rate measured by the flow sensor. The integration of the PID controller within the experimental setup and the interaction between the components and their respective input and output variables is schematically shown in Figure 6.5.

6.2.4 Application of the adaptive pressure control

6.2.4.1 Flow sensor calibration

The employed liquid flow meter SLI-1000 determines flow rates indirectly from heat distribution profiles within the fluid [270]. As such, it is substantially influenced by the specific thermal conductivity properties of the specific fluid [256] and requires individual calibrations when working with a variety of inks. Accordingly, calibration curves were determined for P30, P25 and A2L7 that allowed converting the sensor output data to flow rate values. To generate a defined volumetric flow rate through the SLI-1000 liquid flow meter, a Nemesys 290N syringe pump with a 10 mL syringe (both Cetoni GmbH, Korbußen, Germany) was employed. A slightly adapted version of the described Python software tool was applied to record the output data of the sensor and to adjust the syringe pump to different flow rates by operating the control software of the syringe pump (QmixElements, version 20140605). A screenshot of the software tool and the QmixElements software is shown in the supplementary material. Data points for the calibration curves were determined by setting a fixed flow rate for 30 s and determining the mean value of the sensor output of the last 20 s of this period. The flow rate was increased step-wise, until the sensor output limit was reached. The obtained data points were fitted with a linear equation. The resulting calibration curves are shown

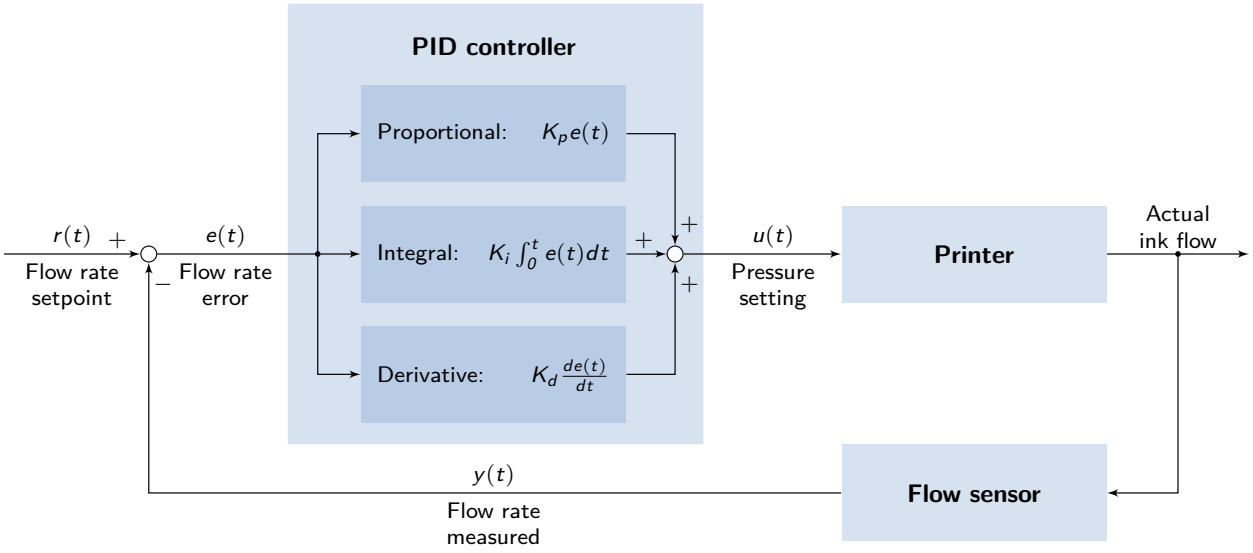

Figure 6.5 Schematic block diagram of the employed PID feedback loop showing the interaction between printer, flow sensor and PID controller in combination with the respective input and output variables. Scheme adapted from [268, 269].

in the supplementary material and the equation parameters were stored in an Excel file that served as an input for the Python-based PID software tool.

6.2.4.2 Continuous dispensing

Continuous dispensing runs were performed as an initial performance test of the adaptive pressure control. For each ink, three runs were carried out with active PID control and three runs with a constant pressure setting ($n = 3$). Ink was dispensed from a 10 mL cartridge continuously for 30 min through a 1 inch straight nozzle with an inner orifice diameter of 0.58 mm (Vieweg GmbH, Kranzberg, Germany, see Figure 6.2D). During the runs with adaptive pressure, a target flow rate of 300 µL/min was specified and the pressure was continuously adapted by the Python-based PID control tool described in Section 6.2.3.2. The applied pressure of the first run with adaptive pressure control was averaged over a period of 10 min and used as the pressure setting of the runs with constant pressure. The obtained constant pressure settings are presented in Table 6.1.

6.2.4.3 Adaptation to ink inhomogeneities

To verify the capability of the PID control to generate a constant flow independent of changing rheological properties of the ink, two cartridges were filled with alternating layers of P30 and P25. In order to highlight the different layers optically, P30 was spiked with blue and P25 with red food coloring. Before the cartridge was filled, the inks were liquefied by cooling to allow the handling with pipettes. After addition to the cartridge, each layer was allowed to solidify at room temperature, before the next layer was added. At the bottom of the cartridge was a layer of 2 mL P30, followed by 4 alternating 1 mL layers of P25 and P30, and at the top was a 2 mL layer of P25. A photograph of one of the cartridges is shown in Figure 6.2C.

Hollow cylinders with a diameter of 10 mm and a height of 3 mm were printed as simple test objects onto a glass plate heated to 35 °C to avoid ink spreading. The layer height of the cylinders was 300 µm and the printing speed 10 mm/s. All prints were carried out with a straight 1 inch nozzle with an inner orifice diameter of 0.58 mm. One cartridge was used for each printing run. To evaluate the performance of the adaptive pressure control, the first run was performed with active adaptive pressure control and a target flow rate of 300 µL/min. Before starting the printing process, the adaptive pressure control was run for 30 to 60 s, until a constant flow was reached. The second printing was carried out with a constant pressure of 436 kPa which was determined to be suitable for P30 during the continuous dispensing runs (see Table 6.1).

6.2.4.4 Process transfer to other nozzle types

To investigate whether a flow rate-based process control facilitates the process transfer between different nozzle types, additional prints of hollow cylinders were carried out with the already employed 1 inch straight nozzle, a 1.5 inch straight nozzle and a tapered nozzle, all with an inner orifice diameter of 0.58 mm and obtained from Vieweg GmbH. The three nozzle types are depicted in Figure 6.2D. Again, runs with adaptive pressure control were compared to runs with fixed extrusion pressure. With every run, two 3 mm high cylinders with a diameter of 10 mm and a layer height of 300 µm were printed at a speed of 10 mm/s on a plate heated to 35 °C. Before the runs with adaptive pressure control, the target flow rate was set to 300 µL/min and the adaptive pressure control was run for 30 to 60 s, until a constant flow was reached. The runs with constant pressure setting were carried out with the pressure that was determined to be suitable for the respective ink in combination with the 1 inch straight nozzle during the continuous dispensing runs (see Table 6.1).

6.3 Results and discussion

6.3.1 Implementation of the experimental setup

As the application of flow sensors is not not an established practice in 3D bioprinting, a customized setup was designed to implement a Sensirion SLI-1000 liquid flow meter on a GeSiM BioScaffolder 3.1 bioprinter. As shown in Figure 6.2B, the flow sensor was attached between the cartridge and the nozzle using a 3D-printed mount which allowed fast and easy assembly. However, the arrangement added a certain amount of complexity and some disadvantages to the experimental setup. The height of the sensor of 53 mm caused a reduction of available space in the z-direction despite the cartridge being mounted above its default location. The capillary of the sensor and the required Luer lock adapters added some dead volume which may be problematic when working with costly bioinks and sterile operation of the setup was made more difficult. These disadvantages can largely be attributed to the lack of optimization of the established setup. The employed flow sensor was neither optimized for the use with hydrogels, nor for the interoperability with a bioprinter. A more wide-spread application of flow sensors in bioprinting would require targeted adaptations like a reduction in size and cost. Smaller sensors with Luer locks would reduce both space requirements and dead volumes. Lower cost could enable the use of flow sensors as disposable products to simplify sterile operation.

The calibration of the flow sensor with different inks revealed a strong influence of the material on the measurements. The calibration curves for P30 and P25 could be fitted well ($R^2 = 0.9989$ and 0.9987) with an equation of the form $y = mx$, while A2L7 required an additional y-intercept

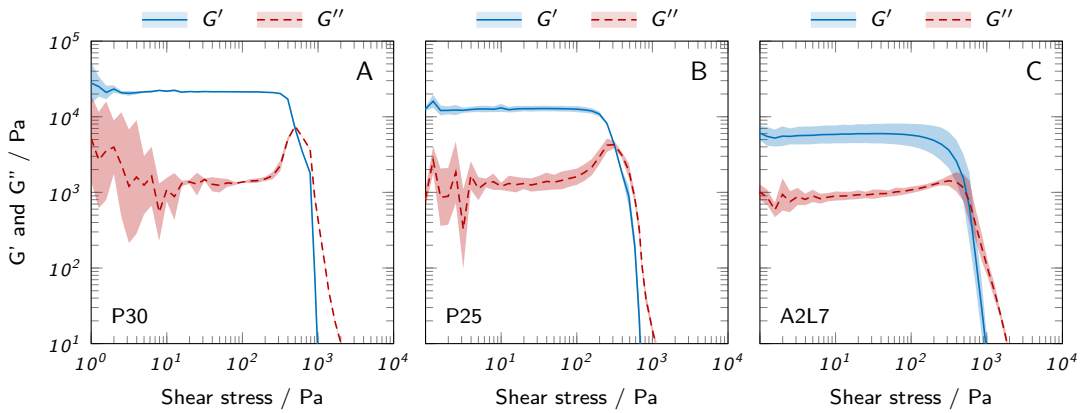

Figure 6.6 Shear stress-controlled oscillatory measurements showing the storage modulus G' and loss modulus G'' for all prepared inks at an angular frequency of $\omega = 10\,\mathrm{s}^{-1}$. The results are depicted as mean values, the shaded areas represent the standard deviation ($n = 3$).

($y = mx + c$) which led to invalid measurement values at low flow rates and has to be considered when assessing the validity of measurements.

6.3.2 Rheology

The rheological behavior of inks is one of the most relevant factors determining printability in extrusion-based bioprinting. The characteristics of the inks employed in this study were analyzed with oscillatory and rotational measurements. The storage and loss moduli (G' and G'') and the loss factor tan δ were determined in oscillatory measurements. Figure 6.6 shows the performed amplitude sweeps in a range of 1 to 10 000 Pa. For all samples, the storage modulus G' was higher than the loss modulus G'' within the linear viscoelastic region, indicating a gel-like behavior for all investigated inks. The exact ratio of G' an G'' is expressed in the loss factor $\tan\delta = G''/G'$ and was derived from the same measurements. The resulting values of tan δ are shown in Figure 6.7, alongside the yield stress values determined in rotational measurements. Gel-like behavior is implied by $\tan\delta < 1$ and lower values indicate a stronger dominance of elastic properties over viscous properties [241]. The lowest tan δ was found for P30 with 0.060 ± 0.006 and the highest for A2L7, but all samples were below $\tan\delta = 0.17$ showing a strong dominance of elastic properties. The same trends are represented in the yield stress which was highest for P30 at (861 ± 32) Pa and lowest for A2L7 at (474 ± 5) Pa. A yield point could be detected for all inks. The results demonstrate the general suitability of the employed inks for bioprinting applications, as they all showed gel-like behavior ($\tan\delta < 1$) and the presence of a yield point. High yield stress is an important factor determining printability [107], as it represents the ability of the ink to maintain its shape after extrusion.

6.3.3 Application of the adaptive pressure control

The performance of the presented setup for an adaptive PID pressure control was investigated employing three separate approaches. a) Continuous dispensing: To generally compare the resulting ink flow with and without adaptive pressure control, ink was continuously dispensed from a cartridge without printing any defined objects. The actual applicability of the setup in realistic scenarios

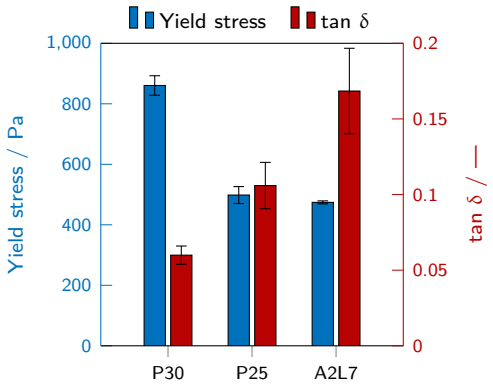

Figure 6.7 Yield stress, as determined from rotational measurements, and loss factor tan δ, as determined from oscillatory measurements, for all evaluated inks. The results show mean values $\pm$ standard deviation ($n = 3$).

was evaluated in two additional studies involving the printing of hollow cylinders as test objects. b) Adaptation to ink inhomogeneities: The ability to compensate for ink inhomogeneities by pressure adjustments was tested by printing from a cartridge with an intentionally inhomogeneous ink created by alternating layers of poloxamer 407 inks of different concentrations. c) Process transfer to other nozzle types: As an example for process transfer, the ability of the setup to adapt to nozzles with different lengths and geometries was investigated.

6.3.3.1 Continuous dispensing

The general capability of the real-time, adaptive pressure control to ensure a constant and reproducible ink flow was initially evaluated by simple, continuous dispensing runs. This approach allowed avoiding interference factors like pressure switching operations between printed layers. A separate ink-filled cartridge was used for each run and the ink was continuously dispensed for 30 min without printing any defined objects. Six runs were performed per ink, three with a constant pressure setting and three with the adaptive pressure control being active. Every run aimed at meeting a target flow of 300 µL/min. For the runs with adaptive pressure control, this could be achieved automatically without any preparatory work apart from the ink-specific flow sensor calibration to convert the sensor output to flow rate values. The continuous dispensing runs were then started with a pressure setting of 0 kPa and the pressure was automatically adapted by the PID control to an appropriate value within roughly 30 s. For the runs with constant pressure setting, a suitable pressure had to be determined first which was derived from the first adaptive run by averaging the applied pressure within a constant region over a period of 10 min. Flow measurements and pressure settings were recorded for the entire duration of each run.

Figure 6.8 shows the recorded flow rate and pressure for P30 over time. A slightly smoothed flow rate is depicted in light blue and represents a rolling average over 15 data points, only including the valid data points as defined in section 6.2.3.2 (absolute value $> 3\,\%$ of the sensor output limit and $< 20\,\%$ change compared to the previous data point, also relative to the sensor output limit). The target flow rate is indicated in dark blue. The graphs A-C show the results of dispensing ink with a constant pressure setting, the graphs D-F represent the runs with adaptive pressure control.

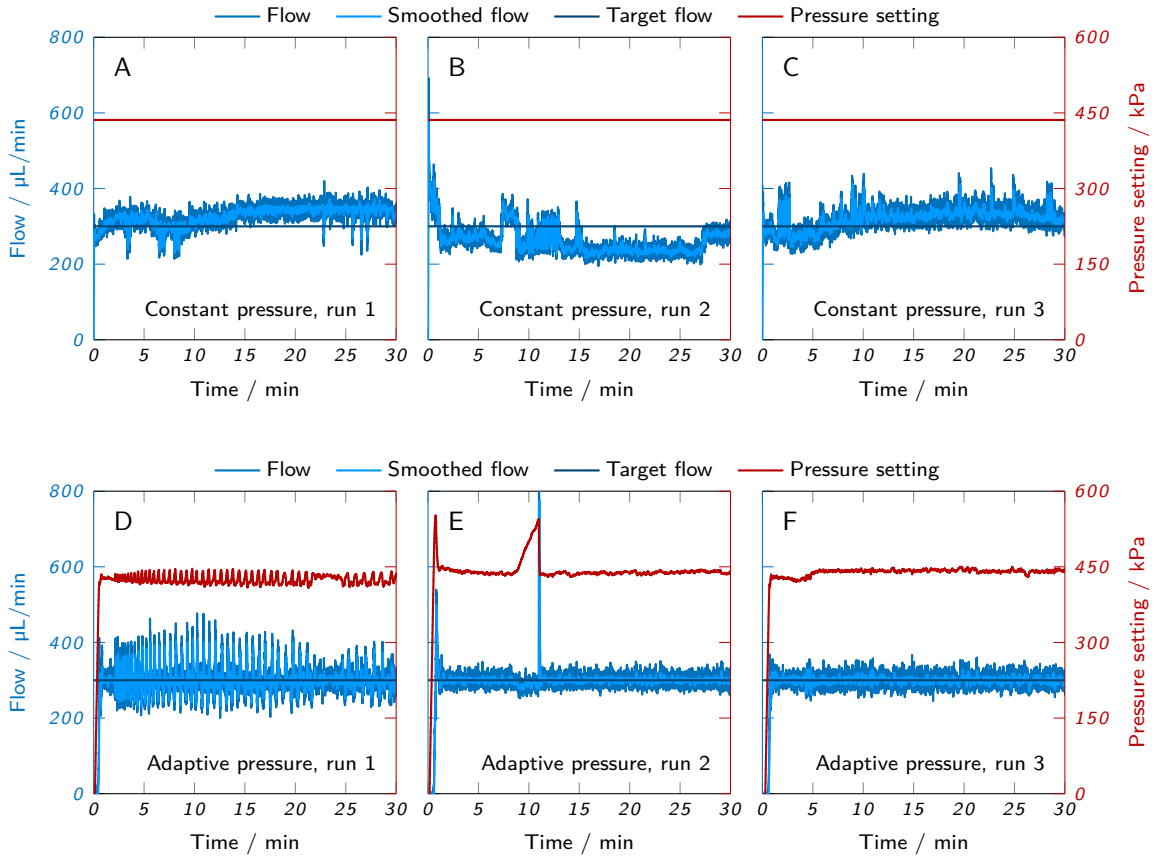

Figure 6.8 Continuous dispensing runs of P30. The measured flow and the pressure setting are plotted over time. (A-C) Runs with constant pressure setting are compared to (D-F) runs with adaptive PID pressure control and a target flow rate of 300 µL/min.

A certain level of relatively uniform noise (roughly ±50 µL/min) was observed for the flow data of all runs, apparently a phenomenon that is inherent to the measurement method in combination with the investigated inks. It should be noted that the flow sensor is not designed for hydrogels or complex material compositions and showed considerably less noise in combination with water (data not shown). This implies that a large proportion of the observed noise can be attributed to the non-homogeneous nature of the inks containing micelles (P30 and P25) [271] or nanoclay and polymers (A2L7). A noticeably different noise pattern was observed for the first adaptive run with P30 (Figure 6.8D), as the sensor noise was overlayed by additional fluctuations with higher amplitude and longer cycle length. These fluctuations also appeared in the recorded pressure settings indicating that they were not caused by measurement noise but by actual fluctuations of the applied pressure. The regularity of the fluctuations implies that the PID controller entered an oscillatory state, caused by repeatedly overshooting the desired set point and overcorrecting for it. This behavior can be counteracted by retuning the PID control loop, e. g. based on oscillatory characteristics or perturbation signals [272, 273]. The mostly stable amplitude of the oscillations after 5 min implies a marginally stable system. For the second and third run of P30 with adaptive pressure control (Figure 6.8E and F) and all runs with other inks, no oscillations occurred and the amount of noise corresponded to the runs with constant pressure setting, despite the same PID

parameters being applied. As the oscillatory behavior was only observed in one of nine runs, it was not interpreted as an inherent issue of the employed setup. However, it revealed a potential pitfall when working with PID-controlled systems and a more systematic tuning of the PID parameters could increase the stability of the system [273].

Besides noise, additional irregularities on a larger timescale could be observed in the flow signal of the P30 runs with constant pressure setting (Figure 6.8A-C). These irregularities did not follow a certain pattern, but seemed entirely erratic. A relatively similar behavior was observed for the first and third run. During the initial phase, the flow rate of both runs showed considerable variations that stabilized after 10 to 15 min at a flow rate of roughly 350 µL/min. Overall, the flow rate showed a slightly increasing trend and was mostly above the target flow. The second run showed erratic and sudden flow variations during the entire measurement, only with one relatively constant period between 15 min and 25 min where the flow was around 250 µL/min. Overall, the flow rate decreased during the run and was mostly below the target value. These results demonstrate that with regards to flow rate, both the consistency within a single run and the reproducibility between separate runs are limited when applying a constant pressure. Due to their erratic nature, no clear causes could be identified for the observed signal fluctuations and drifts. Potential influencing factors are ink inhomogeneities, temporary and partial nozzle clogging or manufacturing variations of cartridges and plugs [76, 238]. The trends of increasing or decreasing flow rate suggest possible time-dependent parameters like temperature drifts or the cartridge fill level.

A very different behavior was observed for the runs with adaptive pressure control (Figure 6.8D-F). Each run was started with a pressure setting of 0 kPa. The PID control was activated and performed the pressure adaptation automatically. The pressure was increased steadily, until the appropriate flow was achieved. This initial adaptation phase took roughly 30 to 60 s, before the pressure was stabilized at an appropriate level to generate a flow of 300 µL/min on average, corresponding to the desired target flow. For all three runs, the average flow was reliably kept constant for the whole duration of the measurement. However, as mentioned before, the first run showed considerable oscillations around the target value due to a suboptimal pressure regulation. In contrast, the second and third run achieved a similar amount of noise as the runs with constant pressure. During the second run (Figure 6.8E), a continuous pressure increase from roughly 440 kPa to 540 kPa occurred between 9 min and 11 min, accompanied by a minor drop in flow rate. After 11 min, the flow rate suddenly jumped to the output limit of the sensor causing the pressure to drop quickly back to the base level. As a result, the flow rate also returned to the target value. Apparently, a partial clogging of the nozzle occurred here that was appropriately counteracted by the PID control by increasing the pressure, resulting in only a minor and short-term drop of flow rate. This demonstrates the suitability of the adaptive pressure control to compensate for unpredictable and erratic influencing factors like ink inhomogeneities or nozzle clogging and keep the flow at a constant rate.

For a more compact overview and simple comparison of different inks, all runs performed are depicted as swarm plots in Figure 6.9. For P25 and A2L7, the corresponding plots of flow and pressure over time are shown in the supplementary material. Figure 6.9 shows every performed run as a separate swarm of data points. The width of the swarm indicates the kernel density estimation, i. e. the number of data points at the corresponding flow rate. Additionally, all data points are plotted on a color map indicating the time point of the measurement. Thus, trends like a changing flow rate over the course of the measurement can be recognized in the form of color gradients.

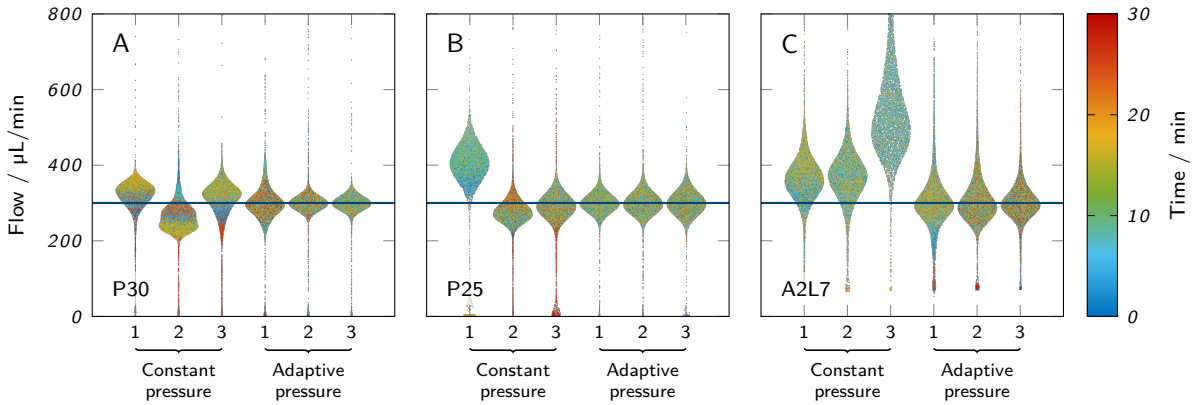

Figure 6.9 Overview of all performed continuous dispensing runs depicted as swarm plots. Each swarm represents the first 30 min of a run performed with (A) P30, (B) P25 or (C) A2L7. The blue horizontal line indicates the target flow rate.

The already discussed runs of P30 are shown in Figure 6.9A. The first three swarms represent the runs with constant pressure, two of which are located largely above the target flow, while one is located below. The color gradients of the swarms indicate that each of these runs was accompanied by a steady change in flow rate implying a time-dependent influencing factor, as discussed before. The inconsistent positioning above and below the target flow demonstrates the lack of reproducibility and the limited capability to constantly meet the desired flow rate. By contrast, the swarms of the runs with an adaptive pressure setting are almost ideally centered around the target flow rate. The high fluctuations of the first run are reflected in the extended spread of the swarm along the y-axis.

Very similar observations could be made for the runs with P25 (Figure 6.9B). While all runs with an adaptive pressure control met the target flow rate very accurately, this was only the case for the third run with constant pressure. The other runs were largely off the target flow, again indicating a lack of reproducibility. The noise of the measurements, represented by the extent of the swarms along the y-axis, was similar for all runs with adaptive pressure control and not larger than for the runs with constant pressure. No pressure oscillations due to inadequate PID tuning occurred.

Figure 6.9C represents the measurements with A2L7. The comparison between runs with constant and adaptive pressure confirmed the previously made observations that the adaptive pressure control leads to an improved agreement between measured flow rate and target flow rate. The most noticeable difference of the A2L7 runs compared to P30 and P25 was the massively increased amount of noise across all runs. This behavior was also observed during the recording of calibration curves and seems to be inherent to the ink composition of A2L7. A systematic evaluation of noise behavior was not within the scope of this study. However, the stark contrast between the noise levels of the different inks implies that certain components typical for bioinks have a strong influence on the behavior and measurement quality of the flow sensor. While P30 and P25 only contain water and polymers, A2L7 has a more complex composition including solid nanoparticles. A systematic evaluation of the impact of different ink components and concentrations on the quality of the flow measurement should be the subject of future investigations. This investigation should also consider alternative types of flow sensors that might be better suited to provide accurate flow data for complex media like bioinks.

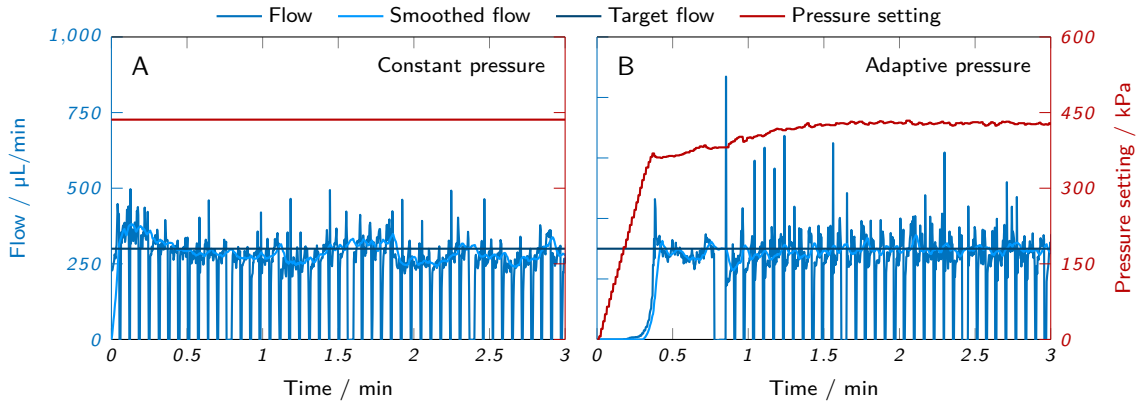

Figure 6.10 Initial phase of hollow cylinder printing with an inhomogeneous ink. The graphs show flow rate and pressure setting over time for (A) a run with constant pressure and (B) a run with adaptive pressure control. With constant pressure, the printing process was started immediately. Adaptive runs were started with an initial adaptation phase of 30 to 60 s during which the pressure was adapted, until a constant ink flow was achieved

The continuous dispensing runs prove the suitability of the adaptive pressure control to rapidly generate a constant and defined ink flow, independent of the material and without the need for extensive parameter screenings. Adopting the flow rate as a relevant parameter in process development could simplify the transfer between different inks by aiming at a common target flow rate. Larger flow rate fluctuations could be shown to be reduced by the adaptive PID pressure control.

6.3.3.2 Adaptation to ink inhomogeneities

While continuous dispensing tests can provide valuable insights about the general behavior of the adaptive pressure control, they do not represent the intended application in 3D bioprinting. To investigate the capabilities of the adaptive pressure control more thoroughly in a realistic use case, simple 3D objects were printed from a cartridge with an intentionally inhomogeneous ink. The inhomogeneity was created by filling the cartridge with alternating layers of P30 and P25 to create a situation where the extrusion conditions change repeatedly over time due to the different rheological properties of both inks. For better visualization, the inks were dyed with food coloring, as depicted in Figure 6.2B. To reduce the complexity of the printing process to a minimum, simple hollow cylinders were printed (10 mm diameter, 3 mm in height, 300 µm layers, 10 mm/s printing speed). For both runs, the sensor output was converted to flow rates based on the calibration curve of P30. A new cartridge containing three layers of P30 and three layers of P25 was used for each run.

Figure 6.10 shows the initial phase of the two runs performed with constant and adaptive pressure side-by-side. Before starting a print with the adaptive pressure control, the pressure was set to zero and a continuous dispensing process was started to allow the PID control to gradually adapt the pressure, until a stable ink flow of 300 µL/min was achieved. This adaptation phase is represented in the first 45 s of Figure 6.10B. The transitions from one printed layer to the next are clearly visible in the form of sudden drops in flow rate, as the pressure is released from the cartridge during the transition and no ink is extruded. Particularly in the run with adaptive pressure, short spikes in

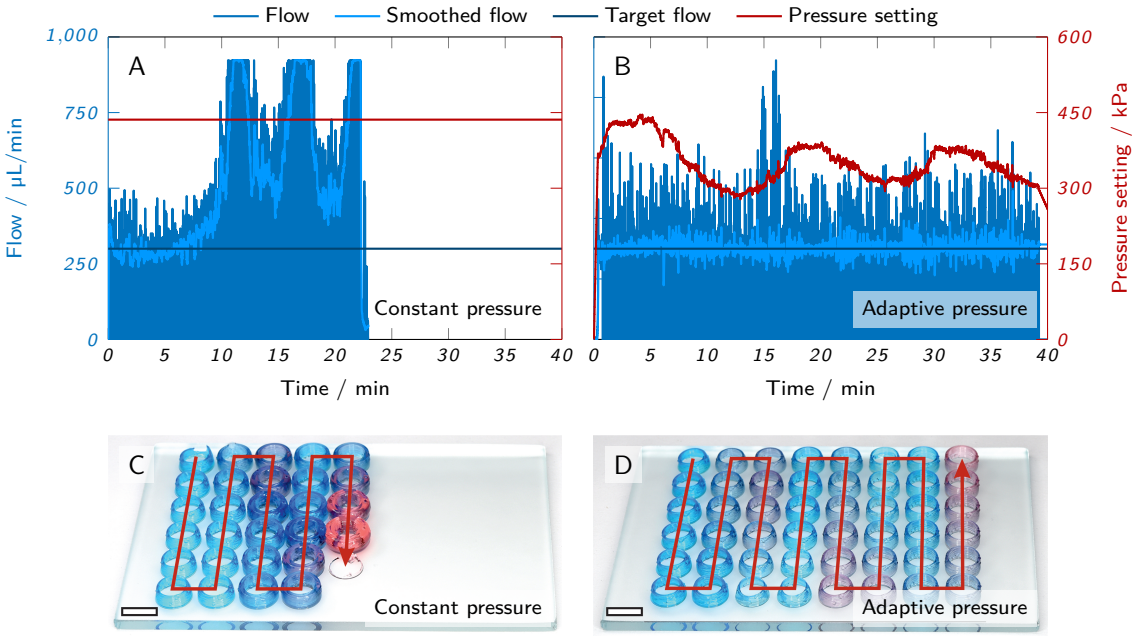

Figure 6.11 Printing of hollow cylinders with an inhomogeneous ink. The graphs show flow rate and pressure setting over time, the photographs the printed cylinders of (A and C) a run with constant pressure and (B and D) a run with adaptive pressure control. The scale bars in (C) and (D) represent 10 mm.

flow rate occured when the pressure was reapplied for the next layer. The PID control and the smoothed flow rate, depicted in the graphs light blue, were not affected by the flow rate drops and spikes, as they ignored invalid data points. All data points that were higher than 3 % of the sensor output limit and changed less than 20 % relative to the output limit compared to the previous data point were regarded as valid.

Figure 6.11 presents the entire results of the two performed printing runs. Figure 6.11A clearly visualizes the fluctuating flow rate when printing with a constant pressure setting optimized for P30. The measured flow rate was close to the target value of 300 µL/min at the beginning of the run when only P30 was extruded. The beginning extrusion of P25 after approximately 7 to 8 min was accompanied by a massive increase in flow rate. Thus, the three layers of P25 are reflected in the graph as three peaks of flow rate exceeding the output limit of the flow sensor. Between the layers, the flow rate did not return to the target value, but constantly exceeded it due to the mixing of the layers. As a result of the increased ink flow, the cartridge was already emptied after less than 23 min.

The PID control proved to be effective in compensating the rheologically different ink layers by continuously adapting the extrusion pressure. The three pressure peaks in Figure 6.11B reflect the three layers of P30 which require a higher extrusion pressure than P25. The pressure minima of the same graph correspond to the layers of P25. The change in pressure was not sudden, but relatively gradual, indicating a certain degree of blending between the two inks. This effect is also manifested in the absolute values of the pressure maxima and minima that did not reach the same values as in the dispensing tests of the unblended inks. The frequent and relatively regular spikes in flow rate,

especially observed in the run with adaptive pressure, were mainly caused by the sudden application of pressure to the cartridge at the start of a layer. They were accompanied by spikes of negative flow rate when the pressure was suddenly released again (not shown in the graph due to the cut-off at $y = 0$). In general, these spikes were randomly observed in several printing runs and were not related to the PID control, but probably the presence of air bubbles in the cartridge. The available data are not sufficient to assess whether these spikes are negligible measurement artifacts or a real and significant effect with potential negative impacts on the printed objects.

The printed cylinders are shown in Figure 6.11C and D. It is obvious that the cylinders printed with constant pressure exhibited a large range of different wall thicknesses due to the non-constant flow rate. Also, the cartridge was empty after only 28 cylinders, while 48 cylinders could be printed with the adaptive pressure control without emptying the cartridge entirely. Here, the wall thicknesses of the cylinders were relatively constant, independent of the extruded ink, but slight deviations in the wall thicknesses could still be observed. This can partially be attributed to drying effects, as the whole printing process lasted for nearly 40 min, but another important contributor is the suboptimal calibration applied in this experiment. For every ink, a specific calibration curve was determined that allowed converting the sensor output data to flow rate values. In this case, the calibration curve of P30 was applied whose slope was about 12 % higher than for P25 (see supplementary material). This resulted in a deviation between measured and real flow rate and caused a reduced ink flow when P25 was extruded.

The test prints with an inhomogeneous ink demonstrate the capability of the adaptive pressure control to perform real-time corrections of the extrusion pressure. The ink flow can be kept at a relatively constant value, even when conditions like ink viscosity vary over time due to inhomogeneities or environmental changes. Unlike the continuous dispensing, these experiments also demonstrate the applicability of the setup for printing and its potential profound impact on the resulting prints.

6.3.3.3 Process transfer to other nozzle types

Changing certain parameters in the experimental setup like nozzles, cartridges or printers usually requires adapting the extrusion pressure in order to achieve satisfactory printing results. Determining the appropriate pressure requires extensive parameter screenings and is often not done systematically based on objective criteria. Consequently, the process is susceptible to subjective, user-specific influences. To evaluate whether the adaptive pressure control based on flow measurements can facilitate the process transfers from one experimental setup to another, printing runs were performed with different nozzles. Besides the rheological properties of the ink, the employed nozzle has the most substantial effect on the required pressure for printing. Due to different lengths, diameters and geometries (straight vs. tapered), the pressure drop along the nozzle can vary drastically. Here, the straight 1 inch nozzle employed in all other experiments was compared to another straight nozzle with a length of 1.5 inch and a tapered nozzle, as shown in Figure 6.2C. All nozzles had the same orifice diameter of 0.58 mm. The underlying assumption of this experiment was that satisfactory printing results should be achievable with every nozzle, as long as the same flow rate of 300 µL/min is maintained. To examine the capability of the PID control to adapt to a new nozzle, four hollow cylinders were printed with each nozzle, two with a constant pressure setting, as determined for the 1 inch nozzle, and two with the adaptive pressure control being active. As before, the PID control was run for 30 to 60 s, until a relatively constant pressure was reached and the printing process could be started.

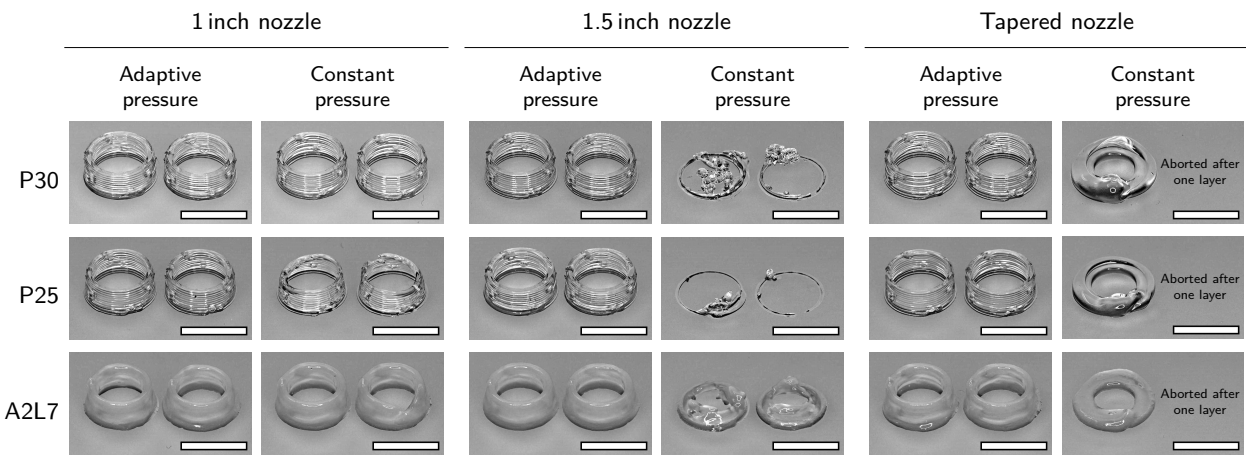

Figure 6.12 Hollow cylinders printed with different inks and nozzles. The prints were performed with either a constant pressure optimized for a 1 inch straight nozzle or with adaptive pressure control after an adjustment phase of 30 to 60 s. The scale bars represent 10 mm.

Figure 6.12 shows an overview of all printed cylinders. With the 1 inch nozzle, there was hardly any difference between cylinders printed with constant pressure compared to the adaptive pressure control. For the 1.5 inch nozzle, there was an entirely different outcome. All cylinders printed with the adaptive pressure control looked virtually identical to the ones printed with the 1 inch nozzle. When applying the constant pressure setting optimized for the 1 inch nozzle, hardly any ink could be extruded, resulting in failed prints. The opposite effect was observed for the tapered nozzle. Here, the constant extrusion pressure caused an excessive amount of ink to be extruded which is why all prints were aborted after a single layer. In combination with the adaptive pressure control, intact cylinders could be printed with the tapered nozzle.

These results demonstrate the need to adjust the pressure for every nozzle separately. Typically, such adjustments are done manually and iteratively. The PID pressure control established here was shown to achieve this adjustment within a short time frame of 30 to 60 s and with a minimal loss of sample volume. Further improvements of time and material need are possible by systematically tuning the employed PID parameters. Regarding the change of nozzle types as a pars pro toto, it can be assumed that the adaptive pressure control also allows transfers to other experimental systems like different bioprinters. However, this would require basic process variables like printing speed, layer height and nozzle orifice diameter to remain unchanged.

6.3.4 Potential challenges of working with complex cell-laden bioinks

When working with cells or biological material, maintaining sterile conditions is an important aspect which can be accounted for by employing low-cost disposable sensors or autoclavable models. Wireless sensors may facilitate the handling in a biosafety cabinet. Considering the high sensitivity of cells, the sensor and connector design should be chosen carefully to minimize shear stress by avoiding sharp edges and using high-diameter capillaries.

Due to the commonly high cost of bioinks and cells, the potential loss of material should be considered in the design of sensors and connectors to minimize dead volumes. Optimizing the PID settings may contribute to minimizing the loss of material during the initial flow adaptation phase.

It should be considered that the addition of cells and the optimization of the biological functionality of inks may impair other ink properties like flow behavior, homogeneity, printability and the interaction with the flow sensor. As a result, limitations of the calibration range and differences in noise behavior and reproducibility have to be investigated in a material-specific approach. Within the scope of this paper, we already observed the influence of different additives at several concentrations on sensor noise and calibration range (see calibration curves in the supplementary material). To assess the applicability of the presented flow control method for a wider range of complex bioinks, a systematic investigation about the influence of additives (e. g. nanoclay and polymers) and cells or special ink types (e. g. emulsions) on sensor performance is necessary. Incompatibilities with commercially available flow sensors may occur with certain types of bioinks that require more specialized equipment to guarantee printability. This includes thermo-sensitive bioinks, e. g. based on gelatin or agarose, that need to be extruded at a controlled temperature. Employing these inks in combination with the presented flow control would require either a controlled environment with constant temperature or a specialized flow sensor with an integrated temperature control.

6.3.5 Implications for process development, monitoring and control

Currently, process development for bioprinting applications often involves testing different settings for a range of parameters like pressure or printing speed. The results are assessed and suitable parameters chosen by the user in an iterative process. There is a range of approaches to find and provide objective and quantifiable criteria to determine suitable printing parameters. This includes mostly off-line analytics like evaluations of the fibre formation and rheological properties of inks [239] or filament collapse and fusion tests by image analysis [242]. Printability windows are often expressed as functions of extrusion pressure [239]. The presented application examples of the adaptive pressure control show an alternative approach based on flow rate as the leading parameter. When keeping certain parameters like nozzle orifice diameter, printing speed and layer height constant, processes can simply be transferred between different experimental systems, e. g. nozzle types or printers, by aiming at the same target flow rate. Transfers between different inks could be achieved with the same strategy, providing a material-independent approach. Adopting the flow rate as a material-independent, system-independent and user-independent parameter could lead to a paradigm shift in process development by allowing the definition of printability windows as a function of flow rate instead of pressure.

Flow rate measurements can also provide process monitoring data which are mostly not available in bioprinting. Often, there is no process monitoring at all or only qualitative monitoring, e. g. in the form of video recordings. Collecting data of the flow rate as an objective and quantifiable measurement parameter could support process validation and troubleshooting.

The main goal of the present study was to demonstrate the feasibility of an automatic adaptation of the extrusion pressure in real-time. Changes of extrusion conditions can occur when the viscosity of the extruded ink varies, e. g. due to inhomogeneities, time-dependent effects or shifting environmental conditions like temperature. Other factors like cartridge fill levels can alter extrusion conditions, as well. The performed case studies demonstrate the significant impact of actively and dynamically adapting the extrusion pressure to control the resulting ink flow. Thus, the PID-controlled setup provides a material-independent, system-independent and user-independent method to actively control and improve the printing process.

6.4 Conclusion

A PID-regulated pressure control for pneumatic extrusion-based bioprinting was established to monitor and control the flow rate of the dispensed ink. A Python-based software tool was implemented to process real-time data from a liquid flow meter and to continuously adapt the pressure in the bioprinter software to meet the specified target flow rate. The performance of the setup was evaluated with three different inks. A distinction was made between experiments with an active adaptive pressure control and experiments with a constant pressure setting. As use case we investigated the following three scenarios: a) continuous dispensing, b) adaptation to ink inhomogeneities, c) process transfer to other nozzle types.

a) Continuous dispensing: Several runs of continuous dispensing demonstrated the successful automatic adjustment of pressure to consistently meet a specified target flow rate independently of the user. Compared to the constant pressure setting, the adaptive pressure control proved effective in compensating for environmental or system-related influences like nozzle clogging.

b) Adaptation to ink inhomogeneities: A more realistic use case was investigated by printing hollow cylinders from a cartridge filled with layers of two differently concentrated poloxamer 407 inks to simulate ink inhomogeneities. The adaptive pressure control proved effective in keeping a constant flow rate by adapting the pressure appropriately during the printing process. As a result, relatively consistent cylinders could be printed, whereas the constant pressure setting resulted in cylinders with strongly deviating wall thicknesses.

c) Process transfer to other nozzle types: To demonstrate the simple process transferability between different experimental setups, test prints were carried out with three different nozzle types with the same orifice diameter. The adaptive pressure control was able to generate the same constant flow rate with all three nozzle types within 30 to 60 s. The resulting cylinders were of consistent quality, independent of the nozzle. Prints with constant pressure setting suffered from a lack or abundance of extruded ink, if not performed with a pressure specifically determined for the corresponding nozzle type.

The presented PID-regulated adaptive pressure control proved effective in generating a specified target flow, compensating in real-time for varying extrusion conditions and adapting to changes of the experimental setup. The method provides a user-independent, material-independent and system-independent approach for process development, monitoring and control. A remaining challenge is the observed high noise level in the flow rate signal of the employed sensor depending on ink type. The employment or development of more suitable sensors for complex fluids like bioinks should be considered.

Conflict of interest

The authors declare that the research was conducted in the absence of any commercial or financial relationships that could be construed as a potential conflict of interest.

Author contributions

Lukas Wenger: Conceptualization, data curation, investigation, methodology, software, validation, visualization, writing – original draft. Svenja Strauß: Conceptualization, data curation, investigation, methodology, validation, writing – original draft. Jürgen Hubbuch: Conceptualization, writing – review & editing.

Acknowledgments

Funding: This work was supported by the German Federal Ministry of Education and Research (BMBF) as project SOP-Bioprint under contract number 13XP5071B. Furthermore, special thanks go to Bianca Schroth for her support.

Chapter references

[15] I. Gibson, D. Rosen, B. Stucker, and M. Khorasani, *Additive Manufacturing Technologies*. 2021.

[46] C. Parra-Cabrera, C. Achille, S. Kuhn, and R. Ameloot, „3D printing in chemical engineering and catalytic technology: structured catalysts, mixers and reactors“, *Chemical Society Reviews*, vol. 47, pp. 209–230, 2018.

[68] K. Hölzl, S. Lin, L. Tytgat, S. Van Vlierberghe, L. Gu, and A. Ovsianikov, „Bioink properties before, during and after 3D bioprinting“, *Biofabrication*, vol. 8, no. 3, pp. 1–19, 2016.

[70] J. Malda, J. Visser, F. P. Melchels, T. Jüngst, W. E. Hennink, W. J. A. Dhert, J. Groll, and D. W. Hutmacher, „25th Anniversary Article: Engineering Hydrogels for Biofabrication“, *Advanced Materials*, vol. 25, no. 36, pp. 5011–5028, 2013.

[72] S. V. Murphy and A. Atala, „3D bioprinting of tissues and organs“, *Nature biotechnology*, vol. 32, no. 8, pp. 773–785, 2014.

[73] I. T. Ozbolat, W. Peng, and V. Ozbolat, „Application areas of 3D bioprinting“, *Drug Discovery Today*, vol. 21, no. 8, pp. 1257–1271, 2016.

[74] L. R. Darwish, M. T. El-Wakad, and M. M. Farag, „Towards an Ultra-Affordable Three-Dimensional Bioprinter: A Heated Inductive-Enabled Syringe Pump Extrusion Multifunction Module for Open-Source Fused Deposition Modeling Three-Dimensional Printers“, *Journal of Manufacturing Science and Engineering*, vol. 143, no. 12, 2021.

[75] D. Bociaga, M. Bartniak, K. Sobczak, and K. Rosinska, „An Integration of a Peristaltic Pump-Based Extruder Into a 3D Bioprinter Dedicated to Hydrogels“, *Materials*, vol. 13, no. 19, 2020.

[76] P. Fisch, M. Holub, and M. Zenobi-Wong, „Improved accuracy and precision of bioprinting through progressive cavity pump-controlled extrusion“, *Biofabrication*, vol. 13, no. 2021, pp. 1–18, 2021.

[77] L. Ning, B. Yang, F. Mohabatpour, N. Betancourt, M. D. Sarker, P. Papagerakis, and X. Chen, „Process-induced cell damage: pneumatic versus screw-driven bioprinting“, *Biofabrication*, vol. 12, no. 2, 2020.

[91] S. Krishnamoorthi, A. Banerjee, and A. Roychoudhury, „Immobilized Enzyme Technology: Potentiality and Prospects“, *Journal of Enzymology and Metabolism*, vol. 1, no. 1, pp. 1–11, 2015.

[100] B. Schmieg, J. Döbber, F. Kirschhöfer, M. Pohl, and M. Franzreb, „Advantages of Hydrogel-Based 3D-Printed Enzyme Reactors and Their Limitations for Biocatalysis“, *Frontiers in Bioengineering and Biotechnology*, vol. 6, no. January, pp. 1–12, 2019.

[101] A. S. Hoffman, „Hydrogels for biomedical applications“, *Advanced Drug Delivery Reviews*, vol. 64, no. SUPPL. Pp. 18–23, 2012.

[107] V. H. M. Mouser, F. P. W. Melchels, J. Visser, W. J. A. Dhert, D. Gawlitta, and J. Malda, „Yield stress determines bioprintability of hydrogels based on gelatin-methacryloyl and gellan gum for cartilage bioprinting.“, *Biofabrication*, vol. 8, no. 3, p. 035 003, 2016.

[193] L. Wenger, C. P. Radtke, J. Göpper, M. Wörner, and J. Hubbuch, „3D-Printable and Enzymatically Active Composite Materials Based on Hydrogel-Filled High Internal Phase Emulsions“, *Frontiers in Bioengineering and Biotechnology*, vol. 8, no. July, pp. 1–17, 2020.

[230] E. Kroll and D. Artzi, „Enhancing aerospace engineering students' learning with 3D printing wind-tunnel models“, *Rapid Prototyping Journal*, vol. 17, no. 5, pp. 393–402, 2011.

[231] B. Blakey-Milner, P. Gradl, G. Snedden, M. Brooks, J. Pitot, E. Lopez, M. Leary, F. Berto, and A. du Plessis, „Metal additive manufacturing in aerospace: A review“, *Materials and Design*, vol. 209, p. 110 008, 2021.

[232] K. V. Wong and A. Hernandez, „A Review of Additive Manufacturing“, *ISRN Mechanical Engineering*, vol. 2012, pp. 1–10, 2012.

[233] N. J. Castro, C. Meinert, P. Levett, and D. W. Hutmacher, „Current developments in multifunctional smart materials for 3D/4D bioprinting“, *Current Opinion in Biomedical Engineering*, vol. 2, pp. 67–75, 2017.

[234] R. Langer and J. P. Vacanti, „Tissue Engineering“, *Science*, vol. 260, no. 5110, pp. 920–926, 1993.

[235] J. Groll, J. A. Burdick, D. W. Cho, B. Derby, M. Gelinsky, S. C. Heilshorn, T. Jüngst, J. Malda, V. A. Mironov, K. Nakayama, A. Ovsianikov, W. Sun, S. Takeuchi, J. J. Yoo, and T. B. Woodfield, „A definition of bioinks and their distinction from biomaterial inks“, *Biofabrication*, vol. 11, no. 1, 2019.

[236] M. Hospodiuk, M. Dey, D. Sosnoski, and I. T. Ozbolat, „The bioink: A comprehensive review on bioprintable materials“, *Biotechnology Advances*, vol. 35, no. 2, pp. 217–239, 2017.

[237] C. P. Radtke, N. Hillebrandt, and J. Hubbuch, „The Biomaker: an entry-level bioprinting device for biotechnological applications“, *Journal of Chemical Technology and Biotechnology*, vol. 93, no. 3, pp. 792–799, 2018.

[238] S. Seiffert and J. Sprakel, „Physical chemistry of supramolecular polymer networks“, *Chemical Society Reviews*, vol. 41, no. 2, pp. 909–930, 2012.

[239] N. Paxton, W. Smolan, T. Böck, F. Melchels, J. Groll, and T. Jungst, „Proposal to assess printability of bioinks for extrusion-based bioprinting and evaluation of rheological properties governing bioprintability“, *Biofabrication*, vol. 9, no. 4, p. 44 107, 2017.

[240] Y. Zhao, Y. Li, S. Mao, W. Sun, and R. Yao, „The influence of printing parameters on cell survival rate and printability in microextrusion-based 3D cell printing technology“, *Biofabrication*, vol. 7, no. 4, 2015.

[241] T. G. Mezger, *The Rheology Handbook*, 4th ed. Hanover: Vincentz Network GmbH & Co. KG, 2014.

[242] A. Ribeiro, M. M. Blokzijl, R. Levato, C. W. Visser, M. Castilho, W. E. Hennink, T. Vermonden, and J. Malda, „Assessing bioink shape fidelity to aid material development in 3D bioprinting“, *Biofabrication*, vol. 10, no. 1, 2018.

[243] N. Soltan, L. Ning, F. Mohabatpour, P. Papagerakis, and X. Chen, „Printability and Cell Viability in Bioprinting Alginate Dialdehyde-Gelatin Scaffolds“, *ACS Biomaterials Science and Engineering*, vol. 5, no. 6, pp. 2976–2987, 2019.

[244] B. Webb and B. J. Doyle, „Parameter optimization for 3D bioprinting of hydrogels“, *Bioprinting*, vol. 8, no. July, pp. 8–12, 2017.

[245] M. Matamoros, J. C. Gómez-Blanco, Á. J. Sánchez, E. Mancha, A. C. Marcos, J. P. Carrasco-Amador, and J. B. Pagador, „Temperature and Humidity PID Controller for a Bioprinter Atmospheric Enclosure System“, *Micromachines*, vol. 11, no. 11, 2020.

[246] R. Opel, W. ” Hynes, and M. Moya, *Flow Sensor Integration for Precision Dispensing of Visco-Elastic Biomaterials*, 2017.

[247] S. Strauß, B. Schroth, and J. Hubbuch, „Evaluation of the Reproducibility and Robustness of Extrusion-Based Bioprinting Processes Applying a Flow Sensor“, *Frontiers in Bioengineering and Biotechnology*, vol. 10, pp. 1–14, 2022.

[248] W. J. Fleming, „Overview of Automotive Sensors“, *IEEE Sensors Journal*, vol. 1, no. 4, pp. 296–308, 2001.

[249] U. Schmid, G. Krötz, and D. Schmitt-Landsiedel, „A volumetric flow sensor for automotive injection systems“, *Journal of Micromechanics and Microengineering*, vol. 18, no. 4, 2008.

[250] Y. Li, W. Yang, C. G. Xie, S. Huang, Z. Wu, D. Tsamakis, and C. Lenn, „Gas/oil/water flow measurement by electrical capacitance tomography“, *Measurement Science and Technology*, vol. 24, no. 7, 2013.

[251] R. Thorn, G. A. Johansen, and B. T. Hjertaker, „Three-phase flow measurement in the petroleum industry“, *Measurement Science and Technology*, vol. 24, no. 1, 2013.

[252] D. L. Polla, A. G. Erdman, W. P. Robbins, D. T. Markus, J. Diaz-diaz, R. Rizq, Y. Nam, H. T. Brickner, A. Wang, and P. Krulevitch, „Microdevices in Medicine“, *Annual Review of Biomedical Engineering*, vol. 2, no. 1, pp. 551–576, 2000.

[253] C. J. Okereke, O. A. Lasode, and I. O. Ohijeagbon, „Exergoeconomic analysis of an industrial beverage mixer system: Process data“, *Data in Brief*, vol. 32, p. 106 125, 2020.

[254] L. D. Pedersen, „Assessment of sensors used in the food industry“, *Food Control*, vol. 2, no. 2, pp. 87–98, 1991.

[255] N. T. Nguyen, „Micromachined flow sensors - A review“, *Flow Measurement and Instrumentation*, vol. 8, no. 1, pp. 7–16, 1997.

[256] J. T. Kuo, L. Yu, and E. Meng, „Micromachined Thermal Flow Sensors - A Review“, *Micromachines*, vol. 3, no. 3, pp. 550–573, 2012.

[257] S. Silvestri and E. Schena, „Micromachined Flow Sensors in Biomedical Applications“, *Micromachines*, vol. 3, no. 2, pp. 225–243, 2012.

[258] C. Li, P. M. Wu, J. A. Hartings, Z. Wu, C. H. Ahn, D. Ledoux, L. A. Shutter, and R. K. Narayan, „Smart catheter flow sensor for real-time continuous regional cerebral blood flow monitoring“, *Applied Physics Letters*, vol. 99, no. 23, pp. 10–14, 2011.

[259] G. Dumortier, J. L. Grossiord, F. Agnely, and J. C. Chaumeil, „A Review of Poloxamer 407 Pharmaceutical and Pharmacological Characteristics“, *Pharmaceutical Research*, vol. 23, no. 12, pp. 2709–2728, 2006.

[260] J. A. Rowley, G. Madlambayan, and D. J. Mooney, „Alginate hydrogels as synthetic extracellular matrix materials“, *Biomaterials*, vol. 20, no. 1, pp. 45–53, 1999.

[261] A. D. Augst, H. J. Kong, and D. J. Mooney, „Alginate hydrogels as biomaterials“, *Macromolecular Bioscience*, vol. 6, no. 8, pp. 623–633, 2006.

[262] F. Pahlevanzadeh, H. Mokhtari, H. R. Bakhsheshi-Rad, R. Emadi, M. Kharaziha, A. Valiani, S. A. Poursamar, A. F. Ismail, S. RamaKrishna, and F. Berto, „Recent Trends in Three-Dimensional Bioinks Based on Alginate for Biomedical Applications“, *Materials*, vol. 13, no. 18, p. 3980, 2020.

[263] S. Duin, K. Schütz, T. Ahlfeld, S. Lehmann, A. Lode, B. Ludwig, and M. Gelinsky, „3D Bioprinting of Functional Islets of Langerhans in an Alginate/Methylcellulose Hydrogel Blend“, *Advanced Healthcare Materials*, vol. 8, no. 7, pp. 1–14, 2019.

[264] F. F. Cai, S. Heid, and A. R. Boccaccini, *Potential of Laponite® incorporated oxidized alginate-gelatin (ADA-GEL) composite hydrogels for extrusion-based 3D printing*, 2021.

[265] M. Shen, Y. Sun, J. Xu, X. Guo, and R. K. Prud'Homme, „Rheology and Adhesion of Poly(acrylic acid)/Laponite Nanocomposite Hydrogels as Biocompatible Adhesives“, *Langmuir*, vol. 30, no. 6, pp. 1636–1642, 2014.

[266] G. Schnell and R. Schäfer, „Ein thermischer Durchflußsensor für die Infusionstechnik“, *Biomedizinische Technik*, vol. 40, no. 3, pp. 50–53, 1995.

[267] Sensirion, *STEP file Sensirion SLI*, `https://sensirion.com/resource/cad/sli`, Accessed: 2022-01-26, 2021.

[268] V. Dubey, H. Goud, and P. C. Sharma, „Role of PID Control Techniques in Process Control System: A Review“, in *Data Engineering for Smart Systems*, P. Nanda, V. K. Verma, S. Srivastava, R. K. Gupta, and A. P. Mazumdar, Eds., Singapore: Springer, 2022, pp. 659–670.

[269] R. A. Paz, „The Design of the PID Controller“, PhD thesis, Klipsch School of Electrical and Computer Engineering, 2001.

[270] G. Wolterink, A. Umrani, M. Schouten, R. Sanders, and G. Krijnen, „3D-Printed Calorimetric Flow Sensor“, *2020 IEEE Sensors*, pp. 1–4, 2020.

[271] I. R. Schmolka, „Physical Basis for Poloxamer Interactions“, *Annals of the New York Academy of Sciences*, vol. 720, no. 1, pp. 92–97, 1994.

[272] H. Seki and T. Shigemasa, „Retuning oscillatory PID control loops based on plant operation data“, *Journal of Process Control*, vol. 20, no. 2, pp. 217–227, 2010.

[273] H. O. Bansal, R. Sharma, and P. R. Shreeraman, „PID Controller Tuning Techniques: A Review“, *Journal of Control Engineering and Technology*, vol. 2, no. 4, pp. 168–176, 2012.

7

Conclusion

The aim of the present work was to advance the field of 3D-printed biocatalytic devices by establishing new inks in combination with specifically adapted printing methods and suitable analytical techniques to evaluate the performance of the developed materials. In an initial study (Chapter 3), high internal phase emulsions (HIPEs) were established as suitable inks for the fabrication of composite materials containing active β-galactosidase. The inks displayed excellent printability in combination with a customized cure-on-dispense setup allowing *in situ* polymerization. The yield stress of HIPEs was determined as an important predictor of printability using rheological measurements. It was found to be highest for HIPEs with a high concentration of surfactant and a high aqueous phase volume fraction. Even complex structures involving overhangs were shown to be printable. Microplate-based activity assays were employed to determine both the enzymatic activity and leaching behavior of the printed materials. Mass transfer limitations and partial enzyme inactivation were found to be drawbacks of applying HIPEs in the given context. However, a systematic screening identified ink- and process-related parameters relevant for the preservation of activity. The presence of monomer in the aqueous phase caused a more than fivefold increase in measured specific activity compared to HIPEs without monomer in the aqueous phase. Reducing diffusion path lengths by printing with low-diameter nozzles also proved effective, resulting in a fourfold difference between samples printed with a 110 µm nozzle compared to a 840 µm nozzle.

To cover a wider range of ink types, the second and third study of the thesis aimed at investigating inks based on agarose and agar. The very different material properties of these inks compared to HIPEs required specifically adapted printing methods and analytical techniques. Diffusibility was identified as one of the most important properties of the materials used for the entrapment of enzymes. Thus, a microfluidics-based method to estimate the diffusion coefficient of an analyte within transparent hydrogels was established in Chapter 4. By creating an interface between hydrogel and an analyte solution within a microfluidic channel and monitoring the diffusion of the analyte through the hydrogel, diffusion coefficients could be estimated by fitting the obtained

analyte concentration profiles along the microfluidic channel with an analytical solution of Fick's second law of diffusion. As a case study, the diffusion coefficient of lysozyme was determined and compared in a range of hydrogels made from different concentrations of unmodified agarose and low-melt hydroxyethyl agarose.

In a third study (Chapter 5), inks based on agarose and agar were investigated as a less complex alternative to HIPE-based inks. The thermogelling behavior of agarose- and agar-based inks required a customized printing setup including a heatable nozzle to ensure ink extrusion in a liquid state at a defined temperature and to avoid nozzle clogging. The inks were extruded onto a cooled substrate to accelerate the gelation process and reduce ink spreading. While the customized setup enhanced printability significantly compared to previous studies with agarose-based inks, it was still drastically inferior to the printability of HIPEs, both regarding strand thickness and achievable complexity like overhangs. Employing a polymer concentration of at least 4.5 % (w/w) was found to be beneficial for printing. Using rheological methods, the inks were analyzed for their flow properties and their melting and gelling behavior. The solidified hydrogels were subjected to mechanical testing. A set of analytical methods established in the previous studies was reapplied to obtain more data about the agarose- and agar-based hydrogels. Microplate-based activity assays, as established in Chapter 3, were used to analyze the enzymatic activity and leaching behavior, while the microfluidics-based method for diffusion coefficient estimation (Chapter 4) was used to determine the diffusibility of the hydrogels. The agar-based hydrogels showed higher diffusibility and activity, but also increased enzyme leaching. Due to their low enzyme leaching and acceptable printability, agarose inks with a concentration of at least 4.5 % (w/w) were recommended as suitable inks for the application in biocatalytic reactors.

Independent of ink type, the previous studies revealed a general lack of reproducibility in pneumatically driven bioprinting caused by unsteady and poorly reproducible ink flow rates. Besides ink viscosity and extrusion pressure, additional factors like cartridge fill level, partial nozzle clogging and ink inhomogeneities were suspected to influence the extrusion flow rate and cause imperfections in the resulting prints. Batch-to-batch variations and temperature fluctuations influencing the ink viscosity posed additional challenges. In the study investigating agarose- and agar-based inks (Chapter 5), every printed sample was weighed before being used for activity assays and discarded if it did not comply with the set target weight within a specified margin of error. When necessary, the extrusion pressure was manually adapted to ensure the comparability of the printed samples. As a consequence, a study was initiated to establish an automated and reproducible method to generate a constant target flow rate by continuously adapting the extrusion pressure based on real-time flow rate measurements (Chapter 6). To obtain the required data in an in-line measurement, a liquid flow meter was integrated into the setup of a pneumatically driven bioprinter. A Python-based software tool was developed to process the data input and control the extrusion pressure of the printer using a PID loop. Case studies demonstrated the setup to be effective in generating a constant ink flow, handling ink inhomogeneities and facilitating the process transfer between different nozzle types. Thus, the study provides an alternative, data-driven approach towards process development, monitoring and control in bioprinting.

Overall, the present work provides a toolbox of enhanced and customized printing methods, novel inks and suitable analytical techniques relevant for the printing of biocatalytically active materials. The application of emulsion-based inks demonstrated the wide range of materials that can be employed for the immobilization of enzymes despite not being suitable matrices in tissue

engineering. Microplate-based activity assays for printed samples accelerated material screenings. The ink-specifically adapted printing methods revealed the still available potential for optimization in extrusion-based bioprinting. A universal approach to improve reproducibility for pneumatic bioprinters was provided by the PID-based pressure control. In general, process monitoring, process control and reproducibility are important aspects in bioprinting to be further addressed in the future.

8

Outlook

The first generation of 3D-printed biocatalytic reactors was based on printed synthetic grids onto which the enzyme was immobilized in a second step. In the following generation, extrusion-based bioprinting was employed to directly print enzymatically active materials, as performed in the present thesis. To use this method for the fabrication of perfusable reactors, a separate casing is necessary to contain the printed hydrogel grid. The third generation of 3D-printed biocatalytic reactors could aim at printing both the enzymatically active core and the inert casing in a single step which could be achieved by extrusion-based multi-material printing.

A leverage point to improve the performance of the enzymatically active, printed hydrogel grids is to reduce mass transfer limitations. This could be achieved by enhancing the diffusibility of the matrix or by reducing diffusion path lengths. The diffusibility of polyHIPEs could be improved by using oil-in-water instead of water-in-oil emulsions. To reduce diffusion path lengths, scaffold designs with extremely thin walls and a high surface-area-to-volume ratio are desirable. Due to the inherently limited resolution achievable with extrusion-based bioprinting, alternative printing methods like stereolithography should be explored which potentially allows feature resolutions below 100 µm and the fabrication of more complex, flow-optimized geometries. A remaining challenge when working with costly compounds like enzymes is the typically high amount of material loss associated with stereolithography, especially for the printing of small objects.

Enzyme inactivation and leaching were identified as additional parameters impairing the performance of 3D-printed biocatalytic reactors. Protection of the enzyme could be achieved by attaching poly(ethylene glycol) molecules (PEGylation) or by embedding the enzyme molecules in nanogels resulting in single-enzyme nanogels (SENs) which have demonstrated superior stability towards pH, elevated temperature and organic solvents compared to the free enzyme. To assess the effect of the stabilization methods, analytical methods would be required to differentiate between activity loss due to mass transfer limitations and activity loss caused by enzyme inactivation. Applying SENs

could also have a beneficial influence on the leaching behavior of the enzyme due to their increased size. Alternatively, the enzyme could be covalently attached to the polymer network of the hydrogel.

A disadvantage of the presented pressure control is the large footprint of the experimental setup making its application in combination with the cure-on-dispense setup or the heatable nozzle impossible. Developing the approach further with the use of a more compact flow sensor would allow the combination of the experimental setups which is the prerequisite for applying the PID-based pressure control with the developed inks.

References

[1] T. D. Ngo, A. Kashani, G. Imbalzano, K. T. Nguyen, and D. Hui, „Additive manufacturing (3D printing): A review of materials, methods, applications and challenges“, *Composites Part B: Engineering*, vol. 143, no. February, pp. 172–196, 2018.

[2] A. M. Sousa, A. C. Pinho, and A. P. Piedade, „Mechanical properties of 3D printed mouthguards: Influence of layer height and device thickness“, *Materials and Design*, vol. 203, p. 109 624, 2021.

[3] J. Saunders, M. Lißner, D. Townsend, N. Petrinic, and J. Bergmann, „Impact behaviour of 3D printed cellular structures for mouthguard applications“, *Scientific Reports*, vol. 12, no. 1, pp. 1–12, 2022.

[4] U. B. Sheela, P. G. Usha, M. M. Joseph, J. S. Melo, S. T. Thankappan Nair, and A. Tripathi, *3D printing in dental implants*. Elsevier (Singapore) Pte Ltd, 2020, pp. 83–104.

[5] A. Dawood, B. M. Marti, V. Sauret-Jackson, and A. Darwood, „3D printing in dentistry“, *British Dental Journal*, vol. 219, no. 11, pp. 521–529, 2015.

[6] K. Liang, S. Carmone, D. Brambilla, and J. C. Leroux, „3D printing of a wearable personalized oral delivery device: A first-in-human study“, *Science Advances*, vol. 4, no. 5, pp. 1–12, 2018.

[7] K. Y. Lee and D. J. Mooney, „Hydrogels for Tissue Engineering“, *Chemical Reviews*, vol. 101, no. 7, pp. 1869–1879, 2001.

[8] E. M. Ahmed, „Hydrogel: Preparation, characterization, and applications: A review“, *Journal of Advanced Research*, vol. 6, no. 2, pp. 105–121, 2015.

[9] E. Eisenbarth, „Biomaterials for Tissue Engineering“, *Advanced Engineering Materials*, vol. 9, no. 12, pp. 1051–1060, 2007.

[10] S. Hinderer, S. L. Layland, and K. Schenke-Layland, „ECM and ECM-like materials - Biomaterials for applications in regenerative medicine and cancer therapy“, *Advanced Drug Delivery Reviews*, vol. 97, pp. 260–269, 2016.

[11] J. Choi, O. C. Kwon, W. Jo, H. J. Lee, and M. W. Moon, „4D Printing Technology: A Review“, *3D Printing and Additive Manufacturing*, vol. 2, no. 4, pp. 159–167, 2015.

[12] B. Schmieg, A. Schimek, and M. Franzreb, „Development and performance of a 3D-printable poly(ethylene glycol) diacrylate hydrogel suitable for enzyme entrapment and long-term biocatalytic applications“, *Engineering in Life Sciences*, vol. 18, no. 9, pp. 659–667, 2018.

[13] S. C. Ligon, R. Liska, J. Stampfl, M. Gurr, and R. Mülhaupt, „Polymers for 3D Printing and Customized Additive Manufacturing“, *Chemical Reviews*, vol. 117, no. 15, pp. 10 212–10 290, 2017.

[14] A. Gebhardt, *Understanding Additive Manufacturing*. Munich: Hanser Publishers, 2011.

[15] I. Gibson, D. Rosen, B. Stucker, and M. Khorasani, *Additive Manufacturing Technologies*. 2021.

[16] K. Rajaguru, T. Karthikeyan, and V. Vijayan, „Additive manufacturing - State of art“, *Materials Today: Proceedings*, vol. 21, no. 1, pp. 628–633, 2020.

[17] H. Kodama, „Automatic method for fabricating a three-dimensional plastic model with photo-hardening polymer“, *Review of Scientific Instruments*, vol. 52, no. 11, pp. 1770–1773, 1981.

[18] J. J. Beaman, J. W. Barlow, D. L. Bourell, R. H. Crawford, H. L. Marcus, and K. P. McAlea, *Solid Freeform Fabrication: A New Direction in Manufacturing*. New York: Springer Science + Business Media, LLC, 1997.

[19] A. Su and S. J. Al'Aref, „History of 3D printing“, in *3D Printing Applications in Cardiovascular Medicine*, Elsevier Inc., 2018, pp. 1–10.

[20] C. W. Hull, *Apparatus for production of three-dimensional objects by stereolithography*, 1986.

[21] C. R. Deckard, *Apparatus for producing parts by selective sintering*, 1997.

[22] S. S. Crump, *Modeling apparatus for three-dimensional objects*, 1994.

[23] B. Panda, M. J. Tan, I. Gibson, and C. K. Chua, „The disruptive evolution of 3D printing“, *Proceedings of the International Conference on Progress in Additive Manufacturing*, vol. Part F1290, pp. 152–157, 2016.

[24] J. B. Roca, P. Vaishnav, J. Mendoņa, and M. G. Morgan, „Getting Past the Hype about 3-D Printing“, *MIT Sloan Management Review*, vol. 58, no. 3, pp. 57–62, 2017.

[25] B. P. Conner, G. P. Manogharan, A. N. Martof, L. M. Rodomsky, C. M. Rodomsky, D. C. Jordan, and J. W. Limperos, „Making sense of 3-D printing: Creating a map of additive manufacturing products and services“, *Additive Manufacturing*, vol. 1, pp. 64–76, 2014.

[26] N. Hopkinson and P. Dickens, „Analysis of rapid manufacturing - Using layer manufacturing processes for production“, *Proceedings of the Institution of Mechanical Engineers, Part C: Journal of Mechanical Engineering Science*, vol. 217, no. 1, pp. 31–40, 2003.

[27] H. Paris, H. Mokhtarian, E. Coatanéa, M. Museau, and I. F. Ituarte, „Comparative environmental impacts of additive and subtractive manufacturing technologies“, *CIRP Annals - Manufacturing Technology*, vol. 65, no. 1, pp. 29–32, 2016.

[28] J. R. Tumbleston, D. Shirvanyants, N. Ermoshkin, R. Janusziewicz, A. R. Johnson, D. Kelly, K. Chen, R. Pinschmidt, J. P. Rolland, A. Ermoshkin, E. T. Samulski, and J. M. DeSimone, „Continuous liquid interface production of 3D objects“, *Science*, vol. 347, no. 6228, pp. 1349–1352, 2015.

[29] J. P. Kruth, G. Levy, F. Klocke, and T. H. Childs, „Consolidation phenomena in laser and powder-bed based layered manufacturing“, *CIRP Annals - Manufacturing Technology*, vol. 56, no. 2, pp. 730–759, 2007.

[30] Z. X. Low, Y. T. Chua, B. M. Ray, D. Mattia, I. S. Metcalfe, and D. A. Patterson, „Perspective on 3D printing of separation membranes and comparison to related unconventional fabrication techniques“, *Journal of Membrane Science*, vol. 523, no. May 2016, pp. 596–613, 2017.

[31] J. M. Chacón, M. A. Caminero, E. García-Plaza, and P. J. Núñez, „Additive manufacturing of PLA structures using fused deposition modelling: Effect of process parameters on mechanical properties and their optimal selection“, *Materials and Design*, vol. 124, pp. 143–157, 2017.

[32] D. Syrlybayev, B. Zharylkassyn, A. Seisekulova, M. Akhmetov, A. Perveen, and D. Talamona, „Optimisation of strength properties of FDM printed parts - A critical review“, *Polymers*, vol. 13, no. 10, 2021.

[33] D. M. Zuev, A. K. Nguyen, V. I. Putlyaev, and R. J. Narayan, „3D printing and bioprinting using multiphoton lithography“, *Bioprinting*, vol. 20, no. May, e00090, 2020.

[34] Z. Liu, Y. Wang, B. Wu, C. Cui, Y. Guo, and C. Yan, „A critical review of fused deposition modeling 3D printing technology in manufacturing polylactic acid parts“, *International Journal of Advanced Manufacturing Technology*, vol. 102, no. 9-12, pp. 2877–2889, 2019.

[35] O. A. Mohamed, S. H. Masood, and J. L. Bhowmik, „Optimization of fused deposition modeling process parameters: a review of current research and future prospects“, *Advances in Manufacturing*, vol. 3, no. 1, pp. 42–53, 2015.

[36] P. K. Penumakala, J. Santo, and A. Thomas, „A critical review on the fused deposition modeling of thermoplastic polymer composites“, *Composites Part B: Engineering*, vol. 201, no. May, p. 108 336, 2020.

[37] A. K. Ravi, A. Deshpande, and K. H. Hsu, „An in-process laser localized pre-deposition heating approach to inter-layer bond strengthening in extrusion based polymer additive manufacturing“, *Journal of Manufacturing Processes*, vol. 24, pp. 179–185, 2016.

[38] J. Huang, Q. Qin, and J. Wang, „A Review of Stereolithography: Processes and Systems“, *Processes*, vol. 8, no. 9, 2020.

[39] R. Felzmann, S. Gruber, G. Mitteramskogler, P. Tesavibul, A. R. Boccaccini, R. Liska, and J. Stampfl, „Lithography-based additive manufacturing of cellular ceramic structures“, *Advanced Engineering Materials*, vol. 14, no. 12, pp. 1052–1058, 2012.

[40] F. Kotz, K. Arnold, W. Bauer, D. Schild, N. Keller, K. Sachsenheimer, T. M. Nargang, C. Richter, D. Helmer, and B. E. Rapp, „Three-dimensional printing of transparent fused silica glass“, *Nature*, vol. 544, no. 7650, pp. 337–339, 2017.

[41] A. Mazzoli, „Selective laser sintering in biomedical engineering“, *Medical and Biological Engineering and Computing*, vol. 51, no. 3, pp. 245–256, 2013.

[42] S. L. Sing, W. Y. Yeong, F. E. Wiria, B. Y. Tay, Z. Zhao, L. Zhao, Z. Tian, and S. Yang, „Direct selective laser sintering and melting of ceramics: A review“, *Rapid Prototyping Journal*, vol. 23, no. 3, pp. 611–623, 2017.

[43] A.-N. Chen, J.-M. Wu, K. Liu, J.-Y. Chen, H. Xiao, P. Chen, C.-H. Li, and Y.-S. Shi, „High-performance ceramic parts with complex shape prepared by selective laser sintering: a review“, *Advances in Applied Ceramics*, vol. 117, no. 2, pp. 100–117, 2017.

[44] N. Shahrubudin, T. C. Lee, and R. Ramlan, „An Overview on 3D Printing Technology: Technological, Materials, and Applications“, *Procedia Manufacturing*, vol. 35, pp. 1286–1296, 2019.

[45] Y. Wang and Y. F. Zhao, „Investigation of Sintering Shrinkage in Binder Jetting Additive Manufacturing Process“, *Procedia Manufacturing*, vol. 10, pp. 779–790, 2017.

[46] C. Parra-Cabrera, C. Achille, S. Kuhn, and R. Ameloot, „3D printing in chemical engineering and catalytic technology: structured catalysts, mixers and reactors“, *Chemical Society Reviews*, vol. 47, pp. 209–230, 2018.

[47] S. Sandron, B. Heery, V. Gupta, D. A. Collins, E. P. Nesterenko, P. N. Nesterenko, M. Talebi, S. Beirne, F. Thompson, G. G. Wallace, D. Brabazon, F. Regan, and B. Paull, „3D printed metal columns for capillary liquid chromatography“, *The Analyst*, vol. 139, no. 24, pp. 6343–6347, 2014.

[48] F. Krujatz, A. Lode, J. Seidel, T. Bley, M. Gelinsky, and J. Steingroewer, „Additive Biotech—Chances, challenges, and recent applications of additive manufacturing technologies in biotechnology“, *New Biotechnology*, vol. 39, no. September, pp. 222–231, 2017.

[49] U. Simon and S. Dimartino, „Direct 3D printing of monolithic ion exchange adsorbers“, *Journal of Chromatography A*, vol. 1587, pp. 119–128, 2019.

[50] A. J. Capel, R. P. Rimington, M. P. Lewis, and S. D. Christie, „3D printing for chemical, pharmaceutical and biological applications“, *Nature Reviews Chemistry*, vol. 2, no. 12, pp. 422–436, 2018.

[51] W. G. Patrick, A. A. Nielsen, S. J. Keating, T. J. Levy, C. W. Wang, J. J. Rivera, O. Mondragón-Palomino, P. A. Carr, C. A. Voigt, N. Oxman, and D. S. Kong, „DNA Assembly in 3D Printed Fluidics“, *PLoS ONE*, vol. 10, no. 12, pp. 1–18, 2015.

[52] F. Kotz, M. Mader, N. Dellen, P. Risch, A. Kick, D. Helmer, and B. E. Rapp, „Fused Deposition Modeling of Microfluidic Chips in Polymethylmethacrylate“, *Micromachines*, vol. 11, no. 9, pp. 5–8, 2020.

[53] U. Simon, L. C. Scorza, S. Teworte, A. J. McCormick, and S. Dimartino, „Demonstration of protein capture and separation using three-dimensional printed anion exchange monoliths fabricated in one-step“, *Journal of Separation Science*, pp. 1078–1088, 2020.

[54] F. Guillemot, V. Mironov, and M. Nakamura, „Bioprinting is coming of age: Report from the International Conference on Bioprinting and Biofabrication in Bordeaux (3B'09)“, *Biofabrication*, vol. 2, no. 1, 2010.

[55] J. Groll, T. Boland, T. Blunk, J. A. Burdick, D. W. Cho, P. D. Dalton, B. Derby, G. Forgacs, Q. Li, V. A. Mironov, L. Moroni, M. Nakamura, W. Shu, S. Takeuchi, G. Vozzi, T. B. Woodfield, T. Xu, J. J. Yoo, and J. Malda, „Biofabrication: Reappraising the definition of an evolving field“, *Biofabrication*, vol. 8, no. 1, pp. 1–5, 2016.

[56] T. Billiet, E. Gevaert, T. De Schryver, M. Cornelissen, and P. Dubruel, „The 3D printing of gelatin methacrylamide cell-laden tissue-engineered constructs with high cell viability“, *Biomaterials*, vol. 35, no. 1, pp. 49–62, 2014.

[57] A. G. Tabriz, M. A. Hermida, N. R. Leslie, and W. Shu, „Three-dimensional bioprinting of complex cell laden alginate hydrogel structures“, *Biofabrication*, vol. 7, no. 4, 2015.

[58] C. A. Mandon, L. J. Blum, and C. A. Marquette, „Adding Biomolecular Recognition Capability to 3D Printed Objects“, *Analytical Chemistry*, vol. 88, no. 21, pp. 10 767–10 772, 2016.

[59] C. D. Devillard, C. A. Mandon, S. A. Lambert, L. J. Blum, and C. A. Marquette, „Bioinspired Multi-Activities 4D Printing Objects: A New Approach Toward Complex Tissue Engineering“, *Biotechnology Journal*, vol. 13, no. 12, 2018.

[60] C. D. Spicer, „Hydrogel scaffolds for tissue engineering: The importance of polymer choice“, *Polymer Chemistry*, vol. 11, no. 2, pp. 184–219, 2020.

[61] D. Richards, J. Jia, M. Yost, R. Markwald, and Y. Mei, „3D Bioprinting for Vascularized Tissue Fabrication“, *Annals of Biomedical Engineering*, vol. 45, no. 1, pp. 132–147, 2017.

[62] W. Zhao, X. Jin, Y. Cong, Y. Liu, and J. Fu, „Degradable natural polymer hydrogels for articular cartilage tissue engineering“, *Journal of Chemical Technology and Biotechnology*, vol. 88, no. 3, pp. 327–339, 2013.

[63] U. S. Madduma-Bandarage and S. V. Madihally, „Synthetic hydrogels: Synthesis, novel trends, and applications“, *Journal of Applied Polymer Science*, vol. 138, no. 19, pp. 1–23, 2021.

[64] M. C. Hacker and A. G. Mikos, *Synthetic Polymers*, Second Edi. Elsevier Inc., 2011, pp. 587–622.

[65] T. Iizawa, H. Taketa, M. Maruta, T. Ishido, T. Gotoh, and S. Sakohara, „Synthesis of Porous Poly(N-isopropylacrylamide) Gel Beads by Sedimentation Polymerization and Their Morphology“, *Journal of Applied Polymer Science*, vol. 104, pp. 842–850, 2007.

[66] L. Yang, J. S. Chu, and J. A. Fix, „Colon-specific drug delivery: New approaches and in vitro/in vivo evaluation“, *International Journal of Pharmaceutics*, vol. 235, no. 1-2, pp. 1–15, 2002.

[67] Z. Maolin, L. Jun, Y. Min, and H. Hongfei, „The swelling behavior of radiation prepared semi-interpenetrating polymer networks composed of polyNIPAAm and hydrophilic polymers“, *Radiation Physics and Chemistry*, vol. 58, no. 4, pp. 397–400, 2000.

[68] K. Hölzl, S. Lin, L. Tytgat, S. Van Vlierberghe, L. Gu, and A. Ovsianikov, „Bioink properties before, during and after 3D bioprinting“, *Biofabrication*, vol. 8, no. 3, pp. 1–19, 2016.

[69] H. Rastin, R. T. Ormsby, G. J. Atkins, and D. Losic, „3D Bioprinting of Methylcellulose/Gelatin-Methacryloyl (MC/GelMA) Bioink with High Shape Integrity“, *ACS Applied Bio Materials*, vol. 3, no. 3, pp. 1815–1826, 2020.

[70] J. Malda, J. Visser, F. P. Melchels, T. Jüngst, W. E. Hennink, W. J. A. Dhert, J. Groll, and D. W. Hutmacher, „25th Anniversary Article: Engineering Hydrogels for Biofabrication“, *Advanced Materials*, vol. 25, no. 36, pp. 5011–5028, 2013.

[71] A. GhavamiNejad, N. Ashammakhi, X. Y. Wu, and A. Khademhosseini, „Crosslinking Strategies for 3D Bioprinting of Polymeric Hydrogels“, *Small*, vol. 16, no. 35, pp. 1–30, 2020.

[72] S. V. Murphy and A. Atala, „3D bioprinting of tissues and organs“, *Nature biotechnology*, vol. 32, no. 8, pp. 773–785, 2014.

[73] I. T. Ozbolat, W. Peng, and V. Ozbolat, „Application areas of 3D bioprinting“, *Drug Discovery Today*, vol. 21, no. 8, pp. 1257–1271, 2016.

[74] L. R. Darwish, M. T. El-Wakad, and M. M. Farag, „Towards an Ultra-Affordable Three-Dimensional Bioprinter: A Heated Inductive-Enabled Syringe Pump Extrusion Multifunction Module for Open-Source Fused Deposition Modeling Three-Dimensional Printers“, *Journal of Manufacturing Science and Engineering*, vol. 143, no. 12, 2021.

[75] D. Bociaga, M. Bartniak, K. Sobczak, and K. Rosinska, „An Integration of a Peristaltic Pump-Based Extruder Into a 3D Bioprinter Dedicated to Hydrogels“, *Materials*, vol. 13, no. 19, 2020.

[76] P. Fisch, M. Holub, and M. Zenobi-Wong, „Improved accuracy and precision of bioprinting through progressive cavity pump-controlled extrusion“, *Biofabrication*, vol. 13, no. 2021, pp. 1–18, 2021.

[77] L. Ning, B. Yang, F. Mohabatpour, N. Betancourt, M. D. Sarker, P. Papagerakis, and X. Chen, „Process-induced cell damage: pneumatic versus screw-driven bioprinting“, *Biofabrication*, vol. 12, no. 2, 2020.

[78] C. Colosi, S. R. Shin, V. Manoharan, S. Massa, M. Costantini, A. Barbetta, M. R. Dokmeci, M. Dentini, and A. Khademhosseini, „Microfluidic Bioprinting of Heterogeneous 3D Tissue Constructs Using Low-Viscosity Bioink“, *Advanced Materials*, vol. 28, no. 4, 677–684a, 2016.

[79] W. Liu, Z. Zhong, N. Hu, Y. Zhou, L. Maggio, A. K. Miri, A. Fragasso, X. Jin, A. Khademhosseini, and Y. S. Zhang, „Coaxial extrusion bioprinting of 3D microfibrous constructs with cell-favorable gelatin methacryloyl microenvironments“, *Biofabrication*, vol. 10, no. 2, 2018.

[80] A. Illanes, Ed., *Enzyme Biocatalysis - Principles and Applications*. Springer Science + Business Media B.V., 2008, pp. 15–24.

[81] K.-E. Jaeger, A. Liese, and C. Syldatk, Eds., *Einführung in die Enzymtechnologie*. Berlin: Springer Spektrum, 2018.

[82] H. Bisswanger, *Enzyme Kinetics - Principles and Methods*, 3rd ed. Weinheim: Wiley-VCH Verlag GmbH, 2017.

[83] G. Manco, E. Adinolfi, F. M. Pisani, G. Ottolina, G. Carrea, and M. Rossi, „Overexpression and properties of a new thermophilic and thermostable esterase from Bacillus acidocaldarius with sequence similarity to hormone-sensitive lipase subfamily“, *Biochemical Journal*, vol. 332, no. 1, pp. 203–212, 1998.

[84] G. De Simone, S. Galdiero, G. Manco, D. Lang, M. Rossi, and C. Pedone, „A snapshot of a transition state analogue of a novel thermophilic esterase belonging to the subfamily of mammalian hormone-sensitive lipase“, *Journal of Molecular Biology*, vol. 303, no. 5, pp. 761–771, 2000.

[85] M. Maier, C. P. Radtke, J. Hubbuch, C. M. Niemeyer, and K. S. Rabe, „On-demand production of flow reactor cartridges by 3D printing of thermostable enzymes“, *Angewandte Chemie International Edition*, vol. 57, no. 19, pp. 5539–5543, 2018.

[86] RCSB Protein Data Bank, *PDB ID 1EVQ (carboxylesterase Est2 from Alicyclobacillus acidocaldarius)*, `https://www.rcsb.org/structure/1EVQ`, Accessed: 2022-03-15.

[87] M. M. Maksimainen, A. Lampio, M. Mertanen, O. Turunen, and J. Rouvinen, „The crystal structure of acidic β-galactosidase from Aspergillus oryzae“, *International Journal of Biological Macromolecules*, vol. 60, pp. 109–115, 2013.

[88] RCSB Protein Data Bank, *PDB ID 4IUG (β-galactosidase from Aspergillus oryzae)*, `https://www.rcsb.org/structure/4IUG`, Accessed: 2022-03-15.

[89] K. Labus, *Effective detection of biocatalysts with specified activity by using a hydrogel-based colourimetric assay - β-galactosidase case study*, 2018.

[90] E. Górecka and M. Jastrz bska, „Review article: Immobilization techniques and biopolymer carriers“, *Biotechnology and Food Science*, vol. 75, no. 1, pp. 65–86, 2011.

[91] S. Krishnamoorthi, A. Banerjee, and A. Roychoudhury, „Immobilized Enzyme Technology: Potentiality and Prospects“, *Journal of Enzymology and Metabolism*, vol. 1, no. 1, pp. 1–11, 2015.

[92] S. Nisha, S. Arun Karthick, and N. Gobi, „A Review on Methods, Application and Properties of Immobilized Enzyme“, *Chemical Science Review and Letters*, vol. 1, no. 3, pp. 148–155, 2012.

[93] O. Kirk, T. V. Borchert, and C. C. Fuglsang, „Industrial enzyme applications“, *Current Opinion in Biotechnology*, vol. 13, no. 4, pp. 345–351, 2002.

[94] A. Hasan, M. Nurunnabi, M. Morshed, A. Paul, A. Polini, T. Kuila, M. Al Hariri, Y. K. Lee, and A. A. Jaffa, „Recent advances in application of biosensors in tissue engineering“, *BioMed Research International*, vol. 2014, 2014.

[95] G. Rocchitta, A. Spanu, S. Babudieri, G. Latte, G. Madeddu, G. Galleri, S. Nuvoli, P. Bagella, M. I. Demartis, V. Fiore, R. Manetti, and P. A. Serra, „Enzyme biosensors for biomedical applications: Strategies for safeguarding analytical performances in biological fluids“, *Sensors (Switzerland)*, vol. 16, no. 6, pp. 1–21, 2016.

[96] B. M. Nestl, S. C. Hammer, B. A. Nebel, and B. Hauer, „New Generation of Biocatalysts for Organic Synthesis“, *Angewandte Chemie - International Edition*, vol. 53, no. 12, pp. 3070–3095, 2014.

[97] S. C. Mohapatra and J. T. Hsu, „Immobilization of α-chymotrypsin for use in batch and continuous reactors“, *Journal of Chemical Technology and Biotechnology*, vol. 75, no. 7, pp. 519–525, 2000.

[98] B. Rodriguez-Colinas, L. Fernandez-Arrojo, P. Santos-Moriano, A. O. Ballesteros, and F. J. Plou, *Continuous Packed Bed Reactor with Immobilized β-Galactosidase for Production of Galactooligosaccharides (GOS)*, 2016.

[99] C. Zhao, N. Zhang, H. Zheng, Q. Zhu, M. Utsumi, and Y. Yang, „Effective and long-term continuous bio-hydrogen production by optimizing fixed-bed material in the bioreactor“, *Process Biochemistry*, vol. 83, no. April, pp. 55–63, 2019.

[100] B. Schmieg, J. Döbber, F. Kirschhöfer, M. Pohl, and M. Franzreb, „Advantages of Hydrogel-Based 3D-Printed Enzyme Reactors and Their Limitations for Biocatalysis“, *Frontiers in Bioengineering and Biotechnology*, vol. 6, no. January, pp. 1–12, 2019.

[101] A. S. Hoffman, „Hydrogels for biomedical applications“, *Advanced Drug Delivery Reviews*, vol. 64, no. SUPPL. Pp. 18–23, 2012.

[102] M. S. Rehmann, K. M. Skeens, P. M. Kharkar, E. M. Ford, E. Maverakis, K. H. Lee, and A. M. Kloxin, „Tuning and Predicting Mesh Size and Protein Release from Step Growth Hydrogels“, *Biomacromolecules*, vol. 18, no. 10, pp. 3131–3142, 2017.

[103] V. Hagel, T. Haraszti, and H. Boehm, „Diffusion and interaction in PEG-DA hydrogels“, *Biointerphases*, vol. 8, no. 36, pp. 1–9, 2013.

[104] K. S. Rabe, J. Müller, M. Skoupi, and C. M. Niemeyer, „Cascades in Compartments: En Route to Machine-Assisted Biotechnology“, *Angewandte Chemie - International Edition*, vol. 56, no. 44, pp. 13 574–13 589, 2017.

[105] A. Panwar and L. P. Tan, „Current status of bioinks for micro-extrusion-based 3D bioprinting“, *Molecules*, vol. 21, no. 6, pp. 1–26, 2016.

[106] F. P. W. Melchels, W. J. A. Dhert, D. W. Hutmacher, and J. Malda, „Development and characterisation of a new bioink for additive tissue manufacturing“, *Journal of Materials Chemistry B*, vol. 2, p. 2282, 2014.

[107] V. H. M. Mouser, F. P. W. Melchels, J. Visser, W. J. A. Dhert, D. Gawlitta, and J. Malda, „Yield stress determines bioprintability of hydrogels based on gelatin-methacryloyl and gellan gum for cartilage bioprinting.“, *Biofabrication*, vol. 8, no. 3, p. 035 003, 2016.

[108] K. Markstedt, A. Mantas, I. Tournier, H. Martínez Ávila, D. Hägg, and P. Gatenholm, „3D bioprinting human chondrocytes with nanocellulose-alginate bioink for cartilage tissue engineering applications“, *Biomacromolecules*, vol. 16, no. 5, pp. 1489–1496, 2015.

[109] A. L. Rutz, K. E. Hyland, A. E. Jakus, W. R. Burghardt, and R. N. Shah, „A multimaterial bioink method for 3D printing tunable, cell-compatible hydrogels“, *Advanced Materials*, vol. 27, no. 9, pp. 1607–1614, 2015.

[110] A. Skardal, J. Zhang, L. McCoard, X. Xu, S. Oottamasathien, and G. D. Prestwich, „Photocrosslinkable hyaluronan-gelatin hydrogels for two-step bioprinting“, *Tissue Engineering - Part A*, vol. 16, no. 8, pp. 2675–2685, 2010.

[111] W. Wu, A. Deconinck, and J. A. Lewis, „Omnidirectional printing of 3D microvascular networks“, *Advanced Materials*, vol. 23, no. 24, pp. 178–183, 2011.

[112] T. J. Hinton, Q. Jallerat, R. N. Palchesko, J. H. Park, M. S. Grodzicki, H. J. Shue, M. H. Ramadan, A. R. Hudson, and A. W. Feinberg, „Three-dimensional printing of complex biological structures by freeform reversible embedding of suspended hydrogels“, *Science Advances*, vol. 1, no. 9, 2015.

[113] W. Jia, P. S. Gungor-Ozkerim, Y. S. Zhang, K. Yue, K. Zhu, W. Liu, Q. Pi, B. Byambaa, M. R. Dokmeci, S. R. Shin, and A. Khademhosseini, „Direct 3D bioprinting of perfusable vascular constructs using a blend bioink“, *Biomaterials*, vol. 106, pp. 58–68, 2016.

[114] L. A. Hockaday, K. H. Kang, N. W. Colangelo, P. Y. C. Cheung, B. Duan, E. Malone, J. Wu, L. N. Girardi, L. J. Bonassar, H. Lipson, C. C. Chu, and J. T. Butcher, „Rapid 3D printing of anatomically accurate and mechanically heterogeneous aortic valve hydrogel scaffolds“, *Biofabrication*, vol. 4, no. 3, p. 035 005, 2012.

[115] N. A. Sears, P. S. Dhavalikar, and E. M. Cosgriff-Hernandez, „Emulsion Inks for 3D Printing of High Porosity Materials“, *Macromolecular Rapid Communications*, vol. 37, no. 16, pp. 1369–1374, 2016.

[116] W. Y. Maeng, J. B. Lee, Y. H. Koh, and H. E. Kim, „Innovative in situ photocuring-assisted 3D plotting technique for complex-shaped ceramic architectures with high shape retention“, *Ceramics International*, vol. 45, no. 7, pp. 8440–8447, 2019.

[117] N. R. Cameron, P. Krajnc, and M. S. Silverstein, „Colloidal Templating“, in *Porous Polymers*, M. S. Silverstein, N. R. Cameron, and M. A. Hillmyer, Eds., Hoboken, NJ, USA: John Wiley & Sons, Inc., 2011, pp. 119–172.

[118] R. Foudazi, S. Qavi, I. Masalova, and A. Y. Malkin, „Physical chemistry of highly concentrated emulsions“, *Advances in Colloid and Interface Science*, vol. 220, pp. 78–91, 2015.

[119] N. A. Sears, T. S. Wilems, K. A. Gold, Z. Lan, S. N. Cereceres, P. S. Dhavalikar, R. Foudazi, and E. M. Cosgriff-Hernandez, „Hydrocolloid Inks for 3D Printing of Porous Hydrogels“, *Advanced Materials Technologies*, vol. 4, no. 2, p. 1 800 343, 2019.

[120] A. Y. Sergienko, H. Tai, M. Narkis, and M. S. Silverstein, „Polymerized high internal-phase emulsions: Properties and interaction with water“, *Journal of Applied Polymer Science*, vol. 84, no. 11, pp. 2018–2027, 2002.

[121] P. Hainey, I. M. Huxham, B. Rowatt, D. C. Sherrington, and L. Tetley, „Synthesis and Ultrastructural Studies, of Styrene-Divinylbenzene Polyhipe Polymers“, *Macromolecules*, vol. 24, no. 1, pp. 117–121, 1991.

[122] M. S. Silverstein, „Emulsion-templated polymers: Contemporary contemplations“, *Polymer (United Kingdom)*, vol. 126, pp. 261–282, 2017.

[123] T. Gitli and M. S. Silverstein, „Bicontinuous hydrogel–hydrophobic polymer systems through emulsion templated simultaneous polymerizations“, *Soft Matter*, vol. 4, no. 12, p. 2475, 2008.

[124] T. Gitli and M. S. Silverstein, „Emulsion templated bicontinuous hydrophobic-hydrophilic polymers: Loading and release“, *Polymer*, vol. 52, no. 1, pp. 107–115, 2011.

[125] S. Kovačič, K. Jeřabek, and P. Krajnc, „Responsive poly(acrylic acid) and poly(N-isopropylacrylamide) monoliths by high internal phase emulsion (HIPE) templating“, *Macromolecular Chemistry and Physics*, vol. 212, no. 19, pp. 2151–2158, 2011.

[126] C. Fee, S. Nawada, and S. Dimartino, „3D printed porous media columns with fine control of column packing morphology“, *Journal of Chromatography A*, vol. 1333, pp. 18–24, 2014.

[127] C. Fee, „3D-printed porous bed structures“, *Current Opinion in Chemical Engineering*, vol. 18, pp. 10–15, 2017.

[128] M. Konarova, W. Aslam, L. Ge, Q. Ma, F. Tang, V. Rudolph, and J. N. Beltramini, „Enabling Process Intensification by 3D Printing of Catalytic Structures“, *ChemCatChem*, vol. 9, no. 21, pp. 4132–4138, 2017.

[129] F. Kazenwadel, E. Biegert, J. Wohlgemuth, H. Wagner, and M. Franzreb, „A 3D-printed modular reactor setup including temperature and pH control for the compartmentalized implementation of enzyme cascades“, *Engineering in Life Sciences*, vol. 16, no. 6, pp. 560–567, 2016.

[130] M. Peng, E. Mittmann, L. Wenger, J. Hubbuch, M. K. M. Engqvist, C. M. Niemeyer, and K. S. Rabe, „3D-Printed Phenacrylate Decarboxylase Flow Reactors for the Chemoenzymatic Synthesis of 4-Hydroxystilbene“, *Chemistry – A European Journal*, vol. 25, pp. 15 998–16 001, 2019.

[131] A. Saha, T. G. Johnston, R. T. Shafranek, C. J. Goodman, J. G. Zalatan, D. W. Storti, M. A. Ganter, and A. Nelson, „Additive Manufacturing of Catalytically Active Living Materials“, *ACS Applied Materials & Interfaces*, vol. 10, no. 16, pp. 13 373–13 380, 2018.

[132] C. P. Radtke, N. Hillebrandt, and J. Hubbuch, „The Biomaker: an entry-level bioprinting device for biotechnological applications“, *Journal of Chemical Technology & Biotechnology*, vol. 93, no. 3, pp. 792–799, 2017.

[133] Vitroid, *Gyroid surface*, `https://www.thingiverse.com/thing:3091246`, Accessed: 2019-09-01, 2018.

[134] H. Princen, „Rheology of foams and highly concentrated emulsions. I. Elastic properties and yield stress of a cylindrical model system“, *Journal of Colloid and Interface Science*, vol. 91, no. 1, pp. 160–175, 1983.

[135] H. M. Princen, „Rheology of foams and highly concentrated emulsions. II. Experimental study of the yield stress and wall effects for concentrated oil-in-water emulsions“, *Journal of Colloid And Interface Science*, vol. 105, no. 1, pp. 150–171, 1985.

[136] C. Warwar Damouny and M. S. Silverstein, „Hydrogel-filled, semi-crystalline, nanoparticle-crosslinked, porous polymers from emulsion templating: Structure, properties, and shape memory“, *Polymer*, vol. 82, pp. 262–273, 2016.

[137] I. Pulko and P. Krajnc, „High internal phase emulsion templating - a path to hierarchically porous functional polymers“, *Macromolecular rapid communications*, vol. 33, no. 20, pp. 1731–46, 2012.

[138] J. M. Williams, A. J. Gray, and M. H. Wilkerson, „Emulsion Stability and Rigid Foams from Styrene or Divinylbenzene Water-in-Oil Emulsions“, *Langmuir*, vol. 6, no. 2, pp. 437–444, 1990.

[139] T. Zhang, R. A. Sanguramath, S. Israel, and M. S. Silverstein, „Emulsion Templating: Porous Polymers and beyond“, *Macromolecules*, vol. 52, no. 15, pp. 5445–5479, 2019.

[140] P. V. Iyer and L. Ananthanarayan, „Enzyme stability and stabilization - Aqueous and non-aqueous environment“, *Process Biochemistry*, vol. 43, no. 10, pp. 1019–1032, 2008.

[141] I. B. Bekard, P. Asimakis, J. Bertolini, and D. E. Dunstan, „The effects of shear flow on protein structure and function“, *Biopolymers*, vol. 95, no. 11, pp. 733–745, 2011.

[142] R. A. Luse and A. D. McLaren, „Mechamisn of Enzyme Inactivation by Ultraviolet Light and the Photochemistry of Amino Acids“, *Photochemistry and Photobiology*, vol. 2, no. 3, pp. 343–360, 1963.

[143] Y. A. Vladimirov, D. I. Roshchupkin, and E. E. Fesenko, „Photochemical Reactions in Amino Acid Residues and Inactivation of Enzymes During U.V.-Irradiation. A Review“, *Photochemistry and Photobiology*, vol. 11, no. 4, pp. 227–246, 1970.

[144] I. F. Dumitru and M. T. Nechifor, „Decrease in yeast glucose-6-phosphate dehydrogenase activity due to oxygen free radicals“, *International Journal of Biochemistry*, vol. 26, no. 2, pp. 229–233, 1994.

[145] F. I. Ustok, C. Tari, and S. Harsa, „Biochemical and thermal properties of β-galactosidase enzymes produced by artisanal yoghurt cultures“, *Food Chemistry*, vol. 119, no. 3, pp. 1114–1120, 2010.

[146] W. Wang, *Instability, stabilization, and formulation of liquid protein pharmaceuticals*. 1999, vol. 185, pp. 129–188.

[147] R. J. Russell, M. V. Pishko, A. L. Simonian, and J. R. Wild, „Poly(ethylene glycol) Hydrogel-Encapsulated Fluorophore-Enzyme Conjugates for Direct Detection of Organophosphorus Neurotoxins“, *Analytical Chemistry*, vol. 71, no. 21, pp. 4909–4912, 1999.

[148] J. Kunkel and P. Asuri, „Function, Structure, and Stability of Enzymes Confined in Agarose Gels“, *PLOS ONE*, vol. 9, no. 1, pp. 1–6, 2014.

[149] X. Zhao, Q. Lang, L. Yildirimer, Z. Y. Lin, W. Cui, N. Annabi, K. W. Ng, M. R. Dokmeci, A. M. Ghaemmaghami, and A. Khademhosseini, „Photocrosslinkable Gelatin Hydrogel for Epidermal Tissue Engineering“, *Advanced Healthcare Materials*, vol. 5, no. 1, pp. 108–118, 2016.

[150] F. You, B. F. Eames, and X. Chen, „Application of Extrusion-Based Hydrogel Bioprinting for Cartilage Tissue Engineering“, *International Journal of Molecular Sciences*, vol. 18, no. 7, pp. 8–14, 2017.

[151] P. Rastogi and B. Kandasubramanian, „Review of alginate-based hydrogel bioprinting for application in tissue engineering“, *Biofabrication*, vol. 11, no. 4, 2019.

[152] F. Tan, X. Xu, T. Deng, M. Yin, X. Zhang, and J. Wang, „Fabrication of positively charged poly(ethylene glycol)-diacrylate hydrogel as a bone tissue engineering scaffold“, *Biomedical Materials*, vol. 7, no. 5, pp. 1–10, 2012.

[153] H. Zhang, H. Xia, and Y. Zhao, „Poly(vinyl alcohol) Hydrogel Can Autonomously Self-Heal“, *ACS Macro Letters*, vol. 1, no. 11, pp. 1233–1236, 2012.

[154] I. Gibas and H. Janik, „Review: Synthetic Polymer Hydrogels for Biomedical Applications“, *Chemistry & Chemical Technology*, vol. 4, no. 4, pp. 297–304, 2010.

[155] B. Rahfoth, J. Weisser, F. Sternkopf, T. Aigner, K. Von Der Mark, and R. Bräuer, „Transplantation of allograft chondrocytes embedded in agarose gel into cartilage defects of rabbits“, *Osteoarthritis and Cartilage*, vol. 6, no. 1, pp. 50–65, 1998.

[156] W.-H. Tan and S. Takeuchi, „Monodisperse Alginate Hydrogel Microbeads for Cell Encapsulation“, *Advanced Materials*, vol. 19, no. 18, pp. 2696–2701, 2007.

[157] G. Sheelu, G. Kavitha, and N. W. Fadnavis, „Efficient Immobilization of Lecitase in Gelatin Hydrogel and Degumming of Rice Bran Oil Using a Spinning Basket Reactor“, *JAOCS, Journal of the American Oil Chemists' Society*, vol. 85, no. 8, pp. 739–748, 2008.

[158] M. Lovett, K. Lee, A. Edwards, and D. L. Kaplan, „Vascularization Strategies for Tissue Engineering“, *Tissue Engineering: Part B*, vol. 15, no. 3, pp. 353–370, 2009.

[159] L. M. Weber, C. G. Lopez, and K. S. Anseth, „Effects of PEG hydrogel crosslinking density on protein diffusion and encapsulated islet survival and function“, *Journal of Biomedical Materials Research. Part A*, vol. 90, no. 3, pp. 720–729, 2008.

[160] N. Hirota, Y. Kumaki, T. Narita, J. P. Gong, and Y. Osada, „Effect of Charge on Protein Diffusion in Hydrogels“, *Journal of Physical Chemistry B*, vol. 104, no. 42, pp. 9898–9903, 2000.

[161] F. Ye, S. Baldursdottir, S. Hvidt, H. Jensen, S. W. Larsen, A. Yaghmur, C. Larsen, and J. Østergaard, „Role of Electrostatic Interactions on the Transport of Druglike Molecules in Hydrogel-Based Articular Cartilage Mimics: Implications for Drug Delivery“, *Molecular Pharmaceutics*, vol. 13, no. 3, pp. 819–828, 2016.

[162] A. Pluen, P. A. Netti, R. K. Jain, and D. A. Berk, „Diffusion of Macromolecules in Agarose Gels: Comparison of Linear and Globular Configurations“, *Biophysical Journal*, vol. 77, no. 1, pp. 542–552, 1999.

[163] H. Deschout, J. Hagman, S. Fransson, J. Jonasson, M. Rudemo, N. Lorén, and K. Braeckmans, „Straightforward FRAP for quantitative diffusion measurements with a laser scanning microscope“, *Optics Express*, vol. 18, no. 22, p. 22 886, 2010.

[164] C. B. Müller, A. Loman, V. Pacheco, F. Koberling, D. Willbold, W. Richtering, and J. Enderlein, „Precise measurement of diffusion by multi-color dual-focus fluorescence correlation spectroscopy“, *EPL*, vol. 83, no. 4, pp. 1–5, 2008.

[165] M. H. Hettiaratchi, A. Schudel, T. Rouse, A. J. García, S. N. Thomas, R. E. Guldberg, and T. C. McDevitt, „A rapid method for determining protein diffusion through hydrogels for regenerative medicine applications“, *APL Bioengineering*, vol. 2, no. 2, 2018.

[166] C. A. Teske, M. Schroeder, R. Simon, and J. Hubbuch, „Protein-Labeling Effects in Confocal Laser Scanning Microscopy“, *Journal of Physical Chemistry B*, vol. 109, no. 28, pp. 13 811–13 817, 2005.

[167] N. O. Gustafsson, B. Westrin, A. Axelsson, and G. Zacchi, „Measurement of Diffusion Coefficients in Gels Using Holographic Laser Interferometry“, *Biotechnology Progress*, vol. 9, no. 4, pp. 436–441, 1993.

[168] C. Mattisson, P. Roger, B. Jönsson, A. Axelsson, and G. Zacchi, „Diffusion of lysozyme in gels and liquids A general approach for the determination of diffusion coefficients using holographic laser interferometry“, *Journal of Chromatography B: Biomedical Sciences and Applications*, vol. 743, no. 1-2, pp. 151–167, 2000.

[169] D. Karlsson, G. Zacchi, and A. Axelsson, „Electronic Speckle Pattern Interferometry: A Tool for Determining Diffusion and Partition Coefficients for Proteins in Gels“, *Biotechnology Progress*, vol. 18, no. 6, pp. 1423–1430, 2002.

[170] S. J. Gibbs, E. N. Lightfoot, and T. W. Root, „Protein Diffusion in Porous Gel Filtration Chromatography Media Studied by Pulsed Field Gradient NMR Spectroscopy“, *Journal of Physical Chemistry*, vol. 96, no. 18, pp. 7458–7462, 1992.

[171] J. Harmon, C. Coffman, S. Villarrial, S. Chabolla, K. A. Heisel, and V. V. Krishnan, „Determination of Molecular Self-Diffusion Coefficients Using Pulsed-Field-Gradient NMR: An Experiment for Undergraduate Physical Chemistry Laboratory“, *Journal of Chemical Education*, vol. 89, no. 6, pp. 780–783, 2012.

[172] F. Ye, H. Jensen, S. W. Larsen, A. Yaghmur, C. Larsen, and J. Østergaard, „Measurement of drug diffusivities in pharmaceutical solvents using Taylor dispersion analysis“, *Journal of Pharmaceutical and Biomedical Analysis*, vol. 61, pp. 176–183, 2012.

[173] S. S. Jensen, H. Jensen, C. Cornett, E. H. Møller, and J. Østergaard, „Insulin diffusion and self-association characterized by real-time UV imaging and Taylor dispersion analysis“, *Journal of Pharmaceutical and Biomedical Analysis*, vol. 92, pp. 203–210, 2014.

[174] S. Liang, J. Xu, L. Weng, H. Dai, X. Zhang, and L. Zhang, „Protein diffusion in agarose hydrogel in situ measured by improved refractive index method“, *Journal of Controlled Release*, vol. 115, no. 2, pp. 189–196, 2006.

[175] E. N. Dunmire, A. M. Plenys, and D. F. Katz, „Spectrophotometric analysis of molecular transport in gels“, *Journal of Controlled Release*, vol. 57, no. 2, pp. 127–140, 1999.

[176] M. P. Di Cagno, F. Clarelli, J. Vabenø, C. Lesley, S. D. Rahman, J. Cauzzo, E. Franceschinis, N. Realdon, and P. C. Stein, „Experimental Determination of Drug Diffusion Coefficients in Unstirred Aqueous Environments by Temporally Resolved Concentration Measurements“, *Molecular Pharmaceutics*, vol. 15, no. 4, pp. 1488–1494, 2018.

[177] F. Ye, A. Yaghmur, H. Jensen, S. W. Larsen, C. Larsen, and J. Østergaard, „Real-time UV imaging of drug diffusion and release from Pluronic F127 hydrogels“, *European Journal of Pharmaceutical Sciences*, vol. 43, no. 4, pp. 236–243, 2011.

[178] F. Ye, S. W. Larsen, A. Yaghmur, H. Jensen, C. Larsen, and J. Østergaard, „Real-time UV imaging of piroxicam diffusion and distribution from oil solutions into gels mimicking the subcutaneous matrix“, *European Journal of Pharmaceutical Sciences*, vol. 46, no. 1-2, pp. 72–78, 2012.

[179] A. Waldbaur, J. Kittelmann, C. P. Radtke, J. Hubbuch, and B. E. Rapp, „Microfluidics on liquid handling stations (μF-on-LHS): An industry compatible chip interface between microfluidics and automated liquid handling stations“, *Lab on a Chip*, vol. 13, no. 12, pp. 2337–2343, 2013.

[180] C. P. Radtke, M.-T. Schermeyer, Y. C. Zhai, J. Göpper, and J. Hubbuch, „Implementation of an analytical microfluidic device for the quantification of protein concentrations in high-throughput format“, *Engineering in Life Sciences*, vol. 16, no. 6, pp. 515–524, 2016.

[181] K. Haubert, T. Drier, and D. Beebe, „PDMS bonding by means of a portable, low-cost corona system“, *Lab on a Chip*, vol. 6, no. 12, pp. 1548–1549, 2006.

[182] J. Crank, *The Mathematics of Diffusion*, 2nd. Oxford: Oxford University Press, 1975.

[183] R. C. Reid, J. M. Prausnitz, and B. E. Poling, *The Properties of Gases & Liquids*, 4th, B. Sun and G. H. Fleck, Eds. New York: McGraw-Hill, Inc., 1987, pp. 22–46.

[184] N. Zhang, J. Wang, J. Ye, P. Zhao, and M. Xiao, „Oxyalkylation modification as a promising method for preparing low-melting-point agarose“, *International Journal of Biological Macromolecules*, vol. 117, no. 2017, pp. 696–703, 2018.

[185] R. B. Cook, *Derivatized agarose and method of making and using same*, 1982.

[186] T. Blachowicz, G. Ehrmann, and A. Ehrmann, „Metal additive manufacturing for satellites and rockets“, *Applied Sciences*, vol. 11, no. 24, pp. 1–15, 2021.

[187] Z. Chen, Z. Li, J. Li, C. Liu, C. Lao, Y. Fu, C. Liu, Y. Li, P. Wang, and Y. He, „3D printing of ceramics: A review“, *Journal of the European Ceramic Society*, vol. 39, no. 4, pp. 661–687, 2019.

[188] S. C. Joshi and A. A. Sheikh, „3D printing in aerospace and its long-term sustainability“, *Virtual and Physical Prototyping*, vol. 10, no. 4, pp. 175–185, 2015.

[189] R. Leal, F. M. Barreiros, L. Alves, F. Romeiro, J. C. Vasco, M. Santos, and C. Marto, „Additive manufacturing tooling for the automotive industry“, *International Journal of Advanced Manufacturing Technology*, vol. 92, no. 5-8, pp. 1671–1676, 2017.

[190] P. Wu, J. Wang, and X. Wang, „A critical review of the use of 3-D printing in the construction industry“, *Automation in Construction*, vol. 68, pp. 21–31, 2016.

[191] E. Gal-Or, Y. Gershoni, G. Scotti, S. M. Nilsson, J. Saarinen, V. Jokinen, C. J. Strachan, G. Boije Af Gennäs, J. Yli-Kauhaluoma, and T. Kotiaho, „Chemical analysis using 3D printed glass microfluidics“, *Analytical Methods*, vol. 11, no. 13, pp. 1802–1810, 2019.

[192] V. Gupta, M. Talebi, J. Deverell, S. Sandron, P. N. Nesterenko, B. Heery, F. Thompson, S. Beirne, G. G. Wallace, and B. Paull, „3D printed titanium micro-bore columns containing polymer monoliths for reversed-phase liquid chromatography“, *Analytica Chimica Acta*, vol. 910, pp. 84–94, 2016.

[193] L. Wenger, C. P. Radtke, J. Göpper, M. Wörner, and J. Hubbuch, „3D-Printable and Enzymatically Active Composite Materials Based on Hydrogel-Filled High Internal Phase Emulsions“, *Frontiers in Bioengineering and Biotechnology*, vol. 8, no. July, pp. 1–17, 2020.

[194] J. Yin, M. Yan, Y. Wang, J. Fu, and H. Suo, „3D Bioprinting of Low-Concentration Cell-Laden Gelatin Methacrylate (GelMA) Bioinks with a Two-Step Cross-linking Strategy“, *ACS Applied Materials and Interfaces*, vol. 10, no. 8, pp. 6849–6857, 2018.

[195] L. Pescosolido, W. Schuurman, J. Malda, P. Matricardi, F. Alhaique, T. Coviello, P. R. Van Weeren, W. J. Dhert, W. E. Hennink, and T. Vermonden, „Hyaluronic acid and dextran-based semi-IPN hydrogels as biomaterials for bioprinting“, *Biomacromolecules*, vol. 12, no. 5, pp. 1831–1838, 2011.

[196] E. Axpe and M. L. Oyen, „Applications of alginate-based bioinks in 3D bioprinting“, *International Journal of Molecular Sciences*, vol. 17, no. 12, 2016.

[197] N. Contessi Negrini, L. Bonetti, L. Contili, and S. Farè, „3D printing of methylcellulose-based hydrogels“, *Bioprinting*, vol. 10, 2018.

[198] N. Law, B. Doney, H. Glover, Y. Qin, Z. M. Aman, T. B. Sercombe, L. J. Liew, R. J. Dilley, and B. J. Doyle, „Characterisation of hyaluronic acid methylcellulose hydrogels for 3D bioprinting“, *Journal of the Mechanical Behavior of Biomedical Materials*, vol. 77, pp. 389–399, 2018.

[199] C. W. Peak, J. Stein, K. A. Gold, and A. K. Gaharwar, „Nanoengineered Colloidal Inks for 3D Bioprinting“, *Langmuir*, vol. 34, no. 3, pp. 917–925, 2018.

[200] S. A. Wilson, L. M. Cross, C. W. Peak, and A. K. Gaharwar, „Shear-Thinning and Thermo-Reversible Nanoengineered Inks for 3D Bioprinting“, *ACS Applied Materials and Interfaces*, vol. 9, no. 50, pp. 43 449–43 458, 2017.

[201] D. W. Renn, „Agar and Agarose: Indispensable Partners in Biotechnology“, *Industrial and Engineering Chemistry Product Research and Development*, vol. 23, no. 1, pp. 17–21, 1984.

[202] A. Sassolas, A. Hayat, and J.-L. Marty, „Entrapment Within an Agarose Gel“, in *Immobilization of Enzymes and Cells*, J. M. Guisan, Ed., Third, Humana Press / Springer, 2013, ch. Enzyme Imm, pp. 229–240.

[203] R. Armisén, „Agar and agarose biotechnological applications“, *Hydrobiologia*, vol. 221, no. 1, pp. 157–166, 1991.

[204] R. Greifenstein, T. Ballweg, T. Hashem, E. Gottwald, D. Achauer, F. Kirschhöfer, M. Nusser, G. Brenner-Weiß, E. Sedghamiz, W. Wenzel, E. Mittmann, K. S. Rabe, C. M. Niemeyer, M. Franzreb, and C. Wöll, „MOF-hosted enzymes for continuous flow catalysis in aqueous and organic solvents“, *Angewandte Chemie International Edition*, 2022.

[205] C. A. Bonino, J. E. Samorezov, O. Jeon, E. Alsberg, and S. A. Khan, „Real-time in situ rheology of alginate hydrogel photocrosslinking“, *Soft Matter*, vol. 7, no. 24, pp. 11 510–11 517, 2011.

[206] L. Wenger and J. Hubbuch, „Investigation of lysozyme diffusion in agarose hydrogels employing a microfluidics-based UV imaging approach“, *Frontiers in Bioengineering and Biotechnology*, 2022.

[207] T. Jungst, W. Smolan, K. Schacht, T. Scheibel, and J. Groll, „Strategies and Molecular Design Criteria for 3D Printable Hydrogels“, *Chemical Reviews*, vol. 116, no. 3, pp. 1496–1539, 2016.

[208] Y. Gu, L. Zhang, X. Du, Z. Fan, L. Wang, W. Sun, Y. Cheng, Y. Zhu, and C. Chen, „Reversible physical crosslinking strategy with optimal temperature for 3D bioprinting of human chondrocyte-laden gelatin methacryloyl bioink“, *Journal of Biomaterials Applications*, vol. 33, no. 5, pp. 609–618, 2018.

[209] I. T. Ozbolat, H. Chen, and Y. Yu, „Development of 'Multi-arm Bioprinter' for hybrid biofabrication of tissue engineering constructs“, *Robotics and Computer-Integrated Manufacturing*, vol. 30, no. 3, pp. 295–304, 2014.

[210] B. MacCallum, E. Naseri, H. Butler, W. MacNevin, R. A. Tasker, and A. Ahmadi, „Development of a 3D bioprinting system using a Co-Flow of calcium chloride mist“, *Bioprinting*, no. August 2019, e00085, 2020.

[211] S. Wüst, M. E. Godla, R. Müller, and S. Hofmann, „Tunable hydrogel composite with two-step processing in combination with innovative hardware upgrade for cell-based three-dimensional bioprinting“, *Acta Biomaterialia*, vol. 10, no. 2, pp. 630–640, 2014.

[212] B. Mao, T. Divoux, and P. Snabre, „Normal force controlled rheology applied to agar gelation“, *Journal of Rheology*, vol. 60, no. 3, pp. 473–489, 2016.

[213] M. M. Laronda, A. L. Rutz, S. Xiao, K. A. Whelan, F. E. Duncan, E. W. Roth, T. K. Woodruff, and R. N. Shah, „A bioprosthetic ovary created using 3D printed microporous scaffolds restores ovarian function in sterilized mice“, *Nature Communications*, vol. 8, no. May, pp. 1–10, 2017.

[214] D. Chimene, K. K. Lennox, R. R. Kaunas, and A. K. Gaharwar, „Advanced Bioinks for 3D Printing: A Materials Science Perspective“, *Annals of Biomedical Engineering*, vol. 44, no. 6, pp. 2090–2102, 2016.

[215] M. Tako and S. Nakamura, „Gelation mechanism of agarose“, *Carbohydrate Research*, vol. 180, pp. 277–284, 1988.

[216] K. te Nijenhuis, „Advances in Polymer Science Thermoreversible Networks“, *Advances in Polymer Science*, vol. 130, pp. 194–202, 1997.

[217] E. Fernández, D. López, C. Mijangos, M. Duskova-Smrckova, M. Ilavsky, and K. Dusek, „Rheological and Thermal Properties of Agarose Aqueous Solutions and Hydrogels“, *Journal of Polymer Science, Part B: Polymer Physics*, vol. 46, pp. 322–328, 2007.

[218] H. H. Selby and R. L. Whistler, „Agar“, in *Industrial Gums: Polysaccharides and Their Derivatives: Third Edition*, R. L. Whistler and J. N. Bemiller, Eds., Third Edit, Academic Press, 1993, ch. Agar, pp. 87–103.

[219] N. Zhang, J. Wang, J. Ye, P. Zhao, and M. Xiao, „Oxyalkylation modification as a promising method for preparing low-melting-point agarose“, *International Journal of Biological Macromolecules*, vol. 117, no. 2017, pp. 696–703, 2018.

[220] S. Arnott, A. Fulmer, W. E. Scott, I. C. Dea, R. Moorhouse, and D. A. Rees, „The agarose double helix and its function in agarose gel structure“, *Journal of Molecular Biology*, vol. 90, no. 2, pp. 269–284, 1974.

[221] B. Schmieg, M. Nguyen, and M. Franzreb, „Simulative Minimization of Mass Transfer Limitations Within Hydrogel-Based 3D-Printed Enzyme Carriers“, *Frontiers in Bioengineering and Biotechnology*, vol. 8, no. April, pp. 1–13, 2020.

[222] M. Maaloum, N. Pernodet, and B. Tinland, „Agarose gel structure using atomic force microscopy: Gel concentration and ionic strength effects“, *Electrophoresis*, vol. 19, no. 10, pp. 1606–1610, 1998.

[223] B. Amsden, „Solute diffusion within hydrogels. Mechanisms and models“, *Macromolecules*, vol. 31, no. 23, pp. 8382–8395, 1998.

[224] N. Kusukawa, M. V. Ostrovsky, and M. M. Garner, „Effect of gelation conditions on the gel structure and resolving power of agarose-based DNA sequencing gels“, *Electrophoresis*, vol. 20, no. 7, pp. 1455–1461, 1999.

[225] Z. H. Mohammed, M. W. Hember, R. K. Richardson, and E. R. Morris, „Kinetic and equilibrium processes in the formation and melting of agarose gels“, *Carbohydrate Polymers*, vol. 36, no. 1, pp. 15–26, 1998.

[226] N. R. Mohamad, N. H. C. Marzuki, N. A. Buang, F. Huyop, and R. A. Wahab, „An overview of technologies for immobilization of enzymes and surface analysis techniques for immobilized enzymes“, *Biotechnology and Biotechnological Equipment*, vol. 29, no. 2, pp. 205–220, 2015.

[227] P. Zucca, R. Fernandez-Lafuente, and E. Sanjust, „Agarose and its derivatives as supports for enzyme immobilization“, *Molecules*, vol. 21, no. 11, pp. 1–25, 2016.

[228] H. P. Erickson, „Size and shape of protein molecules at the nanometer level determined by sedimentation, gel filtration, and electron microscopy“, *Biological Procedures Online*, vol. 11, no. 1, pp. 32–51, 2009.

[229] K. C. Labropoulos, D. E. Niesz, S. C. Danforth, and P. G. Kevrekidis, „Dynamic rheology of agar gels: Theory and experiments. Part II: Gelation behavior of agar sols and fitting of a theoretical rheological model“, *Carbohydrate Polymers*, vol. 50, no. 4, pp. 407–415, 2002.

[230] E. Kroll and D. Artzi, „Enhancing aerospace engineering students' learning with 3D printing wind-tunnel models“, *Rapid Prototyping Journal*, vol. 17, no. 5, pp. 393–402, 2011.

[231] B. Blakey-Milner, P. Gradl, G. Snedden, M. Brooks, J. Pitot, E. Lopez, M. Leary, F. Berto, and A. du Plessis, „Metal additive manufacturing in aerospace: A review“, *Materials and Design*, vol. 209, p. 110 008, 2021.

[232] K. V. Wong and A. Hernandez, „A Review of Additive Manufacturing“, *ISRN Mechanical Engineering*, vol. 2012, pp. 1–10, 2012.

[233] N. J. Castro, C. Meinert, P. Levett, and D. W. Hutmacher, „Current developments in multifunctional smart materials for 3D/4D bioprinting“, *Current Opinion in Biomedical Engineering*, vol. 2, pp. 67–75, 2017.

[234] R. Langer and J. P. Vacanti, „Tissue Engineering“, *Science*, vol. 260, no. 5110, pp. 920–926, 1993.

[235] J. Groll, J. A. Burdick, D. W. Cho, B. Derby, M. Gelinsky, S. C. Heilshorn, T. Jüngst, J. Malda, V. A. Mironov, K. Nakayama, A. Ovsianikov, W. Sun, S. Takeuchi, J. J. Yoo, and T. B. Woodfield, „A definition of bioinks and their distinction from biomaterial inks“, *Biofabrication*, vol. 11, no. 1, 2019.

[236] M. Hospodiuk, M. Dey, D. Sosnoski, and I. T. Ozbolat, „The bioink: A comprehensive review on bioprintable materials“, *Biotechnology Advances*, vol. 35, no. 2, pp. 217–239, 2017.

[237] C. P. Radtke, N. Hillebrandt, and J. Hubbuch, „The Biomaker: an entry-level bioprinting device for biotechnological applications“, *Journal of Chemical Technology and Biotechnology*, vol. 93, no. 3, pp. 792–799, 2018.

[238] S. Seiffert and J. Sprakel, „Physical chemistry of supramolecular polymer networks“, *Chemical Society Reviews*, vol. 41, no. 2, pp. 909–930, 2012.

[239] N. Paxton, W. Smolan, T. Böck, F. Melchels, J. Groll, and T. Jungst, „Proposal to assess printability of bioinks for extrusion-based bioprinting and evaluation of rheological properties governing bioprintability“, *Biofabrication*, vol. 9, no. 4, p. 44 107, 2017.

[240] Y. Zhao, Y. Li, S. Mao, W. Sun, and R. Yao, „The influence of printing parameters on cell survival rate and printability in microextrusion-based 3D cell printing technology“, *Biofabrication*, vol. 7, no. 4, 2015.

[241] T. G. Mezger, *The Rheology Handbook*, 4th ed. Hanover: Vincentz Network GmbH & Co. KG, 2014.

[242] A. Ribeiro, M. M. Blokzijl, R. Levato, C. W. Visser, M. Castilho, W. E. Hennink, T. Vermonden, and J. Malda, „Assessing bioink shape fidelity to aid material development in 3D bioprinting“, *Biofabrication*, vol. 10, no. 1, 2018.

[243] N. Soltan, L. Ning, F. Mohabatpour, P. Papagerakis, and X. Chen, „Printability and Cell Viability in Bioprinting Alginate Dialdehyde-Gelatin Scaffolds“, *ACS Biomaterials Science and Engineering*, vol. 5, no. 6, pp. 2976–2987, 2019.

[244] B. Webb and B. J. Doyle, „Parameter optimization for 3D bioprinting of hydrogels“, *Bioprinting*, vol. 8, no. July, pp. 8–12, 2017.

[245] M. Matamoros, J. C. Gómez-Blanco, Á. J. Sánchez, E. Mancha, A. C. Marcos, J. P. Carrasco-Amador, and J. B. Pagador, „Temperature and Humidity PID Controller for a Bioprinter Atmospheric Enclosure System“, *Micromachines*, vol. 11, no. 11, 2020.

[246] R. Opel, W. ” Hynes, and M. Moya, *Flow Sensor Integration for Precision Dispensing of Visco-Elastic Biomaterials*, 2017.

[247] S. Strauß, B. Schroth, and J. Hubbuch, „Evaluation of the Reproducibility and Robustness of Extrusion-Based Bioprinting Processes Applying a Flow Sensor“, *Frontiers in Bioengineering and Biotechnology*, vol. 10, pp. 1–14, 2022.

[248] W. J. Fleming, „Overview of Automotive Sensors“, *IEEE Sensors Journal*, vol. 1, no. 4, pp. 296–308, 2001.

[249] U. Schmid, G. Krötz, and D. Schmitt-Landsiedel, „A volumetric flow sensor for automotive injection systems“, *Journal of Micromechanics and Microengineering*, vol. 18, no. 4, 2008.

[250] Y. Li, W. Yang, C. G. Xie, S. Huang, Z. Wu, D. Tsamakis, and C. Lenn, „Gas/oil/water flow measurement by electrical capacitance tomography“, *Measurement Science and Technology*, vol. 24, no. 7, 2013.

[251] R. Thorn, G. A. Johansen, and B. T. Hjertaker, „Three-phase flow measurement in the petroleum industry“, *Measurement Science and Technology*, vol. 24, no. 1, 2013.

[252] D. L. Polla, A. G. Erdman, W. P. Robbins, D. T. Markus, J. Diaz-diaz, R. Rizq, Y. Nam, H. T. Brickner, A. Wang, and P. Krulevitch, „Microdevices in Medicine“, *Annual Review of Biomedical Engineering*, vol. 2, no. 1, pp. 551–576, 2000.

[253] C. J. Okereke, O. A. Lasode, and I. O. Ohijeagbon, „Exergoeconomic analysis of an industrial beverage mixer system: Process data“, *Data in Brief*, vol. 32, p. 106 125, 2020.

[254] L. D. Pedersen, „Assessment of sensors used in the food industry“, *Food Control*, vol. 2, no. 2, pp. 87–98, 1991.

[255] N. T. Nguyen, „Micromachined flow sensors - A review“, *Flow Measurement and Instrumentation*, vol. 8, no. 1, pp. 7–16, 1997.

[256] J. T. Kuo, L. Yu, and E. Meng, „Micromachined Thermal Flow Sensors - A Review“, *Micromachines*, vol. 3, no. 3, pp. 550–573, 2012.

[257] S. Silvestri and E. Schena, „Micromachined Flow Sensors in Biomedical Applications“, *Micromachines*, vol. 3, no. 2, pp. 225–243, 2012.

[258] C. Li, P. M. Wu, J. A. Hartings, Z. Wu, C. H. Ahn, D. Ledoux, L. A. Shutter, and R. K. Narayan, „Smart catheter flow sensor for real-time continuous regional cerebral blood flow monitoring“, *Applied Physics Letters*, vol. 99, no. 23, pp. 10–14, 2011.

[259] G. Dumortier, J. L. Grossiord, F. Agnely, and J. C. Chaumeil, „A Review of Poloxamer 407 Pharmaceutical and Pharmacological Characteristics“, *Pharmaceutical Research*, vol. 23, no. 12, pp. 2709–2728, 2006.

[260] J. A. Rowley, G. Madlambayan, and D. J. Mooney, „Alginate hydrogels as synthetic extracellular matrix materials“, *Biomaterials*, vol. 20, no. 1, pp. 45–53, 1999.

[261] A. D. Augst, H. J. Kong, and D. J. Mooney, „Alginate hydrogels as biomaterials“, *Macromolecular Bioscience*, vol. 6, no. 8, pp. 623–633, 2006.

[262] F. Pahlevanzadeh, H. Mokhtari, H. R. Bakhsheshi-Rad, R. Emadi, M. Kharaziha, A. Valiani, S. A. Poursamar, A. F. Ismail, S. RamaKrishna, and F. Berto, „Recent Trends in Three-Dimensional Bioinks Based on Alginate for Biomedical Applications“, *Materials*, vol. 13, no. 18, p. 3980, 2020.

[263] S. Duin, K. Schütz, T. Ahlfeld, S. Lehmann, A. Lode, B. Ludwig, and M. Gelinsky, „3D Bioprinting of Functional Islets of Langerhans in an Alginate/Methylcellulose Hydrogel Blend“, *Advanced Healthcare Materials*, vol. 8, no. 7, pp. 1–14, 2019.

[264] F. F. Cai, S. Heid, and A. R. Boccaccini, *Potential of Laponite® incorporated oxidized alginate-gelatin (ADA-GEL) composite hydrogels for extrusion-based 3D printing*, 2021.

[265] M. Shen, Y. Sun, J. Xu, X. Guo, and R. K. Prud'Homme, „Rheology and Adhesion of Poly(acrylic acid)/Laponite Nanocomposite Hydrogels as Biocompatible Adhesives“, *Langmuir*, vol. 30, no. 6, pp. 1636–1642, 2014.

[266] G. Schnell and R. Schäfer, „Ein thermischer Durchflußsensor für die Infusionstechnik“, *Biomedizinische Technik*, vol. 40, no. 3, pp. 50–53, 1995.

[267] Sensirion, *STEP file Sensirion SLI*, `https://sensirion.com/resource/cad/sli`, Accessed: 2022-01-26, 2021.

[268] V. Dubey, H. Goud, and P. C. Sharma, „Role of PID Control Techniques in Process Control System: A Review“, in *Data Engineering for Smart Systems*, P. Nanda, V. K. Verma, S. Srivastava, R. K. Gupta, and A. P. Mazumdar, Eds., Singapore: Springer, 2022, pp. 659–670.

[269] R. A. Paz, „The Design of the PID Controller“, PhD thesis, Klipsch School of Electrical and Computer Engineering, 2001.

[270] G. Wolterink, A. Umrani, M. Schouten, R. Sanders, and G. Krijnen, „3D-Printed Calorimetric Flow Sensor“, *2020 IEEE Sensors*, pp. 1–4, 2020.

[271] I. R. Schmolka, „Physical Basis for Poloxamer Interactions“, *Annals of the New York Academy of Sciences*, vol. 720, no. 1, pp. 92–97, 1994.

[272] H. Seki and T. Shigemasa, „Retuning oscillatory PID control loops based on plant operation data“, *Journal of Process Control*, vol. 20, no. 2, pp. 217–227, 2010.

[273] H. O. Bansal, R. Sharma, and P. R. Shreeraman, „PID Controller Tuning Techniques: A Review“, *Journal of Control Engineering and Technology*, vol. 2, no. 4, pp. 168–176, 2012.

List of Figures

List of Tables

Abbreviations

Acronym	Meaning
3D	three-dimensional
AA	acrylic acid
AaEst2	esterase 2 from *Alicyclobacillus acidocaldarius*
AM	additive manufacturing
ANOVA	analysis of variance
CAD	computer-aided design
CAM	computer-aided manufacturing
CLEA	crosslinked enzyme aggregates
CLIP	continuous liquid interface production
CMOS	complementary metal-oxide-semiconductor
COM	communication port
Darocur® TPO	diphenyl(2,4,6-trimethylbenzoyl)phosphine oxide
DLP	digital light processing
DMSO	dimethyl sulfoxide
DNA	deoxyribonucleic acid
EBB	extrusion-based bioprinting
EBM	electron beam melting
EC	enzyme class
EHA	2-ehtylhexyl acrylate
ESEM	environmental scanning electron microscopy
ESPI	electron speckle pattern interferometry
FCS	dual-focus fluorescence correlation spectroscopy
FDM	fused deposition modeling
FFF	fused filament fabrication
FRAP	fluorescence recovery after photobleaching
GUI	graphical user interface
HIPE	high internal phase emulsion
HLI	holographic laser interferometry

Continued on next page

Acronym	Meaning
IBOA	isobornyl acrylate
IQR	interquartile range
LAP	lithium phenyl-2,4,6-trimethylbenzoylphosphinate
LIFT	laser-induced forward transfer
LVE	linear viscoelastic
MOSFET	metal-oxide-semiconductor field-effect transistor
ONP	2-nitrophenol
ONPG	2-nitrophenyl β-D-galactopyranoside
PBS	phosphate-buffered saline
PEG	poly(ethylene glycol)
PEG-DA 700	poly(ethylene glycol) diacrylate 700
PFG-NMR	pulsed-feld-gradient nuclear magnetic resonance
PID	proportional–integral–derivative
polyHIPE	polymerized high internal phase emulsion
RMSE	root-mean-square error
RNA	ribonucleic acid
RP	rapid prototyping
SEM	scanning electron microscopy
SLA	stereolithography apparatus
SLM	selective laser melting
SLS	selective laser sintering
STL	standard triangle language or standard tessellation language
TDA	Taylor dispersion analysis
TMPTA	trimethylolpropane triacrylate
UV	ultraviolet light
wmv	Windows Media Video (video file format)

Symbols

Symbol	Meaning
$\dot{\gamma}$	shear rate
η	viscosity
γ_A	shear strain (deformation) amplitude
$\lambda_{emission}$	emission wavelength
$\lambda_{excitation}$	excitation wavelength
τ	shear stress
ω	angular frequency
D	diffusion coefficient
F_{max}	maximum achievable compression force
G'	storage modulus
G''	loss modulus
k_B	Boltzmann's constant
R	electrical resistance
R^2	coefficient of determination

A3

Appendix Chapter 3

3D-Printable and Enzymatically Active Composite Materials Based on Hydrogel-Filled High Internal Phase Emulsions

Lukas Wenger[1,2], Carsten P. Radtke[1], Jacqueline Göpper[1], Michael Wörner[1] and Jürgen Hubbuch[1,2]

[1] Institute of Engineering in Life Sciences, Section IV: Biomolecular Separation Engineering, Karlsruhe Institute of Technology (KIT), Karlsruhe, Germany

[2] Institute of Functional Interfaces, Karlsruhe Institute of Technology (KIT), Eggenstein-Leopoldshafen, Germany

A3.1 HIPE preparation

Table A3.1 Compositions of organic phase used in this study. Most HIPEs were prepared with a concentration of 12 % (w/w) surfactant (Pluronic® L-121).

EHA (% (w/w))	IBOA (% (w/w))	TMPTA (% (w/w))	Pluronic® L-121 (% (w/w))	Darocur® TPO (% (w/w))
26.9	48.9	11.7	12.0	0.5
27.8	50.6	12.1	9.0	0.5
28.7	52.2	12.5	6.0	0.5

Table A3.2 Experimental parameters for the preparation of HIPEs with different aqueous phase volume fractions. The amounts of organic and aqueous phase were adapted in order to always produce 20 mL of HIPE in total. The addition rate of aqueous phase was adapted relative to the amount of organic phase and the time points of stirring rate changes were adapted in relation to the duration of the addition process.

				Time points of stirring rate changes	
Aqueous phase volume fraction (% (v/v))	Amount of organic phase (mL)	Amount of aqueous phase (mL)	Addition rate (mL/min)	To 800 rpm (min)	To 1000 rpm (min)
90	2	18	1.00	2.6	9.0
87.5	2.5	17.5	1.25	2.0	7.0
85	3	17	1.50	1.6	5.7
82.5	3.5	16.5	1.75	1.3	4.7
80	4	16	2.00	1.1	4.0

A3.2 Determination of equilibration time

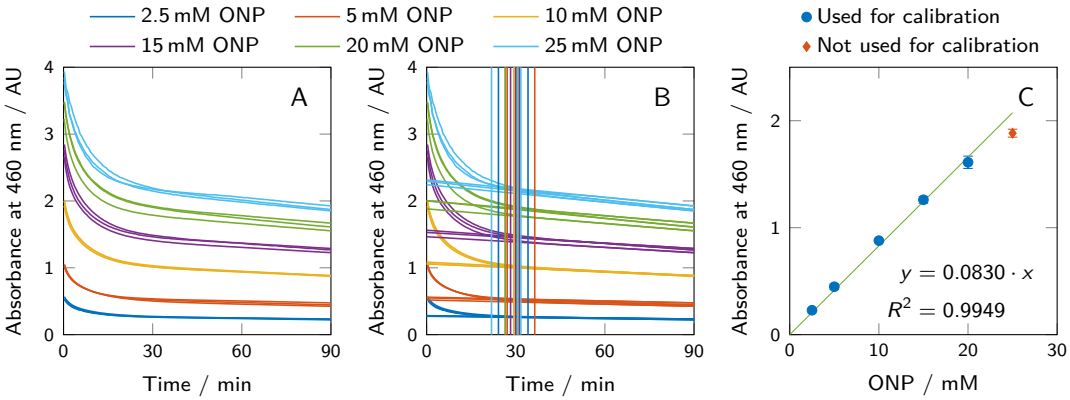

Figure A3.1 (A) Recorded raw data for ONP calibration curves and the determination of equilibration time of HIPE A. Buffered solutions of different concentrations of ONP were added to printed polyHIPE cylinders and the absorbance at 460 nm was measured for 90 min. (B) To determine the equilibration time, the last 30 min of each curve were fitted with a linear equation and the equilibration time was determined by calculating the time point at which the slope averaged over 5 min was within a 1.2-fold range of the end slope (resulting time points indicated by vertical lines). The resulting data were used to generate the equilibration time box plots. (C) ONP calibration curves were determined from the end points of the raw data in a range from 2.5 mM to 20 mM.

A3.3 PolyHIPE morphology

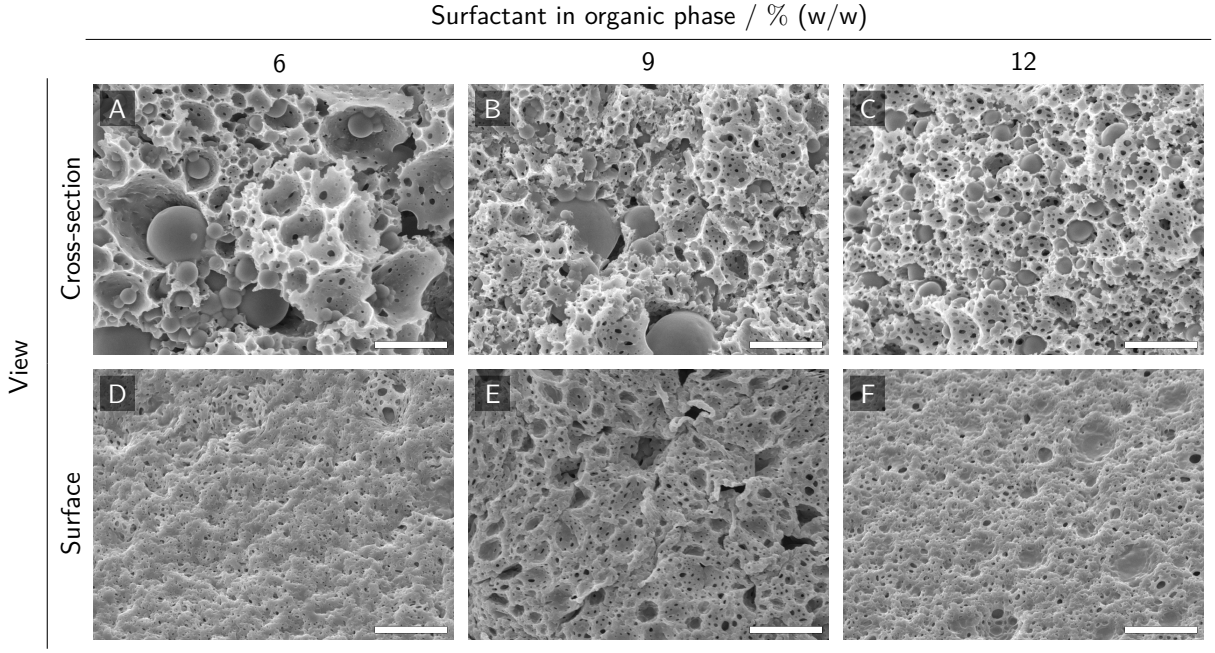

Figure A3.2 (E)SEM micrographs of polyHIPEs printed with a 250 µm conical nozzle. Samples with different surfactant mass fractions in the organic phase are shown. (A-C) View of the cross-section. (D-F) View of the surface. The scale bars represent 10 µm.

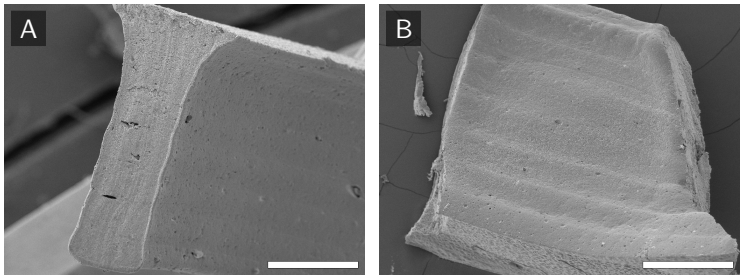

Figure A3.3 (E)SEM micrographs of a polyHIPE cylinder printed with a 250 µm nozzle. (A) View of the cross-section. (B) View of the inner surface of the cylinder. The scale bars represent 500 µm.

A3.4 Activity assay error estimation

Table A3.3 Error estimations analyzing the influence of leached enzyme on the performed activity assays with printed polyHIPE cylinders. Errors for best case and worst case scenarios are calculated based on the apparent volumetric activity $v_{apparent}$ during the polyHIPE activity assay and the volumetric activity of the supernatant after an incubation period of 90 min ($v_{leached,\,90\,\mathrm{min}}$). The values for $v_{leached,\,90\,\mathrm{min}}$ are already corrected for the dilution occuring during the supernatant activity assay.

			Volumetric activity		Error	
		Delay until max. activity	Total (observed)	Supernatant after 90 min	Worst case	Best case
		t_{delay} (min)	$v_{apparent}$ (mM/min)	$v_{leached,\,90\,\mathrm{min}}$ (mM/min)	E_{max} (%)	E_{min} (%)
Monomer (% (w/w))	14	22.2	0.268	1.2×10^{-3}	0.43	0.11
	10.5	20.1	0.256	4.2×10^{-3}	1.62	0.36
	7	19.5	0.272	3.9×10^{-4}	0.14	0.03
	3.5	30.8	0.227	3.6×10^{-3}	1.57	0.54
	1.75	29	0.195	1.4×10^{-3}	0.71	0.23
	0	68.1	0.049	1.1×10^{-3}	2.30	1.74
Surfactant (% (w/w))	12	22.2	0.268	1.2×10^{-3}	0.43	0.11
	9	31.2	0.191	1.0×10^{-3}	0.54	0.19
	6	31.9	0.184	2.5×10^{-4}	0.14	0.05
Aqueous phase (% (v/v))	90	21.3	0.296	1.7×10^{-2}	5.85	1.38
	87.5	22.2	0.268	1.2×10^{-3}	0.43	0.11
	85	38	0.207	1.9×10^{-3}	0.93	0.39
	82.5	33.7	0.149	5.8×10^{-4}	0.39	0.14
	80	22.6	0.157	1.3×10^{-3}	0.82	0.21
Nozzle diameter (µm)	840	23.2	0.249	4.7×10^{-3}	1.89	0.49
	250	22.2	0.268	1.2×10^{-3}	0.43	0.11
	110	9	0.244	3.1×10^{-2}	12.79	1.28

A5

Appendix Chapter 5

Systematic Evaluation of Agarose- and Agar-Based Bioinks for Extrusion-Based Bioprinting of Enzymatically Active Hydrogels

Lukas Wenger[1], Carsten P. Radtke[1], Eva Gerisch[1], Max Kollmann[1], Christof M. Niemeyer[2], Kersten S. Rabe[2] and Jürgen Hubbuch[1]

[1] Institute of Engineering in Life Sciences, Section IV: Biomolecular Separation Engineering, Karlsruhe Institute of Technology (KIT), Karlsruhe, Germany

[2] Institute for Biological Interfaces 1, Karlsruhe Institute of Technology (KIT), Eggenstein-Leopoldshafen, Germany

A5.1 Mass exchange surface estimation

The potential available surface for the mass exchange of printed cylinders with the surrounding liquid was estimated assuming an ideal hollow cylinder as depicted in Figure A5.1. For the calculation, certain assumptions are given by the material properties and production strategy. The material density ρ was approximately identical for all hydrogel compositions, the cylinder mass m was kept constant by adjusting the extrusion pressure to yield the desired target weight and the radius r of the cylinders was defined using the Gesim software. The volume of the hollow cylinders V can be calculated from ρ and m.

$$\begin{aligned} \rho &= 1.0\,\mathrm{g/cm^3} \\ m &= 0.1\,\mathrm{g} \\ V &= \frac{m}{\rho} = 0.1\,\mathrm{cm^3} \\ r &= 5\,\mathrm{mm} \end{aligned}$$

Height measurements showed a maximum deviation of 0.4 mm between the mean height h of cylinders printed from different materials:

$$\begin{aligned} h_{min} &= 3.0\,\mathrm{mm} \\ h_{max} &= 3.4\,\mathrm{mm} \end{aligned}$$

The base area A_{base} of the cylinders is given by:

$$A_{base} = \pi \left(r_o^2 - r_i^2\right) \tag{A5.1}$$

The inner radius r_i and the outer radius r_o can be defined as functions of the mean radius r and the thickness of the cylinder d:

$$r_i = r - \frac{d}{2} \tag{A5.2}$$

$$r_o = r + \frac{d}{2} \tag{A5.3}$$

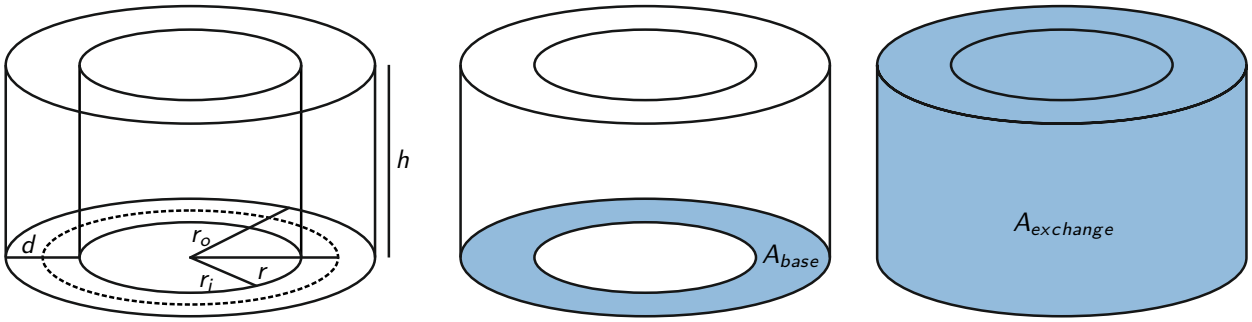

Figure A5.1 Sketches of hollow cylinders indicating the dimensions used for the mass exchange surface area estimation.

With A5.1, A5.2 and A5.3, A_{base} is given as

$$\begin{aligned} A_{base} &= \pi \left(\left(r + \frac{d}{2} \right)^2 - \left(r - \frac{d}{2} \right)^2 \right) \\ &= 2\pi r d \end{aligned} \tag{A5.4}$$

With A5.4, the volume of the cylinders V is given by:

$$V = A_{base} h = 2\pi r d h \tag{A5.5}$$

Consequently, d is given as:

$$d = \frac{V}{2\pi r h} \tag{A5.6}$$

The area available for mass transfer with the surrounding liquid $A_{exchange}$ can be defined as:

$$\begin{aligned} A_{exchange} &= A_{base} + 2\pi r_i h + 2\pi r_o h \\ &= 2\pi r (d + 2h) \end{aligned} \tag{A5.7}$$

From A5.6 and A5.7 follows:

$$\begin{aligned} A_{exchange} &= 2\pi r \left(\frac{V}{2\pi r h} + 2h \right) \\ &= \frac{V}{h} + 4\pi r h \end{aligned} \tag{A5.8}$$

The maximum and minimum exchange surface area $A_{exchange,max}$ and $A_{exchange,min}$ can be calculated from h_{max} and h_{min}:

$$\begin{aligned} A_{exchange,max} &= \frac{V}{h_{max}} + 4\pi r h_{max} \\ &= 2.00\,\mathrm{cm}^3 \end{aligned} \tag{A5.9}$$

$$\begin{aligned} A_{exchange,min} &= \frac{V}{h_{min}} + 4\pi r h_{min} \\ &= 1.84\,\mathrm{cm}^3 \end{aligned} \tag{A5.10}$$

resulting in a difference of 8.7 % between $A_{exchange,max}$ and $A_{exchange,min}$.

A5.2 Estimation of residence time in heat-controlled nozzle

The residence time of ink within the heat-controlled nozzle was calculated to evaluate whether it is sufficient to reach the desired final printing temperature. The printing distance per cylinder l_{print} is given by

$$l_{print} = n_{layers} * U_{cylinder} \tag{A5.11}$$

$$= n_{layers} * 2 * \pi * r_{cylinder} \tag{A5.12}$$

$$= 314\,\mathrm{mm} \tag{A5.13}$$

with the number of layers $n_{layers} = 10$ and a cylinder radius $r_{cylinder} = 5\,\text{mm}$. Neglecting pauses between layers, the maximum printing duration $t_{print,max}$ and minimum printing duration $t_{print,min}$ for one cylinder are dependent on the printing speed ($v_{max} = 7\,\text{mm/s}$ and $v_{min} = 5\,\text{mm/s}$):

$$t_{print,max} = \frac{l_{print}}{v_{min}} = 62.8\,\text{s} \tag{A5.14}$$

$$t_{print,min} = \frac{l_{print}}{v_{max}} = 44.9\,\text{s} \tag{A5.15}$$

The volume of the nozzle V_{nozzle} is given by its length $l_{nozzle} = 25\,\text{mm}$ and inner radius $r_{nozzle} = 0.175\,\text{mm}$:

$$V_{nozzle} = \pi * r_{nozzle}^2 * l_{nozzle} \tag{A5.16}$$

$$= 2.4\,\text{mm}^3 \tag{A5.17}$$

Finally, the residence time of ink inside the nozzle $t_{residence}$ is given by:

$$t_{residence,max} = \frac{t_{print,max} * V_{nozzle}}{V_{ink}} = 1.5\,\text{s} \tag{A5.18}$$

$$t_{residence,min} = \frac{t_{print,min} * V_{nozzle}}{V_{ink}} = 1.1\,\text{s} \tag{A5.19}$$

with $V_{ink} = 100\,\text{mm}^3$ which is given by the target mass of one cylinder $m_{cylinder} = 100\,\text{mg}$ under the assumption that the density of the ink is $\rho_{ink} = 1\,\text{g/mL}$.

A5.3 Trend analysis for activity assays with printed hydrogel cylinders

To investigate whether there was a correlation between polymer concentration of the hydrogels and the enzymatic activity determined in batch experiments, all acquired data points were divided by the substrate concentration and plotted over the polymer concentration, as shown in Figure A5.2. The data points were fitted with a linear fit and the coefficient of determination R^2 was calculated.

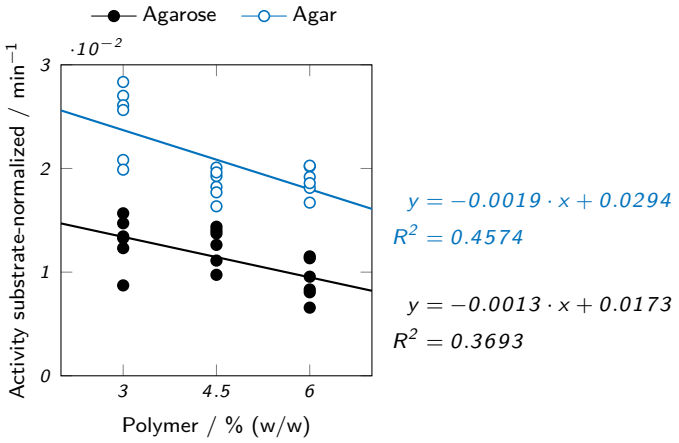

Figure A5.2 Trend analysis for activity assays of printed hydrogel cylinders made from low-melt agarose- and agar-based inks.

A6

Appendix Chapter 6

Automated and Dynamic Extrusion Pressure Adjustment Based on Real-Time Flow Rate Measurements for Precise Ink Dispensing in 3D Bioprinting

Lukas Wenger[1*], Svenja Strauß[2*] and Jürgen Hubbuch[1,2]

[1] Institute of Engineering in Life Sciences, Section IV: Biomolecular Separation Engineering, Karlsruhe Institute of Technology (KIT), Karlsruhe, Germany

[2] Institute of Functional Interfaces, Karlsruhe Institute of Technology (KIT), Eggenstein-Leopoldshafen, Germany

[*] Contributed equally

A6.1 Sensor calibration curves

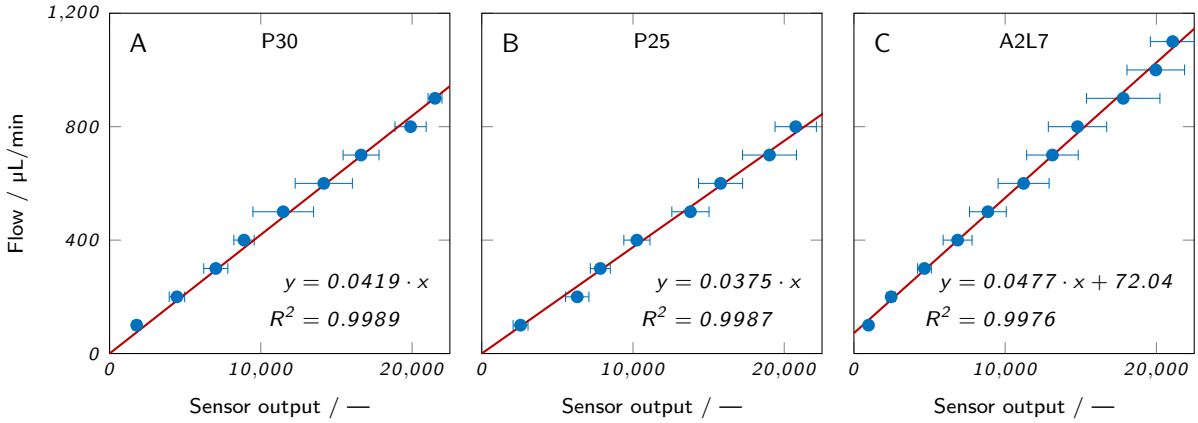

Figure A6.1 Calibration curves of all inks employed in the present study. The calibration data was stored in an Excel file and imported by the Python-based software tool to convert sensor output data to flow rate values.

A6.2 Experimental setup

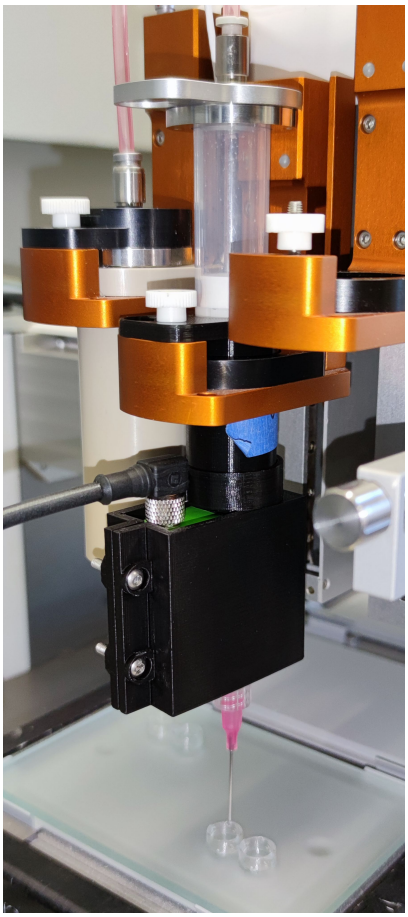

Figure A6.2 Photograph of the employed experimental setup while printing a hollow hydrogel cylinder.

A6.3 Continuous dispensing P25

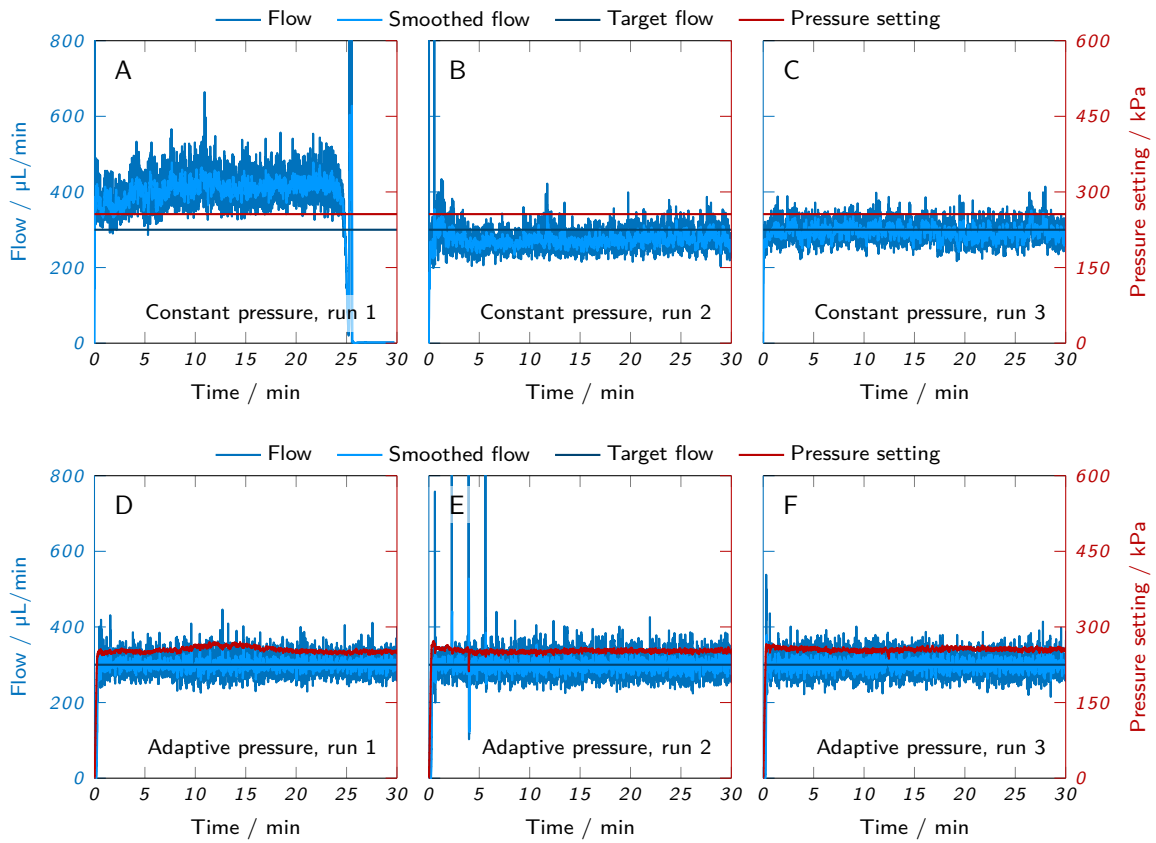

Figure A6.3 Continuous dispensing runs of P25. The measured flow and the pressure setting are plotted over time. (A-C) Runs with constant pressure setting are compared to (D-F) runs with adaptive PID pressure control and a target flow rate of 300 µL/min.

A6.4 Continuous dispensing A2L7

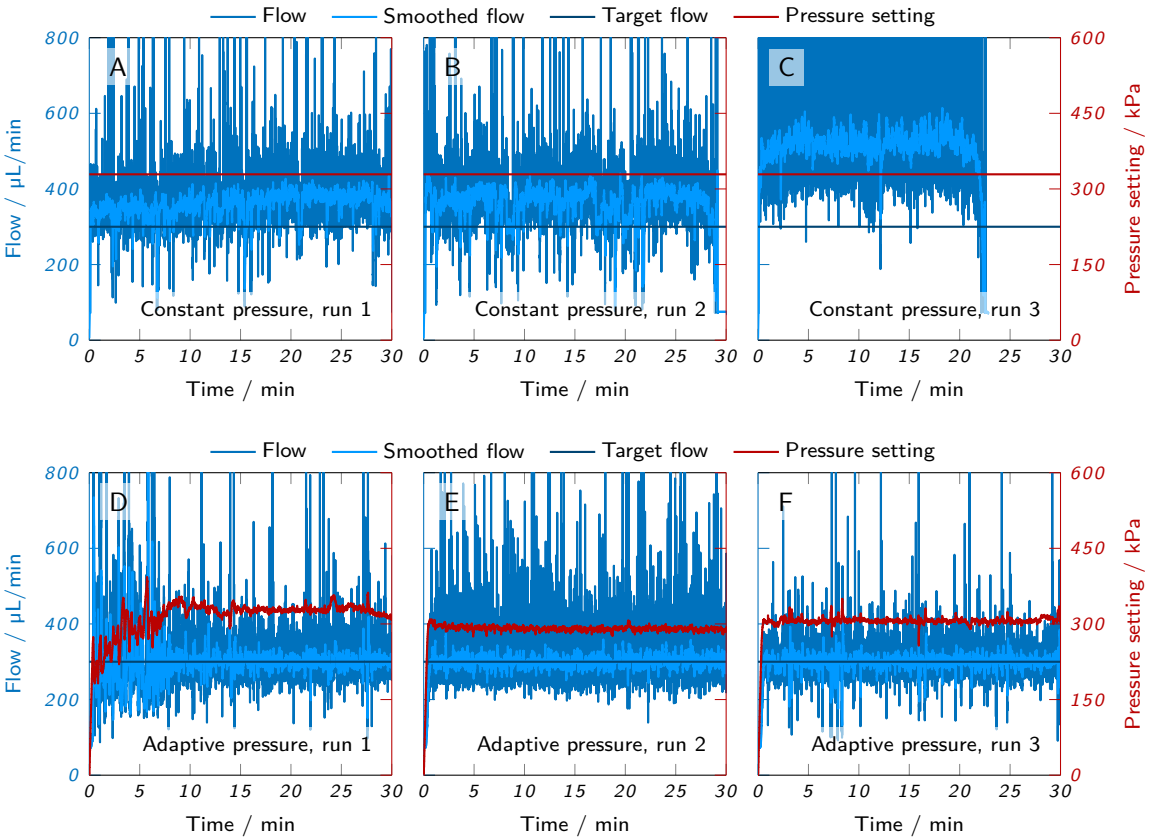

Figure A6.4 Continuous dispensing runs of A2L7. The measured flow and the pressure setting are plotted over time. (A-C) Runs with constant pressure setting are compared to (D-F) runs with adaptive PID pressure control and a target flow rate of 300 µL/min.